Pulse Pressure Testing and Analysis of Steel Plates with Openings

by

Nicholas J. Underwood MEng.

Thesis submitted in accordance with the
requirements of the University of Liverpool for
the degree of Doctor in Philosophy by
Nicholas J. Underwood
November 2013

© 2013
Nicholas J. Underwood

Abstract

Steel plates are widely used in a variety of civil engineering applications for load bearing structural components, due to their favourable strength to weight ratio. Many of these plates have openings that are commonly used for reducing weight, access for utilities or for inspection in shipping and offshore installations. However the influence of these openings to the structural component's robustness and resilience against blast loading is relatively unknown, with limited research conducted in this subject to date.

Due to the high costs associated with offshore facilities they are typically very congested. This coupled with the producing, processing, storing and transporting of hydrocarbon materials means that explosions and subsequent fires are major hazards with severe consequences. In the event of an explosion, the blast load will initially impact the secondary structure (large spanning plated sections) and then transfer through to the primary structure, highlighting their critical consideration in safety assessments. Plated structures are also known to cause confinement, which in turn will results in higher overpressures, making the consequences of an event more severe.

The aim of this research was to investigate the combined influence that openings have on the overpressure and the structural response of thin ductile plates subjected to extreme dynamic transverse loads. This was achieved by conducting a set of well-defined experiments investigating the response of 1/8 scale (0.5 m square) mild steel plates with openings subjected to pulse pressure loading. Six central (scaled) openings were considered; circular (50, 75 and 100 mm) and extended circular (50 by 75, 75 by 100 and 100 by 125 mm) representative of typical offshore and shipping applications. Each plate design was assessed with two boundary conditions (restrained and non-restrained) and two nominal loading conditions. The boundary conditions adopted in this study allowed the response to be bounded, and enabled them to be practicably modelled in FEA-analyses and in the simplified analytical approaches. A pulse pressure test facility was used to generate nominal pulse pressure loads (25 and 50 psi) applied over a time (100 to 200+ ms load duration) representative of extreme explosion loading conditions offshore. All plates exhibited a mode I type failure (large inelastic deformation) highlighting the large reserve strength in such members.

The work has shown that the inclusion of an opening ($<5\%$ of the exposed panel area) does not significantly degrade the structural resistance when damage is restricted to large inelastic deformation. The reduction in stiffness due to the hole is compensated by the reduced area to which the load is applied.

The data generated in the laboratory tests was used to develop and validate finite element models. In general, excellent correlation was observed between the experimental failure modes and the permanent displacements, within an average difference of 12% and 15% for the restrained and non-restrained plates respectively. The finite element models also provided a useful insight into the various failure processes and transient behaviour which could not be observed experimentally.

A simplified analytical model was developed to predict the response of the plates and was validated against the experimental data. The results for the permanent displacements compared favourably with the restrained plates at the two nominal pressures (6.5% at 25 psi and 7% at 50 psi), but correlated less well with the non-restrained ones (10% at 25 psi and 3% at 50 psi). Correct definition of support conditions along with a detailed description of the development of plasticity, as shown in the finite element models was fundamental in accurately predicting response of the non-restrained plates. The simplified techniques developed are cost effective compared with more sophisticated finite element methods making them suitable for preliminary engineering design studies.

Ultimately this study provides evidence to suggest that small (circular or extended circular) openings positioned away from areas of high stress, could be used as a passive system to mitigate the influences of an explosion event offshore. This has many benefits in the form of reducing weight, reducing confinement (thus lowering overpressures) and reducing the loading applied to these members, and subsequently reducing the loading transferred through to the primary structure.

Acknowledgment

I would like to extend my gratitude to my supervisor, Dr. Graham Schleyer, and all the members of the Impact Research Centre, both past and present, at the University of Liverpool. In particular, I would like to extend my sincerest gratitude to Dr. Schleyer for his continued encouragement and belief in me. Without his guidance and enthusiasm, this work would not have been possible.

I am grateful for the financial support of the Engineering and Physical Sciences Research Council (EPSRC) and the Korean government (Basic Science Research Program through the National Research Foundation of Korea (NRF) funded by the Ministry of Education, Science and Technology under Grant No. K20903002030-11E0100-04610). This enabled me to attend various international conferences and conduct several collaborative projects. Hence, I am indebted to Professor Tore Borvik and PhDc Knut Rakvag for the fruitful experimental and numerical collaboration, which included a three-week stay at the Department of Structural Engineering, NTNU.

My thanks also extend to Mr. Hyung Min Do for his help, friendship and enthusiasm, especially during the development of the analytical models. Warm thanks are given to PhDc Shaharudin Zaini for his tireless assistance during the experimental work.

I would like to thank all my friends, both in Liverpool and those from back home, for always being there to give words of support, or to provide a means of distraction when I needed it most.

Most of all, I would like to thank Laura and my family, for their unwavering love and support throughout all my endeavours.

Publications

Journal Articles

Rakvag K.G. Underwood N.J. Schleyer G.K. Borvik T. and Hopperstad O.S. Transient pressure loading of clamped metallic plates with pre-formed holes. *International Journal of Impact Engineering*, (53):44-55, 2013.

Schleyer G.K. Underwood N.J. Do H.M. Paik J.K. and Kim B.J. On pulse pressure loading of plates with holes. *Central European Journal of Engineering*, 2(4):496-508, 2012.

Papers in Conference Proceedings

Underwood N.J. Schleyer G.K. Paik J.K. and Kim B.J. Nonlinear structural consequence analysis of plates with apertures under pulse pressure loads: an experimental and numerical approach. *Proceedings of the 12th International Conference on Structures Under Shock and Impact*, 4-6th September, Kos, Greece, 2012.

Zaini S.S. Schleyer G.K. Barnett S.J. and Underwood N.J. High pressure Static Test on UHPFRC Panels Using Pulse Pressure Loading Rig. *Proceedings of Awam International Conference on Civil Engineering* AICCE' 12, Pearl of the Orient, Malaysia, 2012.

Do H.M. Schleyer G.K. Underwood N.J. Paik J.K. and Kim B.J. Buckling and ultimate strength of damaged plates with openings. *Proceedings of the 2011 World Congress on Advances in Structural Engineering and Mechanics* Techno-Press, Seoul pp 1939-1947, 2011.

Schleyer G.K. Underwood N.J. Do H.M. Paik J.K. and Kim B.J., On the simplified analysis of square plates with holes. *Proceedings of the 30th International Conference on Ocean, Offshore and Arctic Engineering* ASME, Rotterdam pp 1-5, 2011.

Schleyer G.K. and Underwood N.J. Dalzell G. Stacey N. Major Hazards Management - a finishing module for undergraduate engineers on how to manage risk. *EE2010 Engineering Education Conference*, 6-8 July, Aston University, Birmingham, UK, 2010.

Contents

List of Figures

List of Tables

Nomenclature

Acronyms	Definition
ALARP	As Low As Reasonably Practicable.
ALE	Arbitrary Lagrangian Eulerian.
API	American Petroleum Institute.
CFD	Computational Fluid Dynamics.
CMM	Coordinate Measuring Machine.
CSM	Computational Solid Mechanics.
DC01	Docol form 01 mild steel.
DDESB	Department of Defence Explosives Safety board.
DIC	Digital Image Correlation.
DIF	Dynamic Increase Factor.
DLA	Ductility Level Analysis.
DLB	Ductility Level Blast.
FABIG	Fire And Blast Information Group.
FEM	Finite Element Model.
FSI	Fluid Structure Interaction.
HSE	Health and Safety Executive.
HV	Vickers Hardness.
ISO	International Organisation for Standardisation.
JIP	Joint Industry Project.
LVDT	Linear Voltage Displacement Transducer.
PPLR	Pulse Pressure Loading Rig.

PSI	Pounds per Square Inch.
SCI	The Steel Construction Institute.
SDOF	Single Degree Of Freedom.
SHTB	Split Hopkinson Tension Bar.
SIF	Strength Increase Factor.
SLA	Strength Level Analysis.
SLB	Strength Level Blast.
SRI	Selective Reduced Integration.
TNT	Explosive (Trinitrotoluene).
UKOOA	United Kingdom Offshore Operators Association.
UTS	Ultimate Tensile Strength.

Symbols	**Definition**
A	Yield stress parameter in Modified Johnson-Cook model.
a	Typical dimension of a plate in a plane.
B	Strain-hardening parameter in Modified Johnson-Cook model.
C	Strain-rate sensitivity parameter in Modified Johnson-Cook model.
D	Cowper-Symonds coefficient.
E	Young's modulus of elasticity.
H	Storey height.
h	Plate thickness.
n	Strain-hardening parameter in Modified Johnson-Cook model.
q	Cowper-Symonds coefficient.
q	Reduction area.
T	Relative fundamental period of vibration.
w	Maximum transverse deflection of the plate.

Greek Symbols	**Definition**
β	Geometric scale factor.

Δ	Displacement.
δ	Relative sidesway deflection.
$\dot{\varepsilon}$	Average strain rate.
μ	Ductility ratio.
ρ	Mass density.
θ	Maximum member end rotation (degrees).
υ	Poisson's ratio.

Subscripts	**Definition**
Σ_0'	Dynamic flow stress in a large-scale model.
σ_0'	Dynamic flow stress in a small-scale model.
$A_\circ$	Original area.
A_{neck}	Area at fracture.
e_f	Elongation.
$L_\circ$	Original length.
L_f	Final length.
P_{max}	Maximum pressure.
t_d	Time duration of an explosion.
T_d	Depressurisation time.
T_r	Time taken to achieve the maximum pressure.

Chapter 1

Introduction

To civilians, the word *explosion* generally evokes a destructive image, with thoughts of bombs, chemical plant accidents or other violent scenarios. In most cases explosions are not destructive at all, but are planned and controlled events. Such examples are explosion blasting in quarries, tunnelling, earth moving and controlled cratering. Less well-known uses of controlled explosions are for explosive forming of metals, explosive welding and demolition of buildings. This illustrates that the vast majority of explosions are controlled and benign.

The events that do capture the attention of society are accidental explosions or terrorist attacks, which can, and do, cause unplanned destruction, injury and death. Structural response to explosion loading is therefore of concern to many different industries, including transport, offshore, defence and nuclear.

The focus of this study is on accidental explosions that arise on offshore installations, which is an inherent risk when producing, processing, storing and transporting hydrocarbons. Before an explosion can occur a chain of events must unfold, namely the release of a hydrocarbon, the formation of a vapour cloud (caused by confinement) and finally an ignition source. Any break in this chain could prevent such a disaster. Due to the high costs associated with offshore facilities they are typically complex, and highly congested, making identification of leaks and preventing confinement extremely difficult. This coupled with many sources of ignition means that a leak is likely to lead to a hydrocarbon gas explosion and can result in significant levels of structural damage.

This was tragically illustrated in July 1988, with the Piper Alpha platform disaster[22] where the consequences of an ignition led to the complete loss of the

facility and the death of 167 personnel. As a direct result of this disaster several research initiatives were proposed and funded by government and industry. The aim of these projects was to gain a greater understanding of the loadings characteristics and the structural response of offshore structures subjected to hydrocarbon explosions and subsequent fires. Another requirement was to find suitable mitigation options for the offshore industry. Over £1billion has been spent in this area, however accidents continue to occur. Recent disasters include the Deep Water Horizon disaster (2010)[23] and the Amuay refinery in Venezuela (2012), which resulted in 69 personnel losing their lives. This highlights that there are still many uncertainties in our knowledge and that further understanding is required in order to reduce the consequences of such hydrocarbon explosions offshore.

One of the major uncertainties that still remain is the accurate evaluation of explosion loading. Large variations in the level of congestion, confinement, leak parameters, and position of the explosion make it extremely difficult to define nominal blast values to be used in design. Recent large-scale explosion tests[24] have shown that overpressures can be as high as 4 bar, much higher than previously considered and more importantly, designed for. Surprisingly, there are gaps in current knowledge offshore, relating to structural component robustness and resilience against blast loading, especially at these higher overpressures.

1.1 The generic problem

Steel panels are major components of many structures, in particular offshore topsides and attract high loads due to their large surface area. Openings in such structures are essential for access, pathways for piping, general inspection and for reducing weight. In the event of an explosion the blast load will initially impact the secondary structure (large spanning plated sections) and then transfer through to the primary structure, highlighting their critical consideration in safety assessments. Recent research by Ali[25] highlighted that there is a huge opportunity to utilise secondary members in order to absorb more energy and prevent unnecessary damage to the primary structure, potentially averting a catastrophic collapse or subsequent escalation.

1.2 Scope

Improving the ability to predict the behaviour of plates subjected to dynamic loading allows for safer, lighter and more economical protective engineering design solutions. As a result, a considerable amount of research relating to plates subjected to blast loading has been carried out in the past. Topics of interest include the effects of boundary conditions, stiffening and quasi-static, dynamic and impulsive loading conditions. There is a large amount of information regarding the response of full plates subjected to extreme loading in the open literature, while the response of plates with openings has received far less. Large openings are known to decrease the ultimate strength of plates, but they are also known to lower overpressures, through venting. Due to the complexity, safety issues and cost in conducting large scale experiments, they are often left to government research establishments and much of the results are not published openly.

1.3 Aims and Objectives

The primary aim of this research was to gain a better understanding of the effects that openings have on the overall performance of thin plated structures when subjected to pulse pressure loading. The secondary aim of the study was to assess how in-plane displacements at the support can significantly change the response of such a structure. This required a number of objectives to be accomplished:

- To investigate the material behaviour of 1.1 mm thick mild steel plate under uniaxial tensile loading in the quasi-static to the dynamic strain range,
- To develop new novel laboratory scale test procedures to produce controlled, repeatable semi-confined loading conditions on plated specimens with and without openings using a differential pressure device,
- To investigate the overall performance of thin plated structures with and without openings using the differential pressure device whereby opening size/shape and the restraint at the boundary conditions will be assessed, and
- To develop appropriate analytical and numerical models, validated by well-defined experimental data. Thus, allowing further investigations into variations in loading characteristics and the influence of axial restraint.

1.3.1 Arrangement of thesis

This research used a range of techniques, namely material characterisation, experimental component testing, finite element modelling and analytical modelling. Hence, this thesis has been arranged as follows:

Chapter 2: provides a review of relevant literature required to address the objectives of this research. This chapter covers key concepts which will provide the foundation for future chapters.

Chapter 3: investigates the stress-strain relationships for mild steel used within this study. This experimental work enabled suitable constitutive relations to be chosen in future chapters, which were capable of correlating stress, strain and strain rate.

Chapter 4: describes the development of novel laboratory scale test procedures capable of producing controlled, repeatable loading on plated structures using a differential device. Preliminary tests were conducted to determine the parameters and the test rig configuration.

Chapter 5: details the experimental component tests carried out which played a central role in this research project. Using the test configuration developed in Chapter 4, the rig was used to produce an extensive set of well-defined data that was essential for validation of numerical and analytical models.

Chapter 6: details the development of full 3D finite element models of pressure-loaded plates with and without openings. This involved calibrating the material properties against results from Chapter 3 and incorporating the recorded pressure-time histories from the component tests in Chapter 5. Additional modelling of the boundary conditions also considered frictional effects. The results are presented and validated against the component tests conducted in Chapter 5.

Chapter 7: presents an energy approach for predicting the large inelastic deformation in thin plates, with and without a central opening. The results are presented and also validated against the component tests from Chapter 5. This simplified approach demonstrates that adequate engineering estimates can be achieved, for such problems.

Chapter 8: provides a summary, conclusions and recommendations for future work.

Chapter 2

Literature Review

A detailed literature review was conducted to gain an understanding of published works related to plates subjected to transient loading. This review begins with a broad overview of the subject and then narrows into studies directly related to the research topic.

2.1 Plates

Plates resist transverse loads by developing shear forces, bending and twisting moments. For isotropic plates these loads are generally carried in both directions with the influence of twisting rigidity being significant. This means that a plate is considerably stiffer than a beam of comparable span and thickness. Therefore plates can be lightweight yet still deliver a high load-carrying capacity.

This favourable strength to weight ratio leads to economical advantages and is why steel plates are extensively used in all fields of engineering for large-scale structures. Examples of such applications are containers, ships, bridges and offshore installations, and are shown in Figure 2.1.

Plates resist transverse loads by means of bending (flexural response). The flexural properties of a plate are heavily dependent on its thickness in relations to its other dimensions. Plates are therefore typically classified into three groups depending on the ratio between a typical dimension of a plate in a plane [a] and the plate thickness [h].

Figure 2.1: Examples of steel plates utilised in industry.

1. *Thick* plates tend to have ratio approximately:

$$a/h \leq 8 \tag{2.1}$$

2. *Membranes* with a ratio of:

$$a/h \geq 80 \tag{2.2}$$

3. *Thin* plates with a ratio of:

$$8 \leq a/h \leq 80 \tag{2.3}$$

This final category is the most extensively used in industry and is subdivided again depending on a ratio between w/h, where w is the maximum deflection of the plate.

1. The plate is regarded as *stiff* i.e. flexurally rigid when:

$$w/h \leq 0.2 \tag{2.4}$$

2. The plate is regarded as *flexible* when:

$$w/h \geq 0.3 \tag{2.5}$$

The analysis of thick plates requires consideration of all components of stresses, strains and displacements for solid bodies using the general equation of three-dimensional elasticity. For membrane type plates the flexural rigidity (resistance) is

negligible[26]. Membranes carry transverse loads by axial tensile forces (including shear forces) acting in the middle surface of the plate. This is known as membrane forces. As mentioned above the final category is broken down into stiff and flexible thin plates. Stiff plates carry loads two dimensionally, mainly through bending and twisting moments and by transverse shear loads. Membrane forces are considered negligible. Flexible plates are a combination of stiff plates and membranes, carrying loads through internal moments, shear forces and membrane forces. When the maximum transverse deflection is considerably greater than the plate thickness $(w/h > 5)$ it is well established that membrane forces dominate and that the flexural resistance can be neglected. As such the stress is uniformly distributed over the plate thickness. This research focuses on plates that act as a membrane where the thickness is very small in relation to the other planar dimensions. These plates are extensively used in ship bulkheads and topside offshore installations.

2.2 Offshore installations

There are many types of offshore installations and further details along with their applicability can be found in reference 43. The focus of this study is to consider the effect openings have on the performance of thin plated structures found on offshore topsides and ship bulkheads, when subjected to dynamic loading.

2.2.1 Plate applications

Thin plates are an integral part of ship structures and offshore oil platforms and plates usually span between primary structural members. Figure 2.2 shows typical configurations for such applications.

These can be made from flat plate with stiffeners (stiffened plate), corrugated plates (self-stiffened plate) and in more recent times composite materials. Steel plates are still predominately used as they are relatively cheap and members can be replaced, modified and strengthened easily. Figure 2.3 shows the typical beam members (stiffeners) used. Another advantage is that steel has been extensively used throughout the history of the offshore industry, ensuring comprehensive coverage in the design codes, unlike newer composite materials.

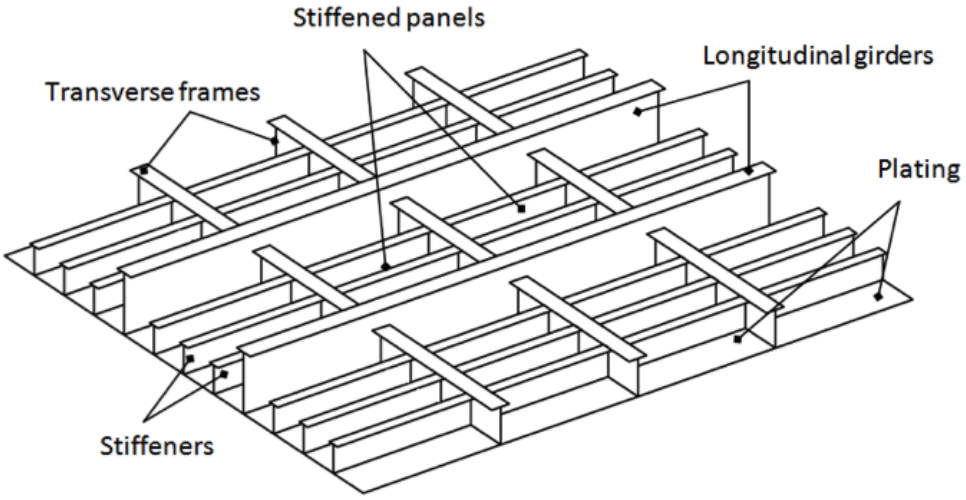

(a) Ship bulkhead.

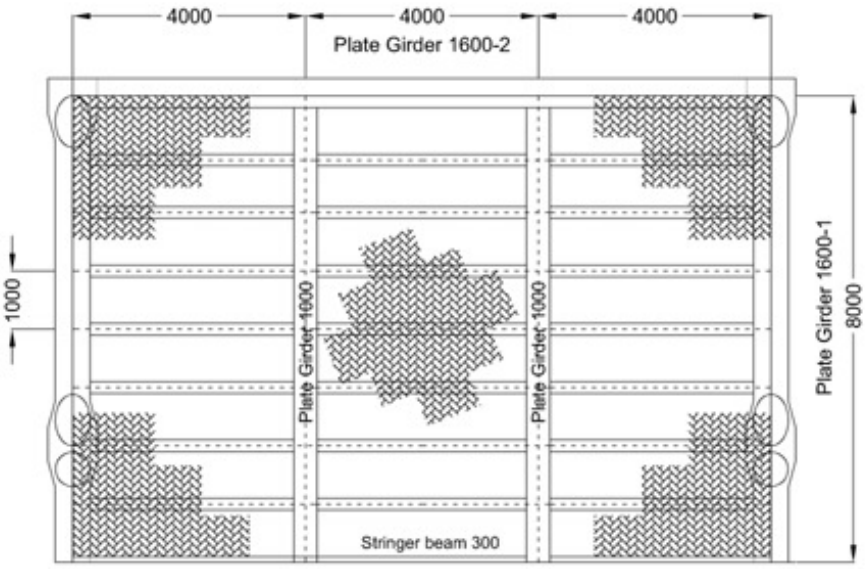

(b) Offshore application[25] - units in mm.

Figure 2.2: Typical steel-plated structures.

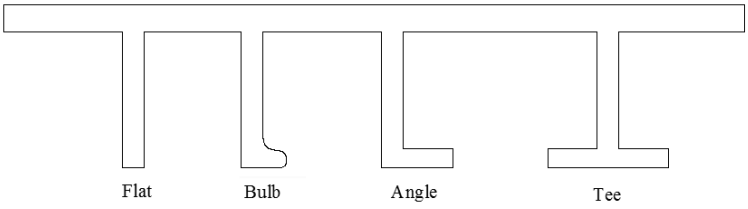

Figure 2.3: Various types of beam members (stiffeners).

Plates with openings

The inclusion of an opening in a plated section is common practice for reducing weight, access for utilities or for general inspection, with typical scenarios shown in Figure 2.4.

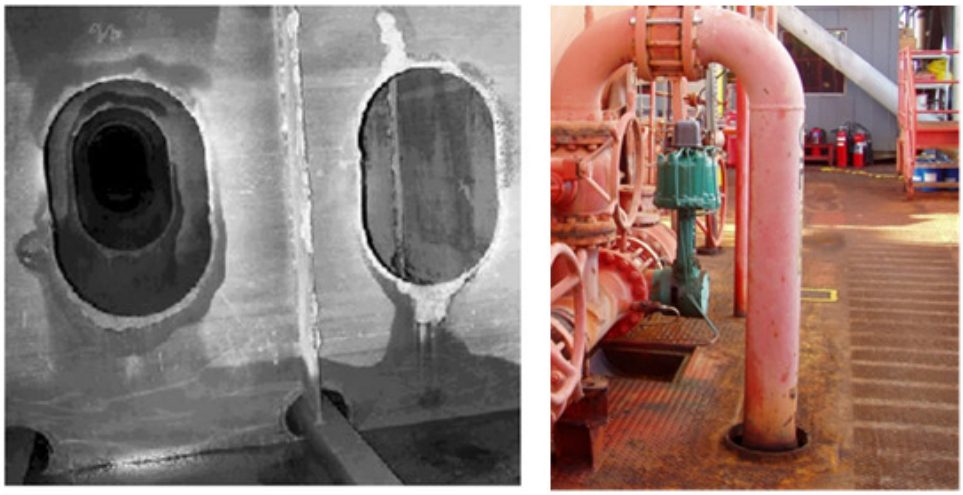

(a) Ship bulkhead. (b) Offshore application.

Figure 2.4: Typical applications where plates with openings are used in (a) bulkheads[1] and (b) offshore structures.

Steel-plated boundary conditions

In continuous plated structures, the edges of plates are usually supported by beam members (e.g., stiffeners). Paik and Thayamballi[27] highlight that the bending rigidity of these boundary support members are normally quite large in comparison to the plate itself. Therefore when analysing such structures it can be assumed that the support members on all four sides remain in the same plane. When the plates are laid on top of the supporting beams continuous fillet welds are applied at the interfaces between deck bottom plates and top flanges of the beams. Ali[25] states that with these connections the boundary conditions of the deck plates can be regarded as fixed supports.

2.2.2 Offshore challenges

Offshore installations face many complex challenges. The first offshore platform was built in 1947 off the coast of Louisiana in just 6 m depth of water. Now there

are over 7,000 offshore platforms around the world with the plants becoming more complex, larger, extracting deeper (in excess of 2500 m) and being placed in more extreme environments, where space is limited and very costly. Due to the high cost of offshore installations these are typically very congested combining living quarters, control rooms, escape routes, evacuation facilities, critical structural supports, and safety-critical items[28] shown in Figure 2.5. Offshore rigs are now based all over the world ranging from the North Sea (off the coast of the UK) to the Gulf of Mexico with a variety of structural solutions. Due to the variety of type, size, environment, function, man power and geometrical configuration along with material selection it is extremely difficult to provide specific design guidance.

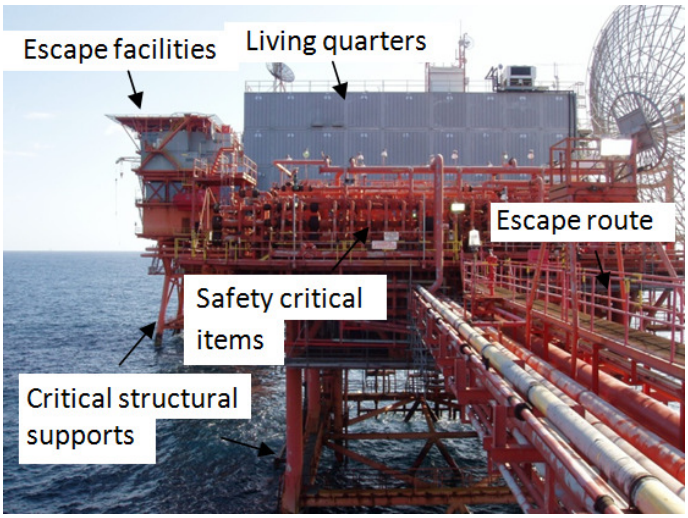

Figure 2.5: Typical offshore installation layout.

As the extraction processes improves and the price of oil increases many offshore installations are being used well beyond their intended and more importantly their designed lifespan. Deterioration is therefore a factor which must be managed vigilantly.

2.2.3 Threat

What are the hazards?

Vinnem[29] highlights that there are four high risk areas associated with offshore installations; explosions, fire, collision and marine hazards. The worse-case scenario being a hydrocarbon gas explosion that could escalate into a fire. Table 2.1 highlights that an explosion is the most prevalent major hazard for this type of structure.

Table 2.1: World statistics between 1990-2007[17].

Explosion/Fire	Structural Failure	Collision/Vendor
41	11	31

What is the risk of an explosion?

The probability may be small however the consequences of an explosion can be catastrophic both in terms of personnel and material losses. Thus the risk is quite high and comparable with other random events taken account in the design of offshore structures[30]. The probability of a hydrocarbon explosion occurring and the magnitude of the overpressure are highlighted in Figure 2.6.

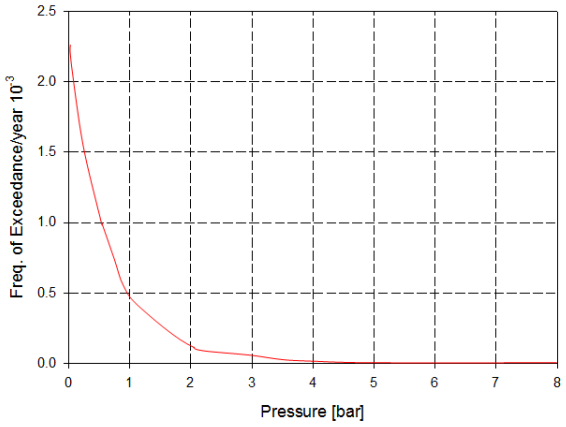

Figure 2.6: Frequency of Exceedance-Pressure[2].

What are the consequences of an explosion?

As shown in Figure 2.6 the probability of such an event occurring is small however the implications are huge. This was tragically illustrated in the July 1988 with the Piper Alpha platform disaster (Figure 2.7), where a small explosion in a compressor module escalated into a large fire which ultimately led to the death of 167 personnel, the worst in the entire history of offshore operations.

As a direct result of this disaster several research initiatives were proposed and funded by government and industry to address recommendations made by Lord Cullen's[22] report (106 recommendations) on the Piper Alpha incident. These led to over £1 billion spent on collaborative projects including the Joint Industry Project (JIP) between Industry and Academia to change regulations and vastly improve health and

Figure 2.7: Images from the Piper Alpha collapse.

safety on offshore structures. A time line showing the progress made through this work and the release of Technical Notes by the Fire and Blast Information Group (FABIG) is shown in Figure 2.8.

This significant investment concentrated on both hardware and the safety culture in the oil and gas industry. The UK Health and Safety Executive (HSE) implemented an assessment conducted by the duty holder to indicate that the risks have been reduced to As Low As Reasonably Practicable (ALARP) philosophy, using goal setting rather than prescriptive methods. The success of these efforts has been highlighted in a recent publication by the HSE[31] looking at the number of Hydrocarbon explosions over the last 15 years (between 1996 and 2012). However accidents continue to occur, which has been publicly highlighted recently. These include the Deep Water Horizon disaster (2010)[23] and the Amuay refinery in Venezuela (2012). Totalling in 69 personnel losing their lives.

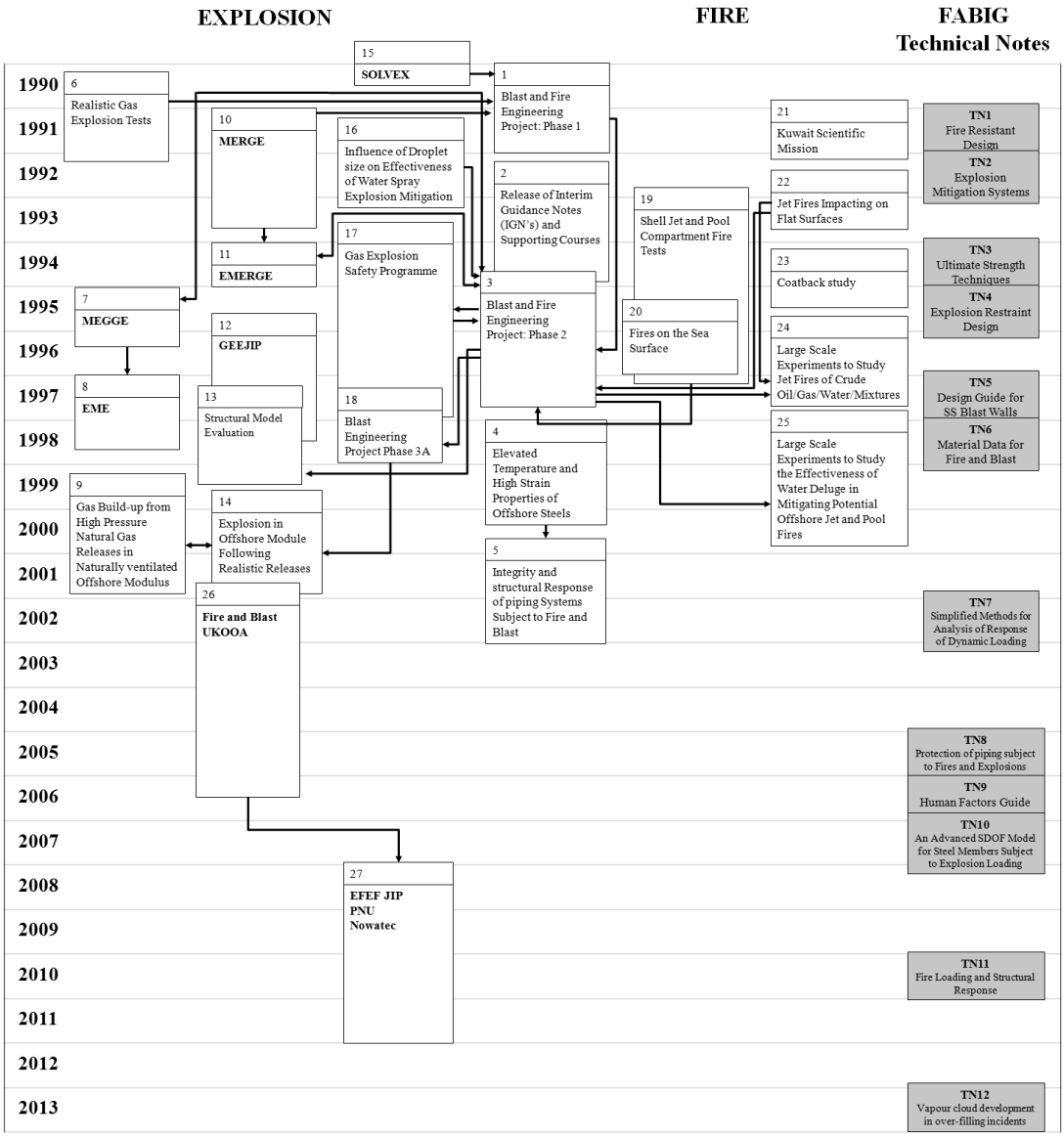

Figure 2.8: Timeline of Joint Industry Projects since Piper Alpha incident.

2.3 Explosions

UFC 3-340-02[20] defines an explosion as a violent release of energy from a detonation which converts the explosive material into a very high pressure gas at very high temperatures. A blast wave propagates radially outwards from the source into the surrounding environment at supersonic or sonic speed. The magnitude and shape of the blast wave, or pressure transient will depend on the nature of the energy release, and on the distance from the explosion epicentre[28]. The two characteristic shapes of blast waves are shown in Figure 2.9.

A shock wave in gas (air) can be defined as a fully developed compression wave of large amplitude, across which density and particle velocity change drastically[32](Figure 2.9(a)). Shock waves are usually caused from high explosives (e.g. TNT) or from an extremely energetic vapour cloud explosion.

A pressure wave can be defined as the air wave set in motion by an explosion[32] (Figure 2.9(b)).

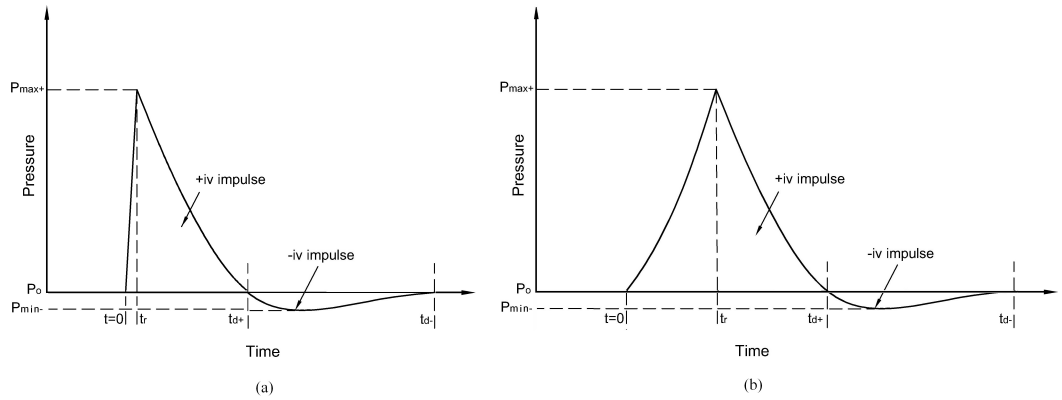

Figure 2.9: Characteristic shapes of (a) Impulsive and (b) Pressure wave.

Figure 2.9 shows the idealised characteristic shapes for impulsive and pressure waves. In reality a typical hydrocarbon explosion pressure wave has a complex variation with respect to time involving many oscillations with varying frequencies.

2.3.1 Explosion mechanism

Due to the highly congested manner of offshore facilities a blast wave will interact with obstacles, such as equipment and piping. The Schelkin feedback mechanism (Figure 2.10) neatly characterises the influencing factors in a hydrocarbon explosion.

Other factors such as wind speed/direction, leak rate/duration/position and concentration ratio have a pivotal effect on the magnitude of an explosion. Such sensitivity to a large array of variables makes predicting the potential consequences extremely difficult.

2.3.2 Fluid structure interaction

In a free-field blast wave event, as shown in Figure 2.9 it is often assumed that the pressure transient strikes a rigid wall. In reality this is not always the case and in some

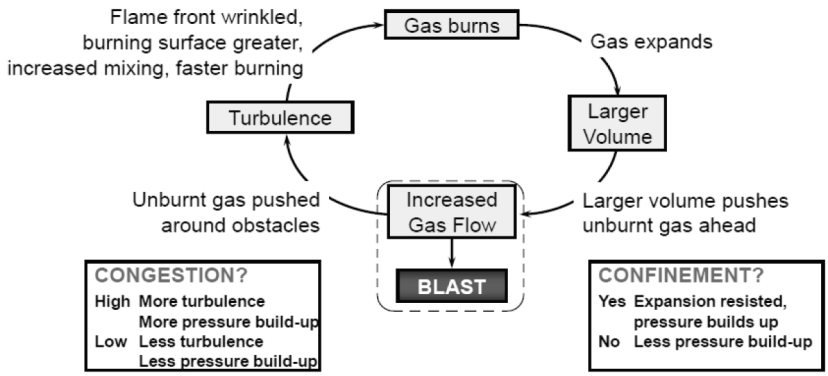

Figure 2.10: The Schelkin Feedback Loop.

instances the structure will deform as the shock waves hits. Kambouchev *et al.* [33] (2006) proved that actual impulse on a deformable structure is less than for the rigid wall case, making this assumption conservative.

2.3.3 Fragmentation

During an explosion event there is the potential for equipment to be damaged, causing flying debris. These fragments can cause great damage to structures when they strike at high speeds. UFC 3-340-02[20] divides fragments into two categories known as primary and secondary fragments. The effects of fragmentation are beyond the scope of this project.

2.3.4 Synergetic effects of blast and fragmentation

The combined effects of blast and fragmentation have been well documented in experiments[34][35]. Rakvag[3] highlights that there are three possible scenarios for this effect, shown in Figure 2.11 and described below:

1. *Close Range:* Blast arrives before fragments.
2. *Medium range:* Blast and fragments arrive simultaneously (approximately).
3. *Long range:* Blast arrives after fragments.

Again these effects are beyond the scope of this thesis, but it is important to highlight them as they can have a significant influence on structural response.

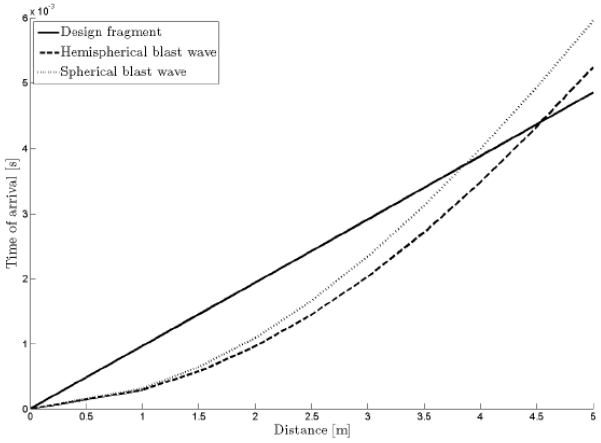

Figure 2.11: Synergetic effect of blast and fragmentation: Time of arrival for M107 155 mm artillery shell[3].

2.4 Blast resistant design

Mays and Smith[36] produced a list of key conditions which usually apply for designing against blast loading for buildings. These have been reproduced below, as they are still applicable for offshore installations, with additional information placed within brackets:

1. The incident will be an unusual event.

2. The threat will be specified in terms of an explosive charge weight at a stand-off, which can only be an estimate and already subject to a risk assessment (in the case of offshore this will be an overpressure load from a hydrocarbon explosion).

3. For economic design, some plastic deformation is normally permitted. The level of damage is specified in terms of the limiting member deflection or support rotations.

4. The strength of the materials will be enhanced because of high rate of strain to which they will be subjected.

5. The strengths of in situ materials often exceed the characteristic values.

The most important function of a blast resistant design is its ability to absorb blast energy without leading to a partial or total collapse, which could result in loss of life, earnings or damage to the environment.

2.4.1 Mitigation

The most common method used to mitigate the effects of a blast onshore is to increase the stand off distance between a flammable material and an ignition point. Another is to use concrete as a barrier due to its mass and ability to absorb large amounts of energy including fragments. However as discussed previously in Section 2.2.2 this is often impracticable for offshore facilities as space and weight are key factors in design. Therefore to mitigate blasts offshore structures usually employ the following:

1. *Water deluge systems* - these systems are flexible and relatively inexpensive to install and have shown to decrease the overpressure from a gas explosion[37]. However concerns over system detection of gas/fires along with the potential risk of ignition initiated by the water contacting electrical components are still prominent issues to be solved.

2. *Blast and fire walls* - increased energy absorption usually accomplished through plastic deformation and design guidance considering ductility ratios and maximum support rotation[38].

3. *Venting* - carefully considered layout of equipment and venting arrangements can significantly reduce the magnitude of potential overpressures from an explosion.

2.4.2 Offshore material characteristics

For offshore blast resistant designs it is desirable for a structure to be lightweight and deform plastically. The structure must therefore combine strength with ductility. The yield strength of a steel material can actually be greater than the specified minimum values given in the codes and standards. A strength increase factor (SIF) is used to account for this in design and UFC-3-340-02[20] suggests using SIF = 1.1 for yield strengths lower than 345 MPa. Ductility is the ability of a metal to flow plastically before fracture. A high ductility indicates that a material is forgiving and likely to deform locally without fracture[39].

The constitutive relationship of the material and rate effects have a direct and significant influence on the response and subsequent failure modes of blast resisting structure[40]. The loading rate is a fundamental quantity in the structural response. Dey[18] describes the different impact velocity regimes in relation to strain rate, testing

methods and their effects on a material. This is reproduced here for reference in Table 2.2. Typical overpressures from accidental explosions on topside structures are between 0.3 bar and 2 bar, with load durations generally between 50 ms to 200 ms[41]. However, research conducted by the Steel Construction Institute proved that these overpressures can be as high as 4 bar[24].

Table 2.2: Influence of strain rate on material response, including testing methods and typical applications for each velocity regime[18].

Velocity regime	Strain rate (s^{-1})	Testing method for the material	Effect on material	Application
Low velocity 0-50 m/s	< 10	Quasi-static: testing machines: - hydraulic - servo-hydraulic - screw-driven	- primarily elastic - some local plasticity	- dropped weight - vehicle impact - ship collision - crashworthiness of containers for hazardous materials
Sub-ordnance 50-500 m/s	$10 - 10^4$	- pneumatic - hydraulic - Taylor tests - Split Hopkinson Tension bar (SHTB)	- primarily plastic	- design of nuclear containment - free falling bombs and missiles - fragment due to accidental explosions
Ordnance 500-1300 m/s	$10^3 - 10^4$	- Taylor tests - SHTB	- viscous material - strength still significant	- military applications - military projectiles like bullets, missiles - high kinetic energy penetrators with/ without explosives
Ultra-ordnance 1300-3000 m/s	$10^4 - 10^6$	- plate impact	- fluid behaviour in materials - pressures approach/exceed material strength - material density significant	- warhead fragments - rocket bursted penetrators
Hypervelocity 3000-12000 m/s	$10^6 - 10^8$	- plate impact	- hydrodynamic material - compressibility - vaporisation	- space vessels exposed to meteoroid impact and space debris

Under dynamic loading it is well known that materials in general achieve a strength increase. The response of mild steel under dynamic loading at high strain rates is significantly different from the response under static loading[42]. This phenomena is highlighted in Figure 2.12 showing that the yield strength can be more than doubled and the ultimate strength increased to up to 30 percent. Such attributes can be described as a dynamic increase factor (DIF).

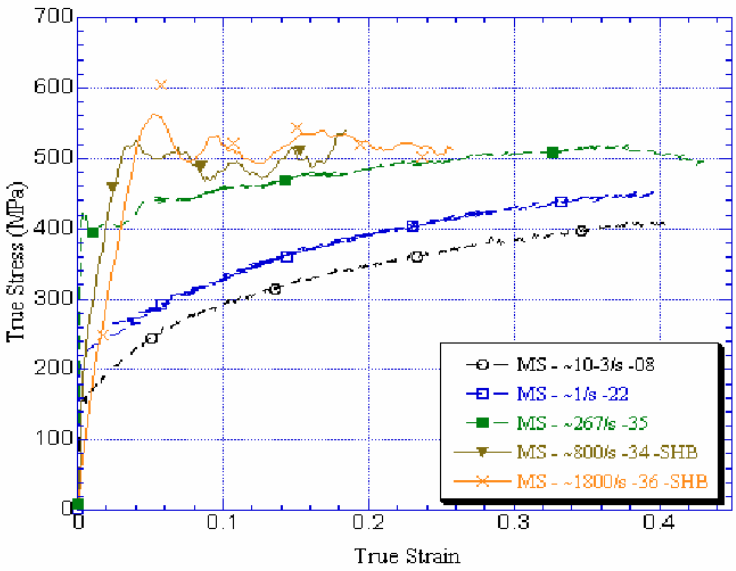

Figure 2.12: Stress-strain curves for mild steel at various strains[4].

These factors must be incorporated into the design phase to be able to accurately understand how a structure will respond and to provide appropriate connection details for an allowable response. If possible the actual stress strain curve material data should be used.

2.5 Vulnerability of plated structures

As mentioned in Chapter 1 steel panels are major components of many structures, in particular offshore topsides and attract high loads due to their large surface coverage. In the event of an explosion the blast load will firstly strike the large spanning plate sections and then transfer through to more critical (primary) structural supports. These supports are normally large in cross-section, when compared to the plate itself.

During an explosion, plates deform in the same direction of the pressure loading (Figure 2.13), implying that the rotational restraint along the support member boundaries are large. Thus, it may be assumed that the plate is clamped on all four edges[43] . The response of the plate is similar in both directions of loading.

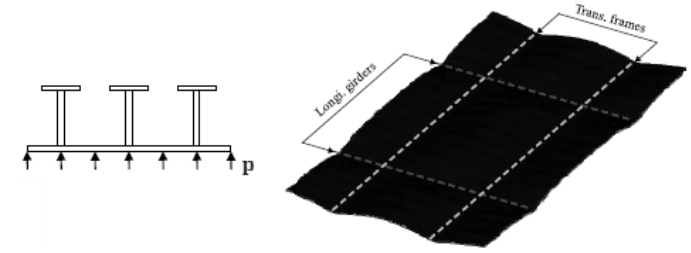

(a) Plate-sided pressure.

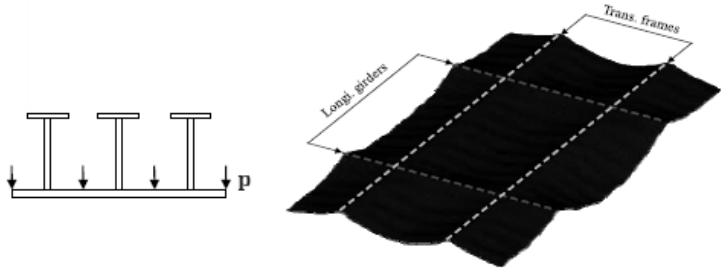

(b) Stiffener-sided pressure.

Figure 2.13: Typical steel-plated structure under blast loading.

2.5.1 Components response

As discussed in Section 2.1 the plate's response is heavily influenced by its thickness in relation to its other dimensions. Standard decking sections are usually constructed of 8, 10 or 12 mm mild steel plate typically spanning 4 m x 1 m sections (Figure 2.2(b)), with 8 mm plating being the most commonly used offshore[44]. These ratios mean the plates are very slender and when they are subjected to large transverse displacement the plate responds predominately in membrane action. A report by SCI[5] describes this as having two distinct effects. The first is that it provides a form of support additional to the beam action in the stringer. The second is that membrane action creates in-plane tensile stress in the beam members incorporated within the membrane. This in turn creates a compressive stress in the perimeter support members as shown in Figure 2.14.

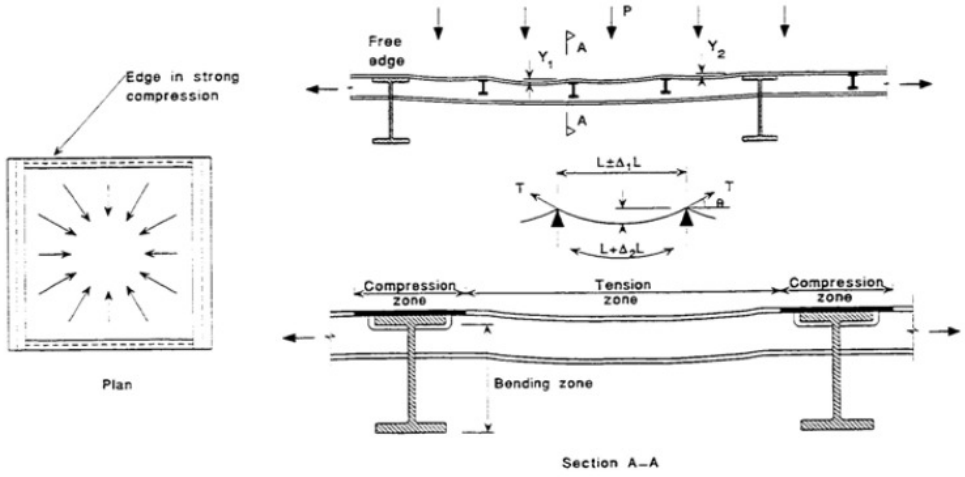

Figure 2.14: Effect of membrane action[5].

This membrane action causes very large forces, meaning the tensile members, the plate, compression members and the connections between all of these needs to be carefully checked in order to prevent potential failure. In light of this FABIG discuss this in detail in Technical notes 4[44] and 5[45]. Membrane action is well known to substantially enhance the load carrying capacity of plates, which can be advantageous. However, a negative consequence of this is the plate becomes stiffer, thus reducing the amount of energy it can absorb in bending, resulting in higher loads being transferred through to the primary structure.

2.5.2 Strengthening of offshore topsides structures

A recent HSE report[5] provides guidance on the re-assessment and strengthening methods for blast walls, decks and floor sections. The document highlights that many of the earlier structures had structural capacities, which were estimated through using several simplifications. These included simplifying structural models, the blast load, material dynamic behaviour, material at elevated temperatures, yield and ultimate values of strain and stress and the failure strain limits. These approximations were thought to be conservative, however through improvements in modelling of explosion events it has become apparent that this is not always the case. The report provides guidelines for the strengthening of decks and topsides, namely:

1. Addition of plates to the deck floors.

2. Tying decks together using vertical connections.

3. Filling voids between top module support frames and bottom of modulus.

All of these methods involve additional weight and stiffening of the structure, which will actually reduce the member's ductility and ability to absorb energy. Further details of methods for improving the structural connections on topside structures can be found in reference 25.

2.5.3 Failure modes

Many deformation and fracture modes of structures have been observed experimentally over the years and comprehensively compiled in excellent reviews and books[46][47]. Menkes and Opat[6] were the first to establish the three basic failure modes for clamped beams when subjected to blast loadings. These failure modes are illustrated in Figure 2.15.

(a) Mode I: Large inelastic deformation.

(b) Mode II: Tensile tearing at the support.

(c) Mode III: Transverse shear loading.

Figure 2.15: Failure modes for a clamped beam subjected to blast loading[6].

Teeling and Nurick[48] later observed similar modes on fully clamped circular plates and Nurick and Shave[49] for fully clamped rectangular plates. Nurick and Shave's[49] investigation on the thinning and subsequent tearing at the boundary conditions further divided these, fully listed below:

1. Mode I: Large ductile deformation - deflection increase with increasing impulse.
2. Mode II*: Partial tensile tearing and shear lift over supports midpoint deflection increase with increasing impulse.
3. Mode IIa: Complete tensile tearing with increasing deformation - midpoint deflection increase with increasing impulse.
4. Mode IIb: Complete tensile tearing with decreasing deformation - midpoint deflection increase with increasing impulse.
5. Mode III: Plate completely torn from the supports - negligible midpoint deflection.

2.6 Structural response modelling

Structural response to explosion loading is investigated using several methodologies, namely experimental studies, theoretical modelling and numerical simulations. These can be used independently or in conjunction with one another. The choice depends on the level of accuracy desired, which is based on time, cost and expertise available.

2.6.1 Experimental methods

Physical explosion testing on large-scale structures can be dangerous and requires specific, large and expensive testing facilities. To be able to accurately describe an explosion event it is important that both the loading and the response of structures are measured in a controlled, repeatable and accurate manner. This can be very difficult when dealing with a blast event. There are several techniques used to do this:

1. Air pressure waves from TNT or shock tubes.
2. Impulse loading using plastic sheet explosives directly mounted.

3. Under water explosives.

4. Pressure pulse created by a Pulse Pressure Loading Rig (PPLR).

Problems arise with the use of types 1,2 and 3 mainly with the repeatability of the loading. Each explosion will have heat and light losses unique to each experiment. The PPLR on the other hand can apply a pulse pressure load with finite rise time by creating a pressure differential between two chambers. This produces controlled and repeatable loading representative of typical overpressures from accidental explosions on topside structures.

Due to the complexity, safety issues and cost in conducting such experiments, tests are often left to government research establishments and much of the results are not published openly. The PPLR will be utilised in this research in order to provide valuable insights into the problem herein, and will be discussed in greater detail in Chapter 4.

2.6.2 Analytical modelling

Structural response modelling to blast loading has been studied extensively for many decades and can be broken down in exact and approximate solutions.

Exact theoretical solutions[26][50] can be mathematically laborious to derive often involving the use of numerical methods. This can be time consuming and expensive with solutions limited in application to structures with infinitesimal displacements or elastic response. This is often unrealistic for the response of thin structures subjected to extreme transverse loading as considerable plasticity is expected.

Due to the severe limitations of exact solutions several approximate analytical methods were developed. Approximate methods are usually considered adequate for dynamic structural response due to many uncertainties of the spatial and temporal characteristic of dynamic impact loads and of the dynamic material properties. This permits rapid analysis with reasonable engineering accuracy for even complex structures. Several excellent reviews are available in literature[47], and the key details are briefly highlighted here.

One of the earliest methods developed was by Biggs[51] who developed an approximate method using an equivalent spring-mass system with a single degree of freedom (SDOF). This has been a very popular design tool with structural designers

due to its simplicity in calculating transformation factors between the actual structure and the equivalent SDOF model. A series of dimensionless design charts can then be used to rapidly calculate an approximate dynamic response of a structure. These are known as Pressure-Impulse charts or P-I charts, as shown in Figure 2.16. This SDOF method has recently been extended to include strain-rate effect. Details can be found in FABIG Technical Note 10[52].

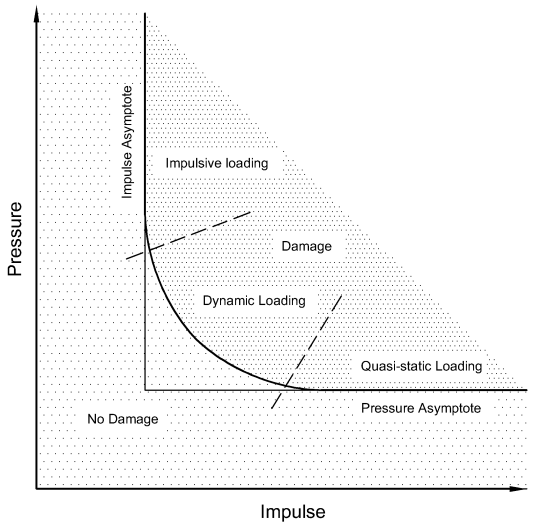

Figure 2.16: Pressure-Impulse chart.

Kaliszky[53][54] was also a pioneering contributor to the approximate structural response method. He assumed the structure was a rigid-plastic material and had a kinematically admissible velocity field, thus simplifying the problem to statical analysis. This means that the velocity profiles satisfy the boundary and initial conditions for the problem, and are continuous between the phases of motion[47]. This could then be substituted with an equivalent single-degree-of-freedom (SDOF). However this method was constrained to impulsive or rectangular pressure loading.

Martin and Symonds[55] introduced the mode approximation methods to solve the response of structures to blast loading. Symonds and Chon[56][57][58] further extended this work to account for finite deflections. In doing so they had to resort to a series of instantaneous mode shapes throughout the response. This implied the requirement of numerical methods and meant that the analytical simplicity of characterising a structure was lost.

Schleyer and Mihsein[59] also developed mathematical models based on the Lagrange equation[51], for predicting the behaviour of stiffened and un-stiffened plates. Springs were used to vary the in-plane restraint and stiffeners were discretely modelled to provide a global response. Louca and Harding extended this model further by including initial imperfections[60] and by more accurately representing the membrane effect due to both lateral and in-plane displacement. This work highlighted that the influence of imperfections can significantly increase the stiffness of the plate when in the positive direction (i.e. the imperfection is in the same direction as the applied pressure), illustrated in Figure 2.17.

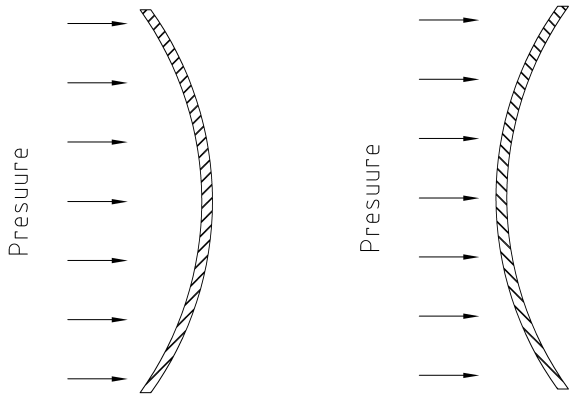

(a) Positive direction. (b) Negative direction.

Figure 2.17: The difference between applying pressure in (a) positive direction and (b) negative direction with respect to the plate imperfection.

Adapting this further to account for in-plane displacements Louca and Wadee[61] found it made no significant difference to the out-of-plane displacement, however it significantly changed the strains and made comparison with the FEA more favourable. Schleyer and Hsu[62] also utilised mode approximation techniques to model structural response in the quasi-static to dynamic range.

Analytical methods require simplifying assumptions in order to approximate or disregard some of the physics of the problem. These simplifications will inevitably create inaccuracies in the results. However when done correctly, within a validated range of parameters, these inaccuracies are minimal (or within an acceptable range), and the method is suitable for a particular problem[63].

2.6.3 Computation modelling

Ngo *et al.* [19] (2007) summaries current computer programs for modelling blast effects and structural response. This is reproduced here for reference in Table 2.3.

Table 2.3: Various computer programs used to simulate blast-effects [19].

Name	Purpose and Type of Analysis	Author/Vendor
BLASTX	Blast prediction, CFD code	SAIC
CTH	Blast prediction, CFD code	Sandia National Laboratories
FEFLO	Blast prediction, CFD code	SAIC
FOIL	Blast prediction, CFD code	Applied Research Associates, Waterways Experiment Station
SHARC	Blast prediction, CFD code	Applied Research, Associates, Inc.
DYNA3D	Structural response + CFD code (Couple analysis)	Lawrence Livermore National Laboratory (LLNL)
ALE3D	Coupled analysis	Lawrence Livermore National Laboratory (LLNL)
LS-DYNA	Structural response + CFD code (Couple analysis)	Livermore Software Technology Corporation (LSTC)
Air3D	Blast prediction, CFD code	Royal Military of Science College, Cranfield University
CONWEP	Blast prediction, (empirical)	US Army Waterways Experiment Station
AUTO-DYN	Structural response + CFD code (Couple analysis)	Century Dynamics
ABAQUS	Structural response + CFD code (Couple analysis)	ABAQUS Inc.

Generally computation approaches either predict the blast loads on a structure or they calculate the structural response. Computational programs use a combination of first-principle and semi-empirical methods to predict such events. Programs using first-principle methods can be either coupled or uncoupled.

In an *uncoupled* approach the blast load is calculated by assuming the structure in question remains rigid as the blast wave strikes it. The loads calculated are then applied to an equivalent model of the structure. ProSAir[64] is a recent example of such software which can provide history of pressure, velocity, density and temperature. However this method is known to often over-predict the loads on a structure. Ngo

et al. [19] states that this over-prediction becomes more prominent when significant motion or failure of the structure occurs during the loading phase.

In a *coupled* approach the blast load and structural response are inter-linked. CFD (Computational Fluid Mechanics) is used to predict the blast loading which is solved simultaneously with the CSM (Computational Solid Mechanics) model for structural response. This provides a more accurate prediction of overpressures and structural response. Examples of such computational codes are DYNA3D, LS-DYNA, AUTO-DYN and ABAQUS, highlighted in Table 2.3.

As computational power has improved over the last two decades this has become an accessible and popular tool to evaluate the structural response to transient loading. However considerable skill is required to ensure that meaningful results are obtained from such computer software. Specific engineering knowledge is required to ensure an appropriate method is followed for each individual case. Hitchings[7] provides a description of the factors that must be accounted for in a highly non-linear analysis such as a blast event, shown in Figure 2.18.

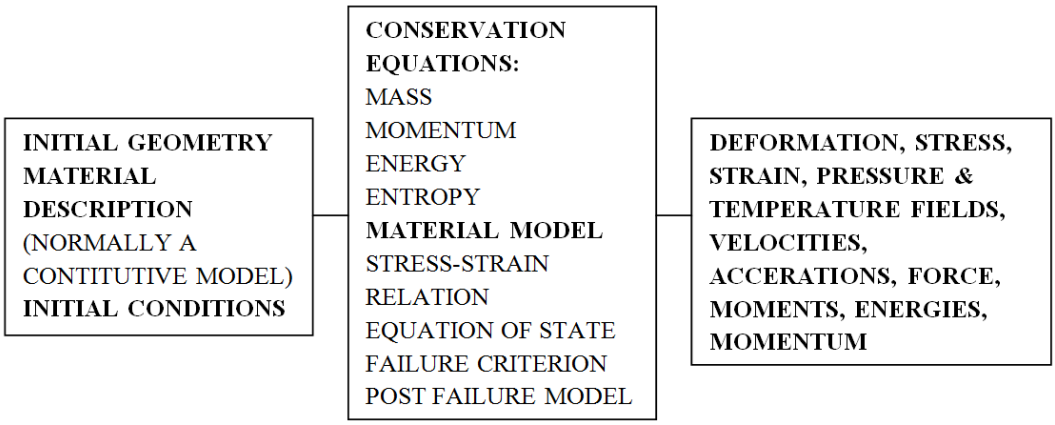

Figure 2.18: Typical non-linear analysis approach[7].

2.6.4 Factors considered when selecting method

As mentioned previously the choice depends on several factors from time, expertise, cost and the level of accuracy required. Table 2.4 briefly discusses the advantages and disadvantages for each.

Table 2.4: Advantages and disadvantages for the different methods of modelling structural response to blast.

Method	Advantages	Disadvantages
Experimental	- Physical data can be used to validate other methods	- May require large test facilities - Potentially dangerous - Expensive
Analytical	- Fast - Versatile screening tool - Parametric studies	- Over simplifies problem - Unable to predict plasticity over the plate - Solution accuracy decreases for more complex material and member configurations
Numerical	- Very accessible - Accurate description of non-linear geometric and material effects - Parametric/ optimisation studies	- Software expensive - Time consuming - Considerable expertise required

2.7 Previous studies on thin plates subjected to blast

Blast loading or, more generally, transient pressure loading of undamaged plates has been studied extensively since World War II, and Nurick and Martin compiled reviews of theoretical[65] and experimental[46] studies on this problem up to the 1990's. Another excellent review of both these aspects is by Jones[47].

Chung Kim Yuen and Nurick[66] highlights that in the 1990's investigations were extended to include the effect of boundary conditions[67][68], plate stiffeners[69][70] and loading conditions[68] in order to gain a fuller understanding and improved prediction of deformation and tearing. Chung Kim Yuen and Nurick[71] also investigated the significance of plate thickness to localised blast loading. They tested 100 mm diameter mild plates with built in boundary conditions and thicknesses of 1.6 mm, 2.6 mm, and 3.6 mm up to plate tearing. Observations showed thinning of plates over the central region smaller than the load diameter. Thinning was also observed at the boundary but less pronounced than in the centre.

In more recent years and as computational software has become more readily available significant research has been concentrated on numerical simulations of plates subjected to blast loading. Chung Kim Yuen and Nurick[66] highlight that the

dynamic response of structures is difficult to assess due to the dependence on both load history and boundaries. However, predictions using computational software have been extensively reviewed with good correlations found between experimental and numerical studies for maximum deflections and deformation shapes[72][73].

2.7.1 Influence of boundary conditions

Many papers, past and present highlight the large influence that boundary conditions play on the response of blast loaded thin-walled structures[74][68][75]. Jones[74] observed that even remarkably small in-plane displacements at the support can significantly change the response of a structure, potentially removing the strengthening effect beyond the limit load. The limit load is the load carrying capacity of the structure before collapse. Therefore the boundary conditions must be accurately described. Thomas and Nurick[67] conducted a series of experimental studies on fully built-in (machined boundary) circular and square plates subjected to blast loading. They then used previous theoretical methods derived for clamped boundaries to see what influence the change in boundary conditions would bring. For plates with Mode I type failure there was no significant difference. However when Mode II* failure occurred it was found that failure was highly dependant on the edge conditions.

2.7.2 Mode I failure: Large inelastic deformation

Mode I failure of rectangular plates has been been reported by Jones *et al.* [76], Houlston and Slater[77], Gupta[78] Yu and Chen [79] and Zhu[8]. Due to the dynamic nature of explosion loading it is often difficult to capture experimental data during a blast, with most data relying on the final deformation for reference. Zhu[8] was able to investigate the transient deformation profiles of square plates under explosion loading using an optical technique, developed by Huang *et al.* [80]. The results for a clamped mild steel specimen are shown in Figure 2.19, where W is deflection and X represents points along the symmetry line of the square plate (a value to 75 mm represents the clamped edge, while a value of 0 is the maximum global response).

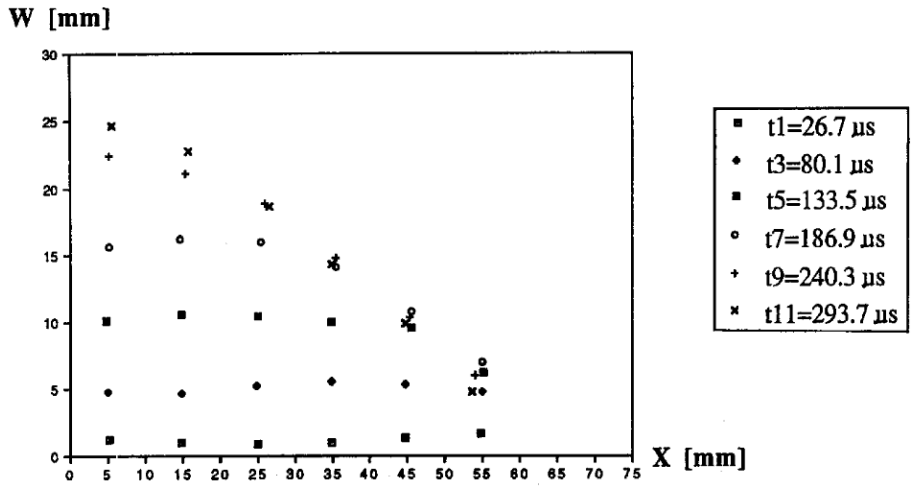

Figure 2.19: Transient deformation profile of a clamped mild steel square plate[8].

2.7.3 Influence of stiffeners

Rudrapatna *et al.* [73] performed experimental and numerical studies and compared the results to experimental data reported by Olson *et al.* [72] They found that the same failure modes occured for stiffened plates as for flat plats. Referring to Figure 2.13 it can be observed that this research will be focused on Mode I type failure. Chung Kim Yuen and Nurick[66] recently conducted a series of experimental and numerical studies on stiffened and unstiffened plates. Their results suggest that stiffening of plates does not reduce tearing, but that it may actually cause it earlier. Their findings highlighted that stiffeners restrict the plate and cause tearing (Mode II and ModeII*) at an impulse that would only cause an unstiffened plate to deform (Mode I). This demonstrates that simply strengthening a structure can have adverse effects.

2.7.4 Influence of pulse shape effects

Florek and Benaroya[81] conducted an extensive review on pulse loading effects on the deflection of structures. This extends to discuss efforts to reduce or eliminate the effect of these pulse shapes using rigid-plastic geometries under uniform loading. Work by Schubak *et al.* [82] highlighted the importance of the rise time in a triangular-shaped pressure pulse, particularly when it is greater than 0.3 times that of the total pulse time. This is demonstrated in a report prepared by ABS Consulting Ltd[9] using a tool they developed called BlastSTAR. In this study, the rise time (t_r) was kept constant as a proportion of the total duration (t_d), so that the analyses were carried out for values

of t_r/t_d of 0, 0.15, 0.3 and 0.5. For each of these groups of analyses, the peak force (F_1) was kept constant, and the proportion between the pulse duration and the natural period of the structure (t_d/T) ranged from 0.1 to 15. The peak maximum displacement (y_{max}) was then obtained for each of the analyses and the maximum dynamic load factor (DLF_{max}) was obtained by dividing y_{max} by the equivalent static displacement y_{stat} for the same value of F_1.

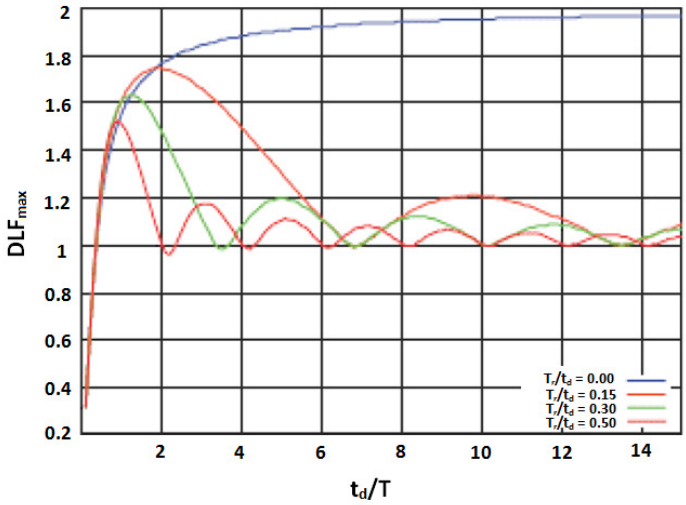

Figure 2.20: Maximum response for SDOF system (undamped) subject to triangular load pulses with different rise times[9].

Figure 2.20 highlights the influence that the rise time has on the maximum response of a structure when subjected to a triangular pulse. This highlights just how sensitive the structural response is to its loading conditions.

Borenstein and Benaroya[83] recently conducted a sensitivity study on blast loading parameters to determine which of the parameters' uncertainties had the greatest effect on the maximum deflection of a clamped aluminium plate. The results of which only compounded the amount of uncertainties, concluding that material parameters and the sensitivity of response to loading models must be thoroughly investigated.

2.7.5 Influence of openings

Openings or cut-outs are often used to lighten structural weight or to provide access. Provision of openings cause stress concentrations due to the abrupt changes in geometry and are known to influence the ultimate strength of plates. Openings also result in less surface area to collect a load, which can be beneficial when mitigating the influences of an explosion event.

An opening through which gas escapes from a confining enclosure as a result of the expansion caused by combustion can also be referred to as a vent[41]. It is well established that venting can be used as a means of relieving pressure during a gas explosion. As the blast wave expands through the opening, the pressure level drops due to the restriction and sudden expansion into the building (additional) volume[28].

The Gas Explosion Handbook[32] states that there are several important factors for effective venting;

1. Size of the vent area.
2. How the vent area is distributed.
3. Direction of the explosion relief.
4. For explosion relief panels: how quickly are they activated.

The Gas Explosion Handbook[32] also states that the guidelines are very simple for vent areas. The vent area should simply be as large as possible. However this does not discuss the implications this would have on the response of such a panel and how altering this would influence the loads being transferred to other parts of the structure.

Langdon *et al.* [84] recently investigated plates with small openings; however this focused on using perforations to mitigate the blast loading rather than their effects on the plate or structure. Li *et al.* [85]studied the explosion resistance of square plates with openings for venting dust explosions for applications in the process industry, however very limited details were provided. Jain[86] investigated the effect of the hole aspect ratio of rectangular plates on the normal stress, shear stress and deflection in the transverse direction when loaded statically. However, to the author's knowledge limited experimental studies have considered dynamic transverse loading on plates with openings. Rakvag *et al.* [16] recently conducted a series of transient pressure tests on thin plates with pre-formed holes to simulate combined blast and fragmentation in

a simplified manner. This highlighted that the pressure immediately within the vicinity of the opening could be of higher pressure than that acting on the rest of the plate. This will be discussed in further detail in Chapter 6.

2.8 Current design codes

Prior to the Piper Alpha incident in 1988 there was very little design guidance for limiting the escalation of fires and explosion. Since then considerable effort has been spent on research and developments in areas of fire and explosions as highlighted in Figure 2.8. This wealth of new information has made it very difficult for duty holders, designers and regulators alike to keep up-to-date in order to modify existing structures, or design new ones to be inherently safer. This section briefly summarises current design manuals for predicting blast loads and the response of structural systems.

2.8.1 UFC 3-340-02

Originally TM5-1300, UFC 3-340-02[20] has been a 5-year effort by the Department of Defence Explosives Safety board (DDESB) to update blast design requirements for explosion safety applications. Its primary objective is to provide design guidance for facilities that protect personnel and valuable equipment against explosions. This is a vast document that provides many examples illustrating and explaining design of protective construction requirements for steel and concrete structures.

The manual provides qualitative differences between steel and concrete protective structures. Concrete is mainly used for close-in high-impulse designs in order to protect against the effects of primary and secondary fragments and to limit deflections. In contrast steel shapes are much more slender and are generally designed to sustain large deformations.

Deformation criteria in UFC 3-340-02 are based on designing a structure for one accident over its entire life cycle. For plates the maximum ductility ratio and the maximum rotation at the end support are used to ensure that adequate resistance to blast loads are provided. Depending on the functionality of the plate structure and the level of protection required, different deformation criteria should be considered. For example plates designed to this manual can sustain support rotation of up to 12 degrees, or a ductility ratio of 20 (whichever governs) without failing as long as

adequate bracing is provided for stability. However, this may need to be limited if the mechanism (such as used to open a door) still needs to function after an explosion has occurred. Table 2.5 displays the deformation criteria set by UFC 3-340-02.

Table 2.5: Summary of deformation criteria for various structural components [20].

Element	Level of protection	Deformation type	Maximum deformation
Frame Structures	1	Rotation, θ Deflection, δ	2° H/25
Plates	1	Rotation, θ Ductility ratio, μ	2° 10
Plates	2	Rotation, θ Ductility ratio, μ	12° 20

θ = maximum member end rotation (degrees).

δ = relative sidesway deflection.

μ = ductility ratio.

H = storey height.

Protection type 1: Protects personnel against the uncontrolled release of hazardous materials.

Protection type 2: Protects equipment, supplies and stored explosives from fragment impact, blast pressures and structural response.

This manual states that it is difficult to state exact rules concerning openings, but their effect on the design is generally a function of location, size and shape[20]. It also states that small compact openings with areas approximately less than 5 percent of the panel area when positioned away from areas of high stress can be ignored in the design.

2.8.2 UKOOA

These guidelines were collated by the United Kingdom Offshore Operators Association (UKOOA) and the Health and Safety Executive (HSE). It does not undertake new research but consolidates the lessons learnt from research and development spanning back from 1988 to present day. The guidance is divided into four parts:

Part 0[87] evaluates fire and hazard management,
Part 1[41] provides guidelines on practices and methodologies that can lead to avoidance and mitigation of explosions,
Part 2[88] provides guidelines for avoidance and mitigation of fires, finally
Part 3 will provide design practices for fire and explosion engineering (currently under development).

This guideline aims to minimise the blast hazard and the risk associated with it by removing personnel from the consequences or escalating events, minimising the potential size/escalation of an explosion event, having adequate detection systems and by installing mitigation systems to remove escalation.

A risk that cannot be eliminated by the application of inherent safety methods may be referred to as a residual risk. Inherent safety methods can also be applied to the management of the residual risk by consideration of the general principles indicated below:

CONTROL is better than
MITIGATION is better than
EMERGENCY RESPONSE.

As regards to systems to reduce risk:

PASSIVE systems are more reliable than
ACTIVE systems are more reliable than
OPERATIONAL systems are more dependable than
EXTERNAL systems.

2.8.3 API RP 2FB

Initiatives to update the API RP 2FB[21] coincided with a similar updates to UKOOA standards. This led to largely consistent methodologies and guidance in regard to explosion loading between the two standards. One major difference is that the UKOOA does not provide nominal blast loads.

This document is predominantly directed at new designs for offshore structures, however it can also be utilised to verify existing offshore structures against fire and blast loading. This document concentrates on preventative measures, using careful design layout of equipment/facilities to help minimise the consequences of a blast event. The three-by-three risk matrix is shown in Table 2.6.

Table 2.6: Risk Matrix[21].

		Consequences of occurrence		
		Low	Medium	High
Probability of occurrence	High	Medium risk	Higher risk	Higher risk
	Medium	Low risk	Medium risk	Medium risk
	Low	Low risk	Low risk	Medium risk

Risk assessment is broken down into three stages.

1. Screening: simple risk based screening using Table 2.6. If the outcome is low risk from a blast event no detailed structural assessment is required.

2. Nominal loads: for blast these are space averaged peak blast overpressures determined for specific platform types. Details of which can be found in API RP 2FB document commentary.

3. Event based: this is a series of evaluations of fire or blast events that could occur over the lifetime of a specific platform.

This guidance provides a methodology for performance criteria when assessing a structure to a blast load to ensure the consequences fit within a consistent risk level determined from the risk matrix. This process is dependant on the operator for an offshore structure and for their specific safety management philosophy. Structural response assessment against blast must meet appropriate performance criteria as set above and can be addressed in one of three methods:

1. Screening.

2. Strength level analysis (SLA).

3. Ductility level analysis (DLA).

2.8.4 N-004 NORSOK standard

Under Annex A.6[89] of the codes, the structural response is categorised into 3 areas, depending on the relationship between time duration (t_d) of the explosion, and the relative fundamental period of vibration (T).

1. $t_d/T < 0.3$ (Impulsive domain).

2. $0.3 < t_d/T < 3$ (Dynamic domain).

3. $3 < t_d/T$ (Quasi-static domain).

This highlights that the structural response to blast loading is significantly influenced by these ratios.

2.8.5 ISO 19900-6

The International Organisation for Standardisation (ISO) has produced a series of design codes ISO 19900-6 to address all design and assessment requirements for structures used in petroleum and natural gas industries worldwide. ISO 19901-3:2010[90] specifically reviews offshore structures.

For blast loading design the international standards refer to separate industry associations for specific operation types and environments.

1. API[21] for Gulf of Mexico type platforms with more venting and less extreme environments.

2. UKOOA[87][41][88] for larger platforms with more extreme environmental conditions, less venting, potentially larger overpressures.

3. NORSOK[89] which contains explicit analytical requirements.

4. ISO 13702:1999[91] provides specific requirements and guidelines of explosions in offshore production installations.

2.8.6 Summary of current design codes

The general approach from the UKOOA and the API RP are consistent. Both use a qualitative risk screening analysis to compare the potential consequence versus the probability of occurrence or frequency, consisting of low, medium and high (API RP and UKOOA respectively). Depending on the risk level a suitable explosion assessment process is chosen to ensure that a structure meets acceptable performance criteria, set by the duty holder. High probability, lower consequence explosion events are defined as a Strength Level Analysis (SLA) and it is usually recommended to use elastic response techniques. Low probability high-consequence events are defined as Ductility Level Analysis (DLA) and require a more refined modelling technique to accurately capture geometric and material non-linearity. ISO 19901-3[90] identifies a minimum blast event likelihood of 10^{-4} for Ductility Level Blast (DLB) events and a higher potential of 10^{-2} for Strength Level Blast (SLB) events.

The primary method of evaluating a structural response to blast is to evaluate the ductility ratio and the hinge rotations. These limits are based on the type of structure or component, material, location of the structure and the desired protection level as highlighted in Table 2.5. UFC-3-340-02[20] defines a maximum rotation of 12 degrees or a ductility of 20 (whichever governs) to ensure protection of the overall structure to blast overpressures. N-004[89] also highlights the large influence the fundamental period of vibration and the time duration have on the defining the response of a structure.

In comparing all the current design codes it is clear to see that even though they have separate approaches in their design methodology, the goals are about inherent safe design and prevention of loss of lives and earnings. UKOOA highlights that the use of passive rather than active control and mitigation systems are better as there is no reliance on personnel to prevent, control or mitigate effects.

The importance of design codes is highlighted by a HSE report[92] that concluded that 29 percent of all releases were due to inadequate design with a further 28 percent due to inadequate inspection. Therefore good design is essential and if the need for inspection was reduced this could also reduce the likelihood of a hydrocarbon release.

2.9 Summary

This chapter presents a review on the current knowledge related to the problem being considered in this study. The focus was initially on plates and their ability to remain lightweight yet still deliver a high load-carrying capacity. This was further extended to consider how they are incorporated into offshore installations and shipping bulkheads, providing typical geometrical configurations, boundary conditions and the inclusion of openings. Following this, a review of challenges and threats attributed to offshore installations was conducted, the worst-case scenario being an explosion. The review highlights that the response of structures to explosion loading, such as generated by a hydrocarbon explosion is a complex matter in which there are spatial and temporal variations. The large variations in the level of congestion, confinement, leak parameters, and position of the explosion make it extremely difficult to define nominal blast values to be used in design.

Since the tragic accident at Piper Alpha in 1988 significant improvements in the understanding of gas explosions on equipment and structures have been made. Research has highlighted the importance of considering the response characteristics of a structure as well as the explosion overpressure, to gain a true representation of the loads imposed on such structures. Joint Industry Project (JIP) research exposed that the actual loads imposed by an explosion can be significantly higher than originally thought and assumed. Therefore further work must be conducted in this area, especially at higher overpressures.

During a blast event, such as on a topside structure, components have to absorb the kinetic energy typically within 20-50 ms. Under these loading conditions the strain hardening and strain rate hardening have a crucial influence on the behavioural response of the structure. Therefore these must be accurately modelled in order to understand and predict the blast response. This is discussed further in chapter 3.

There are several methods of predicting the structural response of structures or components to blast loading, namely experimental, analytical and numerical. These were briefly reviewed with selection primarily based on the levels of accuracy required, available resources and expertise.

The design codes typically use a risk matrix to define the level of risk associated with an event considering the potential consequence against the probability of occurrence. This research is concerned with investigating low probability high-

consequence events where large blast overpressures cause large deformations in plated structures.

UFC 3-340-02[20] suggests that openings, which are less then 5 percent of the exposed panel area when positioned away from areas of high stress can be neglected in design. This requires further investigation to assess if the strength of the plate is reduced and if the plate responds differently when subjected to varying load rates and varying boundary conditions. To the knowledge of the author little research has been openly published in respect to this.

The literature review highlights that the support conditions for plated structures play a large role in the response of a structure when subjected to blast loading. As a result of this the connection detailing needs careful consideration to prevent potential failure. Recent strengthening systems for topsides include adding additional plates to deck floors, tying sections together using vertical connections or filling voids. All these methods stiffen sections to help transfer the membrane action onto the support connections. However this also adds weight and limits the deflection of the plated section, reducing the amount of energy it can absorb in bending, resulting in higher loads being transferred through to the primary structure. Stiffer walls will also tend to exhibit brittle failure modes, which is undesirable.

Plates with openings are a necessary and pivotal part of offshore structures and can be used for reducing weight, access, pathways for pipes or for general inspection. Large openings are known to reduce the ultimate carrying capacity of plates, but openings also result in less surface area to collect load. This thesis suggests that openings, could in theory, be incorporated into the design to enhance the robustness and resilience of a structure against blast loading.

It is known that vents help to reduce the level of overpressure however little research has been conducted on the combined influence these have on the overpressure and the structural response of plates. The location of such openings is critical to ensure beneficial mitigation effects against an explosion. These must not be positioned where personnel or piping can be adversely affected, potentially leading to further escalation.

The primary focus of this study is to investigate the combined influence that openings have on the overpressure and the structural response of thin ductile plates subjected to dynamic transverse loads. From the literature review it is clear that very little research has been published in this area, which strengthens the originality of this work. Examples are provided in literature, however these mainly consider the use

of perforation to mitigate the blast loading, rather than their effects on the plate or structure, with limited details provided.

Chapter 3

Material Tests

3.1 Introduction

In a blast event, steel structures usually undergo large plastic deformation and in so doing, absorb a large amount of energy. When dealing with inelastic deformations, correct description of the material response is essential in order to arrive at accurate and reliable predictions of the member or structural response. To do this, material tests must be performed which enable the macroscopic characteristics of the steel to be quantified within the quasi-static to dynamic regime. These tests identify key material characteristics and inform the selection of an appropriate constitutive relation. A constitutive relation is simply a mathematical model to describe the response of a material under different loads and environments.

3.2 Constitutive relations

In order to model the mechanical response of structures exposed to impact and dynamic loading, it is important to describe the materials stress-strain behaviour that considers large strains, high strain rates, temperature softening, varying stress states and history of loading in addition to the work-hardening behaviour. A mathematical description incorporating all of these phenomena is difficult to obtain, with the model becoming increasing complex by increasing the number of variables. Therefore models often make assumptions to simplify the problem. It is therefore vital to understand which material phenomena are critical in a blast event, to ensure that the chosen constitutive model accurately replicates this dynamic behaviour. It is well understood that a

constitutive model that includes strain rate effects is necessary to get accurate results from simulations of blast. Finally it is important to stress that a material model is never more correct than the experimental data to which it is fitted.

3.3 Mechanical properties of steel

The macroscopic properties of the material were studied using uniaxial tension tests. Despite the simplicity of the test, data analysis and interpretation is not straightforward. To understand the fundamentals behind the macroscopic behaviour, an understanding of microscopic behaviour is required which has been very briefly discussed.

True stress-strain

The engineering (nominal) stress-strains are defined based on the original cross-section dimensions of the tensile specimens. This does not provide a *true* indication of the deformation characterisation as this is based purely on the original dimensions of the specimen, and as such, it cannot predict the strain hardening. In reality due to the Poisson's effect the section area of the tensile specimen reduces continually throughout the test as the specimen is stretched, making the *true* stress larger than the nominal stress. Therefore the true stress-strain curves can be obtained using Equations 3.1 and 3.2.

$$Stress_{true} = stress_{nom}(1 + strain_{nom}) \tag{3.1}$$

$$Strain_{true} = Ln(1 + strain_{nom}) \tag{3.2}$$

Necking

Equations 3.1 and 3.2 should only be used until the onset of necking. Beyond this point the true stress should be determined from the actual measurements of the load and cross-sectional area of the specimen. This is because from this point forward all further plastic deformation is concentrated locally in the necking zone, rather than globally across the specimen. For thin sheet specimens there are two types of necking:

1. Diffuse necking - which occurs during the maximum loading of the test specimen.

2. Localised necking - at this phase rupture occurs soon after.

Diffuse necking is called this because its extent is much greater than the sheet thickness. Localised necking produces a narrow band inclined at an angle, as seen in Figure 3.1. Failure can occur through diffuse necking alone, however rupture usually occurs with a combination of both processes.

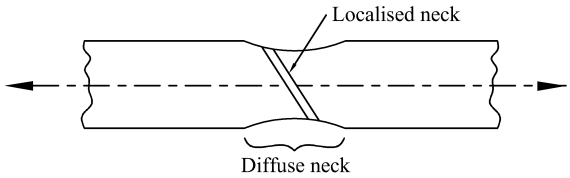

Figure 3.1: Tensile flow instabilities in sheet tensile samples[10].

As the cross-sectional area of the tensile specimen decreases rapidly, the load required for continuing elongation drops off, where as in reality the metal continues to strain-harden right up to fracture[10]. If instantaneous measurements are taken during this phase the true-stress-true-strain curve, or *flow curve* can be plotted. Sovik[93] developed such a device which consists of four inductive displacement gauges attached to a circular frame. The diameter reduction is then calculated using the averaged recording from the four displacement gauges.

The calculation of strain from the onset of necking onwards is shown in Equation 3.3

$$Strain_{true} = Ln\frac{A_\circ}{A_{neck}} \tag{3.3}$$

The general behaviour of materials under loading can be classified as ductile or brittle, depending on its ability to flow plastically before fracture. A ductile material, such as mild steel can undergo large plastic deformation before failure. In contrast a brittle material without flaws, such as glass or concrete would fracture almost at the elastic limit.

The measure of ductility is conventionally measured by the engineering strain at fracture, known as *elongation,* e_f (Equation 3.4) and the *reduction of area,* q (Equation 3.5)[10]. Both of these factors are obtained after fracture by placing the specimen back together and taking measurements of the final length l_f and the area at fracture A_f.

$$e_f = \frac{L_f - L_\circ}{L_\circ} \tag{3.4}$$

$$q = \frac{A_\circ - L_f}{A_\circ} \tag{3.5}$$

Both elongation and reduction of area are usually described as a percentage. Since an appreciable fraction of the plastic deformation will be concentrated on the necked region of the tension specimen, the value e_f will depend on the original gauge length, $L_\circ$. For example, if the gauge length decreases, the contribution of the overall elongation from the necked region will increase, as well as the value of e_f. Therefore the original gauge length should be reported in addition to the percentage elongation value. This problem does not occur when calculating the reduction of area.

Stress distribution at the neck

This necking phase for tensile specimens may be thought of as a mild notch. This subject is discussed briefly below but can be studied in detail through several references on the subject[10][18]. For round specimens this notch introduces complex triaxial stress in the necking region. A notch under tension loading produces radial and transverse stresses which increase the value of longitudinal stress required to cause plastic flow. Hence, the average true stress at the neck, calculated by dividing the axial tensile load by the cross-sectional area of the specimen at the neck, is higher than the stress that is required to cause flow for simple tension. This stress should therefore be corrected for triaxiality.

Bridgman[94], devised a formula for correcting true stress for round tensile specimens. This method assumes uniform strain distribution and axisymmetric stress distribution in the minimum cross-section. This is true for rod sections, however Aronofsky[95] proved that the stress pattern in the minimum cross-section for flat specimens was not uniform, leading to errors in Bridgman's formula.

Several researchers have proposed new corrective formulas for the flat specimen case; Ling[96], Zhang *et al.* [97] and Scheider *et al.* [98]. The formula by Zhang *et al.* [97] requires measurement of the area reduction along with numerical simulations, to calculate the hardening parameters. Ling's methodology also relies on numerical analyses proposing a weighted average method. Finally, the method by Scheider *et al.* [98] uses a combination of numerical analyses to propose a formula suitable for sheet specimens. Figure 3.2 compares the true stress-strain curve with its corresponding engineering stress-strain curve, with the inclusion of such a correction factor.

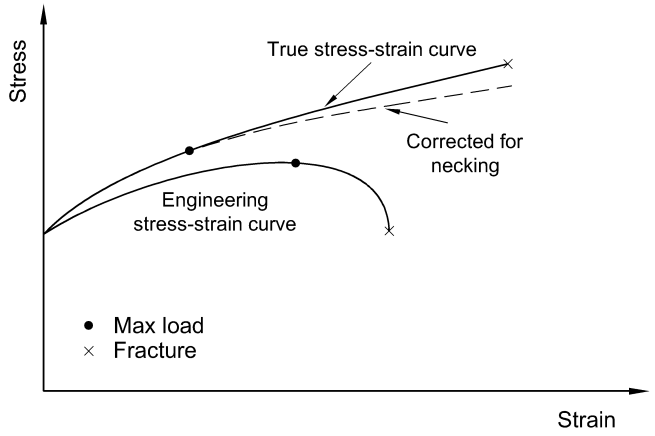

Figure 3.2: Comparison of engineering and true stress-strain curve including the Bridgman correction[10].

Several factors affect the shape and magnitude of such stress-strain curves, based on the micro/macroscopic nature of the material. For steel these are dependent on the chemical composition, the forming process (heat treating and plastic deformation, caused by rolling), strain rate, temperature and the stress imposed during testing.

3.3.1 Microstructure of mild steel

The microstructure of steel is key to its behaviour, as the crystal structure, size, carbon content and the arrangement of it microconstituents determine its properties. Steel alloys can be classified into two well-known categories: ferritic and austenitic. Low carbon mild steel is classed as a ferritic steel. Microstructure investigation of such ferritic steel shows that the plastic deformation is dominated by dislocation gliding[99].

A steel's microstructure can be modified or altered by alloying elements, heating or heat treatment or by plastic deformation. These can create defects that can be advantageous, obstructing dislocation and movement causing a metal to become stronger. For example, heat treating a material causes a refinement in the grain size. This creates a higher dislocation density in the material, meaning a higher resistance to movement of dislocations, leading to a greater force required for plastic deformation.

3.3.2 Strain-rate effect

As discussed in Section 2.4.2 it is well established that the behaviour of mild steel is different depending on the rate of loading. This phenomenon is known as material strain-rate sensitivity or viscoplasticity. Strain-rate sensitivity is exhibited in the stress-strain behaviour of a material when the stress required to achieve a given level of strain increases with increasing strain rate. Generally, both the yield stress and the ultimate stress will increase with an increase in strain rate. Manjoine[100] conducted a series of tests on mild steel over a wide range of strain-rates. He concluded that the yield stress is more sensitive to an increase in strain-rate than the ultimate tensile strength (UTS). This phenomena is highlighted in Figure 3.3 showing that the yield strength can be more than doubled and the ultimate strength increased to up to 30%. Such attributes can be accounted for in the form of a dynamic increase factor (DIF). In contrast to this the ductility is typically reduced with increasing strain rate. Campbell and Cooper[101] demonstrated this by showing that for mild steel the rupture strain decreases with an increase in strain rates up to 106 s^{-1}. This implies the material becomes more brittle at higher strain rates.

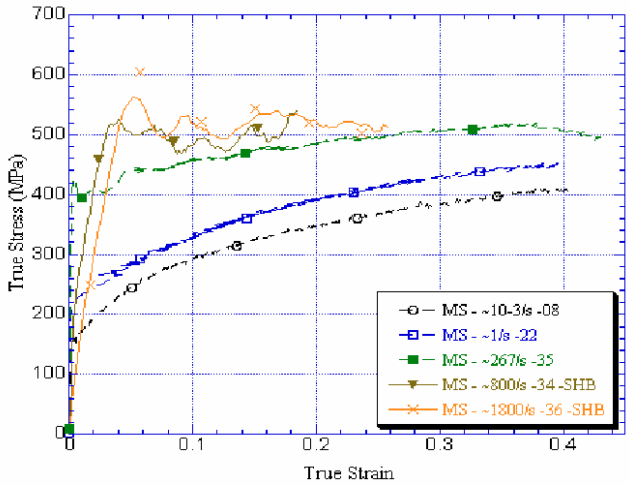

Figure 3.3: Stress-strain curves for mild steel at various strains[4].

3.3.3 Temperature effect

The stress-strain curve and the flow and fracture properties produced from tensile tests are highly dependant on the temperature at which the test was conducted. In general, the strength decreases and ductility increases as the temperature is increased. Hence,

similar stress-strain curves can be achieved by either increasing the strain-rate or by decreasing the temperature. Further information on the combined effects of elevated temperature and high strain rate material properties is given in FABIG Technical Note 6[102].

The influence of thermal softening on the material has not been investigated in this study. With the expected strains and strain rates in the component tests, Chapter 5, adiabatic heating of the material due to plastic dissipation is not expected to have any significant influence on the material behaviour.

3.4 Experiments

3.4.1 Material

The material used in these experiments is Docol Form 01 (DC01), a cold-reduced, mild steel used in a variety of applications for its formability, ideal where ductility is an important criteria as in impact and blast protection. It comes in sheets of various widths and lengths with thickness ranging from 0.5 mm to 3.0 mm. Previous work hardening and residual stresses caused by cold working would increase the yield strength, but this would lead to a loss in ductility. However DC01 is able to combine strength, ductility and has excellent weld-ability[103].

As discussed in previous sections the properties of metals are heavily influenced by their micro/macrostructure. In light of this, a brief investigation has been conducted on the microstructure, which follows on to a more in-depth investigation of the macrostructure.

3.4.2 Microstructure

DC01 is a ferrite mild steel with a body-centred cubic (bcc) structure. It consists mainly of iron with additional nominal chemical composites; (C:0.05%, Mn 0.20%, P:0.01%, S: 0.01%, N: 0.01% and Al 0.04% in terms of % wt) with a maximum yield stress of 260 MPa[103].

Microscopy studies revealed that DC01 used in this study had an average grain size of 29.6 μm, measured using an optical microscope and the line interception method[10]. The microstructure is of randomly distributed grain shapes, without

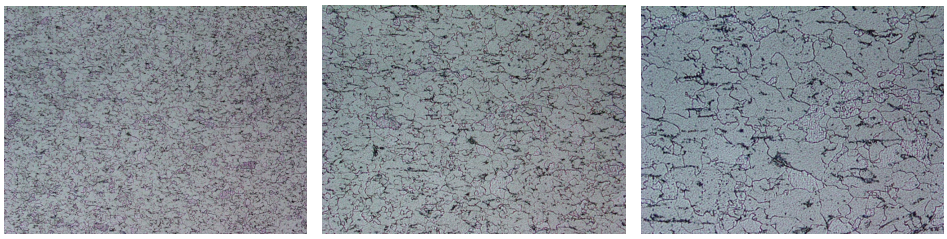

(a) (b) (c)

Figure 3.4: Typical microstructure of DC01 at (a) 100 (b) 200 and (c) 400 magnification.

preference to the direction of rolling, as shown in Figure 3.4. This indicates that the macroscopic behaviour will be almost isotropic. The extent of anisotropy was assessed in the macrostructure investigation.

The hardness of the material was also measured using an Avery hardness tester (type 6407), with a 60 kg weight and diamond point indentor. The results showed there was a small variation, approximately 2% over the entire material batch, indicating excellent conformity. The average Rockwell hardness number was 130.

Keeping these microscopic observations in mind, the macroscopic behaviour was then studied by a series of uniaxial experiments.

3.4.3 Macrostructure

All specimens used in this study were taken from one batch of locally sourced DC01 material, which came in 3 m by 1.5 m sheets and thickness 1.1 mm. All tests were performed at room temperature at a strain-rate in the range of 0.00033 s^{-1} to 534 s^{-1}. This strain-rate range was chosen as typical hydrocarbon explosions offshore are between 10 s^{-1} and 10^2 s^{-1}. A correct description of the material response at these strain rates is essential in order to arrive at accurate and reliable predictions of the member or structural response. Due to the large range in stain-rate, 3 different experimental techniques were used, listed in Table 3.1.

Table 3.1: Tensile testing experimental programme.

Strain-rate	Experimental technique	Avg. strain-rate range
Low	Servo-hydraulic testing machine	0.00033 s^{-1}
Medium	Hydro-pneumatic testing machine	5s^{-1}-72 s^{-1}
High	Split-Hopkinson Tension Bar	189s^{-1}-534 s^{-1}

Thirty-two quasi-static tests were performed using a servo-hydraulic machine, 7 tests in a hydro-pneumatic machine and finally, 7 tests in a Split-Hopkinson Tension Bar. Width and thickness measurements were taken of each specimen, prior to testing.

3.4.4 Tensile tests at high strain-rates

A schematic of the SHTB[104] at the Norwegian University of Science and Technology (NTNU) is shown in Figure 3.5. This was used to conduct high strain-rate tests, from 189 s^{-1} - 534 s^{-1}. Key arrangements are also shown in Figure 3.6.

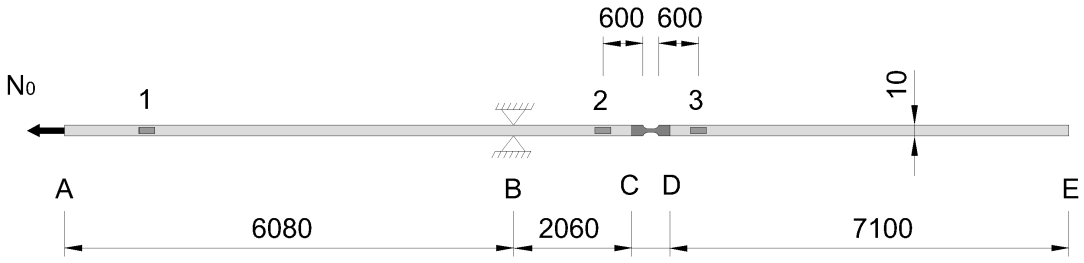

Figure 3.5: Schematic diagram of Spilt Hopkinson Tension Bar (SHTB) set-up - units in mm.

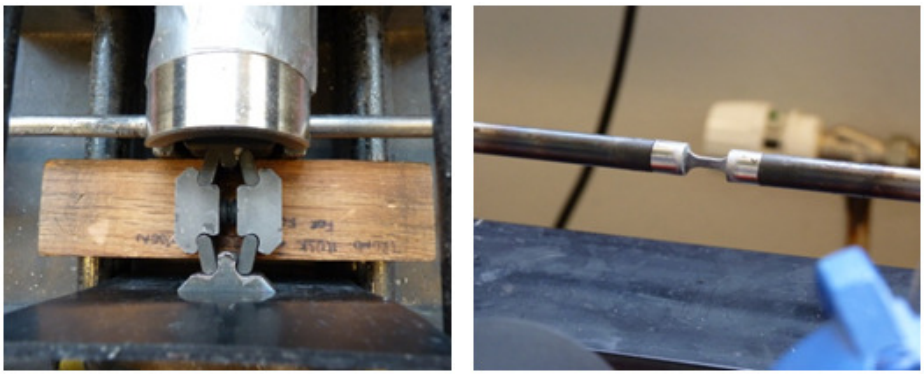

(a) (b)

Figure 3.6: (a) Friction lock and (b) mounted test specimen.

Specimen preparation

For the SHTB the actual bar has threaded holes with a diameter of 5 mm at points C and D, as shown in Figure 3.5. However, the 1.1 mm thick sheets used in this work are thinner than this threaded diameter. Therefore, a fixture arrangement was

needed to connect the specimens with the bars. The specimen was firstly glued to the fixture using Araldite, which bound the two parts and prevented the specimen from sliding. Then the extensions on both fixtures (containing the specimen in the slit) were machined, producing an M5 thread. This provided a mechanical bond with the glue providing additional reinforcement to the joint. The assembly process of the specimen and fixtures is shown in Figure 3.7 and this method has been validated by Tarigopula *et al.* [11].

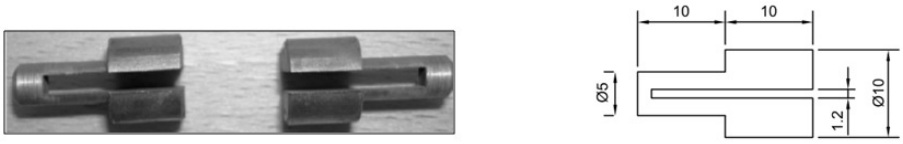

(a) Geometry of fixture.

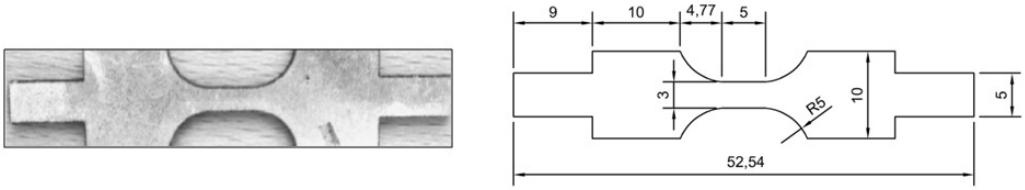

(b) Geometry of specimen.

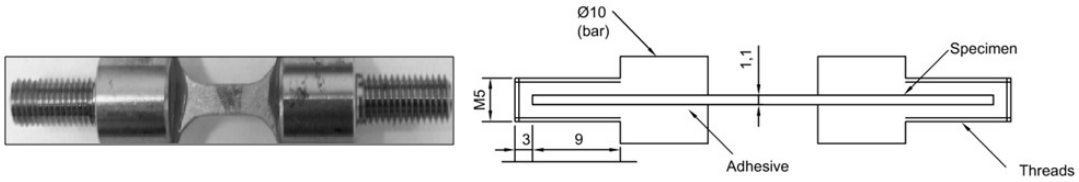

(c) Assembly of specimen and fixture.

Figure 3.7: Tensile specimens conducted at NTNU - units in mm [11].

The Incident, reflected and transmitted strains are analysed following the procedure described by Cluasen and Auestad[104] and Tarigopula *et al.* [11].

3.4.5 Tensile tests at medium strain-rates

For the medium strain-rate tests, from 5 s^{-1} - 72 s^{-1} a hydro-pneumatic machine[104] (Mini bar) was used to determine the dynamic properties of the material. The schematic of the hydro-pneumatic machine at NTNU is shown in Figure 3.8. Further details on the test procedure are provided by Tarigopula *et al.* [105]. Again, the same specimen geometry (Figure 3.7) was used.

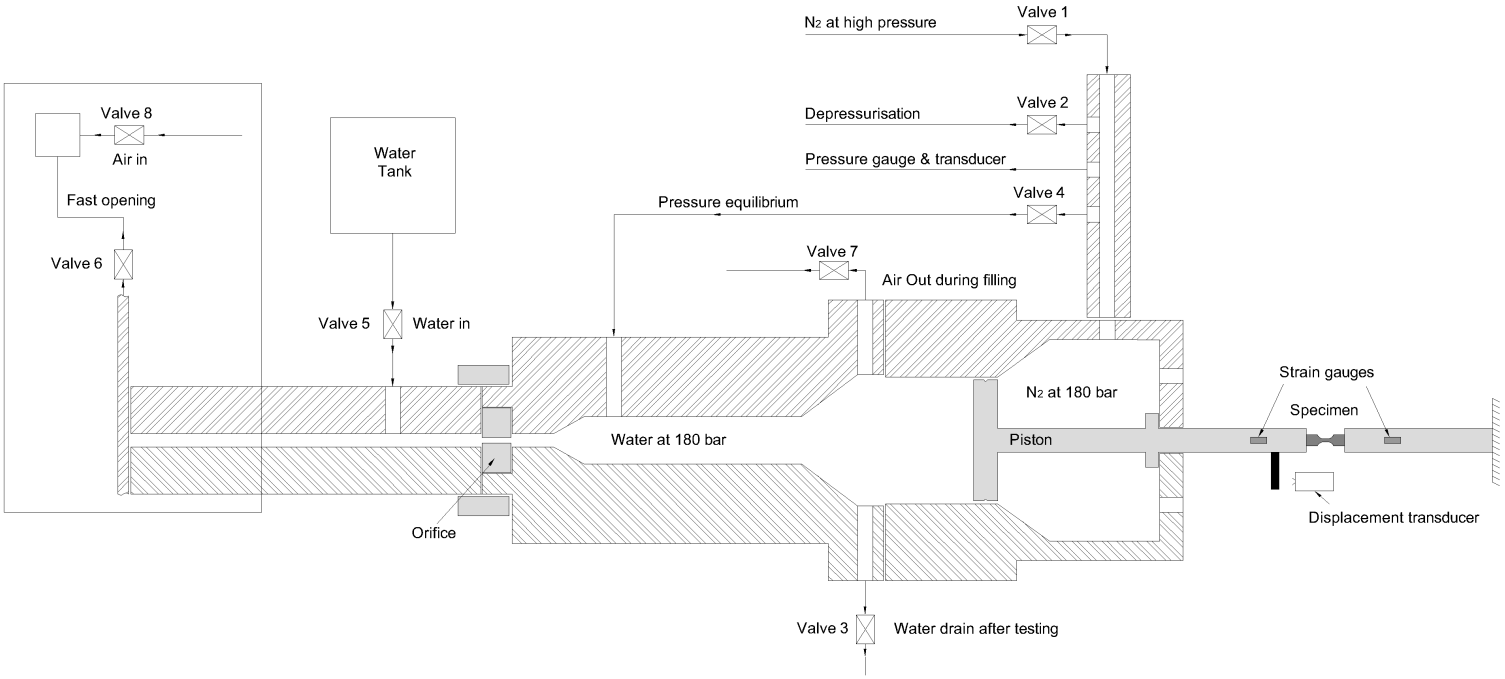

Figure 3.8: Schematic of the novel medium strain rate testing techniques (Mini bar).

3.4.6 Tensile tests at low strain-rates

For the low strain-rate tests at 0.00033 s^{-1}, two conventional servo-hydraulic testing machines were used under displacement control. The first was used at NTNU and is shown in Figure 3.9(a) using the same specimen geometry as Figure 3.7. The second (Figure 3.9(b)) was used at the University of Liverpool (UoL) to assess the material variation over the entire batch. For the investigation at the UoL the geometry of the test specimens are shown in Figure 3.10, prepared following Eurocode Standards. Longitudinal strains were measured with a one-sided extensometer over a 50 mm gauge length.

(a) (b)

Figure 3.9: Servo-hydraulic testing machine used at (a) NTNU and (b) UoL.

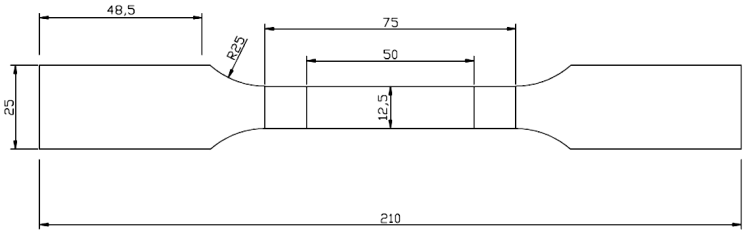

Figure 3.10: Tensile specimens conducted at UoL - units in mm.

The anisotropy of the material was investigated by cutting tensile specimens in different orientations with respect to the rolling direction. Three were cut longitudinally (0°) to the roll and three cut transversely (90°) to the direction of roll for each of the five sheets (1.5 m by 3 m) examined. This made a total of 30 quasi-static specimens tested using the UoL servo-hydraulic machine.

3.5 Experimental results

Forty-six tests were performed: 32 at low strain-rate, 7 at medium strain-rate and 7 at high strain rate, and the corresponding material data are listed in Tables 3.2, 3.3 and 3.4. Sixteen of these tests were conducted using the same geometry (Figure 3.7) allowing for direct comparison of material properties at strain rates from 0.00033 s^{-1} to 534 s^{-1}. Both engineering and true strain-rates are given and these were estimated as the average value of the strain rates recorded from each test.

Table 3.2: Material data for engineering strain-rate tests conducted at NTNU.

	Sample no.	Strain rate [s^{-1}]	Proof stress				UTS [MPa]
			0.2%	2%	5%	8%	
SHTB	DC01-01	238	392	401	424	445	515.7
	DC01-02	285	415	419	443	462	522.8
	DC01-03	372	396	414	437	458	520.4
	DC01-04	418	402	411	432	451	510.5
	DC01-05	549	420	432	448	467	527.7
	DC01-06	559	415	418	448	449	520.8
	DC01-07	667	412	432	447	466	534
Mini bar	DC01-08	4.8	313	333	363	410	529.9
	DC01-09	5	315	354	361	419	529.4
	DC01-10	17.5	332	363	404	448	552.5
	DC01-11	55	391	452	447	478	581.4
	DC01-12	64	290	356	408	434	538.8
	DC01-13	72	382	358	408	439	531.7
	DC01-14	135	381	432	454	479	539

True stress-plastic strain plots until diffuse necking over the entire strain-rate range are shown in Figure 3.11. Clearly DC01 mild steel exhibits rate dependant behaviour over this range of strain-rates. This influence on the strength and on the increase of the dynamic flow stress is approximately 50% within the investigated strain-rate range.

Figure 3.12 presents the material test data from the mini bar tests. Strain-rates were conducted in this range as only low to moderate strain-rates were expected in the component testing. Undesired oscillation or ringing in the force signals are typically observed within this strain-rate range[105]. This phenomenon can be clearly seen and affected the majority of these tests. Filtering of these oscillations can be used, however this may reduce accuracy and representation of important material behaviour. Therefore only tests at 64 s^{-1} and 72 s^{-1} were used from this test machine to calibrate the constitutive models, described in future chapters.

Table 3.3: Material data for true strain-rate tests conducted at NTNU.

	Sample no.	Strain rate [s^{-1}]	Proof stress 0.2%	2%	5%	8%	UTS [MPa]
SHTB	DC01-01	189	368	375	382	392	401.8
	DC01-02	225	378	491	398	402	409.3
	DC01-03	299	381	394	401	409	411.3
	DC01-04	343	394	398	403	409	410.3
	DC01-05	444	418	406	414	420	422.4
	DC01-06	447	415	398	391	408	410
	DC01-07	534	412	431	446	466	416.7
Mini bar	DC01-08	3.7	279	309	316	346	376.6
	DC01-09	3.8	272	320	323	333	379.2
	DC01-10	13.5	318	340	354	388	382
	DC01-11	43	329	432	413	412	419.9
	DC01-12	50	348	332	368	382	396.2
	DC01-13	56	355	337	370	386	398.7
	DC01-14	107	351	410	414	429	429.6

Figure 3.13 presents all of the results from the Split-Hopkinson Tension Bar tests (SHTB). Conducting tests at this higher level removes the dependency on the medium level strain-rate tests, which were plagued with undesired oscillations, and ensures an accurate representation of the behaviour over a large strain-rate spectrum.

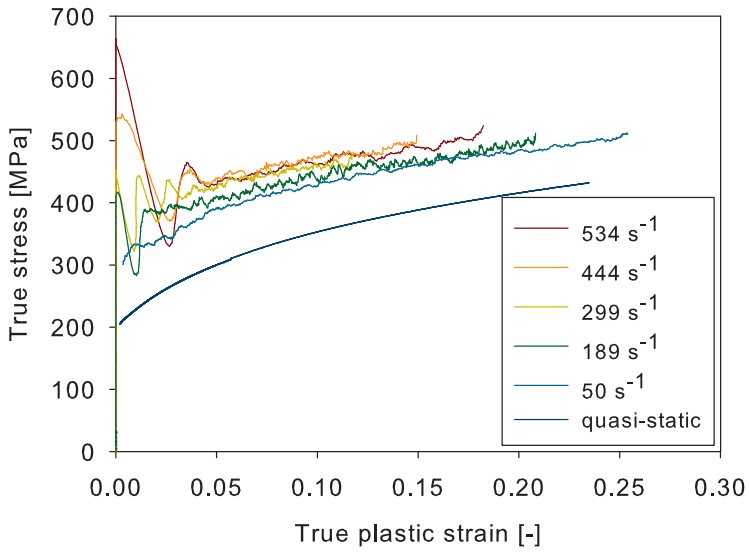

Figure 3.11: True stress versus true plastic strain curves at various strain rates.

The anisotropy of the material was investigated and the results are shown in Table 3.4 and Figure 3.14. It displays the average longitudinally (L)(0°) to the roll and

Table 3.4: Material data for strain-rates tests conducted at UoL.

Test Ref.			Width [mm]	Thickness [mm]	Yield stress 0.2%[MPa]	UTS [MPa]	Ductility [%]
Sheet 1	L	1	12.68	1.12	201.5	341.02	43.35
		2	12.71	1.13	199.8	339.55	43.20
		3	12.69	1.13	200.1	341.33	41.02
		Avg.	12.69	1.13	200.5	340.63	42.54
	T	1	12.72	1.13	211.8	340.03	42.54
		2	12.72	1.13	211.0	340.15	43.22
		3	12.71	1.13	210.1	339.34	46.06
		Avg.	12.72	1.13	211.0	339.84	43.57
Sheet 2	L	1	12.71	1.12	208.5	344.57	42.01
		2	12.71	1.12	205.2	343.52	41.72
		3	12.71	1.12	204.9	343.52	42.64
		Avg.	12.71	1.12	206.2	343.87	42.12
	T	1	12.71	1.12	208.1	336.65	41.45
		2	12.71	1.12	208.6	337.65	42.12
		3	12.70	1.12	208.2	336.85	42.23
		Avg.	12.71	1.12	208.3	337.05	41.93
Sheet 3	L	1	12.68	1.12	192.5	333.18	43.24
		2	12.67	1.12	191.9	332.26	42.53
		3	12.67	1.12	192.3	332.48	42.43
		Avg.	12.67	1.12	192.2	332.64	42.73
	T	1	12.70	1.12	192.4	322.37	40.34
		2	12.70	1.12	194.6	323.34	40.08
		3	12.71	1.11	195.2	324.58	39.87
		Avg.	12.70	1.12	194.1	323.43	40.10
Sheet 4	L	1	12.65	1.12	203.8	346.82	41.98
		2	12.70	1.12	202.1	344.95	43.17
		3	12.70	1.12	201.8	344.95	42.51
		Avg.	12.68	1.12	202.6	345.57	42.55
	T	1	12.71	1.12	211.4	343.62	41.91
		2	12.72	1.12	208.7	343.19	41.71
		3	12.67	1.12	208.0	342.76	41.58
		Avg.	12.70	1.12	209.4	343.19	41.73
Sheet 5	L	1	12.68	1.13	207.1	337.32	45.68
		2	12.68	1.13	196.2	337.75	44.71
		3	12.67	1.13	199.3	339.45	44.36
		Avg.	12.68	1.13	200.9	338.17	42.92
	T	1	12.71	1.13	207.3	335.47	41.49
		2	12.68	1.13	205.3	334.62	40.30
		3	12.70	1.13	207.8	335.73	40.11
		Avg.	12.70	1.13	206.8	335.27	40.63

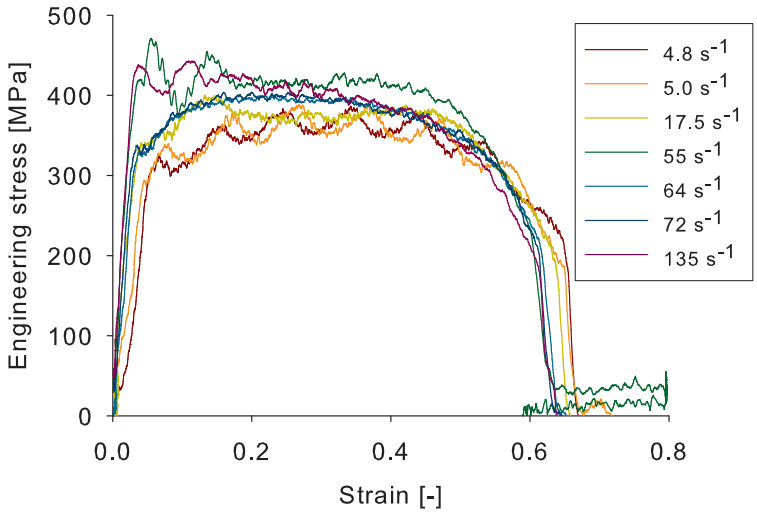

Figure 3.12: Effects of strain rate on the behaviour of Docol form 01 using the hydro-pneumatic testing machine.

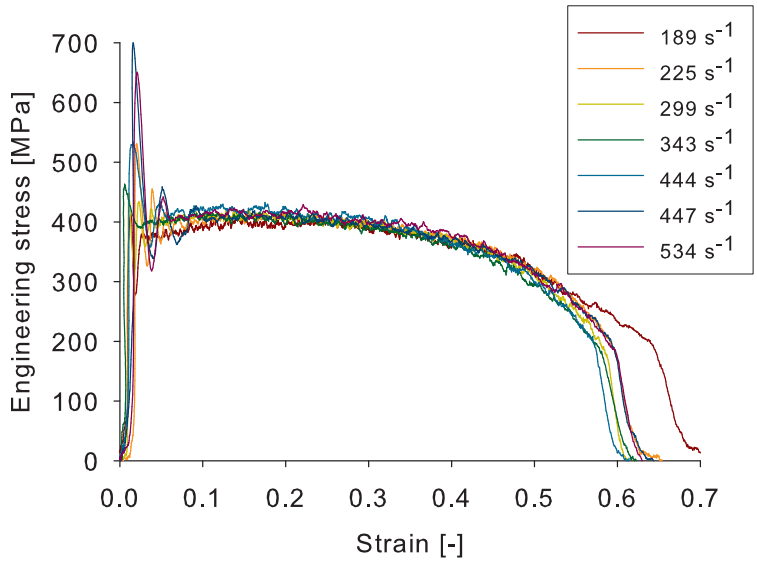

Figure 3.13: Effects of strain rate on the behaviour of Docol form 01 using the SHTB.

the average transversely (T)(90°) to the direction of roll for each sheet of mild steel. All sheets exhibited very similar tensile properties and strain hardening characteristics with the variations highlighted in Table 3.5. The percentage ductility was measured using Equation 3.4 with an original gauge length, $L_\circ$ of 50 mm. The maximum and minimum standard deviation between each sheet (1-5) is 2.4 MPa and 0.4 MPa for yield stress, 5.1 MPa and 0.8 MPa for UTS and 2.4 % and 0.4 % for ductility.

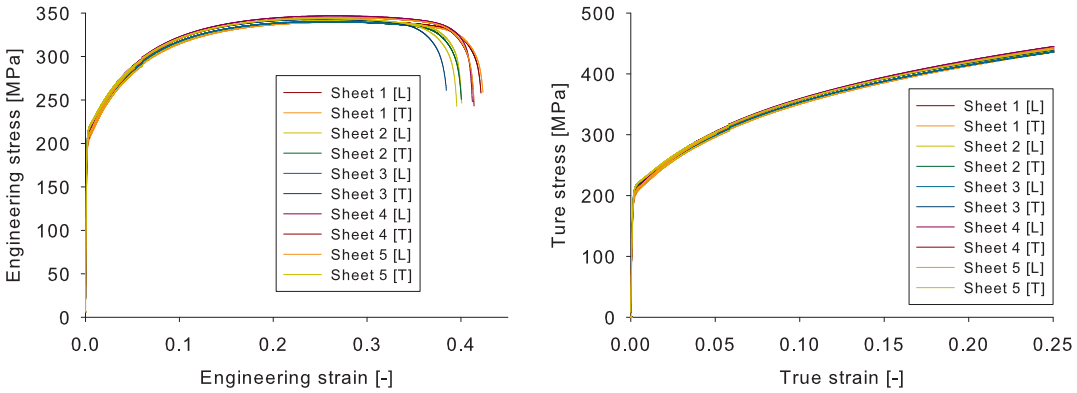

(a) Engineering stress-strain curves.

(b) True stress-strain curves.

Figure 3.14: Variation in stress-strain over entire batch for Docol form 01.

Table 3.5: Average material properties obtained from static tensile tests.

Direction of roll	Yield stress	UTS	Ductility
Longitudinal	200.5	340.2	42.97
Transverse	205.92	335.1	41.59
Deviation	3%	3%	3%

3.6 Selection of constitutive relations

Based on the material test results it can be concluded that the material is highly ductile, tending to yield gradually and exhibits moderate strain rate effects. For all practical purposes the material behaves isotropically and temperature softening can be ignored.

This information is vital as it identifies which phenomena the constitutive model must describe in order to give adequate solutions, and which can be neglected. Ultimately this can lead to using a simpler constitutive relation, saving significant computational time in the FEM analyses.

A number of constitutive models are available to model this dynamic behaviour under blast loading conditions. Each of these models has its own advantages and disadvantages; therefore selection requires expertise by the user to select the most suitable. To be able to realistically predict the behaviour of a structure under various loading conditions the constitutive model needs to be shown to simulate known behaviours at smaller specimen levels up to the full scale structural level[106].

Based on these findings two constitutive relations have been chosen for future modelling. The first being the Modified Johnson-Cook model[107] (MJC) and the second being the Cowper-Symonds[108] (CS). Both models are capable of predicting

strain rate effects which play an important role in the dynamic plastic behaviour of this material.

3.6.1 Advanced non-linear (Numerical) constitutive relation

In advanced FEA-analyses it is necessary to provide a comprehensive constitutive relation, as the software is capable of predicting complex non-linear problems. During and after a blast event a structure undergoes dynamic response in the elastic and plastic regime[102]. In addition to this it experiences varying strength enhancement effects over a range of strains and strain rates. To account for this the Modified Johnson-Cook (MJC) model was utilised which can account for isotropic hardening and strain rate hardening.

The MJC model ignores any coupling between the strain hardening and strain rate effects, by treating each independently. Some coupling is evident in the experimental tests data in Figure 3.11, since strain rate effects decrease with increase in strain.

3.6.2 Simplified (Analytical) constitutive relation

The fundamental material properties that are required for simplified methods are far simpler than those required by the finite element software packages, and are those relating to strength. The Cowper-Symonds (CS) relation was chosen to estimate the strain-rate sensitivity behaviour of the material. This relation alters the flow stress to account for dynamic behaviour based on an average strain level expected in a specific problem. In reality strain rate varies both temporally and spatially throughout the structure during loading.

3.7 Summary

It is imperative for structural impact analysis to know the material behaviour at high strain rates. The mechanical response of mild steel, Docol form 01 (DC01) was therefore assessed using uniaxial tension tests conducted at quasi-static and dynamic strain rates (0.00033 s^{-1} to 534 s^{-1}).

Material characterisation tests were carried out using a servo-hydraulic tensile test machine at a strain rate of 0.00033 s^{-1} and gave average 0.2% engineering proof stress of 200.5 MPa and 205.9 MPa in the longitudinal and transverse directions, respectively. The ductility at failure was around 42%, with an original gauge length of 50 mm. The material was also tested for strain rate sensitivity using a Split Hopkinson Tension Bar over a range of strain rate from 189 s^{-1} to 534 s^{-1} and gave 0.2% engineering proof stress of 368 MPa to 412 MPa. Some tests were also carried out using a Mini-bar at lower strain rates as only low to moderate strain rates were expected in the experiments. These gave a range of 277 MPa to 355 MPa 0.2% engineering proof stress over strain rates of 5 s^{-1} to 72 s^{-1}. It is clear that the material is rate sensitive even at low to moderate strain rates.

It can therefore be concluded that the material is highly ductile, tending to yield gradually and exhibits moderate strain rate effects. For all practical purposes the material behaves isotropically. Strain rate tests at 0.00033 s^{-1} revealed that the yield stress, UTS and ductility between the different directions of roll deviated by approximately 3%.

This information was used to guide the selection of appropriate constitutive material models for future numerical and analytical studies in Chapters 6 and 7 respectively. Two constitutive relations have been chosen; the Modified Johnson-Cook model[107] (MJC) and the Cowper-Symonds[108] (CS). The models were chosen, as they are relatively easy to calibrate and require minimal experimental data. Both material models are capable of predicting strain rate effects, and are commonly used to predict the behaviour of impact in open literature.

Chapter 4

Experimental Method

4.1 Introduction

A differential pressure device capable of producing repeatable uniform static or transient pulse pressure loading on plated specimens up to 1 m square loaded area was developed at the University of Liverpool Impact Research Centre by Schleyer *et al.* [109] and Hsu[68]. A large body of well-defined test data (together with complementary material test data) was produced using this differential pressure device with scaled mild steel plates (Schleyer *et al.* [110][111]), aluminium plates (Langdon and Schleyer[112]), architectural glazing panels (Goodfellow and Schleyer [113]), scaled profiled blast walls (Langdon and Schleyer [75], Schleyer *et al.* [114]), and aircraft structures (Simmons and Schleyer[115]). The well-defined character of the loading and the scale of the device are its notable features, which make it an extremely versatile and widely applicable research tool for studies in this important field of blast loading and response of protective structures.

Recently a smaller version (0.5 m square loaded area) of the original design was built with the advantage of a greater load capacity (800 kN/m^2) and capable of faster loading, typically 0-200 kN/m^2 in under 10 ms. A major objective in this study was to install this facility into a newly built protective concrete enclosure and integrate a new triggering system for dynamic testing.

4.1.1 Objectives of chapter

The objective of this chapter is to present the operation and characteristics of a new fast transient loading rig developed at the University of Liverpool. It will discuss the key instrumentation and how it was arranged to capture pressure-time histories. The test rig was used to produce loading characteristics which are representative of vented hydrocarbon explosions on topside structures.

4.2 Experimental set-up

The Pulse Pressure Loading Rig (PPLR) shown in Figure 4.1 is essentially a three-part pressure vessel. The PPLR consists of two cylindrical half sections (chambers I and II) with domed ends, providing the volume of the vessel and a central section, which provides the support for the test specimens. Both chambers have identical flanged nozzles over which rigid or film diaphragms can be placed, depending on the required loading, as given in Figure 4.2. The PPLR can apply a transient pressure loading over an area of 0.5 m^2 up to a maximum pressure of 8 bar.

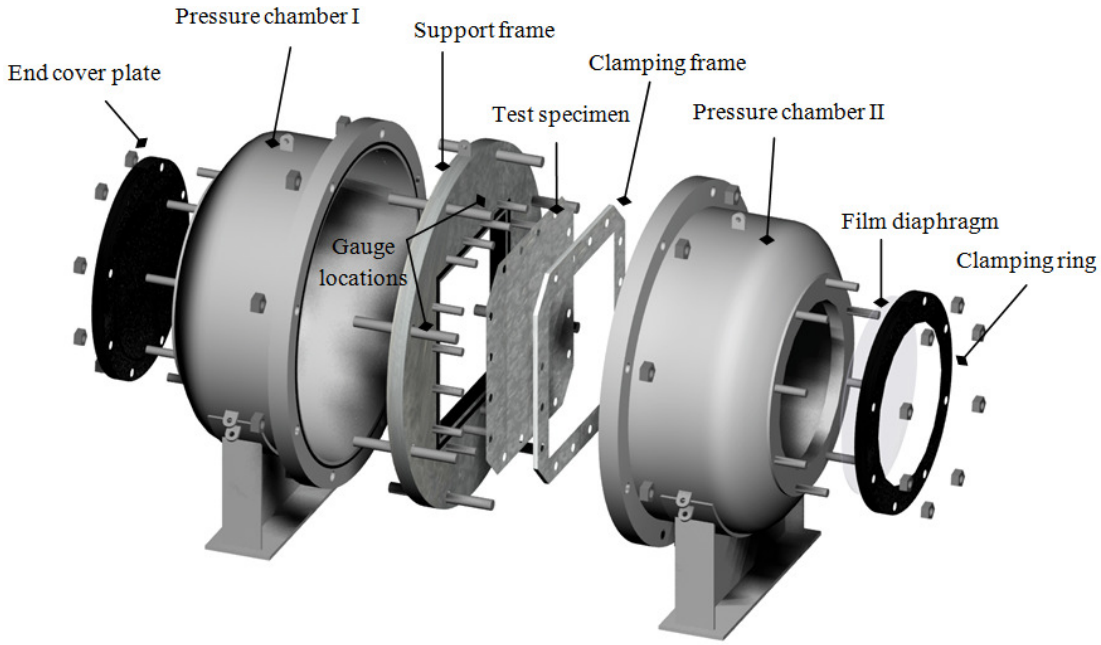

Figure 4.1: Expanded view of pulse pressure loading rig (PPLR).

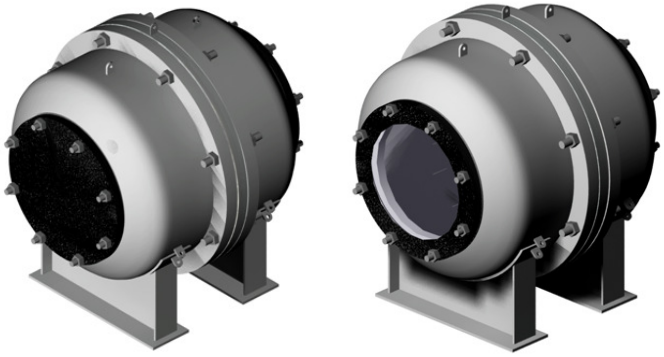

(a) (b)

Figure 4.2: PPLR assembled with (a) end cover plate and (b) film diaphragm.

4.2.1 Instrumentation

The response of test specimens was measured using a variety of sensors and equipment listed in Table 4.1

Table 4.1: Itineracy of equipment required for PPLR.

Instrumentation for capturing transient event
PDA-2MPA Miniature pressure gauges [20 bar capacity]
Flyde transducer amplifiers, with built in bridge conditioning units
Tekronix differential amplifier and bridge conditioning units
Kontron TRA 800 transient recorder

The pressure transducers were miniature devices capable of measuring steady state and dynamic absolute pressure, with high sensitivity and a wide frequency response. Calibration of the transducers was performed by incrementally pressurising the PPLR and recording this on a hand held pressure device (Manometer). At each pressure level an output voltage from each pressure transducer was taken.

The pressure transducers used in this study measure pressure by deforming a strain-gauged diaphragm. When initially fitted to the PPLR and conducting the calibration test the correlation between pressure and voltage was not linear as the pressure increased. The signal output actually decreased. The problem was attributed to air leaking into the transducer from the connection detailing (up through the cabling), as shown in Figure 4.3. This meant that pressure was also acting on the reverse side of the strain-gauged diaphragm leading to a reduction in output voltage as the pressure increased.

To overcome this problem the connection detailing was bedded in silicon there by sealing the leak. This corrected the problem and ensured linearity between pressure and voltage output. A constant was then obtained to convert voltages into equivalent pressures.

A purpose built trigger-delay unit and firing circuit were used to produce a controlled blow-down for the dynamic tests. A TRA 800 transient recorder, capable of a 25 MHz sampling frequency captured the output signals from the pressure transducers. This data was then processed using WinWave software to convert the data to text format so that it could be analysed to obtain the pressure-time histories.

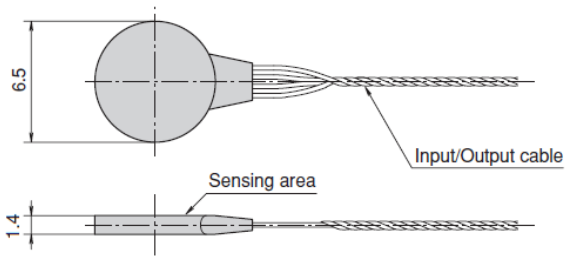

(a)

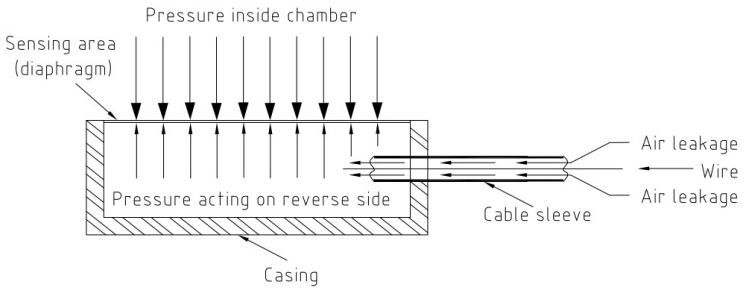

(b)

Figure 4.3: Detailing of (a) miniature pressure gauge and (b) close up of sensing area and air leakage issues - units in mm.

Output data was found to be particularly sensitive to electrical noise. To minimize this effect the pressure transducers were directly connected to the Flyde transducer amplifiers. This eliminated the connections through a multi-pole connector, where several cables are brought into the rig, and allowed screened cable to go from the amplifiers to the transducers without the screen being broken. The screen was grounded at the amplifier end and the noise level was significantly reduced.

4.2.2 Principle of operation

To describe the principle of operation for this equipment a schematic drawing of the whole assembled rig is shown in Figure 4.4. Initially each side (chambers I and II) are pressurised with air, at $t < 0$. The film on the right nozzle is burst creating a pressure differential across the test specimen, t=0. This causes a rapid evacuation of high-pressure air, through the burst diaphragm, $t = t_r$. At $t = t_r$ (determined by the depressurisation time for one side) the second diaphragm is burst (accounting for any delays in the relays) and the pressure is vented to atmosphere.

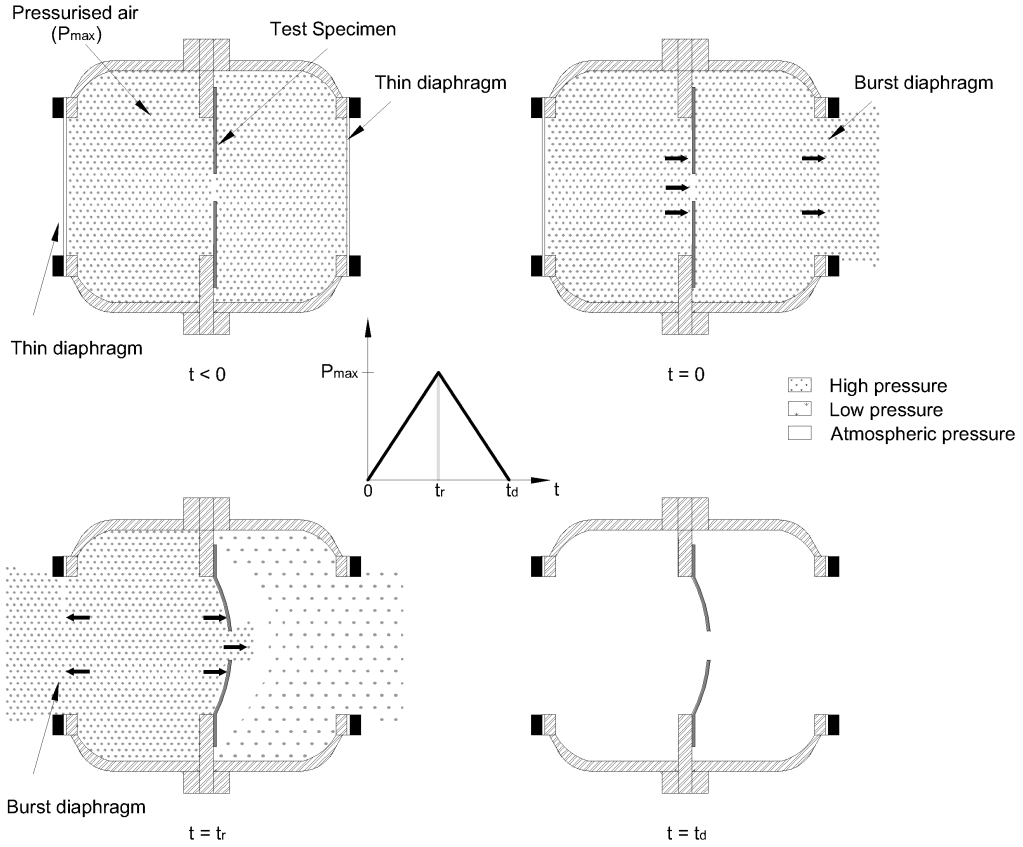

Figure 4.4: Test configuration 1 for dynamic load testing.

Figure 4.4 displays an idealised triangular pressure-time history produced by the timed blow-down of the vessel. It can be seen from Figure 4.4 that there are three key measurements taken during a test; the time taken to achieve the maximum pressure t_r, the maximum pressure P_{max} and the depressurisation time t_d. The dominant factor that influences these key factors, and the shape of the pulse curve, in this study, is the size of the exit area (size of the opening in the burst diaphragm) on each chamber. This can be manipulated to produce a variety of shapes and load durations. A series of characterisation tests were carried out to investigate the influence of this.

4.3 Characterisation tests

The purpose of these tests was to characterise the depressurisation behaviour of the PPLR under various rig configurations at a range of test pressures. From this data it was possible to design PPLR tests that had certain depressurisation characteristics, i.e. were representative of typical accidental explosions in offshore structures.

4.3.1 Procedure

A 10 mm thick characterisation plate was fabricated with interchangeable bolt-on central fixtures to allow for a variety of openings to be simulated, or to simulate a full plate, as shown in Figure 4.5. This was then fixed to the support frame via 36 equi-spaced studs and the PPLR assembled as depicted in Figure 4.2.

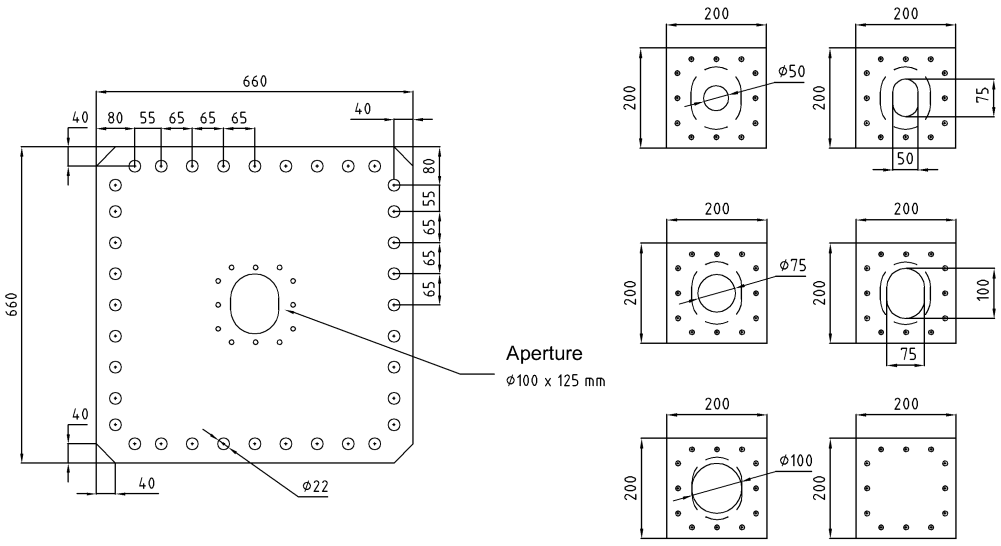

(a) (b)

Figure 4.5: Engineering drawing of (a) characterisation plate and (b) bolt-on apertures - units in mm.

Firing mechanism

Figure 4.6 shows how a controlled and repeatable exit area was achieved by placing a looped wire around the film diaphragm. The film diaphragm material used in all tests was 250 μm thick Melinex with a burst capacity of 30 psi. When energised the wire heated up rapidly and initiated a uniform, circumferential rupture of the diaphragm.

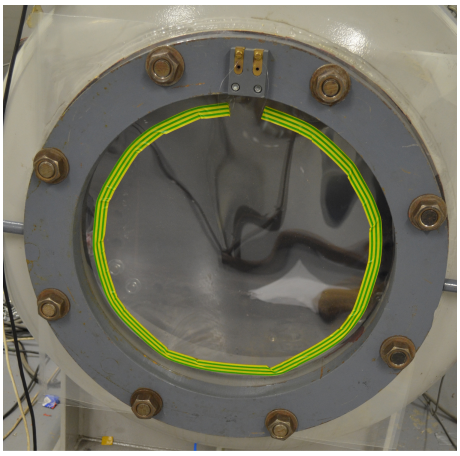

Figure 4.6: Arrangement of looped wire for bursting the thin diaphragm material.

Pressure-time history recording

The internal pressure was recorded by four pressure gauges, two on each side of the support frame, as shown in Figure 4.7. As a first approximation, the load on the plate was simplified to be the pressure difference described by the pressure transducers. This was deemed appropriate as pressure distributions in vented vessel explosion are often quite uniform[30]. An example of this process will be shown at a later stage in this chapter, Section 4.3.4.

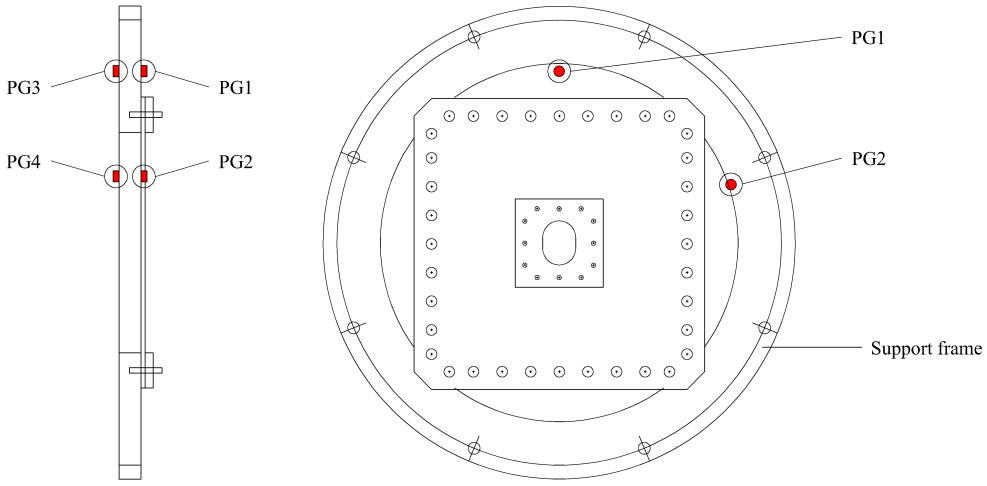

Figure 4.7: Characterisation test configuration with the pressure gauge positions highlighted.

4.3.2 Selection of pressure loadings

A critical part of this study was to ensure that the pressure loads imparted on the test specimens were representative of vented hydrocarbon explosions in offshore structures. As mentioned in Chapter 2, Section 2.4.2, research conducted by the Steel Construction Institute proved that overpressures can be as high as 4 bar[24]. In light of this two nominal peak pressure loads of 1.72 bar (25 psi) and 3.45 bar (50 psi) were selected. These are at the upper limit of expected overpressures and would be low-probability high-consequence events causing large deformations in plated structures.

Representative loading

Once the pressure levels of 25 psi and 50 psi had been selected it was important to ensure that these were applied over a time period representative of a typical overpressures from accidental explosions on topside structures, typically between 50-200 ms[41]. This was achieved by controlling the exit area of the pressurised air through the burst diaphragm.

To demonstrate the influence of exit area on depressurisation time, only one side of the PPLR rig is considered. Figure 4.8 shows a typical depressurisation curve for such a case. An investigation by White[12] using the large PPLR illustrated that the burst area of the film diaphragm significantly influences the depressurisation time t_d. The results of White's study are shown in Figure 4.9 considering a variety of pressures. For example, the depressurisation time t_d, for a 0.75 psi test could be altered from approximately 80 ms to 30 ms, by increasing the burst area threefold.

Preliminary investigations found that a burst area of 0.18 m^2 would provide suitable (scaled) depressurisation times t_d, in this study. The depressurisation time of a single chamber using a burst area 0.18 m^2 was 6.6 ms at 25 psi and 11.2 ms at 50 psi.

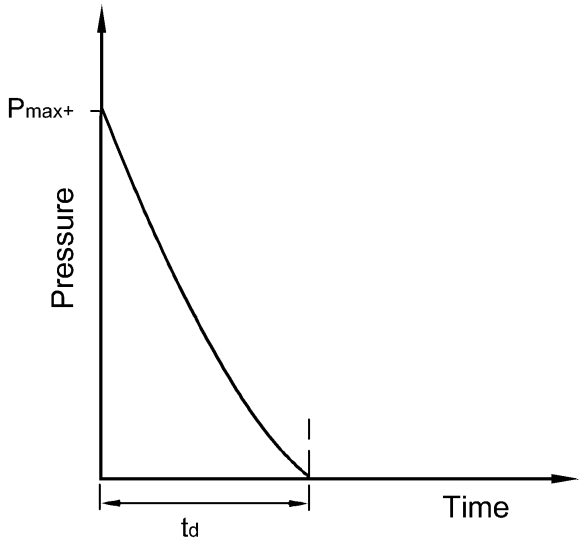

Figure 4.8: Key test measurements during depressurisation of one chamber.

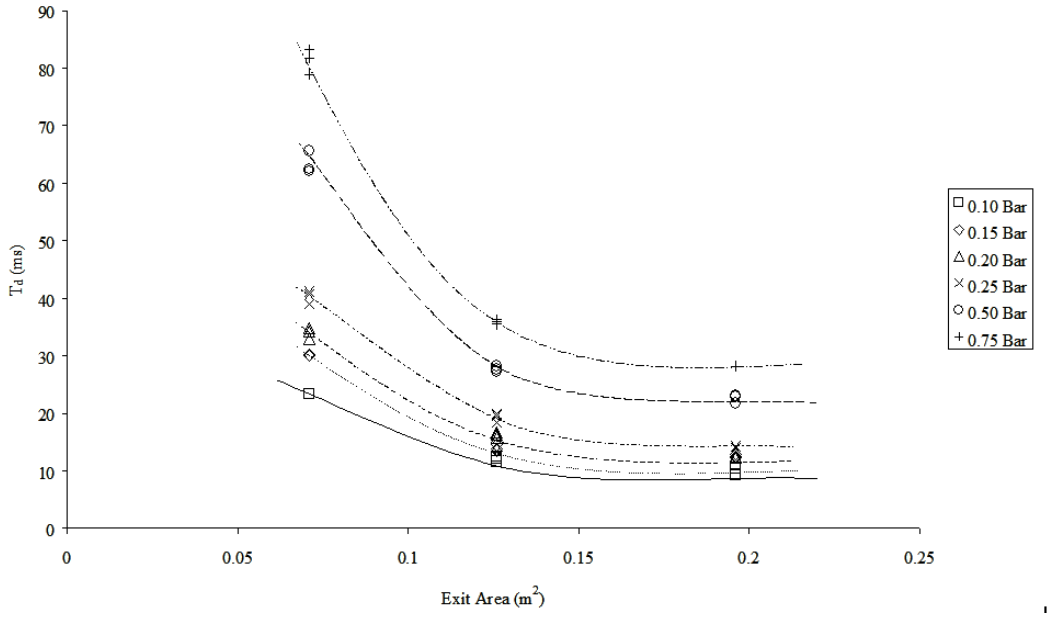

Figure 4.9: Variation in T_d with increasing burst area for single diaphragm[12].

4.3.3 Scaling

The PPLR is capable of testing scaled structures with an area up to 0.5 m^2, approximately $\frac{1}{8}$th of typical decking sections found on offshore structures. The pressure-time histories can be scaled up to full sized structures, keeping the peak pressure constant whilst multiplying the time by 8. The loading was scaled as far as reasonably practicable according to the laws of geometrical scaling[116], see Section

5.5.1 for further details. Applying this scaling rule to the previous rise times calculated of 6.6 ms at 25 psi and 11.2 ms at 50 psi, provides equivalent rise times of 52.8 ms and 89.6 ms respectively. Assuming an idealised triangular pressure-time history, as shown in Figure 4.4 the load durations would be 105.6 ms for the 25 psi test and 179.2 ms for the 50 psi tests. These are within the expected range for vented hydrocarbon explosions, typically between 50-200 ms[24] and ensured that realistic overpressures were simulated.

4.3.4 Example data capture for test configuration 1

As mentioned earlier the load on the plate is approximated by the pressure difference indicated by the pressure transducers on each side of the PPLR (refer to Figure 4.7). Figure 4.10 demonstrates this process. Figure 4.11 compares experimental data with an idealised triangular pulse shape. This clearly highlights that the experimental pressure-time history has a non-linear rise time and depressurisation time. This is due to the configuration of the test rig. Initially there is a quick ramp-up time to peak pressure, due to the high pressure within the PPLR. Then, during the depressurisation time (from peak to ambient pressure) there is a slower ramp down, due to the lower pressure within the PPLR.

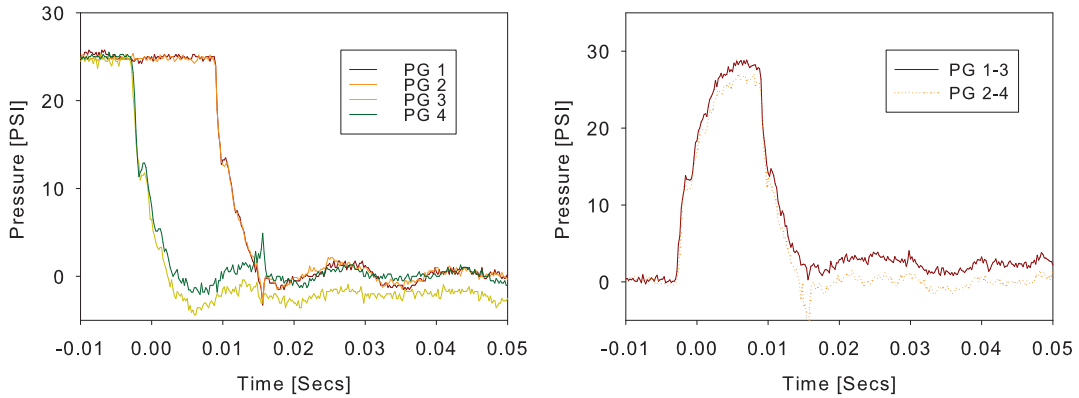

Figure 4.10: Example pressure-time history recorded using test configuration 1 by (a) each pressure transducer and (b) the calculated pressure difference between chamber I and chamber II.

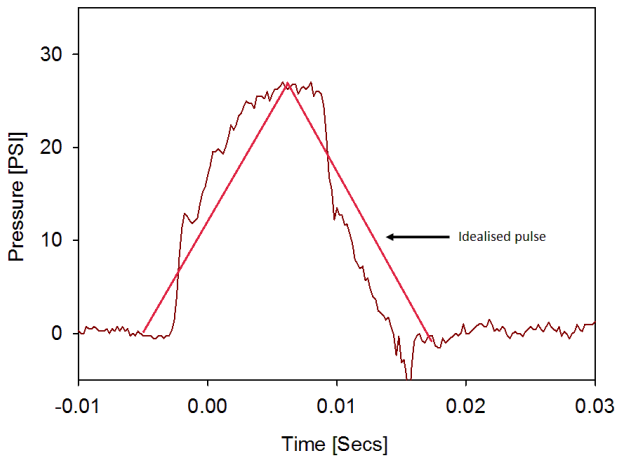

Figure 4.11: Differences between the idealised triangular pulse shape and the actual experimental pressure-time history data.

4.3.5 Repeatability of loading

The repeatability of the pressure loading applied to a structure using a large scale PPLR has been shown in experiments by White[12], Hsu[68] and Schleyer *et al.* [109] for full specimens (without openings). The repeatability of the pressure loading for the smaller test rig was assessed in this current study. This was done by repeating the same test three times at 25 psi and 50 psi using the rigid characterisation plate (without opening). For simplicity only one pressure chamber was exhausted. The results are shown in Figure 4.12. Excellent repeatability was observed with the variation between tests in the order of 0.5%.

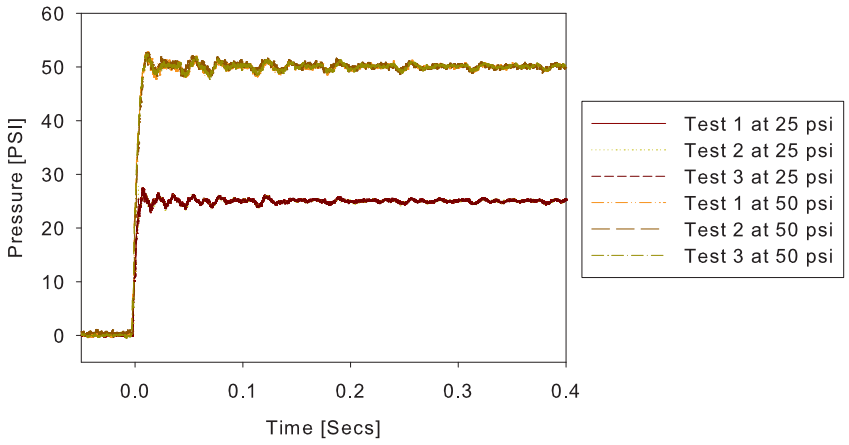

Figure 4.12: Repeatability assessment of the new smaller PPLR at nominal pressures of 25 psi and 50 psi using the rigid characterisation plate.

It can be clearly seen from Figure 4.11 that the shape of the pulse is highly dependant on the exact sequential blow-down between the two chambers to produce a triangular pulse. If the second diaphragm bursts too early, the expected peak pressure will not be reached. If the second diaphragm bursts too late, the pressure-time history will no longer be triangular but be of a rectangular nature. This timing is critical and reliant on the consistent bursting and depressurisation time of the chambers.

When bursting a single layer of Melinix for the 25 psi tests the burst area was of a uniform circumferential manner, making this a highly repeatable process. When conducting the 50 psi tests, using two sheets of the Melinix, only the outer sheet was exposed to the looped wire. This meant that only the outer layer burst in a uniform manner, whilst the inner was more irregular. Examples of both these cases are shown in Figure 4.13. It can be seen that a small narrow piece of diaphragm material is left around the edge of the nozzle. Any variation in the width of this remaining piece could affect the pressure profile. This irregularity is greater for the two diaphragm case causing a greater scatter in the results and White[12] demonstrated this in Figure 4.14.

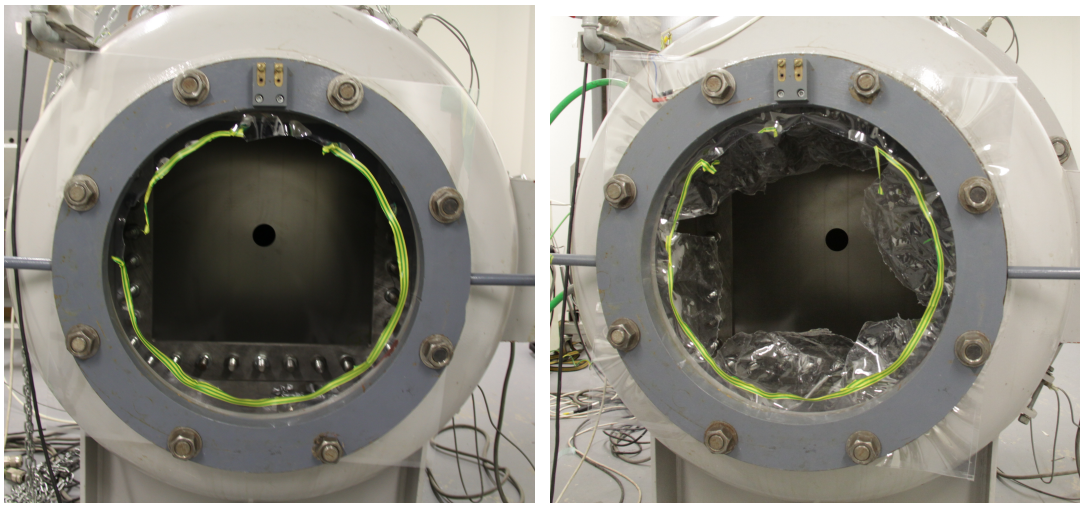

(a) (b)

Figure 4.13: Example burst diaphragms for (a) 25 psi test with a single diaphragm and (b) 50 psi test requiring two diaphragms.

This increase in scatter increases the level of uncertainty making it difficult to produce repeatable and consistent pressure-time histories at the higher-pressure level (50 psi). This is compounded by material defects in the diaphragm material.

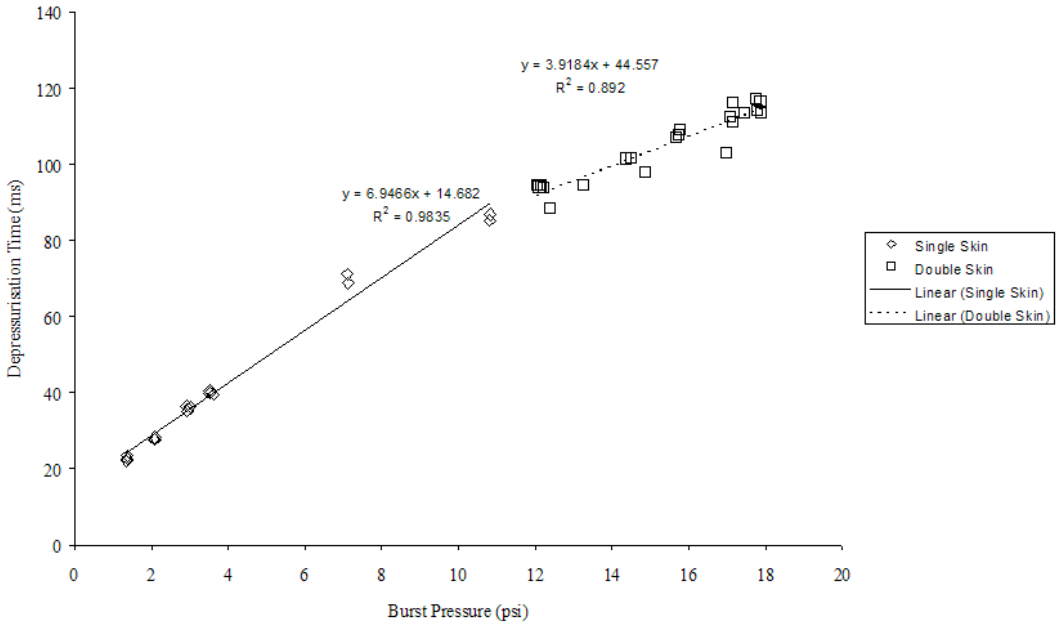

Figure 4.14: Variation in depressurisation time based on number of diaphragms (skins)[12].

Important parameters

As discussed in Chapter 2 the structural response is extremely sensitive to its loading conditions, i.e. in this case the shape of the pressure-time history. Work by Schubak *et al.* [82] highlighted the importance of the rise time in a triangular-shaped pulse pressure, particularly when it is greater than 0.3 times that of the total pulse time, as in the case of this study. The decay time (time from t_d - t_r), is less significant than the rise time and analyses in future chapters confirmed this for geometries, loads and times encountered in this study. With this knowledge a simplified approach to the test configuration was made.

4.3.6 Simplified test configuration

Figure 4.15 is a schematic drawing of the whole assembled rig using a simplified test configuration. As before chambers I and II are pressurised by air, at $t < 0$. The pressure differential is established by bursting the film diaphragm on the right side of the chamber, $t = 0$. This causes a rapid evacuation of high-pressure air, through the burst diaphragm, $t = t_r$. A solid diaphragm is placed on the left hand side nozzle (rather than a diaphragm) preventing the pressurised air escaping through this chamber, which means it must evacuate through the hole in the test specimen, then the burst diaphragm. A pressure difference is created as the pressurised air evacuates much quicker through the burst diaphragm than through the hole in the test specimen.

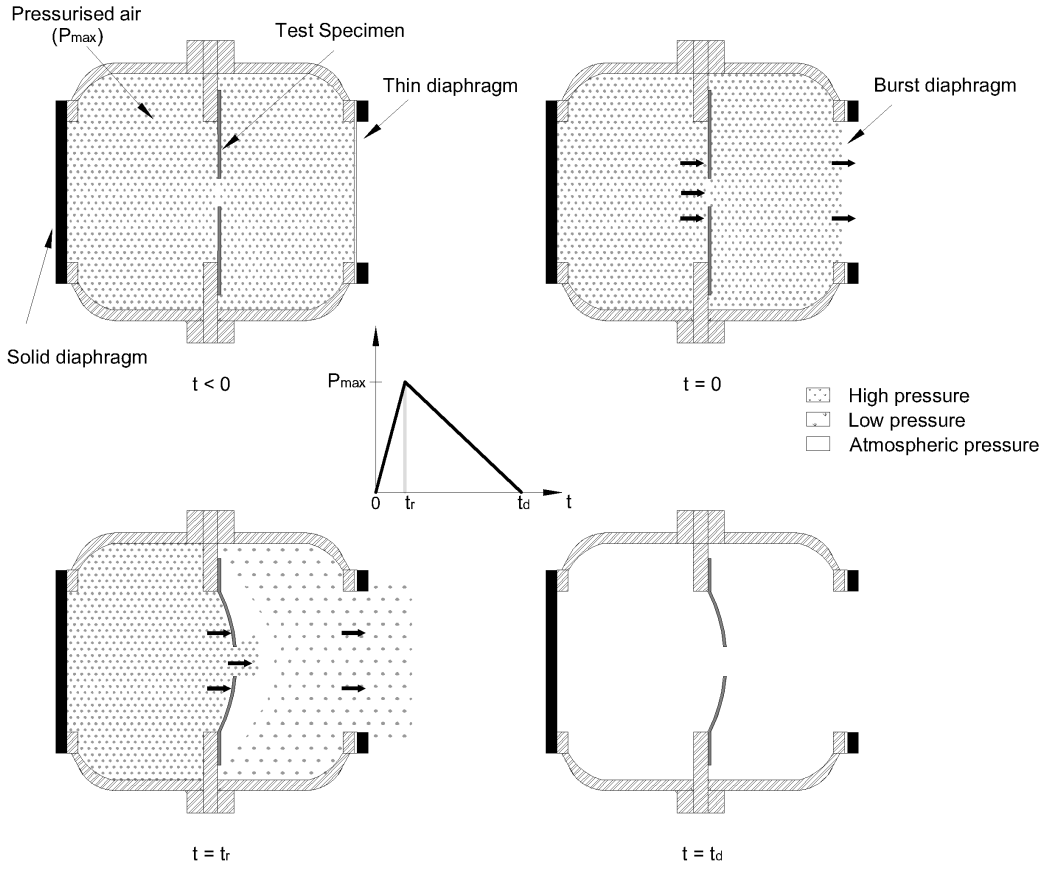

Figure 4.15: Test configuration 2.

Improvement

Conducting PPLR tests in this manner removed the reliance on the timed sequential blow-down time between chambers. This led to increased repeatability between tests, even at the higher pressures.

Example data capture for test configuration 2

Figure 4.16 shows a typical pressure-time curve created by approximating the pressure difference between pressure transducers on each side of the PPLR (refer to Figure 4.7).

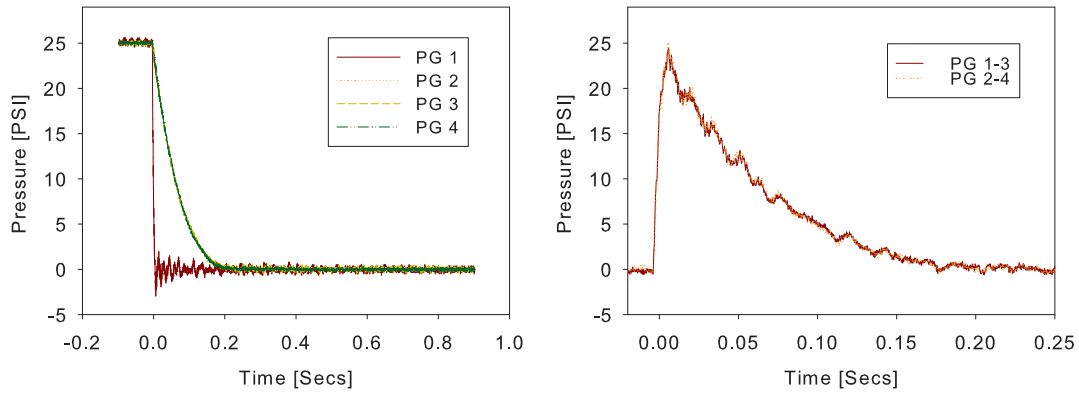

(a) (b)

Figure 4.16: Example pressure-time history recorded using test configuration 2 from (a) each pressure transducer and (b) the calculated pressure difference between chamber I and chamber II.

The rise to peak pressure appears almost instantaneous due to the scale used to capture the full pressure-time history but there is a finite rise. The decay part of the load history is much longer due to the small area of the hole in the test plate compared with the area of the exit nozzle. This can be explained by imagining what would happen if a full plate was placed into the configuration shown in Figure 4.15. With a full plate the thin diaphragm is burst as before creating a pressure differential across the specimen. However, the pressurised air in the second chamber (with the solid diaphragm) is not able to escape through the chamber and out of the burst diaphragm. This means that this chamber pressure remains relatively constant, as shown in Figure 4.12. If a small opening is introduced, the decay time (time from t_d - t_r) will be longer than if a large hole is introduced, as the pressurised air will take longer to escape through it.

Analysis

The pressure data was filtered removing any spike less than 0.125 ms (1 ms scaled) duration[24] on the assumption that pressure with duration less than 1 ms (scaled) would not affect the response of the plate significantly. An idealised triangular pressure pulse can be constructed by extrapolating a line from the point of maximum pressure through a point on the pressure-time history at 10% of the maximum pressure as shown in Figure 4.17.

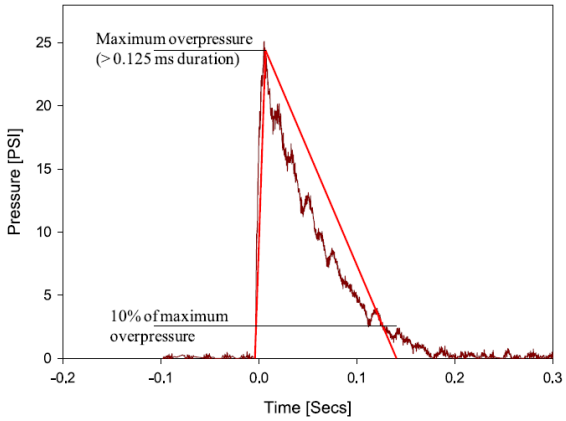

Figure 4.17: Pressure-time history for plate with opening showing construction of idealised triangular pulse load.

4.3.7 Uniformity of pressure distribution over the structure

Previous studies using a large PPLR by White[12], Hsu[68] and Schleyer *et al.* [109] have shown uniform distribution of the pressure across structures (without openings). The introduction of an opening in the centre of the plate will have an effect on the uniformity of the distributed pressure.

To assess any variation in the loading the pressure gauges (PG's) were re-positioned as depicted in Figure 4.18. PG1 and PG3 remained in the same position, while PG2 and PG4 were re-located close to the centre of the plate, 80 mm away from the closest hole. Figure 4.19 shows the results from tests with 15, 25 and 50 psi pressures. It is evident that there is little variation between the pressure recorded on the test specimen and the pressure recorded at the original location on the support plate. With these results in mind the simplification of assuming the load on the plate can be described by the pressure difference of the gauges was deemed acceptable and was used for all further tests.

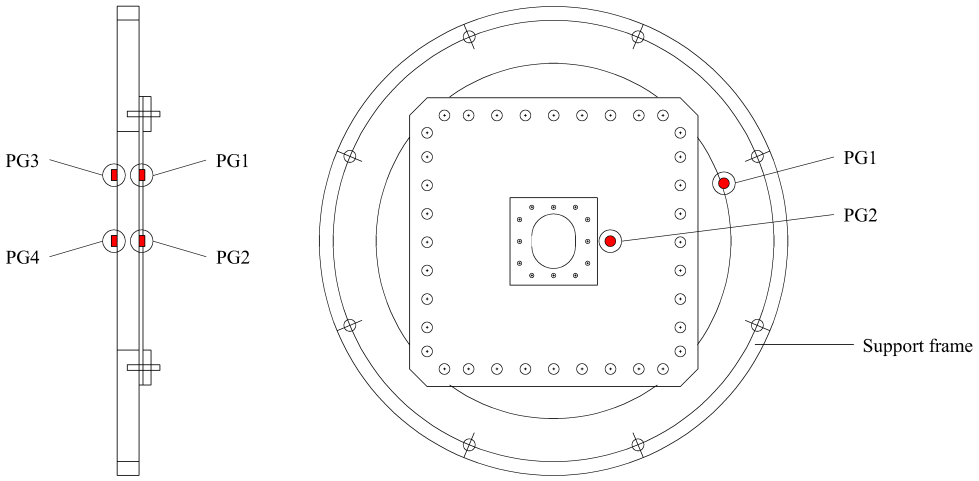

Figure 4.18: Characterisation test configuration with the pressure gauges re-positioned and highlighted.

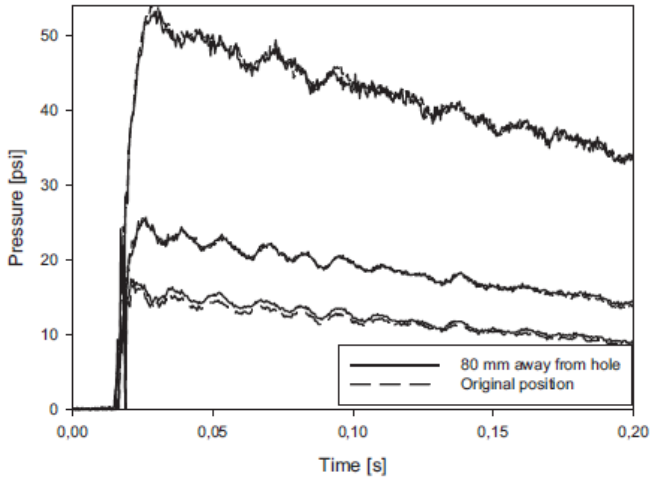

Figure 4.19: Pressure variation near to the opening.

4.3.8 Results

Using the simplified test configuration discussed in Section 4.3.6 a full set of characterisation tests was conducted covering all geometries in Figure 4.5. Figure 4.20 shows the variation in rise time T_r and depressurisation time T_d. Very little scatter is seen for the T_r when tested at 25 psi with a slight increase seen for the 50 psi tests over a variety of openings. The increase in scatter at 50 psi could well be attributed to the irregular rupture of the film diaphragms, discussed in Section 4.3.5. These results proved that the rise time T_r is relatively insensitive to a change in hole area in the test specimen. In contrast the depressurisation time T_d is significantly altered by a change

in the hole area in the centre of the characterisation plate. A change from a hole 0.78% of the plate area to a 4.14% reduces the depressurisation time T_d approximately 79% for both 25 psi and 50 psi tests. This is to be expected due to the configuration of the test rig. The decay time (T_d-T_r) is less significant than the rise time therefore this variation between tests is not important.

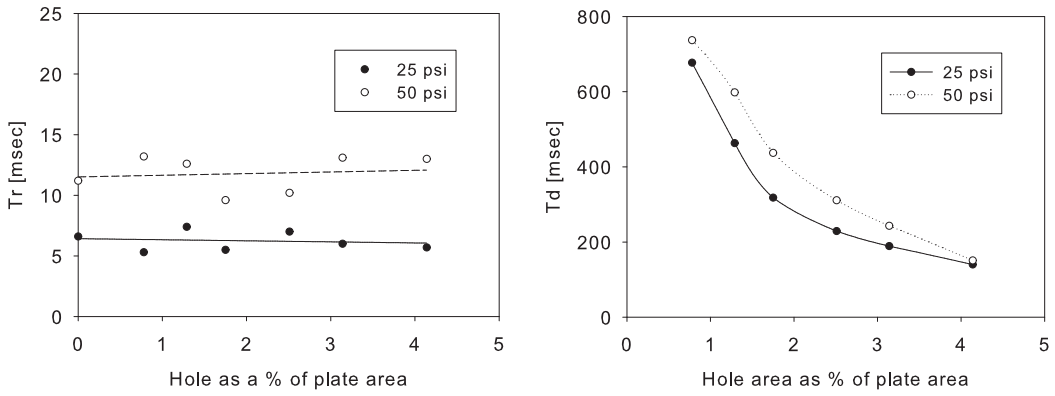

(a) (b)

Figure 4.20: Variation in (a) rise time, T_r and (b) depressurisation time, T_d with increasing area of hole in rigid plate.

4.4 Summary

Pressure-time histories of scaled 0.5 m square plates with varying openings have been developed in this chapter. They have been designed to be representative of vented hydrocarbon explosions on topside structures.

Existing principal modes of operation for the Pulse Pressure Loading Rig (PPLR) have been simplified to improve repeatability over a range of pressure levels. Two nominal peak pressure loads 1.72 bar (25 psi) and 3.45 bar (50 psi) were selected as overpressures from explosions on topside structures have been known to reach up to 4 bar. By controlling the depressurisation times of the chambers the pressure-time histories have been constructed to fall between 50 ms and 200 ms (scaled), typical duration times for such explosions. A diaphragm burst area of 0.18 m^2 was selected to ensure equivalent (scaled) overpressures of approximately 106 ms and 180 ms for nominal pressures of 25 psi and 50 psi respectively. The methodology and experimental procedure will be applied to the component tests in Chapter 5.

Chapter 5

Component Tests

5.1 Introduction

The aim of this chapter is to present the results from the experimental investigation, which play a central role in this research project. The investigation comprises a comprehensive series of carefully planned experiments on 0.5 m square plates of 1.1 mm thickness considering various pressure levels, openings and boundary conditions. Two different boundary conditions were considered in this experimental series, firstly clamped with assumed in-plane restraint and secondly clamped without in-plane restraint. As stated in the objectives, the experimental data generated is essential for the validation of numerical and analytical models.

5.2 Edge conditions of the component tests

Two boundary conditions were considered in this experimental series, namely rotationally fixed with and without in-plane edge restraint. The clamping frame provided the rotational restraint whilst the number of studs provided the in-plane restraint. These configurations were chosen due to the available fixtures within the test rig and in order to bound the response of the loaded plates.

5.2.1 Clamped with assumed in-plane restraint (restrained)

In this configuration the plates were restrained by virtue of 36 equi-spaced studs through the plate specimen/frame and each torqued to the same value of 100 Nm to

the support frame. The geometry of the clamping arrangement is shown in Figure 5.1 with the shaded area indicating the clamped region.

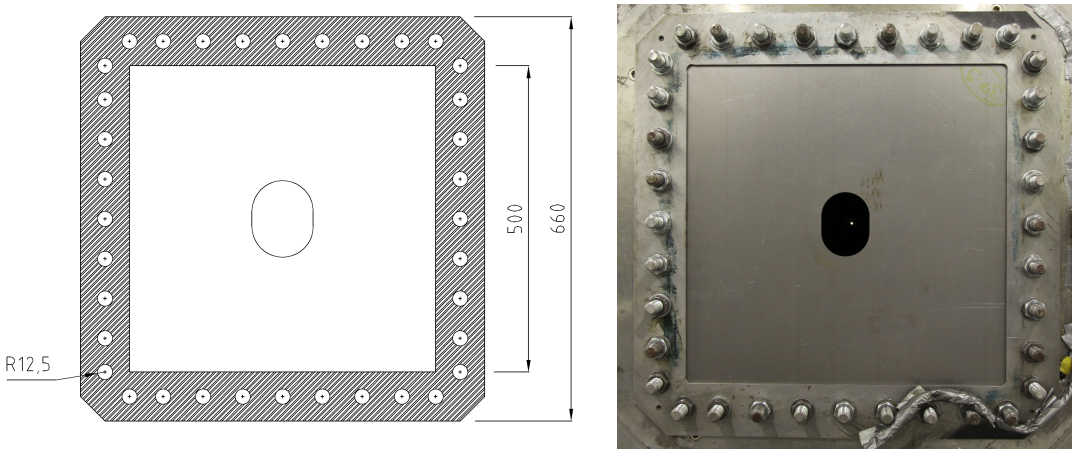

(a) (b)

Figure 5.1: (a) Schematic of the restrained plate specimen with the clamped region shaded and (b) the test rigs support plate and the test specimen which is mounted with 36 bolts - units in mm.

5.2.2 Clamped without in-plane restraint (non-restrained)

In this second arrangement, the clamping frame was mounted 2 mm out from the plate specimen using spacers and all studs were removed except in the corners. This meant that the plates, as shown in Figure 5.2, were reasonably free to move in the plane of the plate. However some frictional resistance was still present in this arrangement due to contact with the support frame. The method is shown in Figure 5.2 and was validated by Hsu[68].

5.3 Test plates

All test plates were mild steel, Docol 01, cut to 660 mm by 660 mm with the direction of roll etched onto each plate ensuring all plates were placed into the test rig in a consistent manner. The clamping frame for both edge conditions was 80 mm wide meaning the applied transient pressure loading was over an area of 500 mm by 500 mm minus the area of the hole when applicable. This meant that the plates were approximately $\frac{1}{8}$th of full sized deck sections used on topside structures.

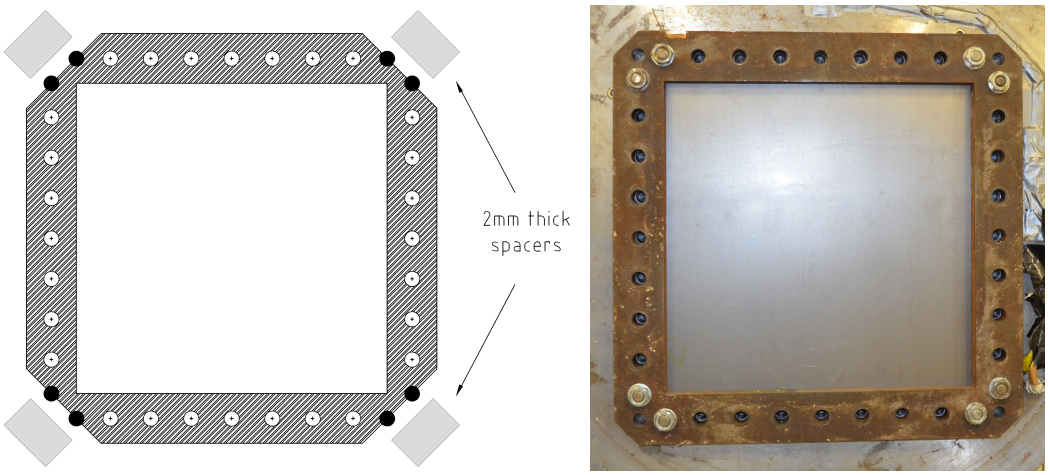

(a) (b)

Figure 5.2: (a) Schematic of the non-restrained plate specimen with the region of the clamping frame shaded and (b) the test rigs support plate and the test specimen which is mounted and restrained with the clamping frame fixed against 2 mm thick spacers via 8 bolts.

5.3.1 Openings

As discussed in Chapter 2 the inclusion of an aperture in a deck section of a topside structure or in bulkheads on ships is common practice for reducing weight, access for piping or for general inspection, with typical scenarios highlighted in Figure 5.3.

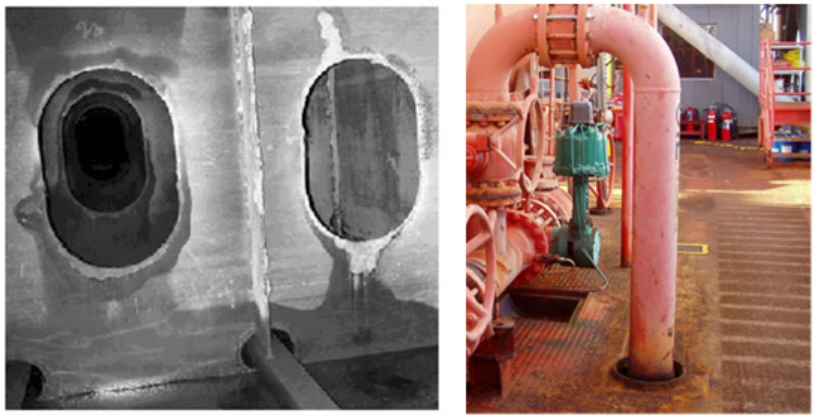

(a) Ship bulkhead. (b) Offshore application.

Figure 5.3: (a) Typical application where plates with openings are used in bulkheads[1] and (b) offshore structures.

In keeping with geometries selected by researchers Wang *et al.* [1] and Kim *et al.* [117] six (scaled) openings were selected as depicted in Figure 5.4.

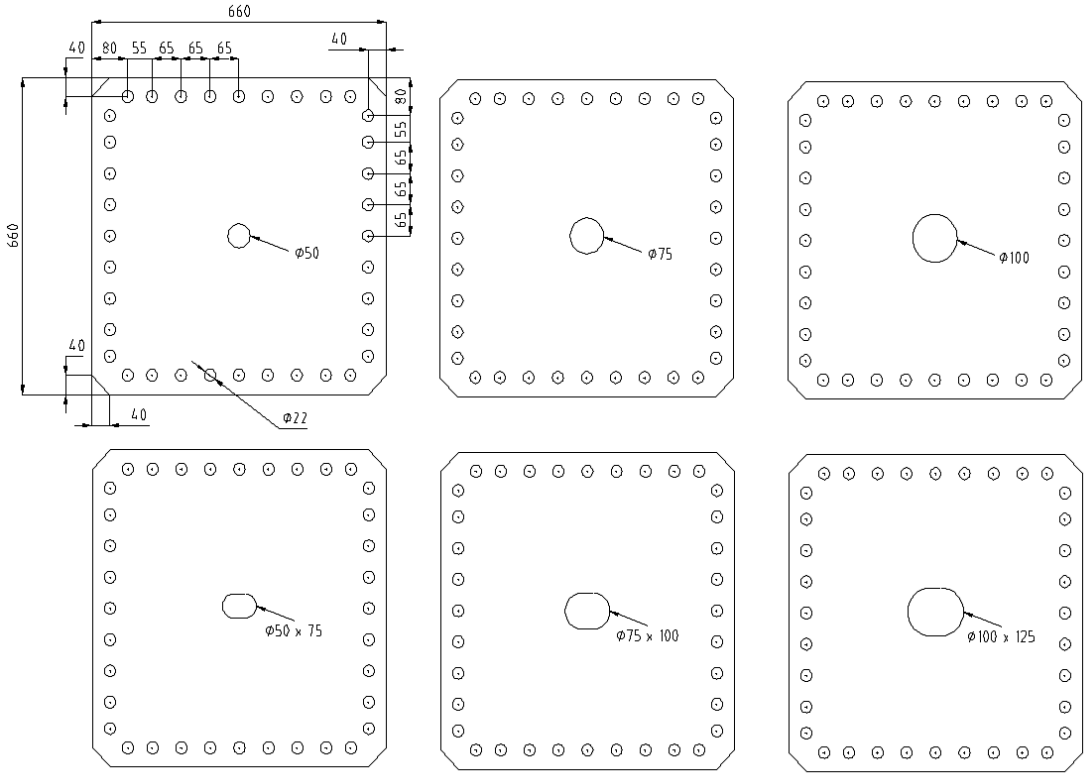

Figure 5.4: Square component test specimens with circular and extended circular holes - units in mm.

5.4 Pressure loading

Two nominal peak pressure loads 1.72 bar (25 psi) and 3.45 bar (50 psi) were selected. The pressure loading was applied over a time duration representative of hydrocarbon explosions on topside structures. Full details can be found in Chapter 4.

5.5 Scaling effects

Dynamic tests are usually conducted on small-scale models in order to obtain the response characteristics of a geometrically similar full-scale prototype [47] which may be too complex or expense to realistically conduct. The 500 mm by 500 mm plate is geometrically $\frac{1}{8}$th of typical full-size panels.

5.5.1 Geometrically similar scaling

Jones[47] has comprehensively studied the effects of scaling laws in impact engineering and hence the theory of scaling will not be discussed in great detail here. The variables required for such studies of the scaling effects are listed in Table 5.1. For simplicity in this presentation, it is assumed that the small-scale model and the large-scale model are made of an elastic material with the same Young's modulus of elasticity (E), mass density (ρ) and Poisson's ratio (υ). The geometric scale factor for a model is:

$$\beta = \frac{l}{L} \tag{5.1}$$

where $\beta \leq 1$

Table 5.1: Scaling relationships.

Quantity	Small-scale	Full Scale	Relationship
Length	l	L	$l = \beta$L
Mass	m	M	$m = \beta^3$
Pressure	p	P	$p = P$
Time	t	T	$t = \beta$T
Displacement	δ	Δ	$\delta = \beta\Delta$
Strain	ε	E	$\varepsilon = E$
Stress	σ	Σ	$\sigma = \Sigma$

5.5.2 Size effect

It is well understood that the phenomenon of material strain rate sensitivity introduces a known size effect shown in §11.3.2 of reference 47, or

$$\frac{\sigma'_o}{\Sigma'_o} = \frac{1 + (\dot{\varepsilon}/\beta D)^{1/q}}{1 + (\dot{\varepsilon}/D)^{1/q}} \tag{5.2}$$

where σ'_o and $\sum'_o$ are the dynamic flow stresses for a model having a geometric scale factor β, and a full-scale prototype, respectively. $\dot{\varepsilon}$ is an average strain rate and D and q are the Cowper-Symonds coefficients based on uniaxial tension tests. This reveals that the dynamic flow stress in a small-scale model (σ'_o) is larger than that in a large-scale prototype (Σ'_o), violating the requirements for geometrically similar scaling. This effect is not insignificant and becomes more of a factor at higher strain rates.

5.6 Measurements

5.6.1 Pressure

The internal pressure of the PPLR was recorded by four pressure gauges, two on each side of the support frame, as was shown in Figure 4.7, which proved to be a good indication of the average pressure loading on the test specimen. The pressure transducers were linked to high frequency response Flyde amplifiers and power supplies with the signal being captured by a TRA800 transient recorder in 12-bit format at a sampling rate of 25 MHz.

5.6.2 Maximum and final displacements

In previous studies on the larger scale PPLR by Langdon[118] and Hsu[68], long-stroke Linear Voltage Displacement Transducers (LVDT) were used to capture in-time deflections to establish the maximum and final displacements. These were for lower pressure tests and for full specimens (without openings). To identify if the same method was applicable for this research, a preliminary study was conducted on two identical plate geometries with openings. One test was conducted with a LVDT attached (Figure 5.5) and one without the LVDT. The LVDT had a rotating coupling that ensured resistance free motion of the rod inside the cylinder.

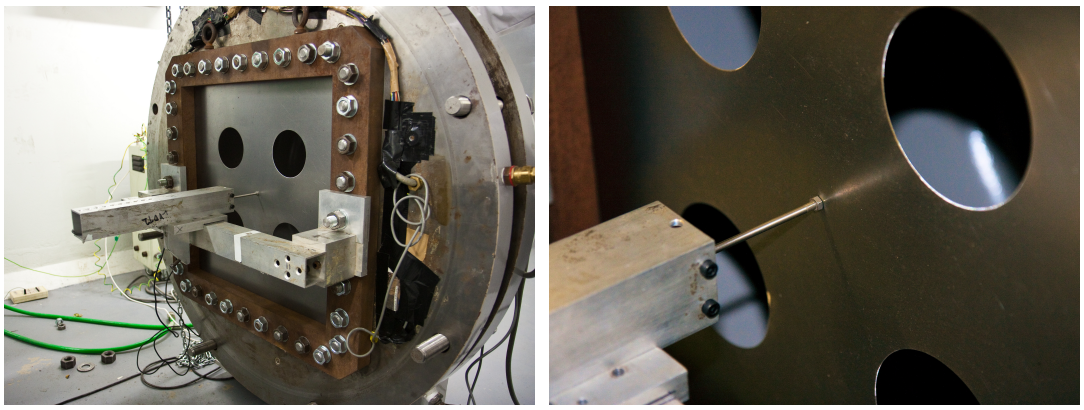

(a) LVDT and mounting structure. (b) Attachment method.

Figure 5.5: (a) General arrangement of LVDT and (b) fixture between plate and LVDT.

A nominal peak pressure load of 25 psi was used for both tests with the known variation in repeat tests of ∼0.5% as discussed in the previous chapter, Section 4.3.5.

Figure 5.6 shows the recorded pressure-time history curves for both tests. Even though the nominal pressure levels were set to 25 psi, the variation in the T_r, P_{max} and the T_d are shown in Table 5.2. These values were obtained using the same filtering technique as described in Section 4.3.6.

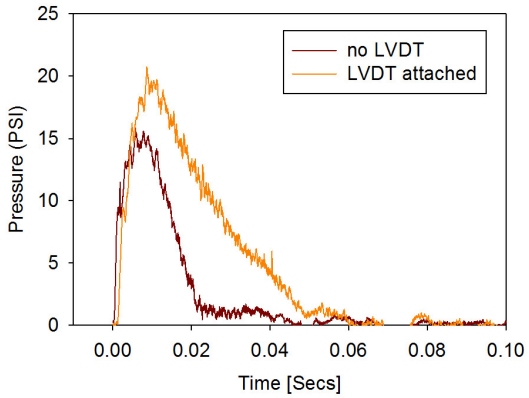

Figure 5.6: Effect of LVDT on pressure-time history curve.

Table 5.2: Key pressure-time history parameters.

General arrangement	T_r [msec]	P_{max} [PSI]	T_d [msec]
no LVDT	4.9	15.86	24.3
LVDT attached	7.1	20.71	46.7

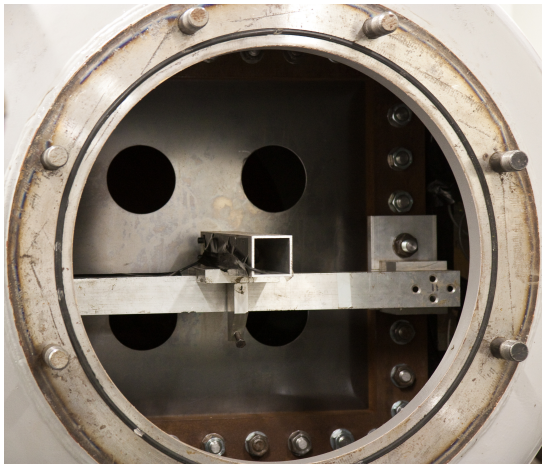

Figure 5.7: LVDT obstruction of burst diaphragm area.

Figure 5.7 clearly shows that the LVDT and mounting bar are obstructing both exit area of the pressure chamber and the two holes in the bottom section of the test plate. This increase in overpressure (Figure 5.6) explains why the final deformation was 9.35 mm without a LVDT and 11.99 mm with it. Due to the influence of the LVDT on the pressure-time loading conditions it was not used in subsequent tests.

3D Digital Image Correlation (DIC) could be utilised to provide a wealth of additional information including 3D surface coordinates, 3D displacements and velocities, surface strain values and strain rates throughout each test. This would also eliminate mechanical interaction between the test sample and the instrumentation, as in Figure 5.5(b) which may lead to further variations in results. The data obtained could be used to further validate numerical modelling. This method requires detailed investigation due to the confined and dynamic nature of the test rig to ensure feasibility. This was beyond the scope of this project, however Tiwari *et al.* [119] developed such a system for full-field plate deformation measurements during blast loading.

The permanent maximum deflection of each tested plate was measured while plates were in post-test situ using a sliding calliper. To have a better basis of comparison, the test plates were also profiled in greater detail and the data points taken for each test specimen are shown in Figure 5.8. Using this method ensured that the overall deformation pattern was correctly predicted by the numerical and analytical methods, not only the midpoint deflection.

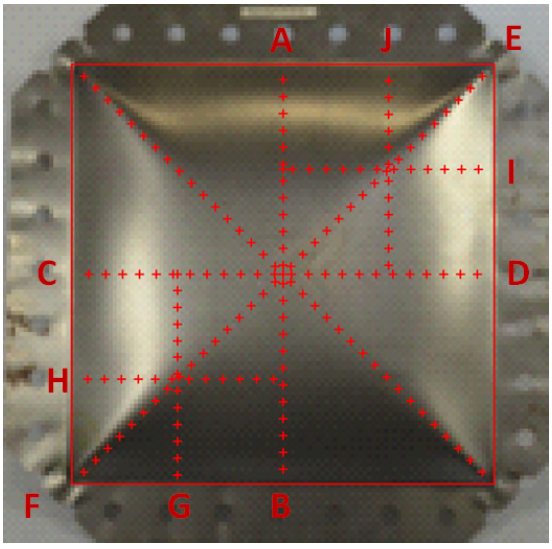

Figure 5.8: Points taken to map displacement fields for comparison with numerical and analytical studies.

Since the plates were assumed to be quarter-symmetric and this symmetry was used in the finite element model and the simplified analytical approach, the average values from the experimental profiles were plotted, as shown in Figure 5.9. In addition, the minimum and maximum measurements for each quarter-symmetric point were plotted as error bars. Referring to the x-axis in the plots shown in Figure 5.9 (Distance from support), a value of zero represents a data point taken at the boundary region, displayed as the red square in Figure 5.8. Figures 5.9(a) and 5.9(b) refer to the global response of each plate. In these plots the value at the maximum distance from the support represents the maximum global response. Figure 5.9(c) was also measured to assess other regions of the permanent deflection. These measured displacement fields were used to compare results obtained from the numerical and analytical models in later chapters for validation purposes.

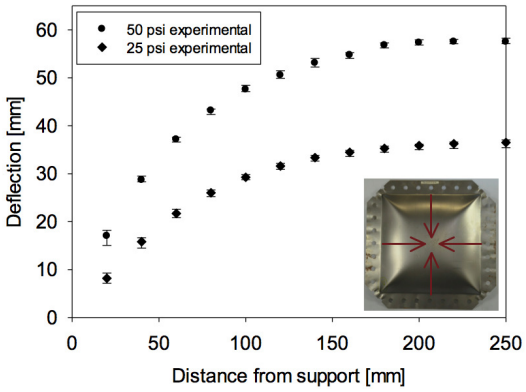

(a) Mid-point section

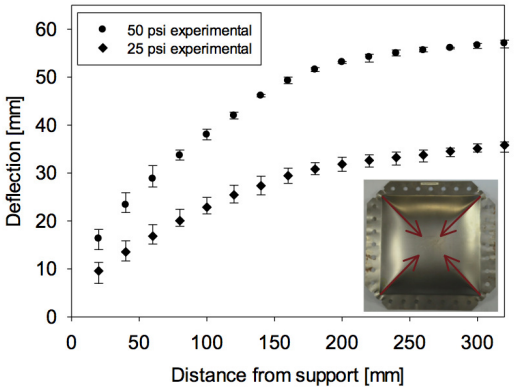

(b) Diagonal section

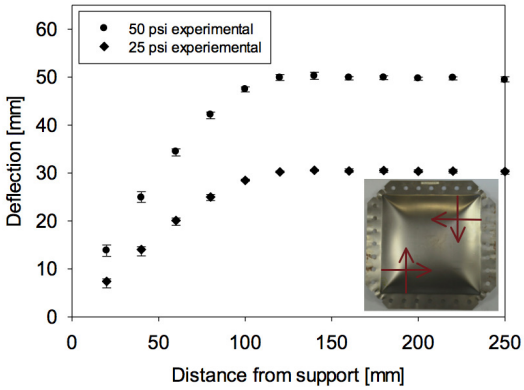

(c) Quarter section

Figure 5.9: Example plot of results taken by mapping the displacement field of each test (a) mid-point, (b) diagonal from corners and (c) quarter sections.

5.7 Experimental programme

Transient pressure pulse tests representative of accidental hydrocarbon explosions on topside structures have been performed on small-scale 1.1 mm thick mild steel plates. The experimental programme consisted of two tests series, one conducted for each of the boundary conditions; fully clamped boundary conditions with in-plane restraint and clamped boundary conditions without in-plane restraint.

In test series 1, a total of 14 tests were conducted on fully clamped boundary conditions with in-plane restraint (restrained). This consisted of applying the two nominal pressure levels (172.4 kPa (25 psi) and 344.8 kPa (50 psi)) to each plate with a hole and also to plates without openings. Selected results from this series of tests were presented in a research article in the Central European Journal of Engineering[120].

In test series 2, a total of 11 tests were conducted for clamped boundary conditions without in-plane restraint (non-restrained). Again this consisted of applying the two nominal pressures levels (25 psi and 50 psi) to all opening geometries plus to plates without openings. Tests at 25 psi on plates with extended hole geometry were not conducted.

5.8 Experimental results and observations

5.8.1 Test results

The pressure-time curves for the 25 dynamic tests (14 plates restrained and 11 non-restrained) are given in Figures 5.10-5.13. Idealised pressure-time histories were produced for each following the method detailed in Figure 4.17. Both the maximum pressure and the duration (and consequently also the impulse defined as the integral of the load with respect to time) increase with decreasing hole area, as expected due to the confinement of the test. The centre permanent displacement for the plate tests and the principal results are given in Tables 5.3-5.6. The general trend is that the final deflection marginally increases as the area of the hole decreases, with the exception of the restrained plates at 25 psi. This general trend can be attributed to the increase in pressure and impulse with decreasing hole area. The increased pressure also acts on a larger surface as the area of the hole decreases, which further amplifies the load transmitted to the plate. All plates failed by large inelastic deformation known as mode I type failure[6]. No material tearing or rupture was observed.

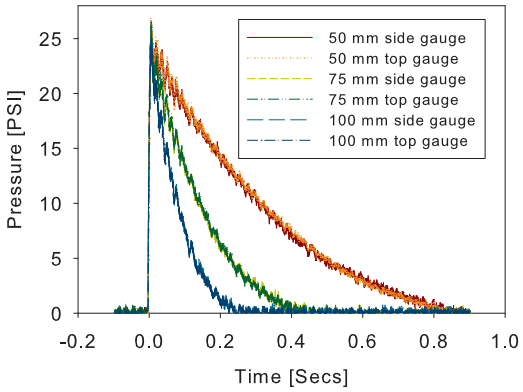

(a)

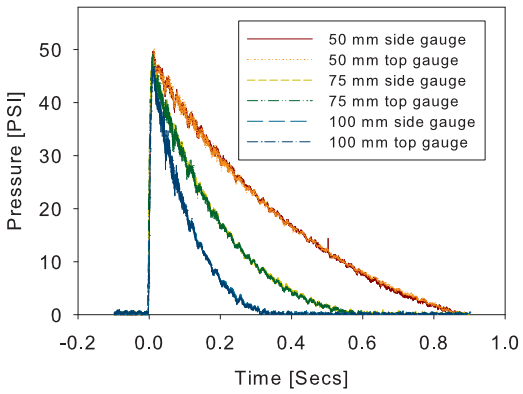

(b)

Figure 5.10: Pressure-time curves for restrained plates with circular holes loaded to (a) nominally 25 psi and (b) nominally 50 psi.

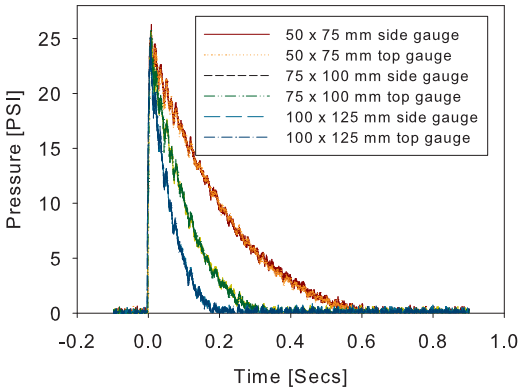

(a)

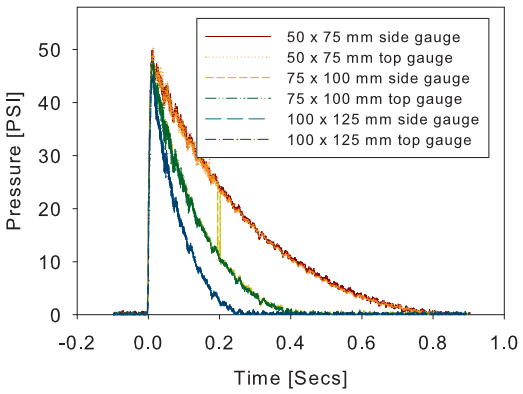

(b)

Figure 5.11: Pressure-time curves for restrained plates with extended circular holes loaded to (a) nominally 25 psi and (b) nominally 50 psi.

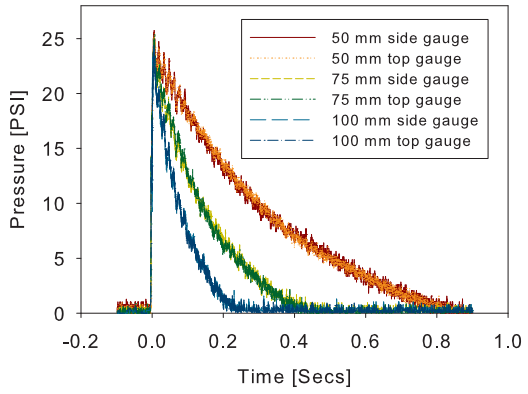

(a)

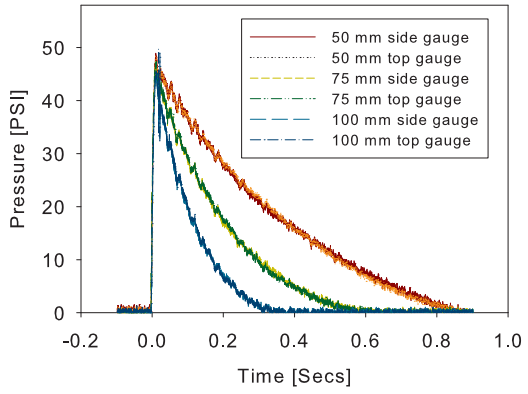

(b)

Figure 5.12: Pressure-time curves for non-restrained plates with circular holes loaded to (a) nominally 25 psi and (b) nominally 50 psi.

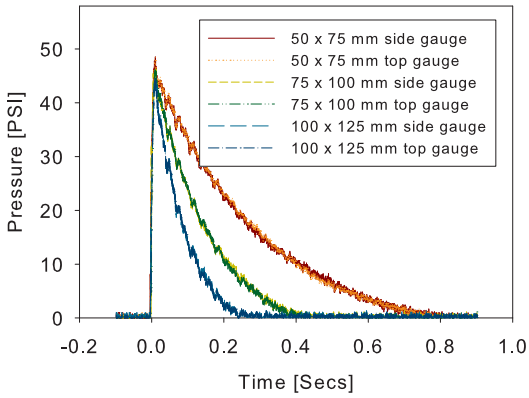

Figure 5.13: Pressure-time curves for non-restrained plates with extended circular holes loaded nominally to 50 psi, 25 psi unavailable.

Table 5.3: Results for the 0.5 m x 0.5 m restrained plates loaded nominally to 25 psi.

Experiment	Hole geometry [mm]	Hole area as ratio wrt ø50 mm hole	Hole area as % of plate area	Rise time tr [msec]	Peak pressure [psi]	Impulse [psi-msec]	Final centre disp. [mm]	Load duration td [msec]
1	Full plate	–	–	6.6	27.59	–	11.5	–
2	50	1.00	0.78	5.3	26.8	9071.8	15.0	677
3	50x75	1.64	1.29	7.4	26.0	6019	12.4	463
4	75	2.25	1.75	5.5	26.3	4181.7	13.7	318
5	75x100	3.20	2.51	7.0	25.7	2942.7	12.4	229
6	100	4.00	3.14	6.0	25.6	2419.2	13.7	189
7	100x125	5.27	4.14	5.7	24.8	1736	14.6	140

Table 5.4: Results for the 0.5 m x 0.5 m restrained plates loaded nominally to 50 psi.

Experiment	Hole geometry [mm]	Hole area as ratio wrt ø50 mm hole	Hole area % as of plate area	Rise time tr [msec]	Peak pressure [psi]	Impulse [psi-msec]	Final centre disp. [mm]	Load duration td [msec]
8	Full plate	–	–	11.2	52.62	–	23.9	–
9	50	1.00	0.78	13.2	49.9	18388.2	23.3	737
10	50x75	1.64	1.29	12.6	50.2	15009.8	22.4	598
11	75	2.25	1.75	9.6	48.9	10684.7	22.8	437
12	75x100	3.20	2.51	10.2	48.0	7464	23.0	311
13	100	4.00	3.14	13.1	46.7	5674.1	21.3	243
14	100x125	5.27	4.14	13.0	45.3	3420.15	22.1	151

Table 5.5: Results for the 0.5 m x 0.5 m non-restrained plates loaded nominally to 25 psi.

Experiment	Hole geometry [mm]	Hole area as ratio wrt ø50 mm hole	Hole area as % of plate area	Rise time tr [msec]	Peak pressure [psi]	Impulse [psi-msec]	Final centre disp. [mm]	Load duration td [msec]
15	Full plate	–	–	4.8	27.74	–	36.52	–
16	50	1.00	0.78	5.4	25.64	9127.8	32.71	712
17	75	2.25	1.75	12.6	25.28	4525.12	31.48	358
18	100	4.00	3.14	9.6	24.19	2322.2	29.74	192

Table 5.6: Results for the 0.5 m x 0.5 m non-restrained plates loaded nominally to 50 psi.

Experiment	Hole geometry [mm]	Hole area as ratio wrt ø50 mm hole	Hole area as % of plate area	Rise time tr [msec]	Peak pressure [psi]	Impulse [psi-msec]	Final centre disp. [mm]	Load duration td [msec]
19	Full plate	–	–	10.3	52.63	–	57.55	–
20	50	1.00	0.78	10.3	48.81	18035.3	56.66	739
21	50x75	1.64	1.29	10.3	48.53	14777.4	53.23	609
22	75	2.25	1.75	9.7	47.40	10641.3	53.55	449
23	75x100	3.20	2.51	10.8	46.61	7504.2	51.06	322
24	100	4.00	3.14	18.0	44.64	5870.2	50.06	263
25	100x125	5.27	4.14	10.0	44.45	4311.7	47.92	194

5.8.2 Restrained plates

The following discussion applies to plate tests 1-14 that were restrained by virtue of the clamping force and the plate location on the studs. As discussed in Section 2.7.1, studies[74] on beams and plates have shown that remarkably small in-plane displacements at the supports (boundaries) can significantly change the response of a structure, from that of an axially restrained beam to one with no appreciable axial resistance. Figure 5.14 shows an example restrained plate with assumed in-plane restraint provided by the studs after the dynamic loading has been applied. It can be seen that the combination of the clamping force and studs have prevented in-plane displacements greater than the order of 1 mm at the edge although this is difficult to quantify. Another confirmation of this was that the plates came easily off the studs after testing.

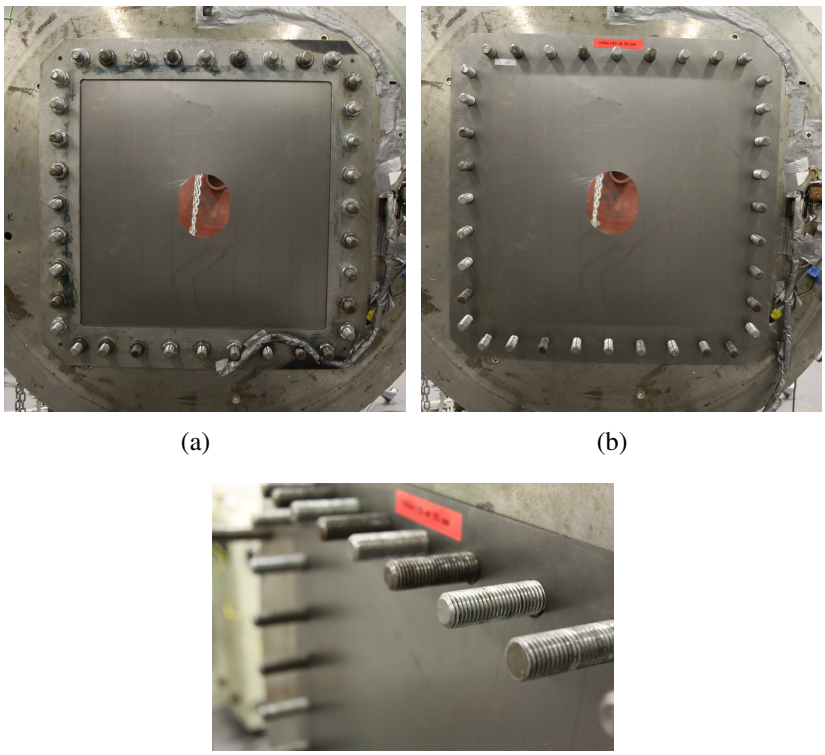

(a) (b)

(c)

Figure 5.14: Restrained plate (a) with clamping frame, (b) clamping frame removed and (c) close up inspection around bolts.

It is well known that large lateral displacements of thin plates (w/h $\gg$ 1) plus axial resistance cause high levels of direct membrane behaviour. The mode of failure for these plates was large permanent ductile deformation, the final centre displacements

ranging from approximately 11 times the thickness at 25 psi to approximately 20 times the plate thickness at 50 psi. The final deformed shape of the restrained plates exhibited a curvature like that of a shallow shell as shown in Figure 5.15, characteristic of direct membrane behaviour with no noticeable diagonal yield line formation. Yield lines formed along the clamping boundary due to the low plastic bending capacity of the plates.

An important feature of this group of results is the effect of the openings. Figure 5.8 shows the series of data points that were measured on all tested specimens to provide a detailed account of the final permanent deflection. These allowed for direct comparisons to be made between all plates to investigate how the opening influenced the response of the plates, i.e. if there were any localised effects. These were critical for successfully validating numerical and analytical models. Example cases for the restrained plates are shown in Figures 5.16 and 5.17 with the remaining results provided in Appendix A.

Sample restrained plates were also measured using a Zeiss Contura G2 co-ordinate measuring machine (CMM), as shown in Figure 5.18, achieving a length measuring error threshold of MPEE = 1.5 + L/333[121]. This is approximately 3 μm error for the measured plates. An example plotted displacement file using the CMM is shown in Figure 5.19. Figure 5.20 shows a section comparing a manually captured plate profile against that measured using the coordinate measuring machine. A maximum variation of ± 1 mm proved that the manual approach was better than acceptable.

The average permanent deflection for all restrained plates at the mid-span were compared, shown in Figures 5.21 and 5.22. Comparing measurements 200 mm away from the support for all plate configurations found a minor variation of ± 4 mm for the 25 psi plates and ± 2 mm for the 50 psi plates. Due to the variation in load parameters for each test it is difficult to make strict conclusions from these tests alone, however this will be investigated in greater detail in Chapter 6.

5.8.3 Unrestrained plates

The following discussion applies to plate tests 15-25 that were rotationally fixed but not restrained axially. The membrane action in these plates was clearly less effective without direct in-plane restraint which resulted in larger transverse displacement than the restrained plates as indicated when comparing Tables 5.3 and 5.4 with Tables 5.5 and 5.6. Figure 5.23 shows an example non-restrained plate without in-plane restraint provided by virtue of spacers and by only using studs in the corners, after the dynamic loading had been applied. It is clear to see that the plates were able to slide (up to a point) at the corners. As the plate deforms it develops complementary compression and tension zones around the plate, changing from compression at the perimeter of the plate to tension towards the centre of the plate. This behaviour is thought to cause indirect membrane action, plus friction effects.

The deformed shape of these unrestrained plates exhibited distinctive diagonal yield line formation and an abrupt change in curvature across the plate with the formation of new yield lines, clearly seen in Figure 5.24. The central area of the deformed plate has a relatively shallow curvature. The mechanism to cause this characteristic profile was considered to be the indirect membrane compression zone that promotes diagonal yield line behaviour.

The final centre displacements ranged from approximately 30 times the thickness at 25 psi and 48 times the plate thickness at 50 psi. The final permanent deflection of the plates were mapped manually using the same data points, shown in Figure 5.8 and examples are shown in Figures 5.25 and 5.26. The remaining results can be found in Appendix A. The coordinate measuring machine was employed again for mapping the final displacement of a non-restrained plate plotted in Figure 5.27.

The full plate in Figure 5.24 shows that the in-plane displacement decreases towards the corners of the plate. It was concluded that this induced the lateral buckling that was observed around the plates. Since the edge of the plate was restrained laterally, the plate could only buckle as far as the gap between the clamping frame and the plate would allow. This behaviour produced a series of wave like buckles (Figure 5.28) which were not associated with the clamping holes in the plate as previous work, directly related to this study (in terms of plate geometry) by Hsu[68] showed that the same phenomenon occurred for plates without holes around this region.

The average permanent deflection for all non-restrained plates at the mid-span were compared, shown in Figures 5.29 and 5.30. Comparing measurements 200 mm away from the support for all plate configurations found a variation of ± 6 mm for the 25 psi plates and ± 10 mm for the 50 psi plates. Variations in the load parameters make it difficult to fully quantify these results, however they will be used for validation of numerical and analytical models. Once validated these can then be used in parametric studies to assess the influence of loading and openings.

5.9 Summary

The experimental investigation of the deformation of pressure loaded restrained and non-restrained plates with and without openings has produced an extensive set of well-defined data. In the experiments, all plates exhibited a mode I type failure (large inelastic deformation). A number of important observations can be drawn from this test series:

- For non-restrained plates, distinct diagonal yield lines were observed. Restrained plates in contrast, deformed with a shallow curvature. Yield lines along the clamping boundary were visible on all specimens.
- All non-restrained plates exhibited lateral buckling along the boundary area. This lateral buckling was not associated with the clamping holes in the plates as work by Hsu[68] showed that the same phenomenon occurred for plates without holes around this region.
- The general trend is that the final deflection marginally increases as the area of the holes decreases, with the exception of the restrained plates at 25 psi. This general trend can be attributed to the increase in pressure and impulse with decreasing hole area, due to the configuration of the test rig.
- Since both the plate stiffness and load parameters vary, it is difficult to make strict conclusions from the experiments alone, but they can be used to validate numerical and analytical methods which in turn can be used for further studies.

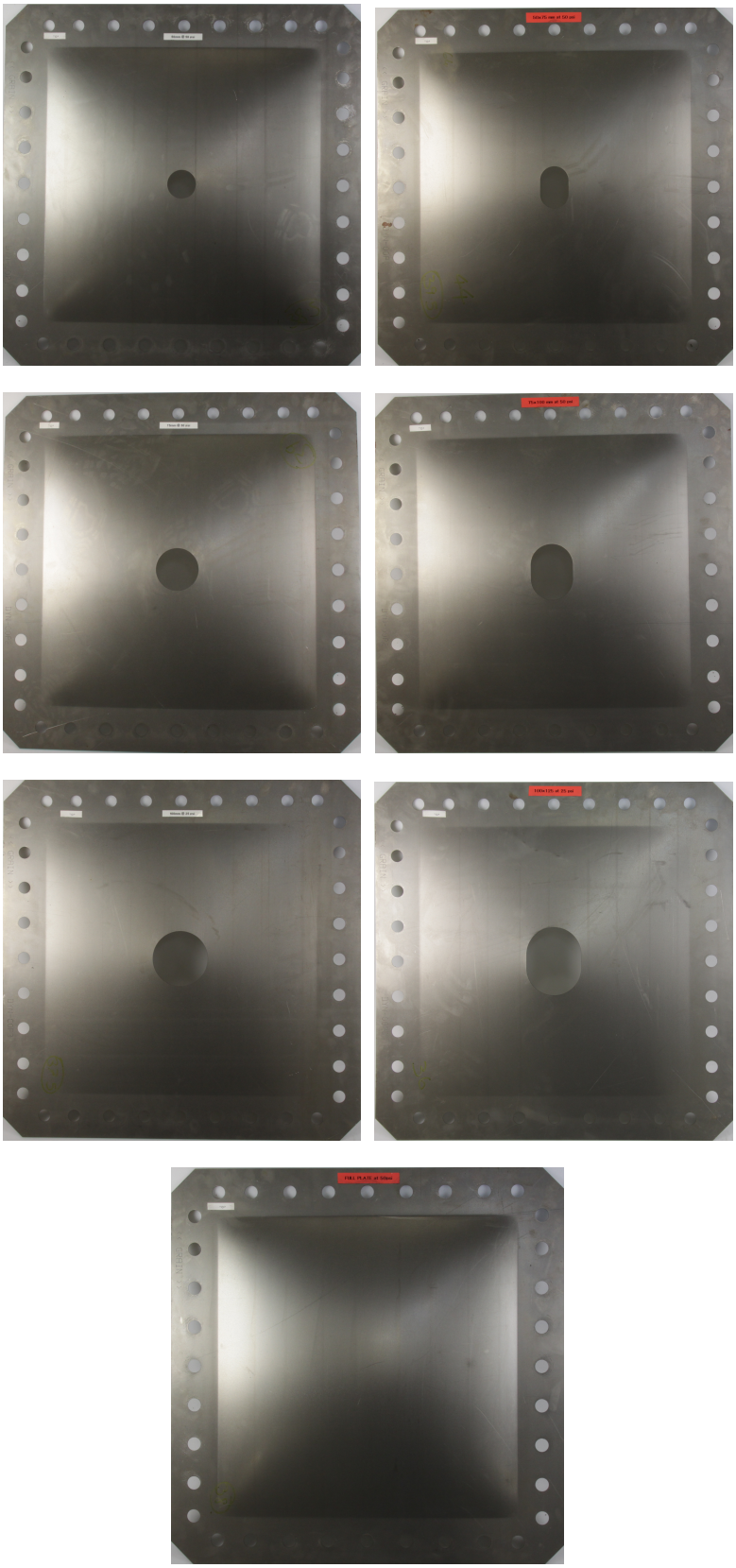

Figure 5.15: Deformed shapes of the restrained plates exposed to 50 psi nominal pressure.

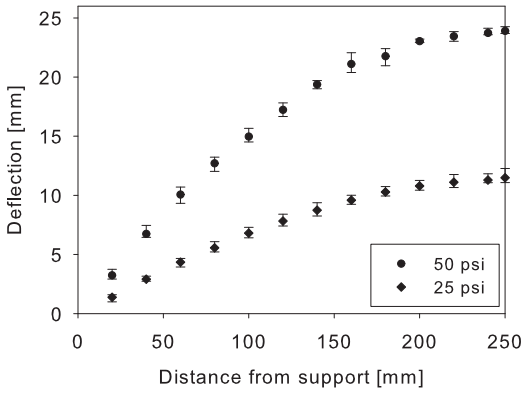

(a)

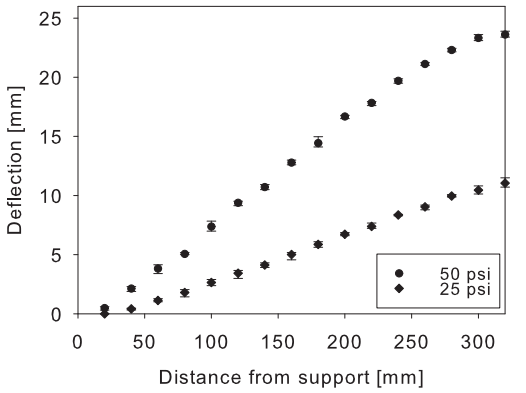

(b)

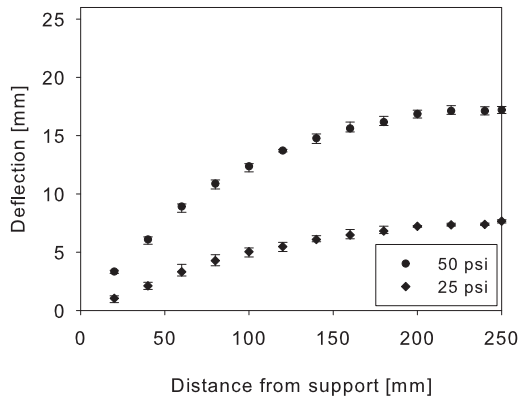

(c)

Figure 5.16: Final permanent deflection of restrained plate without opening taking measurement at (a) mid-point, (b) diagonal from corners and (c) quarter sections.

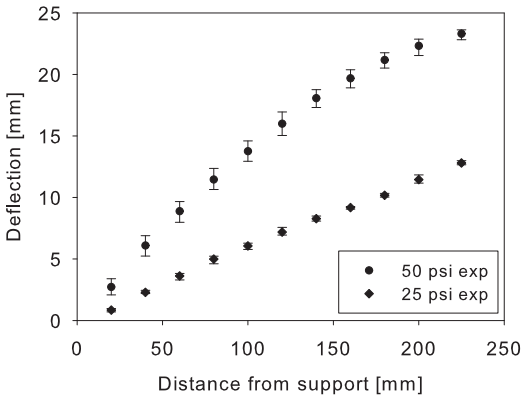

(a)

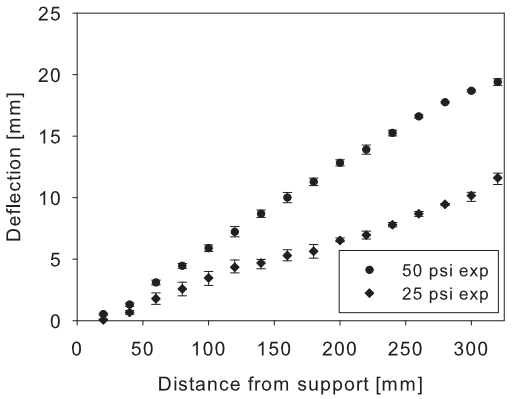

(b)

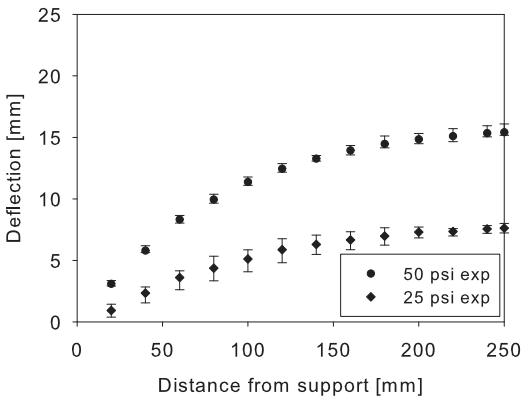

(c)

Figure 5.17: Final permanent deflection of restrained plate with 50 mm opening taking measurement at (a) mid-point, (b) diagonal from corners and (c) quarter sections.

Figure 5.18: Zeiss Contura G2 coordinate measuring machine.

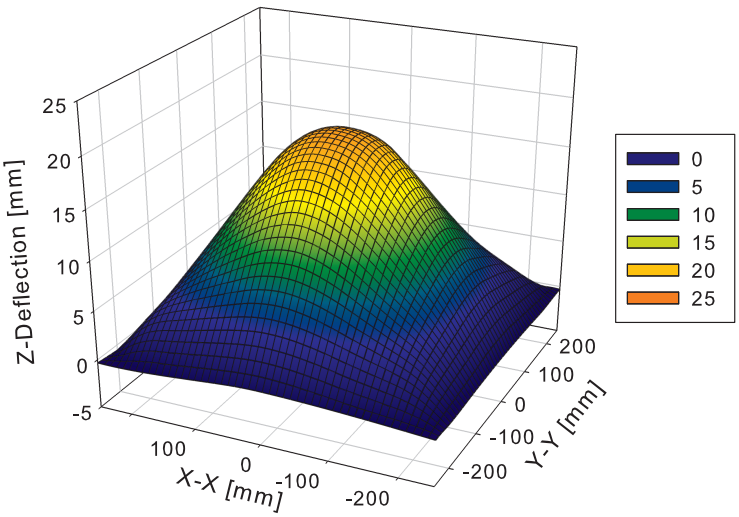

Figure 5.19: Measured displacement field for a restrained plate using Zeiss Contura G2 coordinate measuring machine.

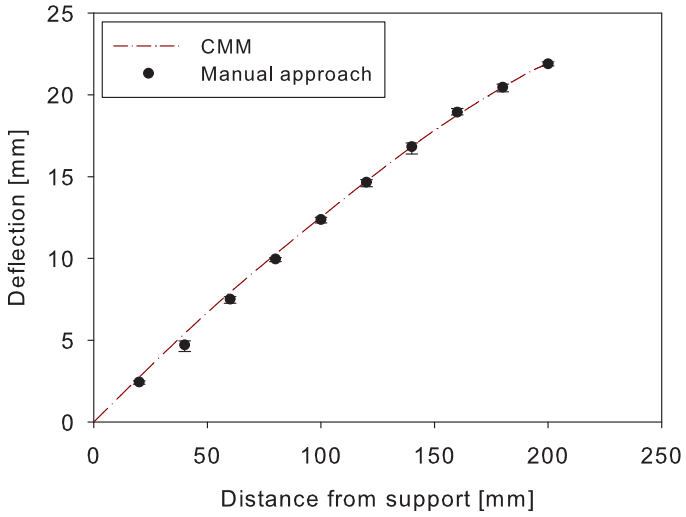

Figure 5.20: Comparison between manual profiling and coordinate measuring machine measurements to obtain the average permanent deflection profile of an experimentally tested restrained plate.

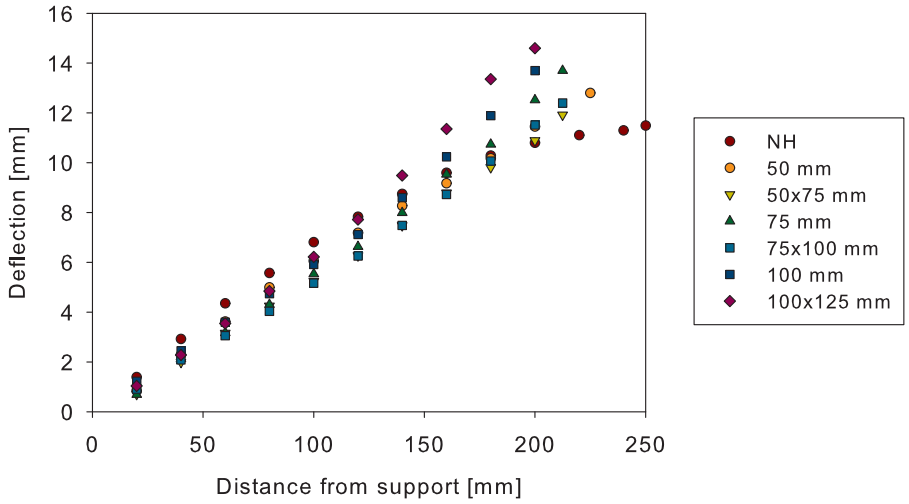

Figure 5.21: Average permanent deflection for all of the restrained plates at the mid-span loaded nominally to 25 psi (NH - No Hole).

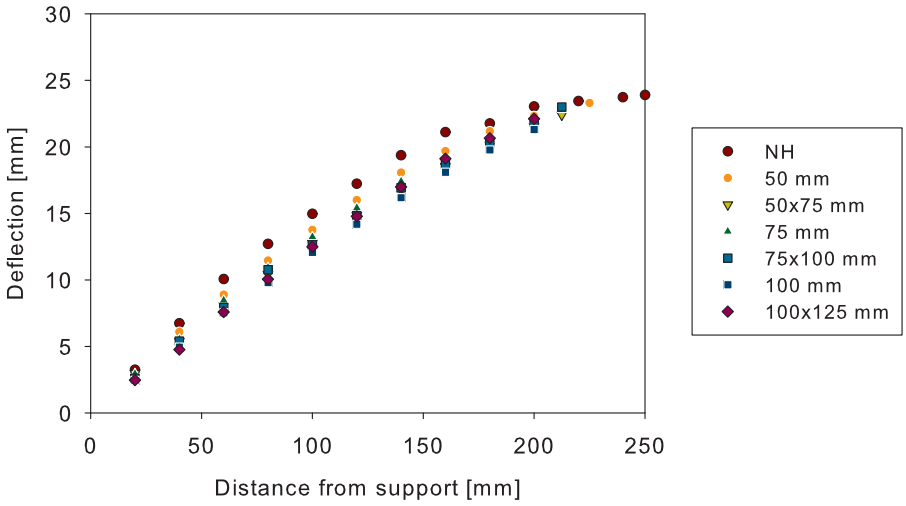

Figure 5.22: Average permanent deflection for all of the restrained plates at the mid-span loaded nominally to 50 psi (NH - No Hole).

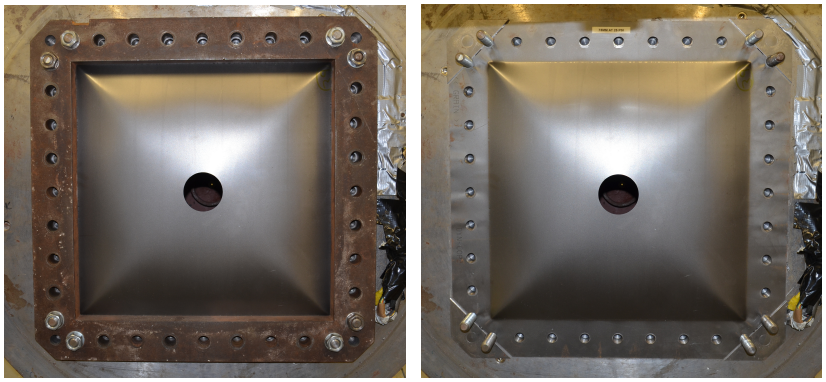

(a) (b)

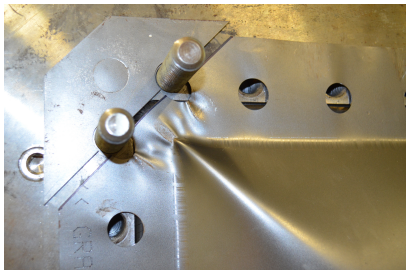

(c)

Figure 5.23: Non-restrained plate (a) with clamping frame, (b) clamping frame removed and (c) close up.

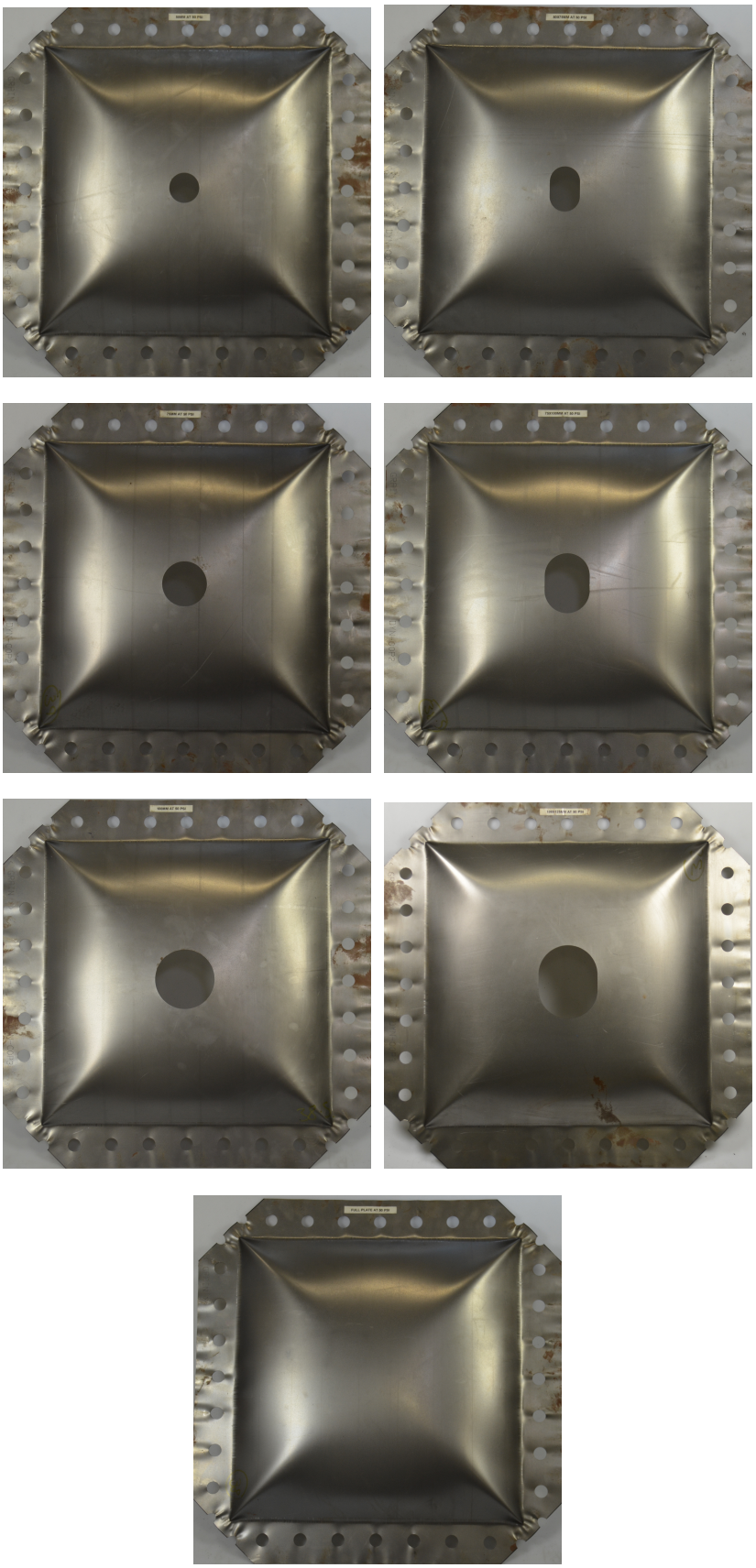

Figure 5.24: Deformed shapes of the non-restrained plates exposed to 50 psi nominal pressure.

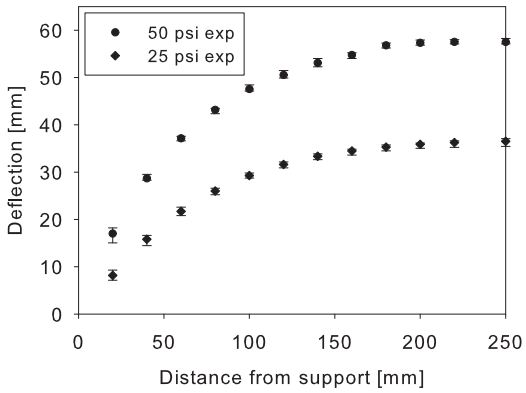

(a)

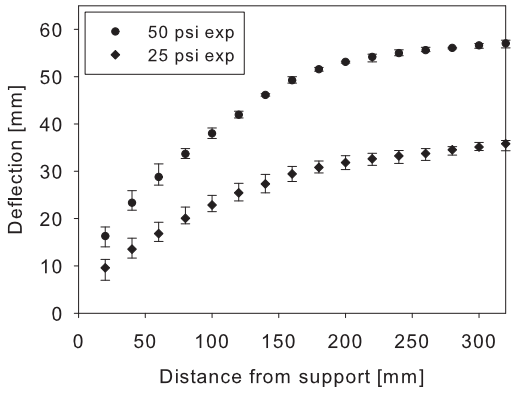

(b)

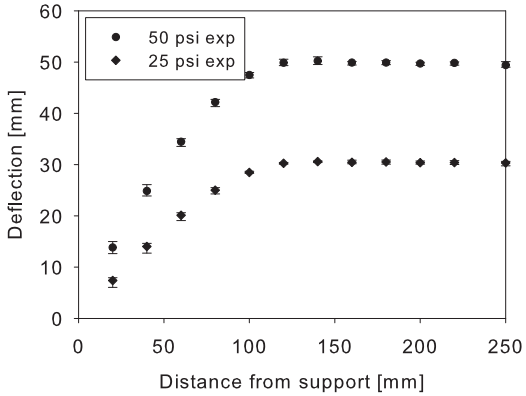

(c)

Figure 5.25: Final permanent deflection of non-restrained plate without opening taking measurement at (a) mid-point, (b) diagonal from corners and (c) quarter sections.

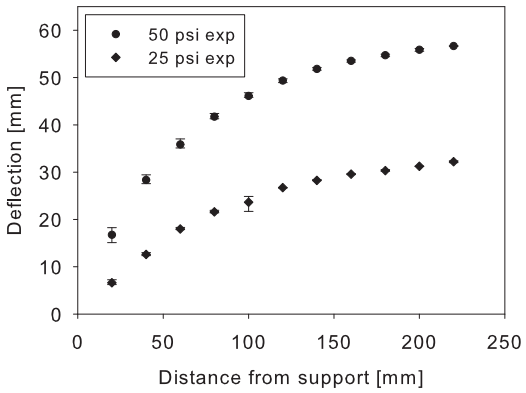

(a)

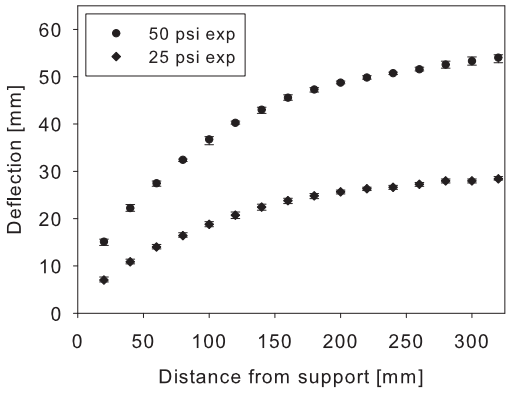

(b)

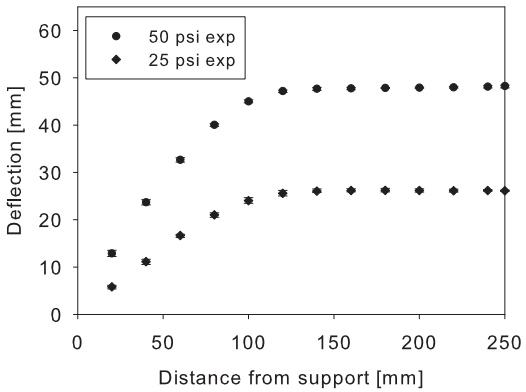

(c)

Figure 5.26: Final permanent deflection of non-restrained plate with 50 mm opening taking measurement at (a) mid-point, (b) diagonal from corners and (c) quarter sections.

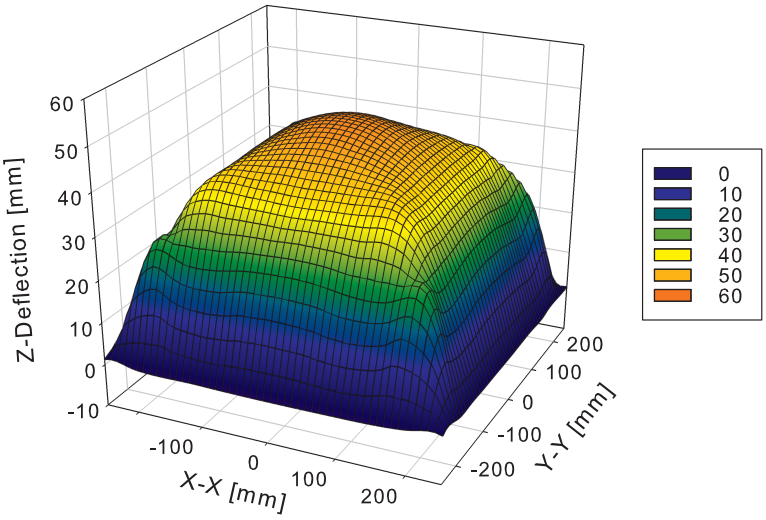

Figure 5.27: Measured displacement field for a non-restrained plate using Zeiss Contura G2 coordinate measuring machine.

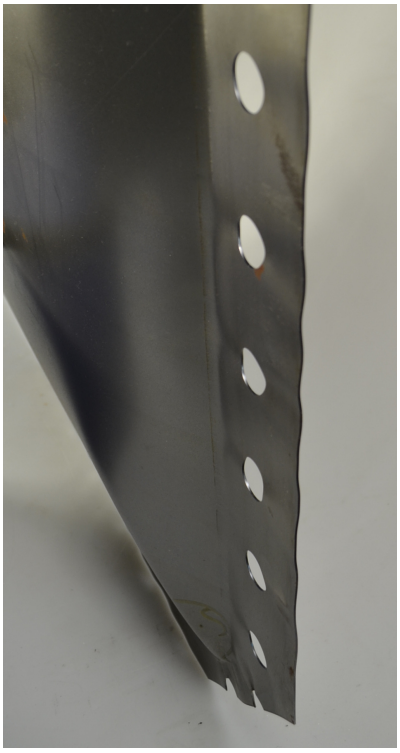

Figure 5.28: Lateral buckling of a non-restrained plate around the clamping frame.

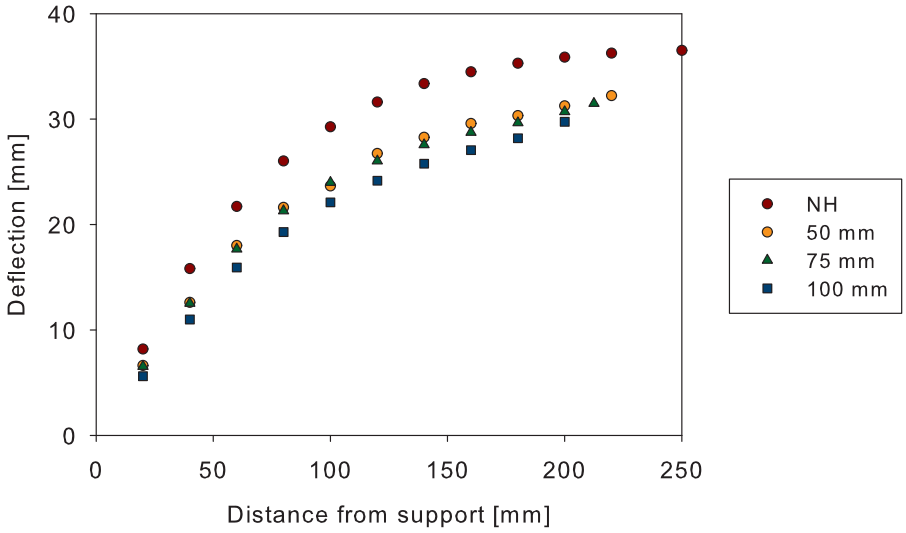

Figure 5.29: Average permanent deflection for all of the non-restrained plates at the mid-span loaded nominally to 25 psi (NH - No Hole).

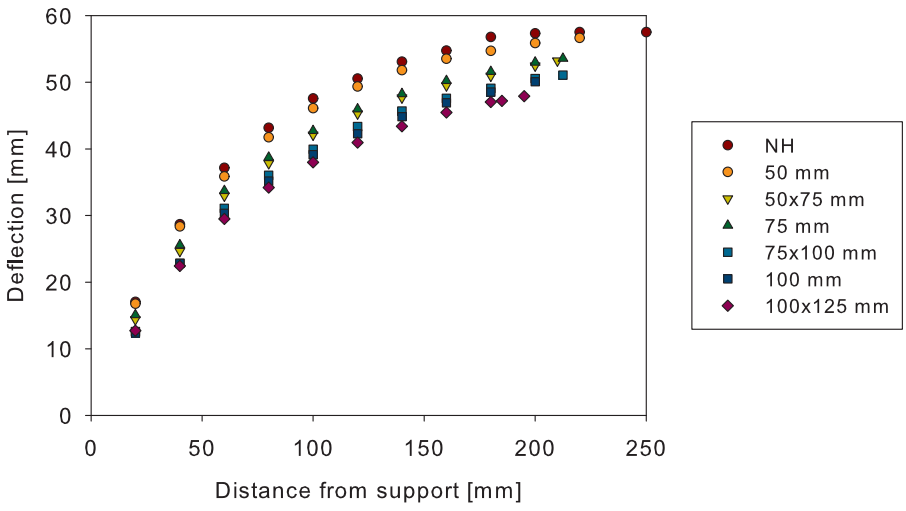

Figure 5.30: Average permanent deflection for all of the non-restrained plates at the mid-span loaded nominally to 50 psi (NH - No Hole).

Chapter 6

Full 3D Modelling of Component Tests

6.1 Introduction

In this chapter several sets of numerical simulations of the pressure-loaded plates are presented. Firstly, numerical simulations of the experimental tests using a Lagrangian solver were conducted to validate the numerical models. Using this validated model a parametric study was carried out to investigate how the openings altered the response of the plate, using idealised pressure-time curves. Secondly the Eulerian solver was utilised to simulate the actual pressure-time histories recorded during experiments. Finally, a fully coupled Lagrangian-Eulerian simulation is presented to discuss the spatial variation of the pressure loading. Quarter symmetric boundary conditions were utilised in all simulations for efficiency.

The need for more sophisticated numerical models to accurately describe a structure's response to blast loading in the offshore industry is very prominent. As computational power increases it makes it possible to more accurately describe the complex response of a structure to blast loading. This has always been a balance between acceptable accuracy and computational time. The computer used in this study was a HP XW8400 workstation with dual Intel Xeon X5355 Quad Core (2.66 Ghz) processors and 16 GB memory.

6.2 The Finite Element code

All numerical modelling contained within this present study has been carried out using LS-DYNA version 971 [122][123]. LS-DYNA is a general-purpose finite element program capable of simulating highly non-linear transient dynamic events using explicit time integration. In a transient dynamic event, such as an explosion it is vital to account for the non-linear material behaviour (plasticity and fracture), contact non-linearity (varying boundary conditions) and geometric non-linearity (large deformations).

6.2.1 Finite Element techniques

Several different finite element techniques can be used to describe the response of structures due to blast loads. Some of these are: (1) pure Lagrangian formulation, (2) an initial Eulerian simulation (to determine the load) followed by a Lagrangian simulation (for the structural response) and (3) a hybrid technique that combines the advantages of the Eulerian and Lagrangian methods [124], known as Arbitrary Lagrangian Eulerian (ALE). These are also known as uncoupled and coupled approaches as described in Chapter 2 Section 2.6.3. These solvers are briefly described in the sections below.

6.2.2 Lagrangian solver

In the Lagrangian code the computational grid is fixed in the material and as such it moves and deforms with the material, as shown in Figure 6.1. This means that the quadrature points will coincide with the material points, ensuring that the boundary nodes remain on the boundary throughout the evolution of the problem (Belytschko *et al.* [125]). This helps to simplify imposition of the boundary conditions in the Lagrangian mesh.

However there are limitations associated with this method. Since Lagrangian meshes deform with the material, they become distorted in simulations with severe deformation. This distortion can lead to inaccuracies in the output and potential termination of the analysis when an element becomes so distorted it effectively folds in on itself, resulting in a negative element volume. This is normally overcome using adaptive meshing techniques.

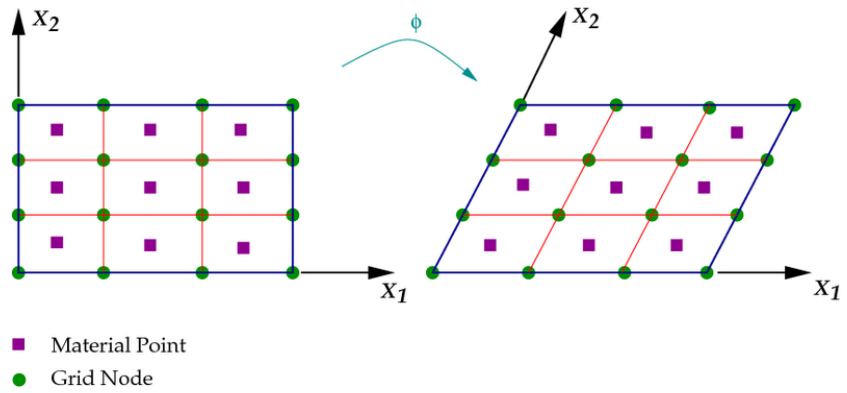

Figure 6.1: Illustration of a two-dimensional shearing of a block showing Lagrangian mesh[13].

6.2.3 Eulerian solver

In the Eulerian code the computational grid is fixed in space, whilst the material passes through it, as illustrated in Figure 6.2. This means that the nodal grid has to be large enough so that the body does not leave the domain whilst deforming, resulting in larger run times.

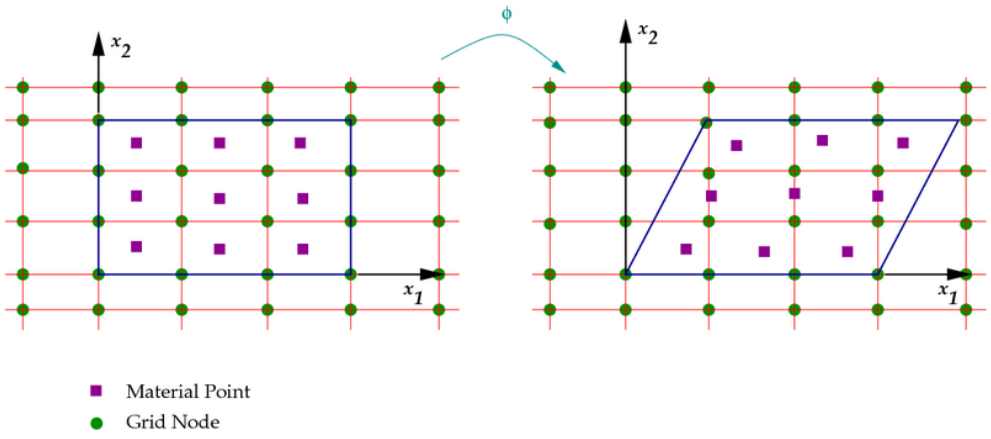

Figure 6.2: Illustration of a two-dimensional shearing of a block showing Eulerian mesh[13].

On the plus side, large deformations in the material do not cause distortion in the meshing, allowing for unlimited material deformation without causing degradation of the elements. Eulerian formulations are best suited for fluid mechanics problems.

6.2.4 Arbitrary Lagrangian Eulerian (ALE)

The Arbitrary Lagrangian Eulerian method has been developed to combine the advantages of both Eulerian and Lagrangian finite elements, whilst minimising the disadvantages. The ALE technique allows the mesh to deform, somewhat independently of the material, allowing the mesh to adapt to the deformation of the material, whilst avoiding overly-distorted elements, depicted in Figure 6.3.

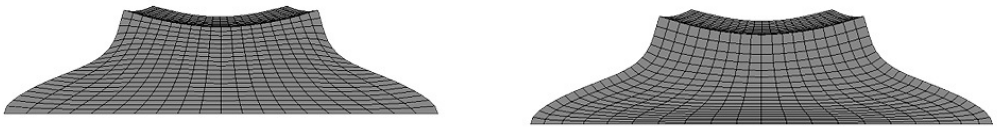

(a) ALE (b) Lagrangian

Figure 6.3: ALE vs Lagrangian mesh[14].

By allowing the mesh to adhere to the deformation of the material, boundaries are more easily treated with ALE than with Eulerian meshing. However because the mesh and material are not bound together, the evaluation of the constitutive equations in the material points are not as convenient as when using a Lagrangian mesh. This problem can be addressed by using an operator split method and further details can be found in various references by Belytscho *et al.* [125] and by Olovosson [126][127].

In ALE formulations the nodes do not follow the material flow, as shown in Figure 6.2. There is a flux of material between the elements and this complicates the governing equations. Using an operator split technique, LS-DYNA first computes the Lagrangian time derivative and updates the history variables. Subsequently the relative motion between mesh and material is computed and the history variables are updated once more[126].

The numerical modelling in the present study was carried out primarily within the Lagrangian domain. The Eulerian and ALE methods are also briefly discussed. Ideally all blast simulations should be carried out using a fully coupled Eulerian-Lagrangian approach, however this is often not practicable as the computational time increases considerably when going from a pure Lagrangian simulation to a fully coupled Eulerian-Lagrangian simulation.

6.2.5 Explicit time integration

Implicit and *explicit* are two types of time integration methods used to perform dynamic simulations. For practical purposes the differences between the two methods are related to stability and cost. The explicit solution is the most common for blast and short impact events. The implicit solution is used for static and long duration events.

In the *explicit* approach, internal and external forces are summed at each node point, and a nodal acceleration is computed by dividing by the nodal mass. Integrating this acceleration in time advances the solution. The maximum time step size is limited by the Courant condition, producing an algorithm which typically requires many relatively inexpensive time steps [123]. Therefore explicit methods are conditionally stable. This method is well suited for dynamic simulations, however it can become prohibitively expensive to conduct long durations, such as static events.

In the *implicit* method, a global stiffness matrix is computed, inverted, and applied to the nodal out-of-balance force to obtain a displacement increment[123]. The advantage to this is that the user can select the time step size, making this method unconditionally stable. The disadvantage with this method is it requires a large numerical effort to form, store, and factorize the stiffness matrix. In general implicit simulations involve a relatively small number of expensive time steps.

All the numerical modelling described in this study was carried out within the explicit time integration domain, unless otherwise stated.

Explicit time integration procedure

An overview of the procedure of explicit time integration is available from LS-DYNA[122]. Dynamic equilibrium is solved from the following equation:

$$Ma + Cv + Kx - F_E = 0 \tag{6.1}$$

where M is the mass matrix, C is the damping matrix, K is the stiffness matrix and F_E represents the applied or external forces acting on the system. The nodal displacements are represented by x while v and a represent the nodal velocities and accelerations, respectively. If damping is considered negligible this can be re-written as:

$$Ma + Kx - F_E = 0 \qquad or \qquad Ma = F_E - Kx \tag{6.2}$$

Internal forces are defined as $F_I = Kx$, thus:

$$Ma = F_E - F_I \tag{6.3}$$

This set of equations are solved at the beginning of each time step. When building a model the mass matrix is known, as it is formulated from the geometry and the material properties. The applied forces are also known, as the user applies these. The unknown parameter is the internal forces, which must be calculated in order to solve the nodal accelerations. These are derived from the displacement at the beginning of each time step and the accelerations are solved from:

$$a = M^{-1}(F_E - F_I) \tag{6.4}$$

Once the accelerations are calculated, the central difference method is used to determine the velocities and nodal displacements at the end of each time step. The stresses and strains are calculated from the nodal displacements. This process is demonstrated below for a single element:

$$F_E = kx_t = ma_t \tag{6.5}$$

$$F_E = kx_{t+dt} = ma_{t+dt} \tag{6.6}$$

$$x_{t+dt} = x_t v_{t+dt/2} dt \tag{6.7}$$

$$v_{t+dt/2} = v_{t-dt/2} dt + a_t dt \tag{6.8}$$

$$ma_{t+dt} = F_E - k(x_t = v_{t-\frac{dt}{2}} dt + a_t dt^2 \tag{6.9}$$

The central difference method does not have any iteration and thus no convergence checks are required. This advantage comes at a price, and this price is that this method is conditionally stable. This means that in order to maintain stability, the time step must be kept within a certain limit (critical time step) to capture meaningful results.

Critical time step

The critical time step Δt_{cr} must not be exceeded when performing explicit integration. For damped materials the size Δt_{cr} is determined by the largest natural frequency ω_{max} and the damping ratio ξ:

$$\Delta t_{cr} \leq \frac{2}{\omega_{max}}\left(\sqrt{1} = \xi^2 - \xi\right) \tag{6.10}$$

When considering an undamped material and applying lumped masses, this reduces to the *Courant-Friedrichs-Lewy-criterion*[128]:

$$\Delta t_{cr} \leq \frac{l}{c} \tag{6.11}$$

where l = the length of the smallest element and c is the speed of sound in the material. This condition effectively limits the time step to be less than the time taken for a sound wave to traverse the smallest element in the model. The speed of sound in a material is defined as:

$$c = \frac{\sqrt{E}}{\rho} \tag{6.12}$$

6.3 Material modelling

A comprehensive materials testing programme was performed to characterise the material properties of the Docol form 01 (DC01) mild steel test specimens at strain rates ranging from 3.3x10^{-4} s^{-1} (quasi static) to 534 s^{-1}. The tensile tests showed that DC01 mild steel was highly ductile, tending to yield gradually and exhibited moderate strain rate sensitivity. Further details are available in Chapter 3. To accurately portray this behaviour the Modified Johnson-Cook constitutive relation and the Cockcroft-Latham fracture criterion have been implemented in LS-DYNA as MAT _ 107:MODIFIED _ JOHNSON _ COOK[123] and are used in this study. The formulation and implementation into LS-DYNA are discussed in the following sections.

6.3.1 Constitutive relation

The material was described using the Modified Johnson-Cook constitutive relation [129]. The von Mises equivalent stress $\bar{\sigma}$ in the Modified Johnson-Cook constitutive relation, including the extended Voce hardening rule, is expressed as

$$\bar{\sigma} = \left[A + \sum_{i=1}^{2} Q_i(1 - exp(-C_i\bar{\varepsilon}))\right]\left[1 + \frac{\dot{\bar{\varepsilon}}}{\dot{\bar{\varepsilon}}_0}\right]^c \left[1 - \left(\frac{T - T_r}{T_m - T_r}\right)^m\right] \tag{6.13}$$

where, A determines the initial yield strength of the material at room temperature. Q_i and C_i, i = 1,2, define the strain hardening. $\bar{\varepsilon}$ is the equivalent plastic strain, $\dot{\bar{\varepsilon}}$ is the equivalent plastic strain rate and $\dot{\bar{\varepsilon}}_0$ is a user-defined reference strain rate. The strain-rate sensitivity is represented by the constant c, while m models the thermal softening effect. The temperature dependence is given by the homologous temperature T^*, defined as T^* = (T - T_r)/(T_m - T_r). T is the absolute temperature, T_r is the ambient temperature and T_m is the melting temperature. The temperature increment due to adiabatic heating may be calculated as

$$\Delta T = \int_0^{\bar{\varepsilon}} \chi \frac{\bar{\sigma} d\bar{\varepsilon}}{\rho C_p} \tag{6.14}$$

where ρ is the material density, C_p is the specific heat and χ is the Taylor-Quinney empirical coefficient that represents the proportion of plastic work converted to heat.

6.3.2 Identification of material parameters

The Modified Johnson-Cook (MJC) constitutive model, Equation 6.13 consists of three terms governing strain hardening, strain rate sensitivity and temperature softening. These parameters are usually calibrated separate to one another, and the processes are described below.

Strain hardening

The parameter A is the initial yield strength of the material at room temperature which is taken as the proof stress at 0.2% plastic strain, using corrected true-stress strain data at room temperature, following procedures outlined by LS-DYNA[122] . The strain hardening parameters Q_i and C_i, $i = 1,2$ are then fitted to the curve beyond the yield point using the method of least squares, as depicted in Figure 6.4.

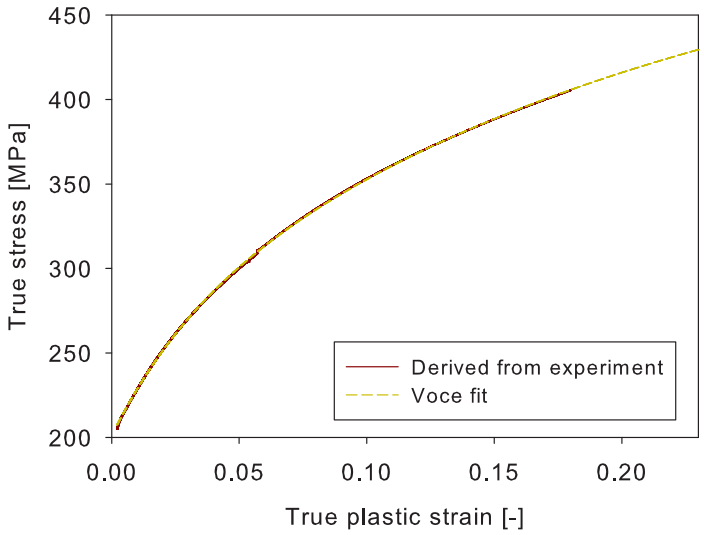

Figure 6.4: Stress-strain (σ-ε^p) curve of DC01 and fit to the extended Voce hardening rule.

Strain rate sensitivity

The strain-rate sensitivity, c is determined by using the dynamic tensile test data shown for reference in Figure 6.5 and described in Chapter 3, when $T^* = 0$. Figure 6.6 shows the flow stress as a function of the logarithmic strain rate at 5% plastic strain. The parameter c is then obtained by fitting a curve to the experimental data using least squares.

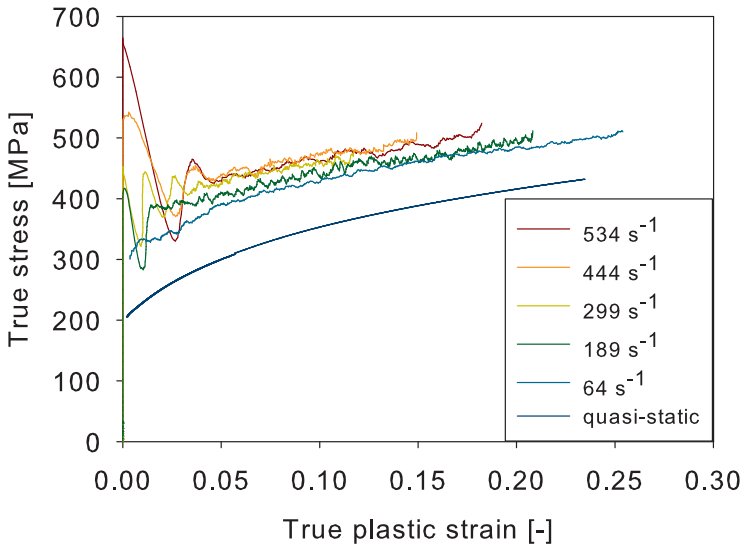

Figure 6.5: True stress versus true plastic strain curves.

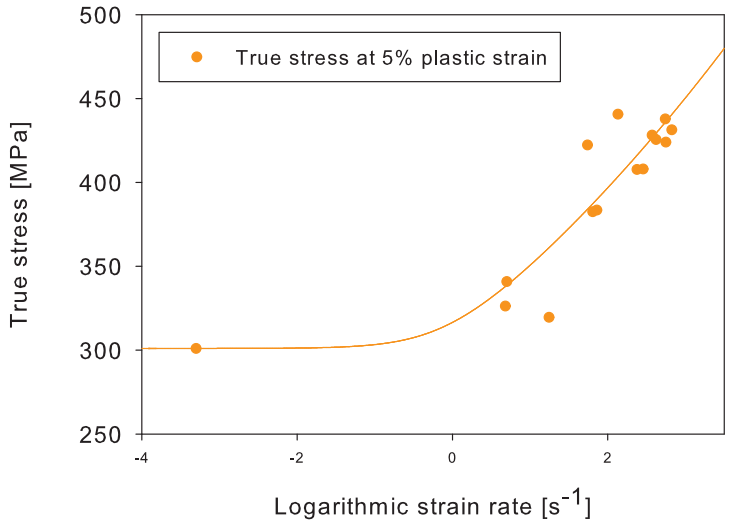

Figure 6.6: Flow stress as a function of strain rate. Experimental data points are shown as dots and the results obtained with the Modified Johnson-Cook model is shown as a line.

Temperature softening

To calibrate the thermal softening a series of quasi static tensile tests are conducted at elevated temperatures. Chung[130] and Langdon *et al.* [131] investigated the influence of incorporating temperature effects in numerical simulations for impulsively blast loaded steel plates. They concluded that it is beneficial to incorporate this parameter when predicting the onset of tearing, however incorporating temperature effects made very little difference when predicting Mode I response. Hsu[68] conducted a series of experimental tests on thin mild steel plates without holes at similar pressure levels and boundary configurations to the ones conducted in this study. She observed no thinning or tearing of the plates. With this taken into consideration it was expected that no thinning or tearing would occur in this present study either. Therefore no testing at elevated temperatures was deemed necessary. This assumption was confirmed when inspecting the plates within this experimental study (Chapter 5).

Borvik *et al.* [132] states that it would be reasonable to assume a linear reduction in equivalent stress with temperature (i.e. $m = 1$) for steel when elevated temperature tests are not available. Therefore a value of $m = 1$ was used in all future simulations.

Fracture criteria

A failure criteria is needed for a complete description of the material behaviour. Ductile failure is highly dependent on the stress triaxiality. One simple fracture criteria that includes stress triaxiality is the Cockcroft-Latham (CL) criteria.

Cockcroft-Latham model

The failure criteria proposed by Cockcroft and Latham[133] is based on the total plastic work per unit volume W, defined as

$$\int_0^{\varepsilon_f} \langle \sigma_1 \rangle d\bar{\varepsilon} = W \tag{6.15}$$

where $\bar{\varepsilon}$ is the major principal stress, $\langle \sigma_1 \rangle = \sigma_1$ when $\sigma_1 \geq 0$ and $\langle \sigma_1 \rangle = 0$ when $\sigma_1 < 0$. Damage accumulates during straining until it reaches a critical value $W = W_{cr}$ at $\bar{\varepsilon} = \bar{\varepsilon}_f$. The material constant W_{cr} is determined from a single uniaxial quasi-static tensile test by calculating the plastic work (area) of the true stress-strain curve[18].

Researchers Rakvag[3] and Judge[134] have demonstrated that this simplified failure criteria is capable of describing the behaviour of a material when subjected to impact loading. Dey *et al.* [135] demonstrated that the single parameter derived using the (W_{cr}) Cockcroft-Latham fracture theory gave similar results to the Johnson-Cook fracture criterion which has a more involved process (five parameters). Therefore the Modified Johnson-Cook constitutive relationship and the Cockcroft-Latham fracture criterion have been used in the present study and are presented in Table 6.1.

Table 6.1: Material parameters for MJC constitutive relation and CL fracture criteria.

Elastic constants and density	Yield stress and strain-hardening	Strain rate sensitivity	Cockcroft-Latham failure
E = 205 [GPa] υ = 0.33 [MPa] ρ = 7850 [kg/m^3]	A = 205 [GPa] Q_1 = 263 [MPa] C_1 = 4.5 Q_2 = 58.3 [MPa] C_2 = 31.72	$\dot{\bar{\varepsilon}}_0$ = 0.341 C = 0.055	W_{cr} = 120 [MPa]

6.4 Pure Lagrangian

6.4.1 Procedure to generate 3D FE model - restrained plate

As discussed in Chapter 5 experimental plates were restrained by virtue of the clamping force and the plate location on the studs. Visual inspection of the plates after the tests showed minimal straining around the bolt holes. Two finite element meshes were considered for simulating this test series shown in Figure 6.7.

Model geometry

A quarter symmetry model of the restrained plate was examined as shown in Figure 6.7. The plate was constructed using under-integrated Belytschko-Tsay (BT) shell elements approximately square to preserve a side-length aspect ratio of unity. In Figure 6.7(b) the bolts were modelled with analytical rigid walls in LS-DYNA. Initial stress that could arise in the vicinity of the holes from the cutting process are neglected in this study. Pulse pressure loads are often idealised as triangular in form, however as discussed in Chapter 4 and shown in Figure 4.11 the pulses are not usually perfectly triangular in shape. To provide the most accurate results the whole pressure-time history curve was implemented and applied to the Lagrangian simulations. This removes the pulse simplification employed during analytical modelling. This pressure-time history was applied uniformly to the shell elements and always normal to the shell face.

Visual inspection of the plates after the experimental tests showed minimal straining around the bolts, i.e. minimal in-plane movement. Because of this it was found unnecessary to include these bolts or the clamping region in the finite model. This was confirmed in preliminary simulations, with the two model configurations shown in Figure 6.7. As such all further models for the restrained plates considered the loaded area of 500 x 500 mm only. Geometric imperfections were not incorporated in the model, with the results comparing favourably with the experimental results without the need to build this into the model.

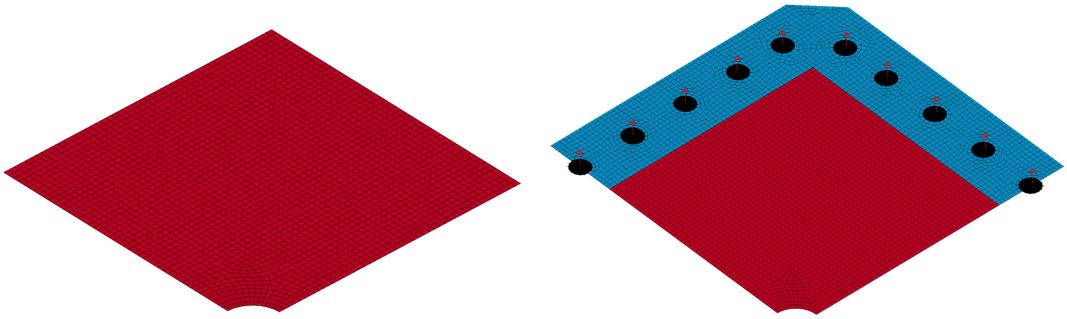

(a) (b)

Figure 6.7: Finite element mesh of a restrained plate with a 50 mm central opening and a characteristic element size of 5 x 5 mm. In (a) the boundary conditions are modelled to simulate the clamped with in-plane restraint boundary conditions. In (b) the boundary conditions are modelled to incorporate the clamped area and the bolts. The bolts are modelled as rigid walls and shown in black. Similar finite element models were generated for the other plate geometries in this investigation.

Mesh sensitivity study

A mesh sensitivity study was then conducted to investigate how the mesh size influences the solution, in relation to the final deformed shape at the maximum deflection point (i.e. around the opening). The plate with the 50 mm opening loaded nominally to 50 psi was chosen for this study. This plate underwent one of the largest deformations and thus would be more likely to be mesh sensitive. It is well understood that under-integrated elements (1-integration point in the centroid) suffer from hourglassing effects. Therefore an analysis was also conducted using Selective Reduced Integration (SRI) with 5 integration points through the thickness.

Results of this can be found in Table 6.2, considering meshes from 10 x 10 mm to 2.5 x 2.5 mm. The results showed that the mesh-size sensitivity for the restrained plates was very minor and a mesh size of 5 x 5 mm was sufficient to accurately describe the problem here in. The results obtained using both element types is very similar and the hourglass effect using the under-integrated BT shells was very minor. Thus the BT shell type was used for all further simulations of the restrained plates due to significant savings in computational run times.

Table 6.2: Details of mesh convergence study on restrained plate with 50 mm hole and 50 psi nominal test pressure.

Characteristic element size [mm]	10x10	5x5	5x5 [SRI]	2.5x2.5
Maximum deflection at perimeter of hole [mm]	24.80	24.85	24.65	24.87
Hour glass as % of internal energy [%]	0.6	0.55	0	0.4
Run time [h:min:s]	0:46:4	1:13:33	87:18:10	52:8:8

6.4.2 Procedure to generate 3D FE model - non-restrained plate

As discussed in Chapter 5 the plates were rotationally fixed but not restrained axially. Visual inspection of the plates after this test series showed that the plates were able to slide freely at the corners and lateral buckling occurred between the support frame and clamping frame. Due to this complex failure mechanism it was found important to model the boundary conditions with a sufficient degree of accuracy.

Model geometry

The finite element model used for this plate series is shown in Figure 6.8. As with the restrained boundary conditions the plates were modelled with under-integrated Belytschko-Tsay shell elements. The boundary conditions are modelled to incorporate the bolts, clamping frame and the support frame which are all modelled as rigid walls in LS-DYNA. Figure 6.9 shows that the clamping frame in the numerical model has been positioned 2 mm away from the plate specimen, consistent with the experimental approach.

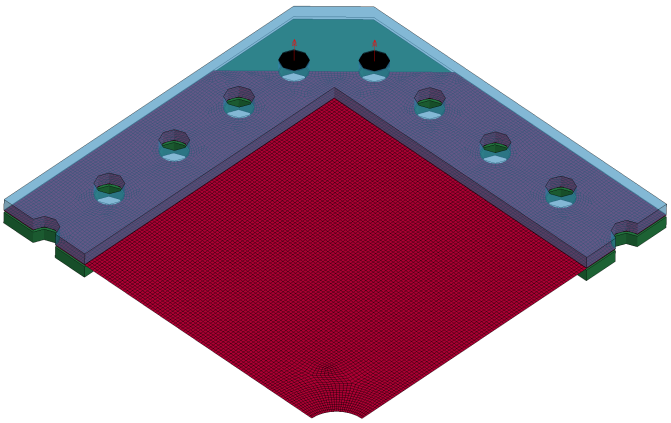

Figure 6.8: Finite element mesh of a non-restrained plate with a 50 mm central opening with a characteristic element size of 2.5 x 2.5 mm. Similar finite element models were generated for the other plates in this investigation.

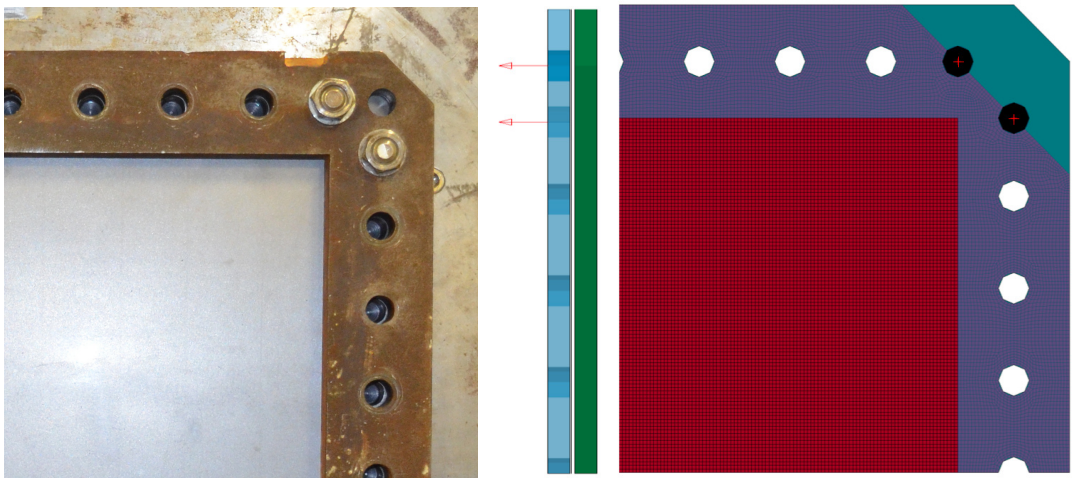

(a) (b)

Figure 6.9: Pre-test configuration of (a) experimental arrangement and (b) numerical simulation.

Mesh sensitivity study

A mesh sensitivity study was then conducted to investigate how the mesh size influences the solution, in relation to the final deformed shape at the maximum deflection point. The plate with the 100 by 125 mm opening loaded nominally to 50 psi was chosen for this study. This caused the plate to undergo one of the largest deformations and thus would be more likely to be mesh sensitive. Results of this can be found in Table 6.3, considering meshes from 10 x 10 mm to 2.5 x 2.5 mm.

The results showed that the mesh-size sensitivity for the non-restrained plates was greater than for the restrained plates. This is to be expected as the deformed profile of these plates were much more complex exhibiting distinctive diagonal yield lines and lateral buckling around the clamping frame. In order to accurately capture this behaviour a finer mesh size of 2.5 x 2.5 mm was used to describe the problem here in. It would be unrealistic to have smaller elements with the current computer capacity available.

Table 6.3: Details of mesh convergence study on non-restrained plate with 100 by 125 mm hole and 50 psi nominal test pressure, without friction coefficient.

Characteristic element size [mm]	10x10	5x5	5x5 [SRI]	2.5x2.5
Maximum deflection at perimeter of hole [mm]	44.40	52.47	53.13	55.54
Run time [h:min:s]	2:27:2	14:3:17	61:48:26	113:11:1

When comparing the maximum final displacement from the simulations to the experimental results it was found the numerical result over predicted the value by 16% with a mesh size of 2.5 x 2.5 mm. As mentioned in Section 5.2.2, some frictional resistance will still be present in the experimental arrangement as the plate is free to slide at the corners of the bolts and presses against the clamping frame. A sensitivity study was conducted to investigate the influence that friction plays in the response of a non-restrained plate. Figure 6.10 displays the results for the non-restrained plate with a 75 mm opening tested nominally to 50 psi with a mesh size of 2.5 x 2.5 mm. It clearly demonstrates the influence that friction has on the response of a non-restrained plate. Based on this investigation a friction coefficient of 0.1 was used in all further simulations for the non-restrained plates to account for steel on steel friction during loading. Jiang *et al.* [136][137] proposed a similar friction value of 0.115 which Judge[134] used on the steel cables subjected to dynamic impact loading.

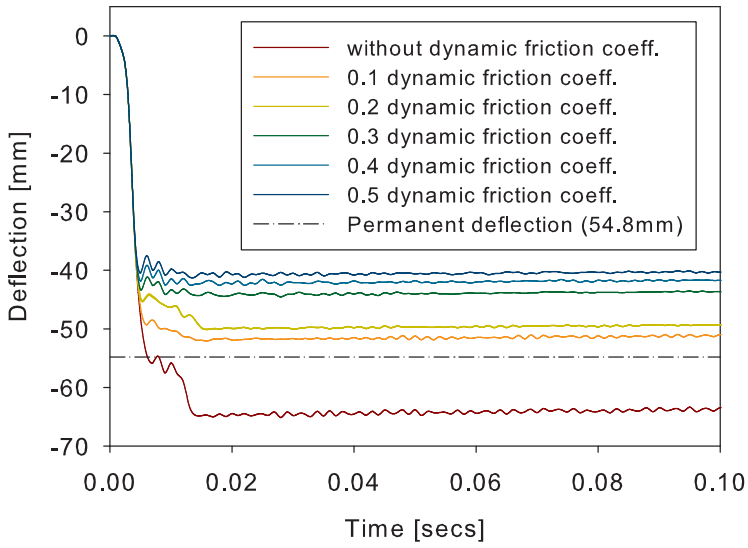

Figure 6.10: Influence of dynamic friction coefficient on non-restrained plate with 75 mm opening loaded nominally to 50 psi.

Using the dynamic friction coefficient of 0.1 the mesh refinement process was repeated with the results displayed in Table 6.4, including the hourglass effect. LS-DYNA recommends that the hourglass energy as % of the internal energy should be $< 10\%$ [122]. Therefore the use of under-integrated Belytschko-Tsay shell elements with a characteristic element size of 2.5 x 2.5 mm were deemed acceptable for all further models of the non-restrained plates. This element type significantly saved on computational time which can be seen when comparing the run times for the 5 x 5 mm meshes using the two methods, as shown in Table 6.4.

Table 6.4: Details of mesh convergence study on non-restrained plate with 100 by 125 mm hole and 50 psi nominal test pressure, with a dynamic friction coefficient of 0.1.

Characteristic element size [mm]	10x10	5x5	5x5 [SRI]	2.5x2.5
Maximum deflection at perimeter of hole [mm]	39.13	42.44	42.85	45.06
Hour glass as % of internal energy [%]	12.2	4.1	0	6.6
Run time [h:min:s]	1:24:41	9:16:0	63:3:4	73:53:56

6.4.3 Results and Discussion

Restrained plates

Numerical results from the simulation of the experimental work conducted on restrained plates from Chapter 5 (see Tables 5.3 and 5.4) are shown in Tables 6.5 and 6.6. Direct comparison between the numerical simulations and permanent deflections of the experimental work are also shown in Figure 6.11.

Table 6.5: Numerical simulations of 0.5 m x 0.5 m restrained plates loaded nominally to 25 psi.

Numerical	Hole geometry [mm]	Maximum deflection [mm]	Permanent deflection [mm]
1	Full plate	15.69	13.3
2	50	15.86	14.04
3	50x75	18.86	16.88
4	75	17.29	15.56
5	75x100	17.41	15.26
6	100	16.78	15.06
7	100x125	16.06	14.32

Table 6.6: Numerical simulations of 0.5 m x 0.5 m restrained plates loaded nominally to 50 psi.

Numerical	Hole geometry [mm]	Maximum deflection [mm]	Permanent deflection [mm]
8	Full plate	26.47	24.9
9	50	26.03	25.08
10	50x75	26.77	25.55
11	75	26.54	25.34
12	75x100	25.69	24.66
13	100	25.29	24.16
14	100x125	25.61	24.33

The numerical simulations are capable of reproducing the experimental permanent deflections with reasonable accuracy. Slight fluctuations in the results are thought to be associated with slight variations in the loading parameters (primarily the rise time and peak pressure). When the loading is idealised as perfectly triangular with a constant peak pressure for all plate opening geometries there is a definite trend in the results, see Section 6.4.4 and Figure 6.31.

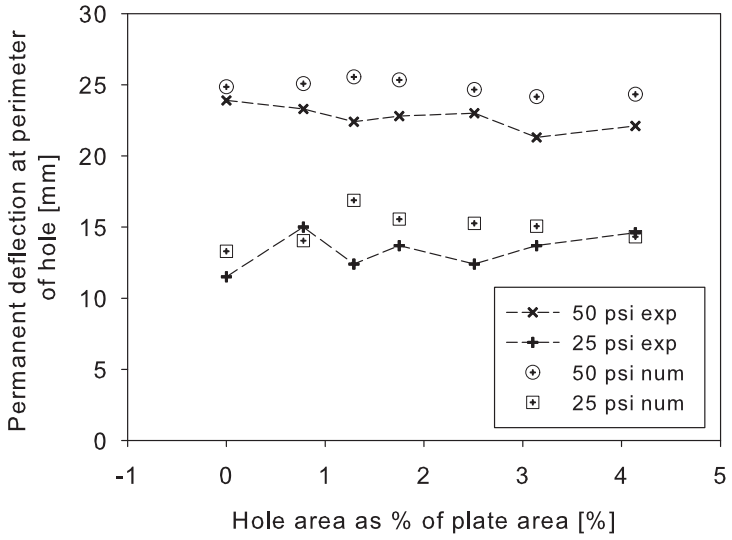

Figure 6.11: Comparison between numerical and experimental permanent deflection of restrained plates.

Validation against experimental work

Figure 6.12 shows a comparison between the permanent deflection of the experimental and numerical simulation, demonstrating that the failure mode is well captured. Rather than simply validating the numerical models against the maximum displacement, rigorous measurements were taken from post-test inspection, by profiling across different points on the plates, as shown in Figure 5.8. This ensured the FEM-analyses were validated against an extensive set of post-test measurements, not just the maximum deflection. Figures 6.13 - 6.16 show some of the measured experimental profiles compared to the corresponding profiles from the numerical simulations. Since the problem is assumed to be quarter-symmetric and this symmetry was used in the finite element model, the average values from the experimental profiles are plotted, as illustrated by Figure 5.9. Figure 6.13 shows the FEM-analyses are capable of accurately capturing the deformation pattern for a plate without openings.

Figures 6.14 - 6.16 show examples of plate with openings. It can be seen that the simulations are still capable of reproducing the global experimental deflection, even if the variation between maximum deflections is greater than for the plates without holes.

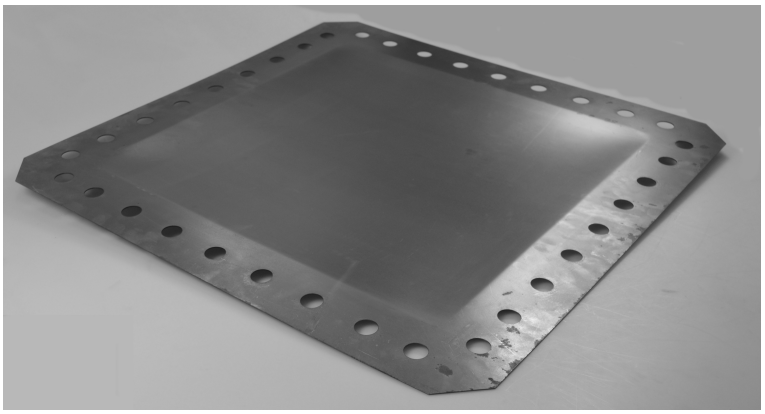

(a)

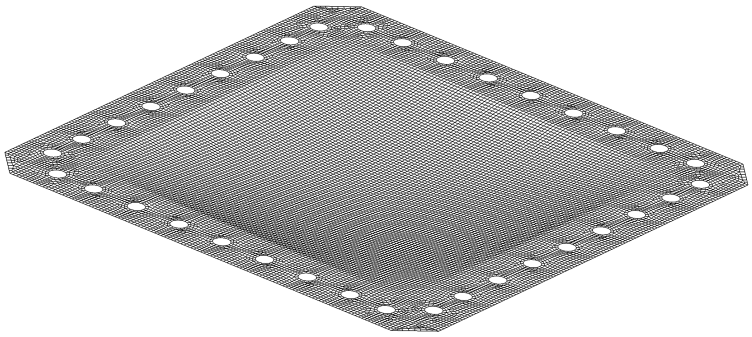

(b)

Figure 6.12: Restrained plate failure mechanism - experimental and numerical comparison (clamped area included for clarity).

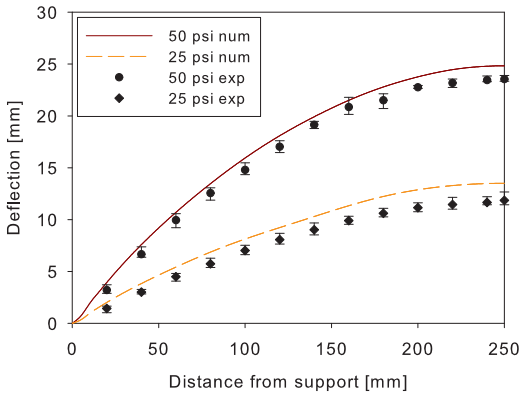

(a)

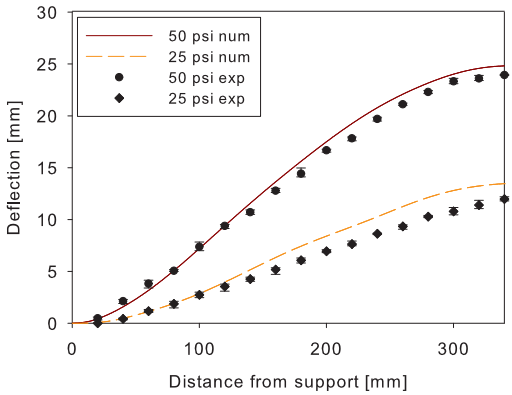

(b)

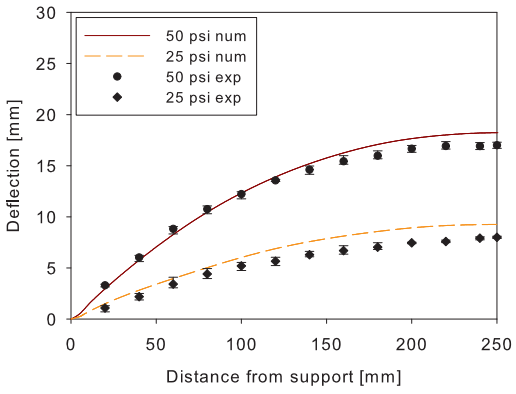

(c)

Figure 6.13: Final permanent deflection of restrained plate without opening taking measurement at (a) mid-point, (b) diagonal from corners and (c) quarter sections. Results from numerical simulations are shown as lines and the experimental data are shown as error bars.

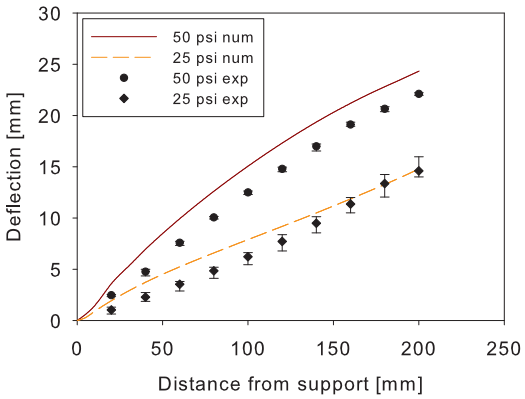

(a)

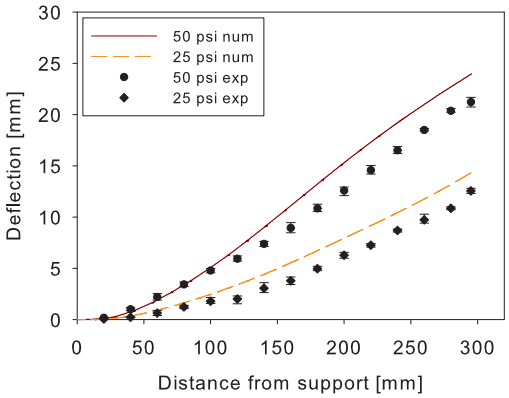

(b)

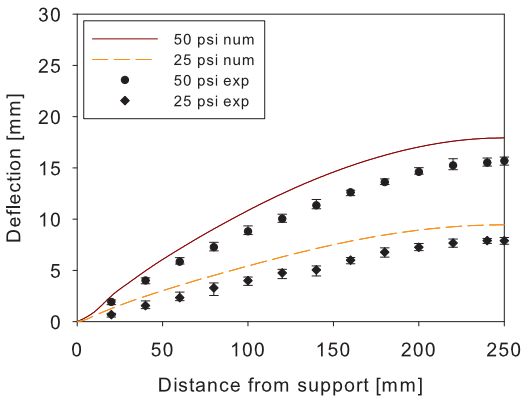

(c)

Figure 6.14: Final permanent deflection of restrained plate with 100 mm by 125 mm opening taking measurement at (a) mid-point, (b) diagonal from corners and (c) quarter sections. Results from numerical simulations are shown as lines and the experimental data are shown as error bars.

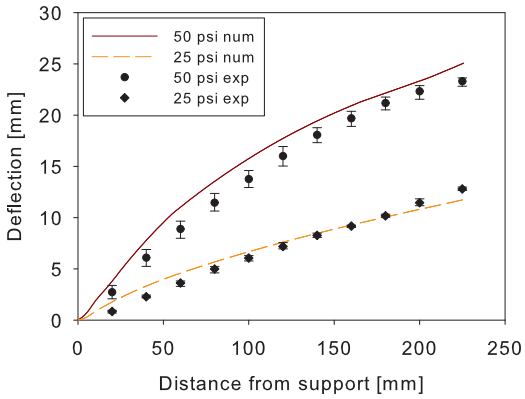

(a)

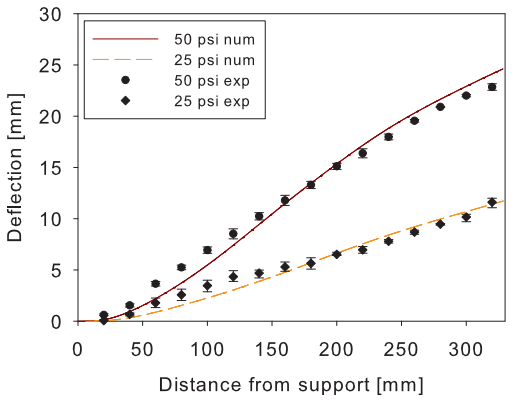

(b)

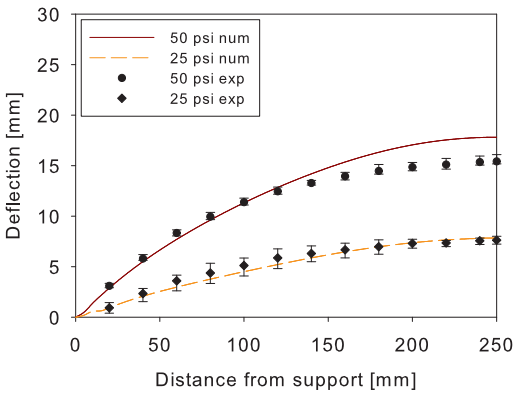

(c)

Figure 6.15: Final permanent deflection of restrained plate with 50 mm opening taking measurement at (a) mid-point, (b) diagonal from corners and (c) quarter sections. Results from numerical simulations are shown as lines and the experimental data are shown as error bars.

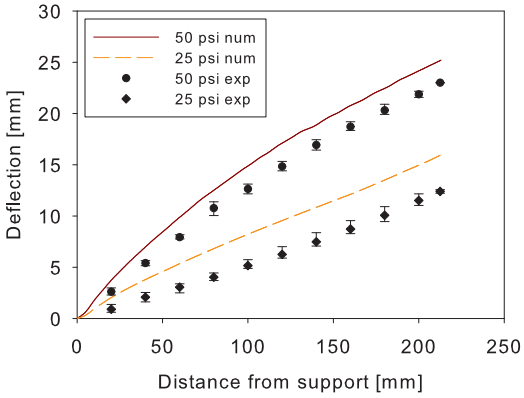

(a)

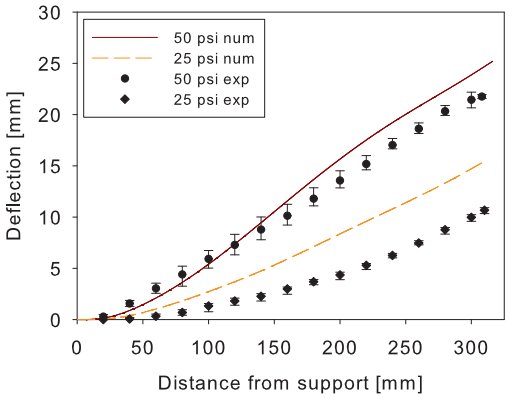

(b)

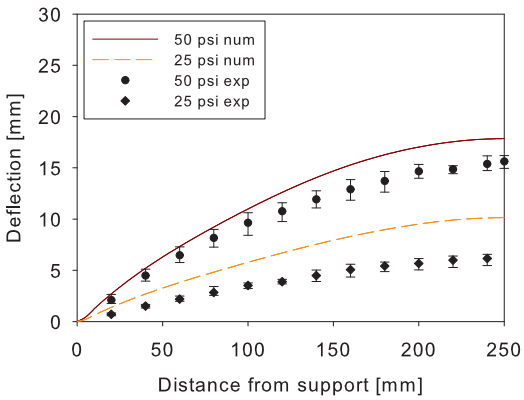

(c)

Figure 6.16: Final permanent deflection of restrained plate with 75 mm by 100 mm opening taking measurement at (a) mid-point, (b) diagonal from corners and (c) quarter sections. Results from numerical simulations are shown as lines and the experimental data are shown as error bars.

Transient deformation

As discussed in the literature review due to the dynamic nature of explosion loading it is often difficult to capture the transient behaviour of a structure during experimental testing, with most data relying on the final deformation for reference. Zhu[8] was able to investigate the transient deformation profiles of square plates under explosion loading using an optical technique, developed by Huang *et al.* [80]. The results for a clamped mild steel specimen are shown in Figure 6.17, where W is deflection and X represents points along the symmetry line of the square plate.

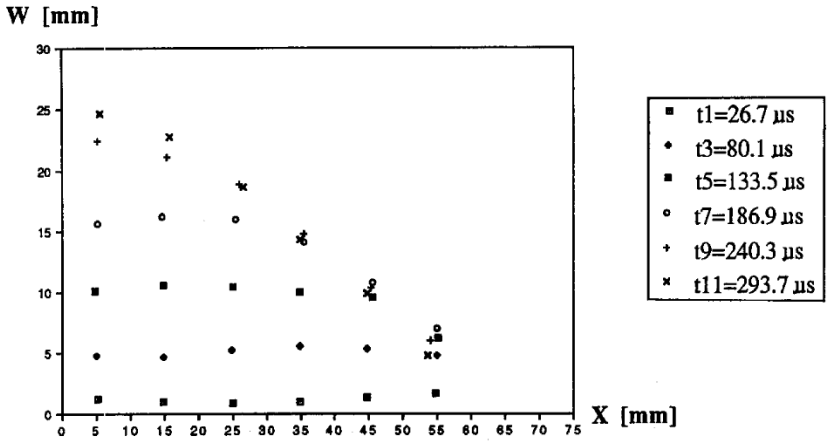

Figure 6.17: Transient deformation profiles of mild steel square plate[8].

One of the major advantages of non-linear finite element simulations of the pressure loading process is the ability to observe phenomena, which is difficult and not always possible to record in an experiment, such as the transient deformation. Since no experimental data was captured for the transient behaviour of the plates tested in this research, the numerical models were utilised.

Figure 6.18 shows the transient deformation profiles for the restrained full plate subjected to a nominal pressure of 25 and 50 psi. The FEM indicates that the maximum and final deformations are very similar in regard to shape and out-of-plane deflection. Since the permanent deflections correlated extremely well with the experimental results and the rebound displacements are relatively small (approximately 5% at 50 psi and 13% at 25 psi), it can be argued that the transient (peak) displacements are similar to the permanent ones.

Therefore the FEM's have been used to investigate the transient response of the plates with varying pressure loads and openings. The results show that the plate deformed with plastic hinges firstly developing at the boundary and then moving toward the centre of the plate. This correlates with findings by Huang *et al.* [80].

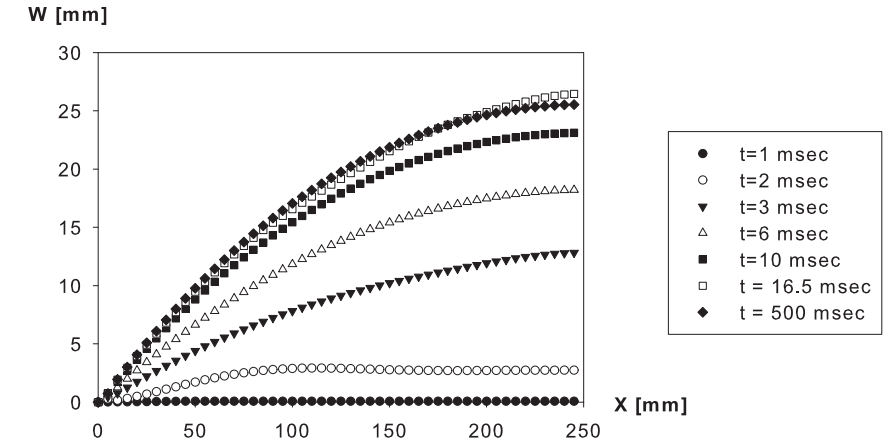

(a)

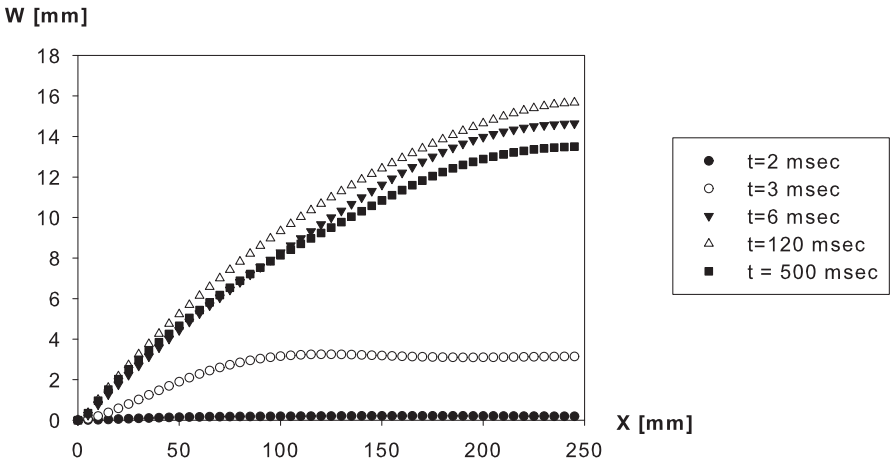

(b)

Figure 6.18: Transient deformation profiles of restrained mild steel square plates based on the numerical simulations for (a) full plate loaded at a nominal pressure of 50 psi (b) full plate loaded at a nominal pressure of 25 psi.

Figure 6.19 shows the transient deformation profile for the restrained plate with a 75 mm by 100 mm opening subjected to a nominal pressure of 50 psi. The FEM again indicates that the maximum and final deformations are very similar in regard to shape and out-of-plane deflection. This shows the transient response appears to be similar for plates with openings than for plates without openings when the size is $<5\%$ of the loaded area. It is interesting to observe that the plate with an opening responds in a similar manner to the plate without an opening up to the maximum displacement. However during the rebound to the permanent deformation the shape deviates from this trend.

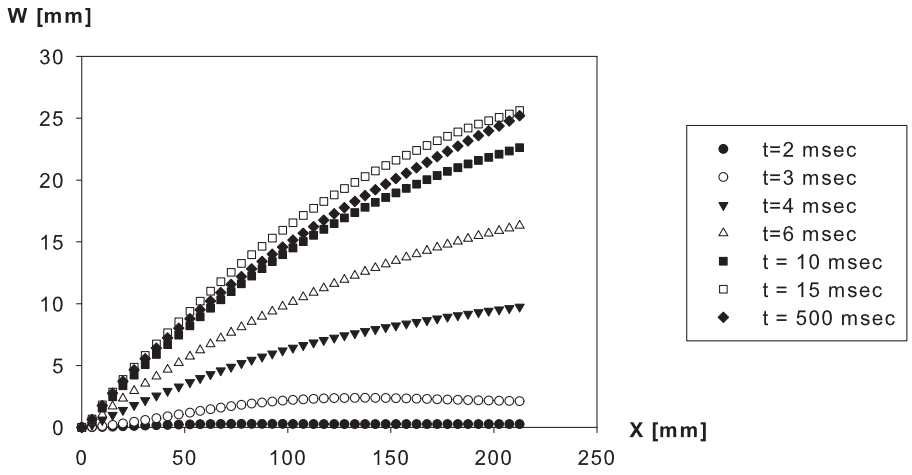

Figure 6.19: Transient response of restrained plate with 75 mm by 100 mm opening at a nominal pressure of 50 psi.

Finally the predicted deformed shape close to the holes of the various plates are plotted in Figure 6.20. The fringes represent the equivalent plastic strain field, where equivalent plastic strain is the integral of the equvialent plastic strain rate, and the equivalent plastic strain rate is defined in terms of the plastic strain rate[123]. Even though the deflections in the plates are in the order of 20 times the plate thickness, the plastic strains are small. The fringe levels in Figure 6.20 have a maximum of 4.2% plastic strain around the openings, with this level only being exceeded around the clamped boundary zone. The plastic hinges that formed in the experimental study are well reproduced in the numerical simulations.

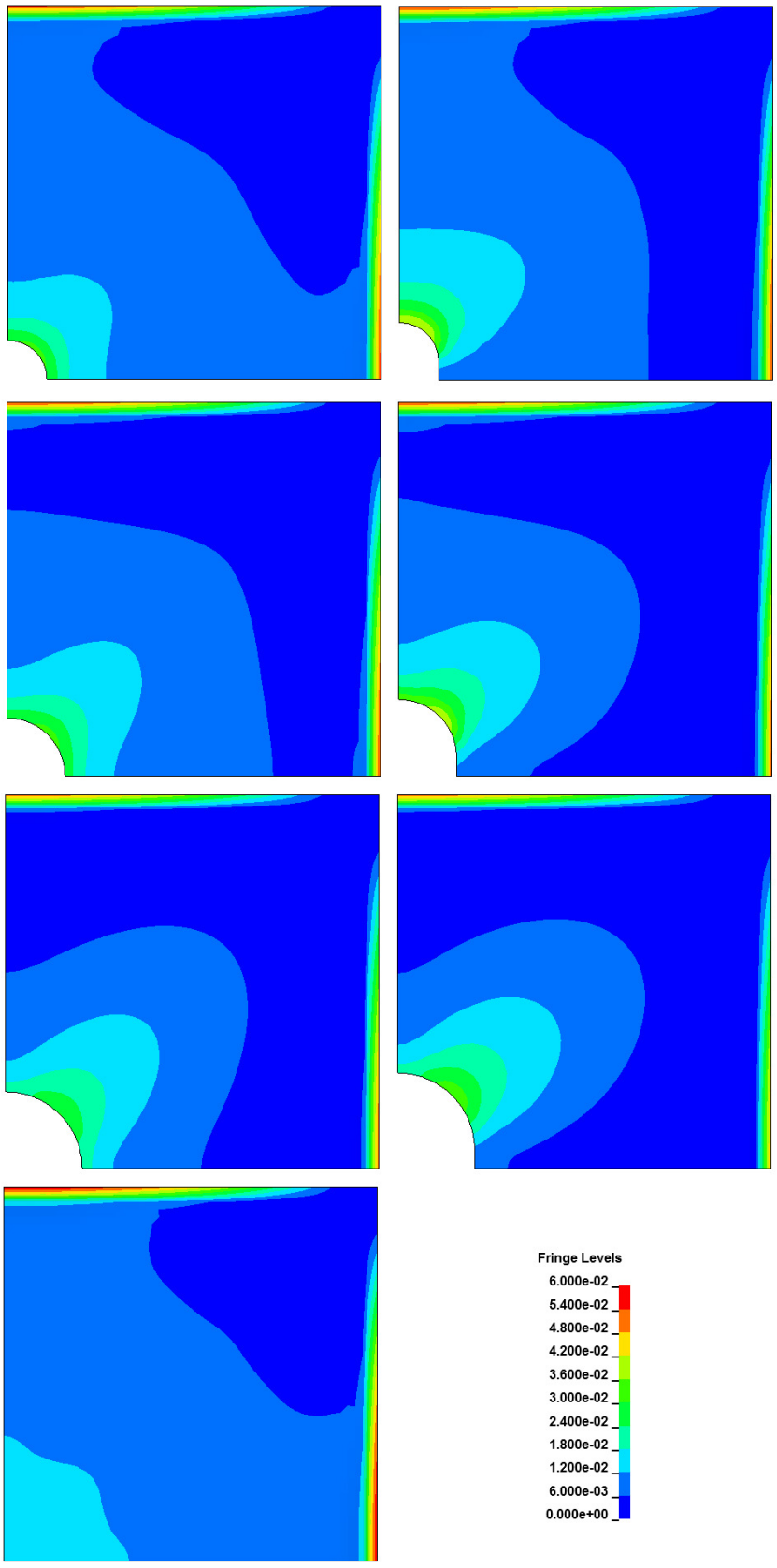

Figure 6.20: Fringes of equivalent plastic strain plotted on the permanent deformed shapes of the various restrained plate designs after 50 psi nominal pressure loading.

Non-restrained plates

Numerical results from the simulation of the experimental work conducted on non-restrained plates from Chapter 5 (see Tables 5.5 and 5.6) are shown in Tables 6.7 and 6.8. Direct comparison between the numerical simulations and final permanent displacements of the experimental work are also shown in Figure 6.21.

Table 6.7: Numerical simulations of 0.5 m x 0.5 m non-restrained plates loaded nominally to 25 psi with 0.1 dynamic friction coefficient.

Numerical	Hole geometry [mm]	Maximum deflection [mm]	Permanent deflection [mm]
15	Full plate	42.29	38.87
16	50	40.77	36.2
17	50x75	–	–
18	75	40.75	36.5
19	75x100	–	–
20	100	39.44	35.01
21	100x125	–	–

Table 6.8: Numerical simulations of 0.5 m x 0.5 m non-restrained plates loaded nominally to 50 psi with 0.1 dynamic friction coefficient.

Numerical	Hole geometry [mm]	Maximum deflection [mm]	Permanent deflection [mm]
22	Full plate	63.03	59.6
23	50	54.94	50.38
24	50x75	53.67	51.34
25	75	52.06	47.35
26	75x100	64.92	61.15
27	100	50.22	45.83
28	100x125	49.50	45.06

The numerical simulations are capable of reproducing the experimental permanent deflections with reasonable accuracy. The one major exception to this is the plate with the 75 mm by 100 mm opening loaded nominally to 50 psi. This was attributed to a spike in the rise time data capture of the pressure-time history, highlighting the sensitivity of the plate response.

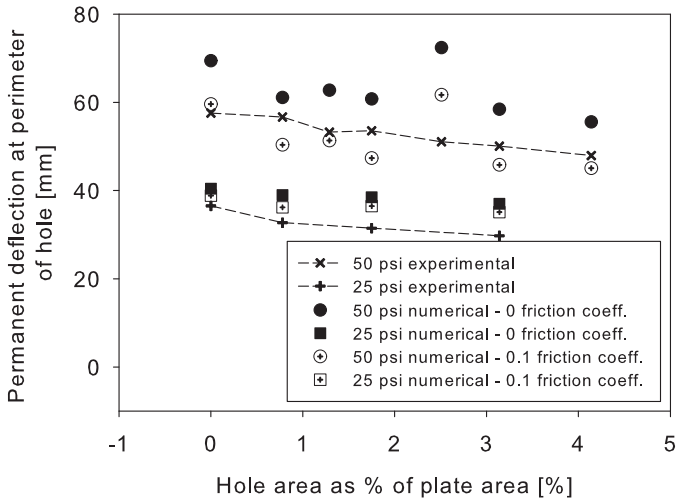

Figure 6.21: Comparison between numerical and experimental permanent deflection of non-restrained plates with and without a dynamic friction coefficient.

Validation against experimental work

Figures 6.22 - 6.25 show some of the measured experimental profiles compared to the corresponding profiles from the numerical simulations. These clearly show that the numerical model is capable of capturing the complete permanent deflection shape of the varying plate designs.

From the results it would appear that the numerical simulations predict the response of the non-restrained plates better than for the restrained plates. This could be attributed to the use of dynamic friction coefficient for the non-restrained plates. It is very difficult to justify an exact value for this as friction is influenced by lubrication, contact area, sliding speeds and temperature among other factors. A friction coefficient of 0.1 was chosen as it provided good correlation with the experiment results and it was similar to values proposed by other researchers for comparable events.

The discrepancies in the maximum permanent deflection could be due to sensitivity to the variations in the peak pressure, as highlighted in Chapter 5 or due to any spatial variation in the pressure load, not captured by the pressure difference described by the pressure transducers in the experimental work. The loading will be further examined in Section 6.5.

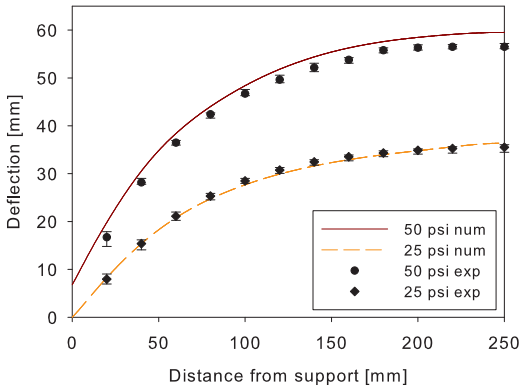

(a)

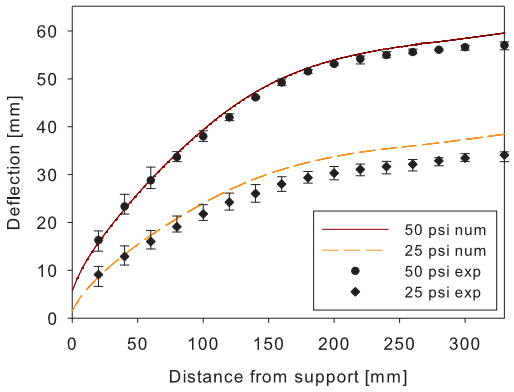

(b)

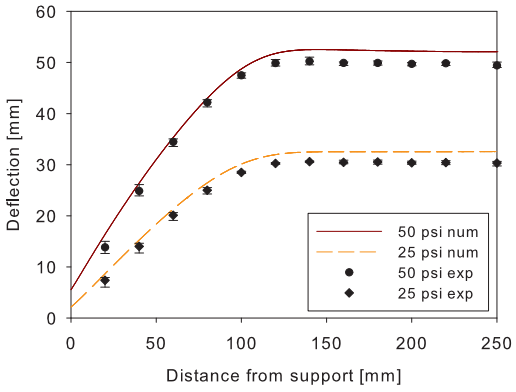

(c)

Figure 6.22: Final permanent deflection of non-restrained plate without opening taking measurement at (a) mid-point, (b) diagonal from corners and (c) quarter sections. Results from numerical simulations are shown as lines and the experimental data are shown as error bars.

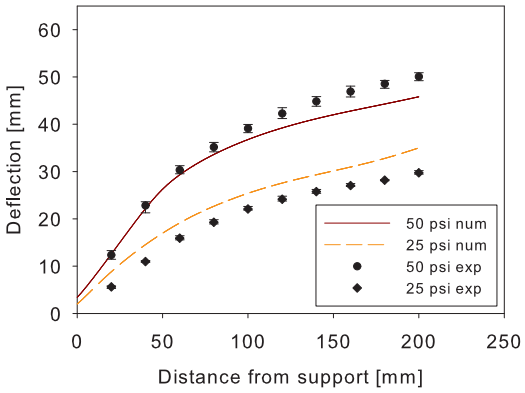

(a)

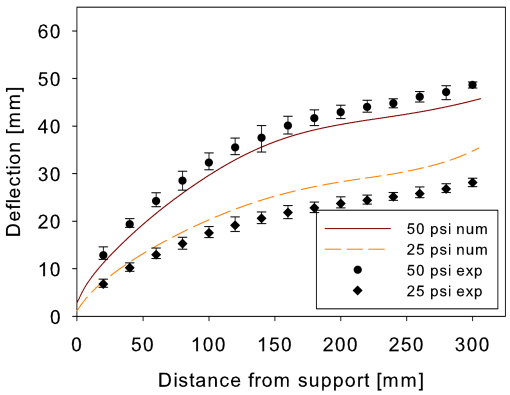

(b)

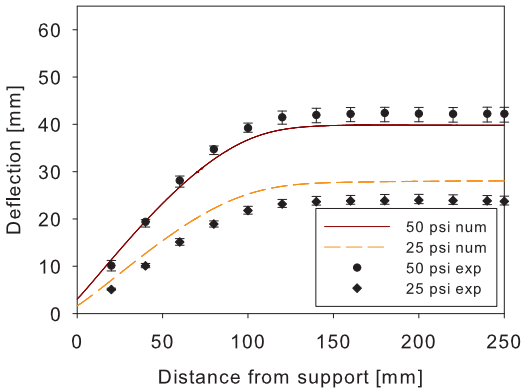

(c)

Figure 6.23: Final permanent deflection of non-restrained plate with 100 mm opening taking measurement at (a) mid-point, (b) diagonal from corners and (c) quarter sections. Results from numerical simulations are shown as lines and the experimental data are shown as error bars.

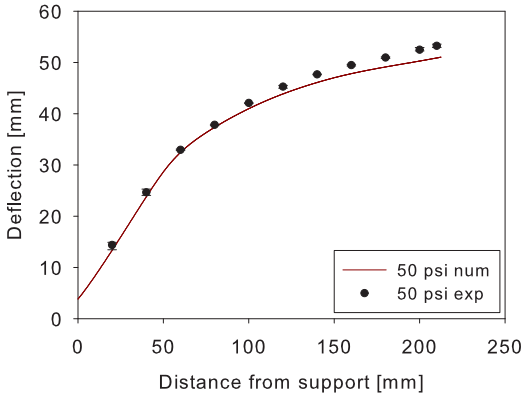

(a)

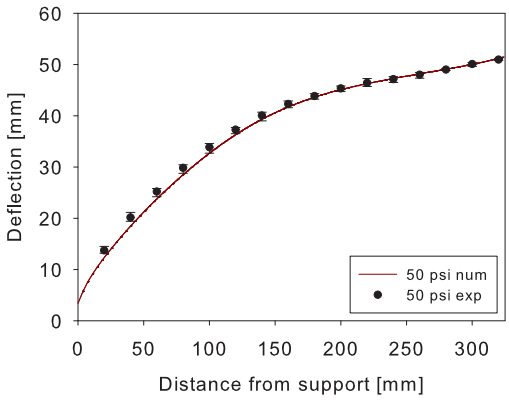

(b)

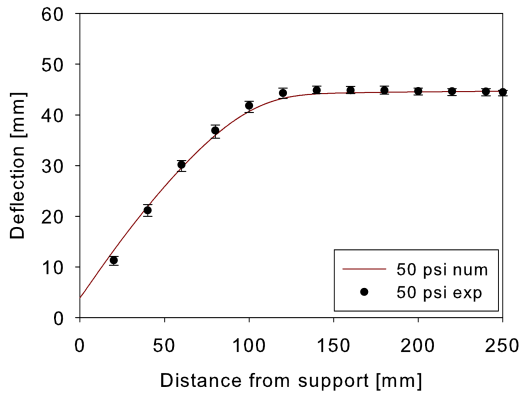

(c)

Figure 6.24: Final permanent deflection of non-restrained plate 50 by 75 mm opening taking measurement at (a) mid-point, (b) diagonal from corners and (c) quarter sections. Results from numerical simulations are shown as lines and the experimental data are shown as error bars.

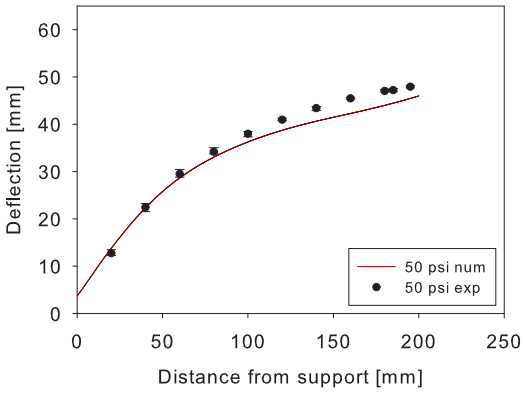

(a)

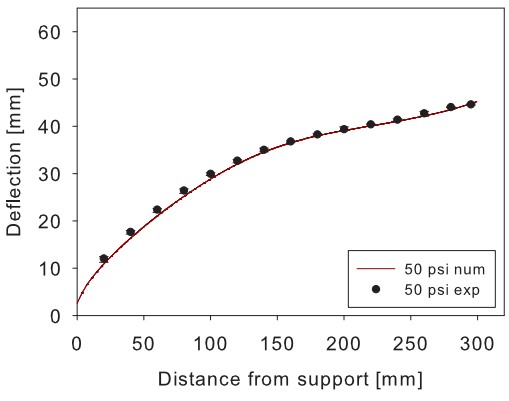

(b)

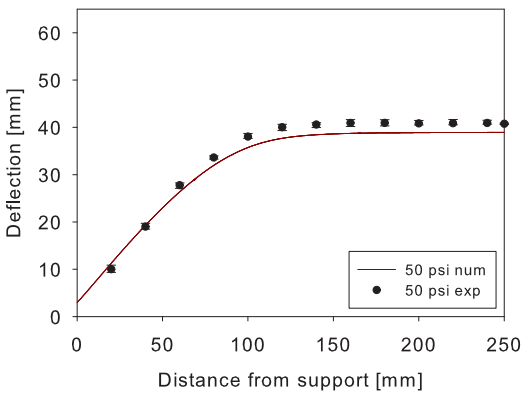

(c)

Figure 6.25: Final permanent deflection of non-restrained plate with 100 by 125 mm opening taking measurement at (a) mid-point, (b) diagonal from corners and (c) quarter sections. Results from numerical simulations are shown as lines and the experimental data are shown as error bars.

Figures 6.26 and 6.27 show that the failure mode was represented extremely well by the simulations demonstrating the applicability of the Modified Johnson-Cook constitutive relation and of including the boundary conditions into the modelling.

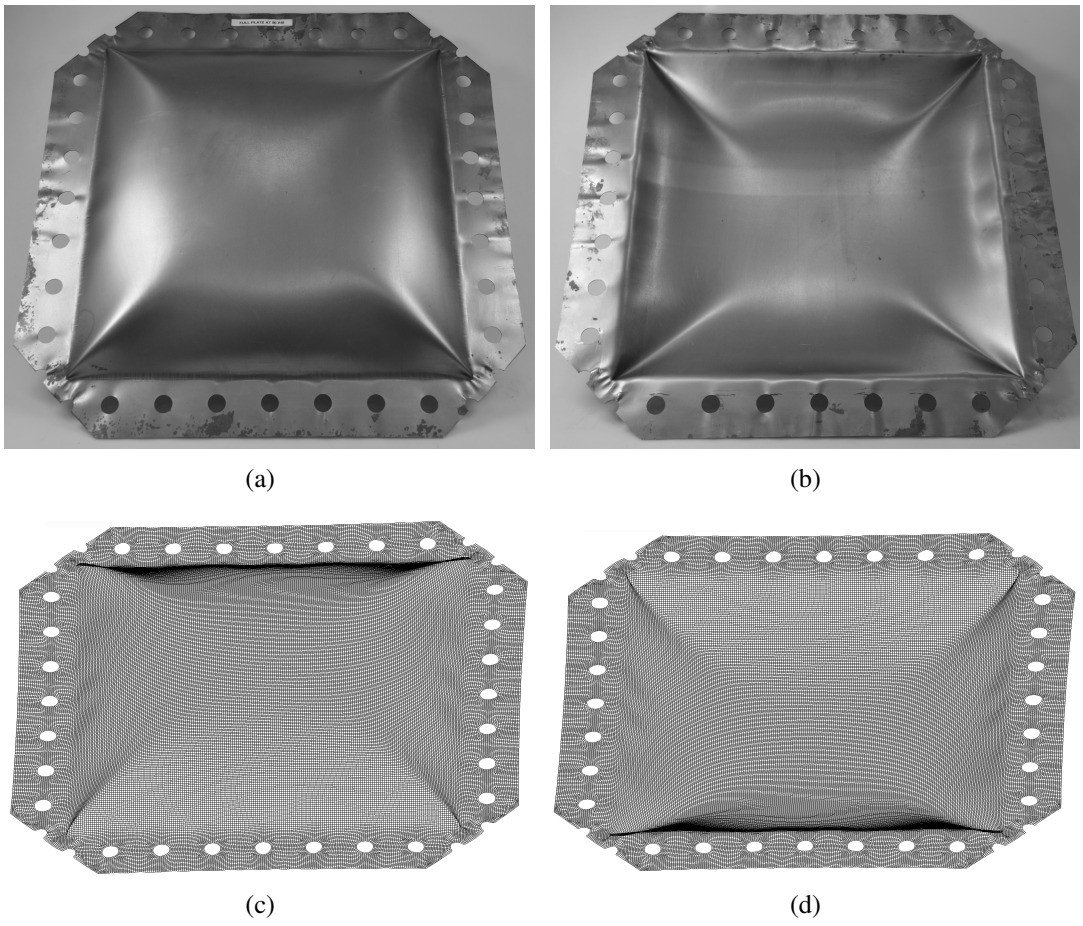

(a) (b)

(c) (d)

Figure 6.26: Non-restrained plate failure mechanism - experimental and numerical comparison.

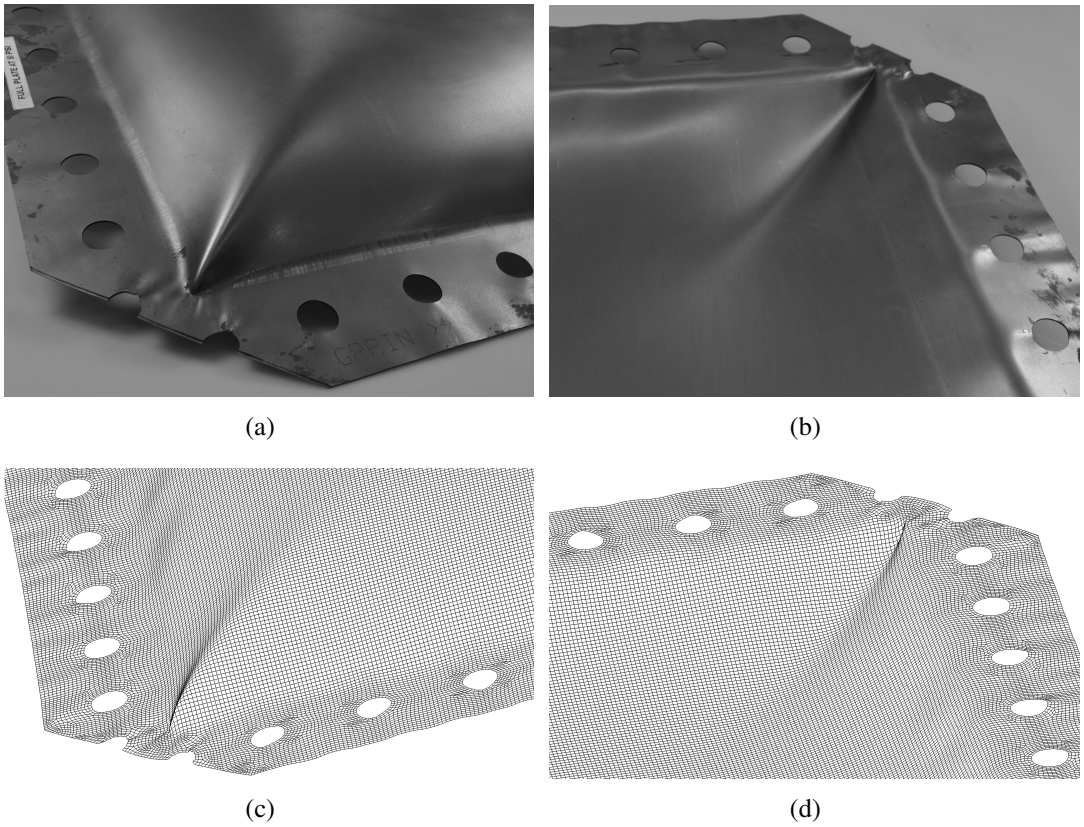

(a) (b)

(c) (d)

Figure 6.27: Non-restrained plate failure mechanism (close-up) - experimental and numerical comparison.

Transient deformation

The transient behaviour of the non-restrained plates tested in this research was investigated using the numerical models. Figure 6.28 shows the transient deformation profiles of the full plate and a plate with 75 mm opening subjected to a nominal pressure of 50 psi. The FEM again indicates that the maximum and final deformations are very similar in regard to shape and out-of-plane deflection (approximately 8% at 50 psi and 12% at 25 psi), as was the case for the restrained plates. Therefore the transient (peak) displacements can be assumed to be similar to the permanent deflection.

The results show that the plate initially develops plastic hinges around the boundary, which move toward the centre of the plate, as for the restrained plates. Since the boundary conditions remove the in-plane restraint the plate moves inwards in the x-y plane. At approximately 4 msec this causes a yield line to form in the corner of the plate. This continues to develop up to the maximum deflection at 16.9 msec. The other plate designs deformed in a similar manner.

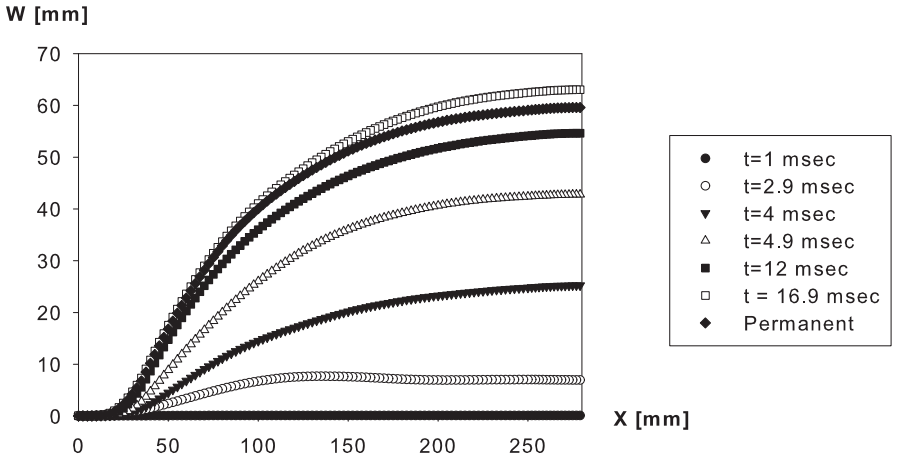

(a)

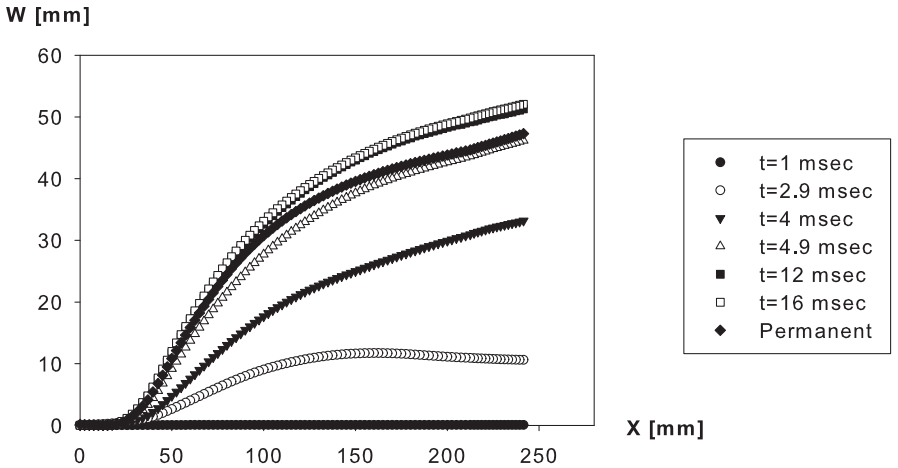

(b)

Figure 6.28: Transient deformation profiles of non-restrained mild steel square plates based on the numerical simulations for (a) full plate loaded at a nominal pressure of 50 psi (b) plate with a 75 mm opening loaded at a nominal pressure of 50 psi.

The predicted deformed shape close to the holes of the various plates are plotted in Figure 6.29. The fringes represent the equivalent plastic strain field. Even though the deflections in the plates are of the order of 50 times the plate thickness, the plastic strains are still relatively small. The fringe levels in Figure 6.29 have a maximum of 4.8% plastic strain around the boundary, with this level only being exceeded in the diagonal yield line developing into the corner. The plastic hinges that formed in the experimental study are again very well reproduced in the numerical simulations.

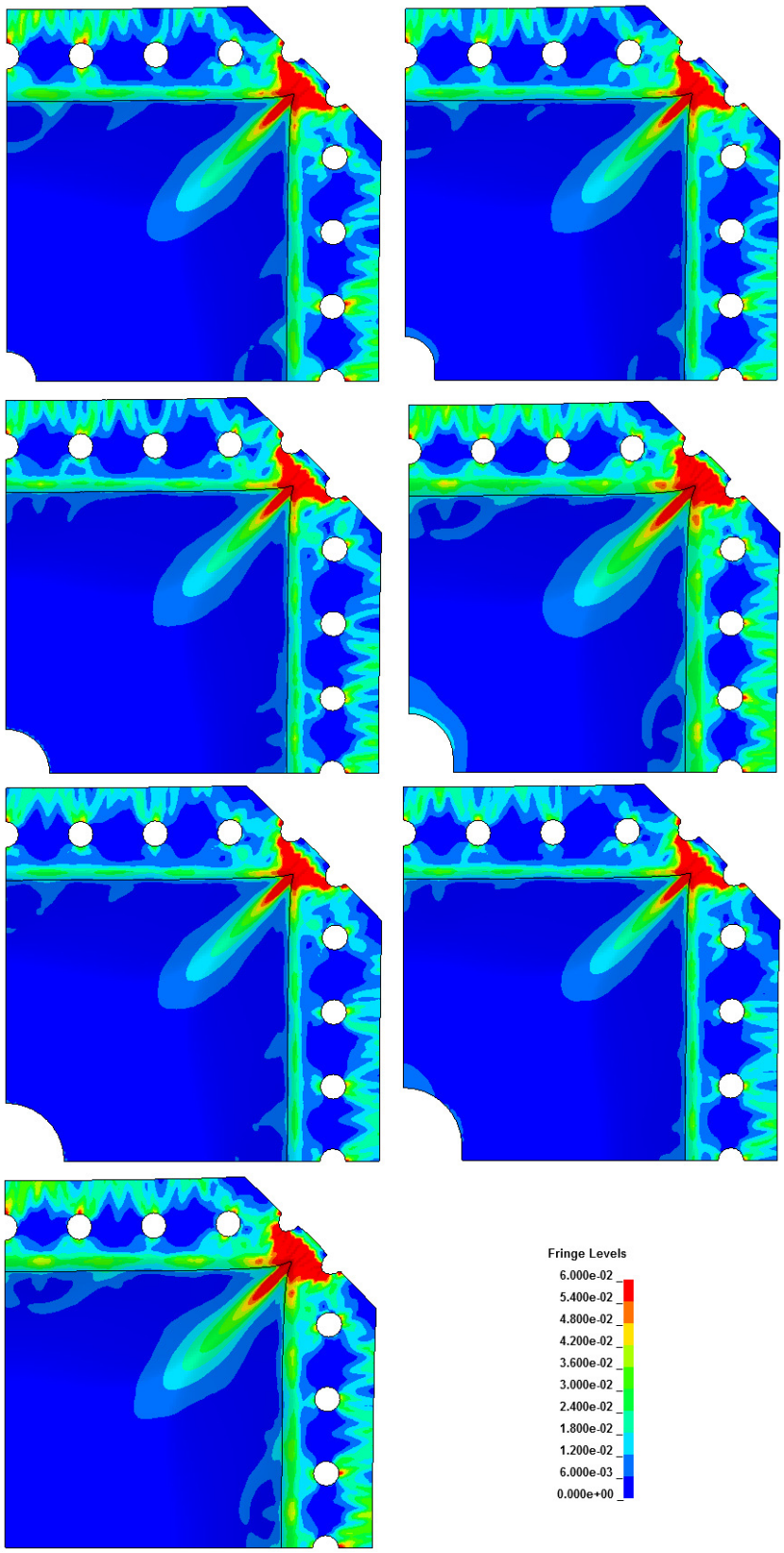

Figure 6.29: Fringes of equivalent plastic strain plotted on the permanent deformed shapes of the various non-restrained plate designs after 50 psi nominal pressure loading.

6.4.4 Parametric study

Now that the FEM has been validated against the experimental studies it can be used to run simulations that were not conducted in the experimental phase of this study. To remove the small variation in rise times and peak pressures observed during the experimental phase, an idealised pressure-time curve was applied to all of the plate designs. The pressure-time history applied is shown in Table 6.9 and Figure 6.30 and the T_r is the average time taken to achieve the maximum pressure from the experimental series, for the two nominal pressures. Even though the pressure-time history is equal for all tests, the total load transmitted to each plate will vary due to the change in hole size. As shown in Chapter 5 the plates were not loaded with a triangular pressure-pulse curve so the following results can not be validated physically but are presented here for reference in future studies. The aim of the simulations was to investigate how the openings influenced an idealised free-field explosion, rather than a semi-confined one. Applying a single pressure-time load curve to all of the plate designs allows greater clarity in the influence that the openings have on the plate's response.

Table 6.9: Equal pressure-time parameters applied to all plate geometries and boundary conditions.

T_r $[msec]$	P_{max} $[PSI]$	T_d $[msec]$
6.2	25.0	12.4
12.2	50.0	24.4

The numerical results for this parametric study are shown in Tables 6.10 and 6.11 for the restrained plates and Tables 6.12 and 6.13 for the non-restrained plates. These results were then compared to the experimental data from Chapter 5 (see Tables 5.3, 5.4, 5.5 and 5.6) in Figures 6.31 and 6.32. Even though the pressure-time histories were different in the experimental work (with much longer decay times) the final permanent deflections compared well. This confirms that the rise time and peak pressure were the critical parameters in this study. The time to maximum deflection was also similar to the numerical models when using the experimental pressure-time histories. The time was typically 11 msec when loaded to 25 psi and 16 msec when loaded to 50 psi. The permanent deflection profiles are also shown in Figures 6.33 and 6.34.

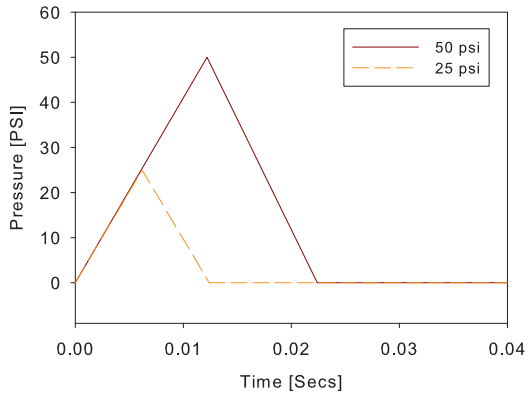

Figure 6.30: Equal pressure-time history applied to each plate geometry.

Table 6.10: Numerical simulations of 0.5 m x 0.5 m restrained plates using a constant pressure-time history with a peak pressure of 25 psi.

Numerical	Hole geometry [mm]	Maximum deflection [mm]	Permanent deflection [mm]
29	Full plate	13.48	10.30
30	50	13.89	11.59
31	50x75	14.14	12.13
32	75	14.22	12.26
33	75x100	15.05	12.98
34	100	14.77	12.98
35	100x125	15.62	13.57

Table 6.11: Numerical simulations of 0.5 m x 0.5 m restrained plates using a constant pressure-time history with a peak pressure of 50 psi.

Numerical	Hole geometry [mm]	Maximum deflection [mm]	Permanent deflection [mm]
36	Full plate	24.31	22.52
37	50	25.15	23.97
38	50x75	25.57	24.51
39	75	25.74	24.70
40	75x100	26.10	25.13
41	100	26.29	25.32
42	100x125	26.55	25.68

When equal pressure-time histories are applied to the different plate designs, the permanent deflection (taken at 200 mm away from the support) is approximately constant. The restrained plates had a variation of $\pm$4mm for the 25 psi plates and $\pm$4.5

Table 6.12: Numerical simulations of 0.5 m x 0.5 m non-restrained plates using a constant pressure-time history with a peak pressure of 25 psi.

Numerical	Hole geometry [mm]	Maximum deflection [mm]	Permanent deflection [mm]
43	Full plate	37.78	30.33
44	50	35.04	28.19
45	50x75	34.72	28.03
46	75	33.98	27.69
47	75x100	33.33	27.25
48	100	32.72	26.95
49	100x125	32.03	26.29

Table 6.13: Numerical simulations of 0.5 m x 0.5 m non-restrained plates using a constant pressure-time history with a peak pressure of 50 psi.

Numerical	Hole geometry [mm]	Maximum deflection [mm]	Permanent deflection [mm]
50	Full plate	54.83	49.18
51	50	54.52	49.64
52	50x75	54.49	48.56
53	75	53.81	49.06
54	75x100	52.83	48.20
55	100	52.03	47.42
56	100x125	51.75	47.30

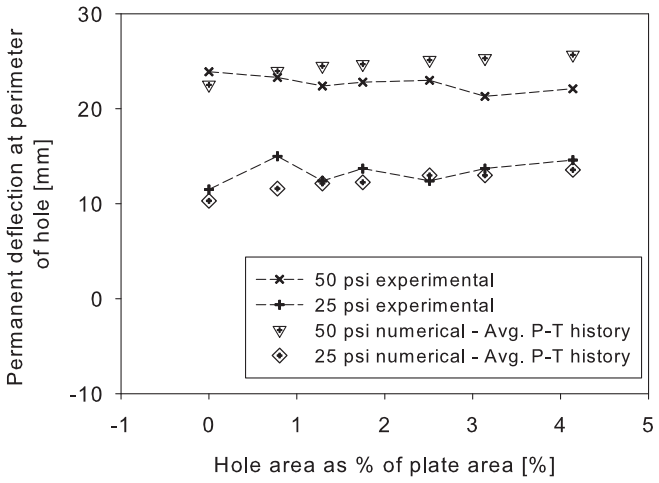

Figure 6.31: Comparison between the numerical and experimental permanent deflection of restrained plates, when applying a constant pressure-time history to all plate geometries at 25 and 50 psi.

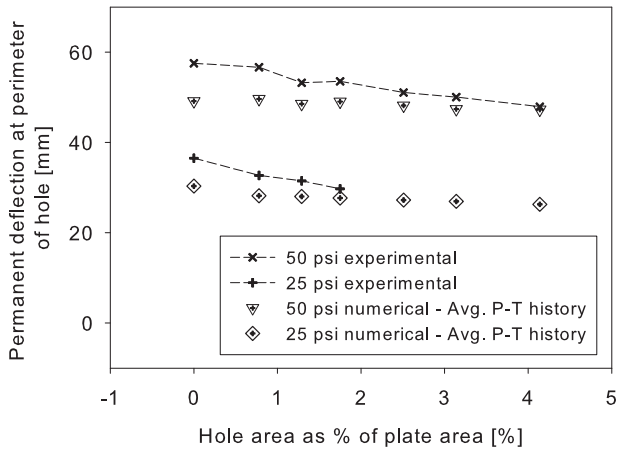

Figure 6.32: Comparison between the numerical and experimental permanent deflection of non-restrained plates with a 0.1 dynamic coefficient, when applying a constant pressure-time history to all plate geometries at 25 and 50 psi.

mm for the 50 psi plates. Similarly, the non-restrained had a variation of ± 4 mm for the 25 psi plates and ± 2 mm for the 50 psi plates It is therefore concluded that the reduction in stiffness due to the holes is compensated by the reduced area to which the load is applied. This supports findings by Rakvag *et al.* [16].

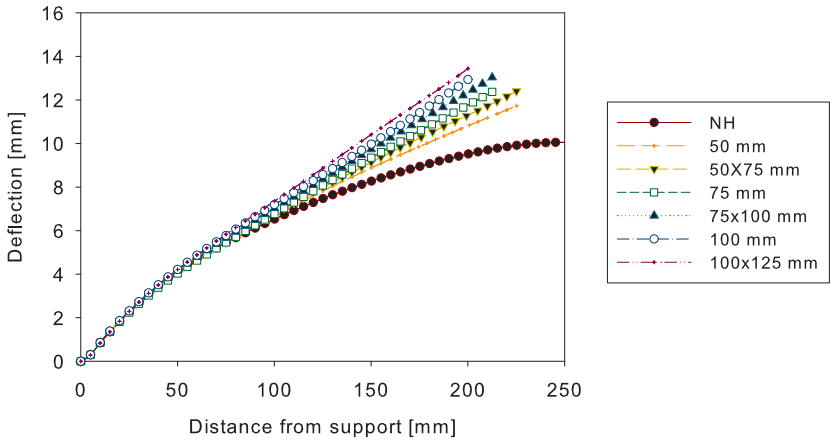

(a)

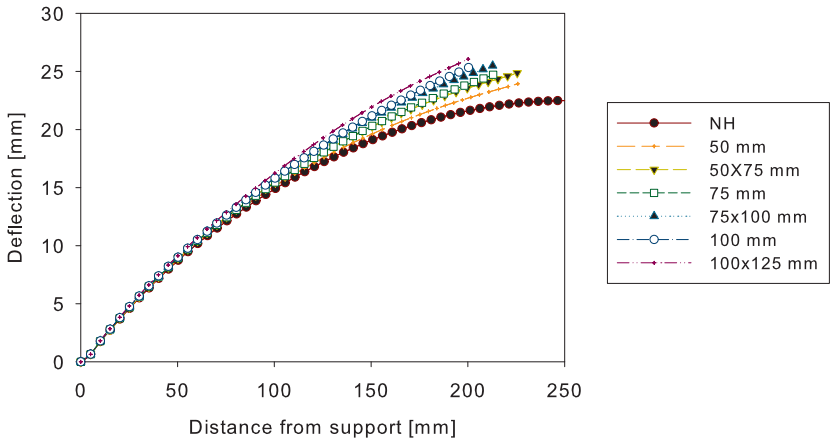

(b)

Figure 6.33: Permanent deflection of restrained plates with an equal pressure-time history applied to all plate geometries at (a) 25 psi and (b) 50 psi (NH - No Hole).

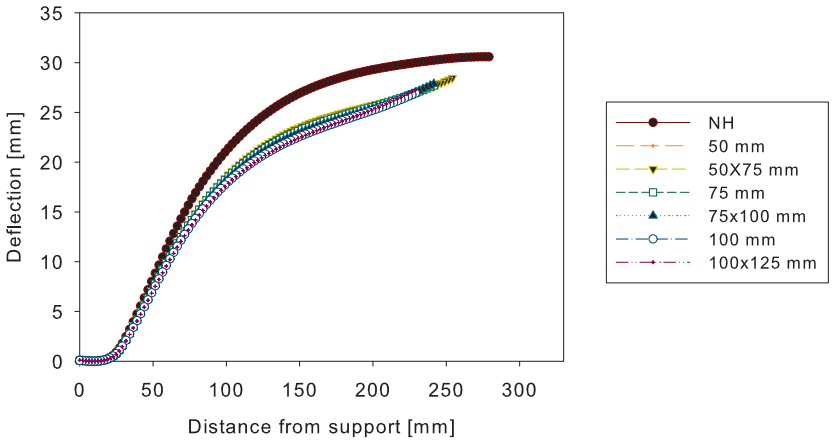

(a)

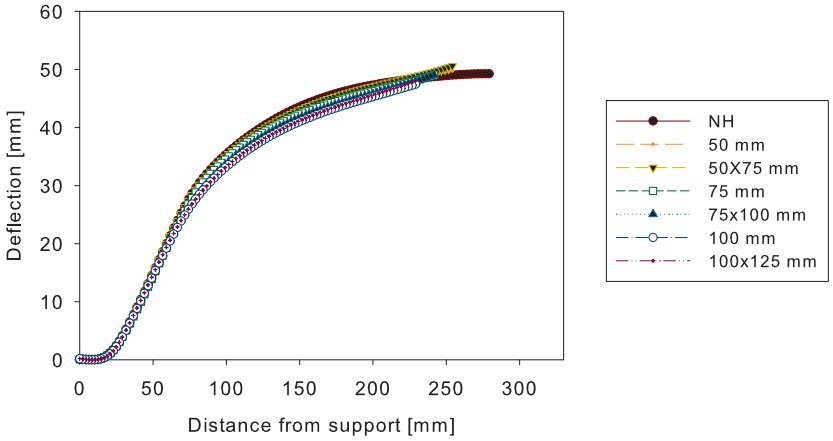

(b)

Figure 6.34: Permanent deflection of non-restrained plates with an equal pressure-time history applied to all plate geometries at (a) 25 psi and (b) 50 psi (NH - No Hole).

All the studies thus far have assumed the pressure-time history has been uniformly distributed over the loaded area for each plate. This has provided acceptable results considering that this is a highly non-linear problem.

6.5 Eulerian

Thanks to a collaborative project during this present study the spatial variation of the pressure loading was investigated experimentally and numerically for plates with openings using the Pressure Pulse Loading Rig (PPLR) from Chapter 4[16][15]. All experimental studies were conducted at the University of Liverpool.

In order to study the spatial variation of the pressure loading numerically, the Fluid Structure Interaction (FSI) capabilities of LS-DYNA were utilised and this study was conducted by Rakvag[16] and Hallset and Haagendrud[15]. Initially a purely Eulerian mesh was used to determine the pressure-time history for comparison with experimental data.

Quarter-symmetry boundary conditions were used. The PPLR (Figure 4.1) was idealised as a rectangular box, with a length of 1 m and a depth and width of 0.37 m, as depicted in Figure 6.35. This meant the total volume was equal to the PPLR. The walls of the pressure chamber (Figure 4.1) were modelled as fixed boundary conditions, except for the burst diaphragm area (Figure 4.15) where the air was allowed to flow out of the model and into an ambient domain with initial atmospheric pressure. The burst diaphragm area was modelled as 0.18 m^2, consistent with the conducted experiments

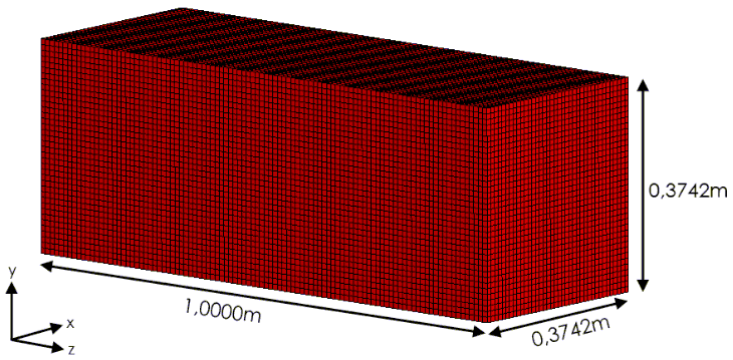

Figure 6.35: Idealised geometry of a quarter section of the test rig[15].

Hallset and Haagenrud[15] provide further descriptions of the numerical model construction. An example simulation is shown in Figure 6.36. The results showed that the Eulerian approach could accurately predict the pressure-time histories recorded for a series of experiments on plates with openings of different sizes and shapes [16]. One such example, is for a plate with circular openings, shown in Figure 6.37.

This demonstrates that the Eulerian approach can accurately describe the pressure-time history for a variety of plate designs, consistent with the experimental results. This could be utilised in future studies. Using this approach would save expensive experimental work in the preliminary stages of a study.

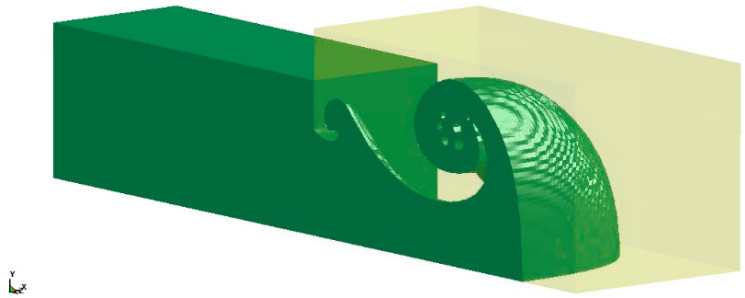

Figure 6.36: High pressure flowing out of idealised pressure tank[15].

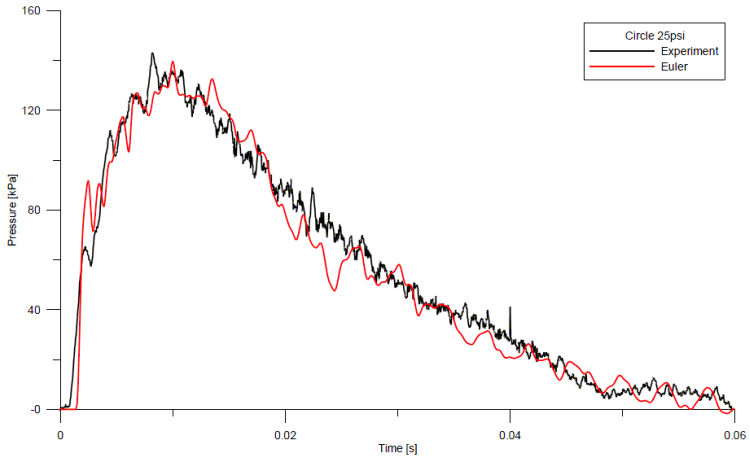

Figure 6.37: Experimental pressure-time curve for a restrained plate with circular holes loaded nominally to 25 psi, compared to the Eulerian model prediction[15].

6.6 Arbitrary Lagrangian Eulerian (ALE)

In this final method a fully coupled FSI simulation of the test plates with openings by Rakvag *et al.* [16] was conducted. Full details of the model construction can be found in reference 16. Only the results are discussed herein. Firstly, the pressure-time histories were calculated from the numerical analysis in the same manner as in the experiments. In the experiments the pressure transducers were in the same positions as shown in Figure 4.7, therefore equivalent points on the numerical model were used to calculate an equivalent pressure difference, i.e. the side-on pressure. The pressure-time histories compared favourably between experimental and numerical results, as shown in Figure 6.38. The numerically predicted pressure-time histories have a peak value, which is approximately 10% less than the experimental results. Borvik *et al.* [124] states that care must be taken when applying pressure loads originating from rigid or stationary references to flexible structures as the response will be overestimated. This is because

the structural flexibility reduces pressure loads and thus the structural response. This could explain this variation. However apart from this peak load discrepancy the predicted and experimental curves are in good agreement.

In the second approach the actual load transmitted to the plate, calculated by the ALE method is shown both for the average on the plate and also for a band of elements that were close to the hole perimeter. These two curves are shown in Figure 6.39. It can be seen that the pressure difference described by the pressure transducers in the experimental study provide a very good approximation for the average pressure on the plate when compared the numerical prediction, as these two curves are virtually the same. However the FSI simulation did highlight that there is a small region of higher pressure in the vicinity of the hole. This is approximately 50% higher than the average pressure load on the plate.

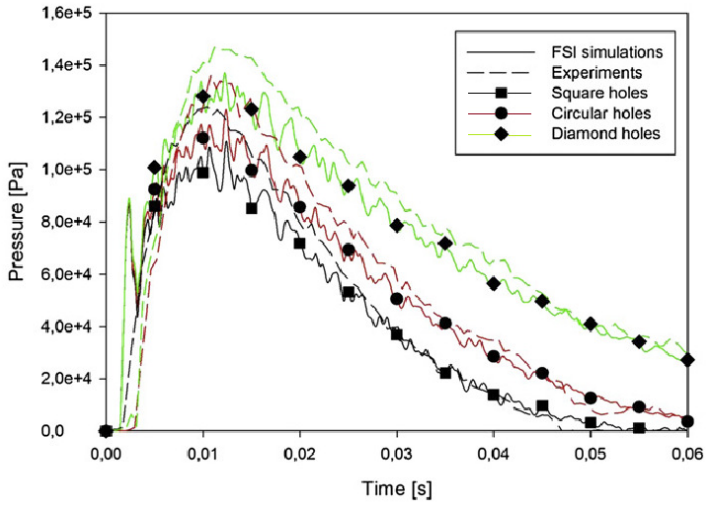

Figure 6.38: Comparison of recorded pressure-time history from experiments and FSI simulations[16].

These results offer an explanation for the discrepancies in the deflection profiles presented in the purely Lagrangian method, using the side-on pressures captured by the transducers. The reduction in peak pressure (by 10%) shown in the ALE models could explain why in general the Lagrangian models slightly over predicted the permanent deflection profiles. Also, this coupled with an increase in the pressure around the proximity of the opening could provide a more accurate prediction of the plate behaviour.

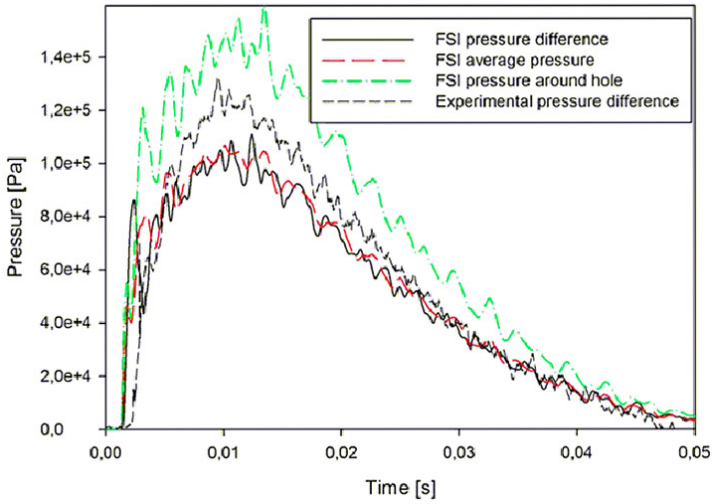

Figure 6.39: Pressure-time history from FSI simulations of the 25 psi nominal pressure test compared with the measured results[16].

6.7 Summary

In this chapter, the dynamic response of scaled plated structures was studied numerically using experimental tests presented in Chapter 5 for validation. The numerical models predicted the permanent deflection of the experimental plates within an average difference of 12% and 15% for the restrained and non-restrained plates respectively. This demonstrates the potential use of Lagrangian, Eulerian and ALE models for use in parametric and optimisation studies.

- The FE predictions using the pure Lagrangian model and the pressure-time histories recorded in the experimental work compared favourably with the experimental deformations. These were able to capture the failure mechanisms found in the experimental tests for both restrained and non-restrained plates. They provided a useful insight into the transient response and failure processes of (scaled) plated structures, subjected to blast loading.

- The ALE simulations predicted that the actual average peak pressure on the plate was 10% less than that calculated using the approximate technique (pressure difference between pressure transducers) used in the experimental pressure-time history. The FSI also shows that there is a narrow region of higher pressure in the vicinity of the opening. This 10% reduction in the peak pressure provides an explanation as to why the Lagrangian simulations in general, over predict the final profile by approximately 14%, making these a conservative prediction.

- The fully coupled ALE simulation required a considerably greater computational time than the pure Lagrangian method, and with the results correlating well from the Lagrangian tests, it was deemed unnecessary to capture the very small FSI highlighted by the ALE method.

- Once the Lagrangian models were validated against the experimental work, an idealised free-field load was applied to all plate designs for the two nominal pressures. The results showed that the maximum deflection is practically the same for all the designs. This highlights that the reduction in stiffness due to the holes is compensated by the reduced area to which the load is applied.

Chapter 7

Simplified Analytical Solution

7.1 Introduction

Structural response to explosion loading is a specialised area of structural dynamics incorporating a variety of analytical tools of varying complexity. Exact solutions can be mathematically laborious to derive often involving the use of numerical models. This can be time consuming and expensive with solutions limited in application to structures with infinitesimal displacements or elastic response. This is often unrealistic for the response of thin structures subjected to extreme transverse loading as considerable plasticity is expected.

Due to the severe limitations of exact solutions several approximate solutions have been developed and were discussed in Chapter 2. These simplified methods allow rapid assessment of even complex structures with reasonable engineering accuracy. These methods usually require that the structure and the loading be idealised in some degree, which can lead to inaccuracies. However the accuracy of such approximate procedures is often acceptable, especially when acknowledging any uncertainties in the dynamic properties of the material, the structural support conditions and the characteristics of the loading[47].

This chapter presents an energy approach for predicting mode I response[6] (large inelastic deformation) in thin plates, with a central rectangular or circular hole subjected to transverse pressure loading. The approximate solution considers both plastic hinge formation and extensional effects.

7.2 Previous work

Analytical studies have demonstrated the applicability of elastic-plastic and rigid plastic analytical methods for determining inelastic response of plated structures under blast loading[62][110]. It is important to consider when one is more appropriate than the other and when more sophisticated numerical systems should be used[138]. The use of approximate design methods also serves to provide a useful physical insight into the underlying mechanics of the problem.

7.2.1 Energy solution

In an energy solution different shape functions are used to represent the different phases of the response of the plate. Hence, the total deformation is then the combined deformation of the various stages. The simple shape functions must satisfy the kinematic and static boundary conditions on all four plate edges.

Hsu[68] and Schleyer and Hsu[62] identified that the non-linear elastic analysis of clamped and simply supported plates can be combined as two stages in the overall response to produce the elastic-plastic analysis of clamped plates for finite deflections. That is, in stage I the clamped mode shape is adopted followed by simply supported plate mode shape in the second phase, which represents the plastic hinge formation around the boundary. This is shown in Figure 7.1.

(a) Stage I

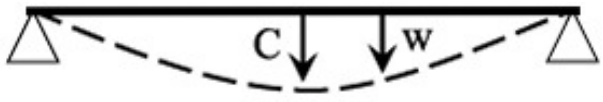

(b) Stage II

Figure 7.1: Velocity profiles at differnet stages of response for a clamped plate.

In light of the large central permanent deformation ($w/h > 5$) observed in the experimental work, Hsu[68] and Schleyer and Hsu[62] proposed it was acceptable to neglect the first stage for simplification purposes. Therefore any transient behaviour caused by travelling hinges is ignored. Consequently, for thin square plates an

appropriate deformed shape of the plate under a uniform pressure load is given as

$$w = Ccos\frac{\pi x}{2L}cos\frac{\pi y}{2L} \tag{7.1}$$

where L is the half span of the plate, w is the transverse displacement at any point, C is the transverse displacement at the centre of the plate, x and y are the plate co-ordinates with their origin at the centre of the plate.

Using this mode shape a quasi-static energy solution for a square plate, is derived below for use in estimating the maximum and residual displacements of thin plates[139]. Since the deformations in the tests plates were so large, it was felt that bending strain energy could be neglected.

For either bending or extension, the strain energy per unit volume is given by

$$\frac{SE}{Vol} = \int_{vol}\left[\sigma_{xx}d\varepsilon_{xx} + 2\sigma_{xy}d\varepsilon_{xy} + \sigma_{yy}d\varepsilon_{yy}\right] \tag{7.2}$$

The subscripts xx and yy represent the normal stresses and strains and the subscripts xy represents the shearing stresses and strains. For an elastic plate the general solution becomes

$$\frac{SE}{Vol} = \frac{E}{2}{\varepsilon_{xx}}^2 + \frac{E}{2(1+\upsilon)}{\varepsilon_{xy}}^2 + \frac{E}{2}{\varepsilon_{yy}}^2 \tag{7.3}$$

For a rigid, perfectly plastic plate that obeys the von Mises maximum shear strain energy per unit volume yield criterion, when the normal biaxial stresses equal σ_0, the shearing stress is zero. Therefore, for a square plate the rigid plastic solution gives

$$\frac{SE}{Vol} = 2\sigma_0\varepsilon_{xx} \tag{7.4}$$

according to the von Mises yield criterion, and when assuming that $\varepsilon_{xx} = \varepsilon_{yy}$ for a square plate loaded uniformly over the entire area. The strain ε_{xx} associated with membrane behaviour is

$$\varepsilon_{xx} = \frac{1}{2}\left(\frac{\partial w}{\partial x}\right)^2 \tag{7.5}$$

The external work done by the load is given by

$$W_k = \int\int pwdxdy, \tag{7.6}$$

where p is the uniformly distributed pressure load and w is the transverse displacement defined by Equation 7.1.

Equating the extensional strain energy to the external work in the elastic analysis gives the quasi-static solution

$$W = \sqrt[3]{\frac{512pL^4}{\left[\frac{9}{32}+\frac{1}{16(1+\upsilon)}\right]EH\pi^6}} \tag{7.7}$$

where H is the plate thickness. Equating the extensional strain energy to the external work in a plastic analysis gives the quasi-static solution

$$W_k = \frac{64pL^2}{\sigma_0 H\pi^4} \tag{7.8}$$

without strain rate effects included, and

$$W_k = \frac{64pL^2}{\sigma_0{}' H\pi^4} \tag{7.9}$$

with strain rate included.

Since the external work done as defined by Equation 7.6 is used in both the elastic and plastic calculations, the total external work done by the pressure loading amounts to the sum of the two parts, the elastic work done and the plastic work by the pressure loading. Further details of this process are given in reference 139. This method, though simple has provided remarkably good correlation with experimental findings and will form the basis of the new approximate model.

7.3 Proposed energy solution

In this section, an energy solution to the problem of large deformations in thin, clamped square plates with a central rectangular or circular hole subjected to transverse pressure loading is presented. The approach is an extension of a previous analysis for thin, clamped square plates with no hole [110], described in the previous section.

The main objective of the proposed approximate technique is to estimate the maximum transient displacement and final (permanent) displacement of a plate with and without openings subjected to uniformly distributed dynamic loading. These two parameters are therefore the key output parameters of the analytical model.

Various assumptions were made in the analytical solution and are described below:

- The material behaves isotropically.
- The material is assumed to be elastic, perfectly plastic.
- No initial imperfections, continuous plate thickness.
- Homogeneous pressure loading across plate.
- It is assumed that the peak amplitude of the plate occurs around the same time as the peak magnitude of the loading (i.e. quasi-static).
- An average value of strain rate was used based on an estimate of the global strain rate in the tests.

The numerical study has demonstrated that using an assumed average, uniform loading across the plates provided excellent predictions of the permanent deformation shape. Thus, it can be concluded that this assumption will have minimum bearing on the results for the analytical approach.

As in the previous analysis, membrane actions governs the behaviour of the plate for displacements greater than the plate thickness. Flexural resistance is considered negligible in this problem. Consequently, for thin plates an appropriate deformed shape of the plate under a uniform pressure load is given as

$$w = Ccos\frac{\pi x}{2X}cos\frac{\pi y}{2Y} \tag{7.10}$$

where $2X$ and $2Y$ are the dimensions of the plate, w is the transverse displacement at any point, C is the transverse displacement at the centre of the plate, x and y are the plate coordinates with their origin at the centre of the plate as shown in Figure 7.2(a) for a rectangular hole of dimensions 2a and 2b, and Figure 7.2(b) for a rectangular hole with circular ends of dimension 2a and 2b where a is the radius of the circular end and 2(b-a) is the distance between centres of the circular ends. For a clamped plate, yield lines will form around the clamped edges but their contribution to the overall resistance of the plate in the large deformation range is small and therefore the deformed shape adopted here is justified [68].

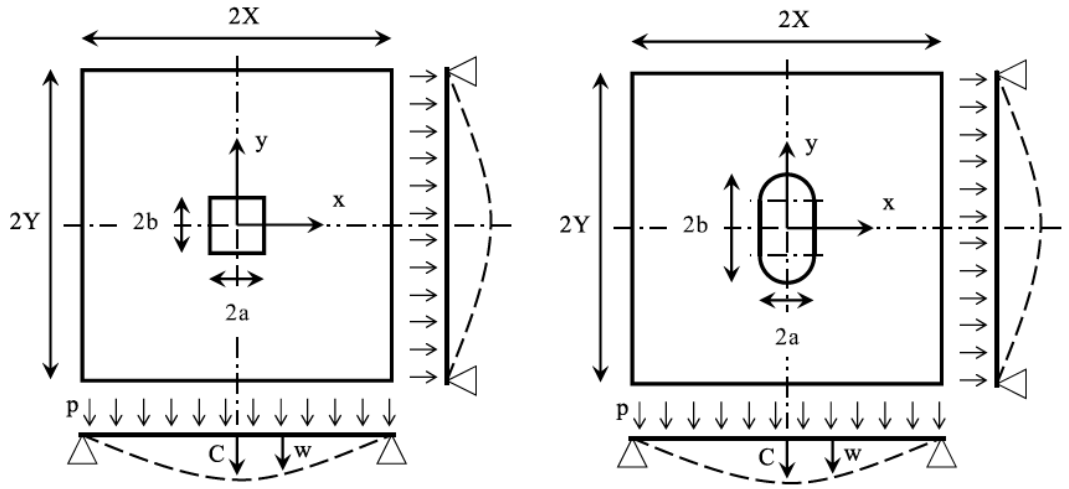

(a) (b)

Figure 7.2: Plate-with-hole geometry and large-deformation mode shape for (a) rectangular hole and (b) rectangular hole with circular ends.

The shape function is differentiated to obtain strains and substituted into the appropriate relationship for strain energy per unit volume. Integrating the strain energy per unit volume over the volume of the structural element gives the total strain energy.

7.3.1 Energy formulation for a restrained rectangular plate with central rectangular hole

The extensional elastic normal strain energy in the plate ($\frac{1}{4}$ geometry) with a central rectangular hole is given by

$$\begin{aligned}
&\frac{Eh\pi^4 Y}{512(1-\upsilon^2)X^3}\left[\frac{9}{16}\left(1-\frac{b}{Y}\right)-\frac{3}{4\pi}sin\frac{\pi b}{Y}-\frac{3}{32\pi}sin\frac{2\pi b}{Y}\right]C^4+\\
&\frac{Eh\pi^4 X}{512(1-\upsilon^2)Y^3}\left[\frac{9}{16}\left(1-\frac{a}{X}\right)-\frac{3}{4\pi}sin\frac{\pi a}{X}-\frac{3}{32\pi}sin\frac{2\pi a}{X}\right]C^4+\\
&\frac{Eh\pi^4}{512(1-\upsilon^2)XY}\left[\frac{1}{16}\left(1-\frac{b}{Y}\right)+\frac{1}{32\pi}sin\frac{2\pi b}{Y}\right]C^4+\\
&\frac{Eh\pi^4}{512(1-\upsilon^2)XY}\left[\frac{1}{16}\left(1-\frac{a}{X}\right)+\frac{1}{32\pi}sin\frac{2\pi a}{X}\right]C^4
\end{aligned} \tag{7.11}$$

where E is the elastic modulus, υ is Poisson's ratio, h is the plate thickness and $2a$ and $2b$ are the dimensions of the central rectangular hole. The extensional elastic shear strain energy in the square plate ($\frac{1}{4}$ geometry) with a central rectangular hole is given by

$$\begin{aligned}&\frac{Eh\pi^4}{512(1+\upsilon)XY}\left[\frac{1}{8}\left(1-\frac{b}{Y}\right)+\frac{1}{16\pi}sin\frac{2\pi b}{Y}\right]C^4+\\&\frac{Eh\pi^4}{512(1+\upsilon)XY}\left[\frac{1}{8}\left(1-\frac{a}{X}\right)+\frac{1}{16\pi}sin\frac{2\pi a}{X}\right]C^4+\end{aligned} \tag{7.12}$$

A quasi-static solution is obtained by equating the total strain energy, Equations 7.11 and 7.12 to the work done ($\frac{1}{4}$ geometry), W_k, by the pressure load p, given by

$$W_k = \frac{4pXY}{\pi^2}\left(1-sin\frac{\pi a}{2X}cos\frac{\pi b}{2Y}\right)C \tag{7.13}$$

If an impulsive solution is sought, then the total strain energy, Equations 7.11 and 7.12, is equated to the kinetic energy ($\frac{1}{4}$ geometry), E_k, given by

$$E_k = \frac{\rho h}{8}\left(XY-\left(a+\frac{X}{\pi}sin\frac{\pi a}{X}\right)\left(b+\frac{Y}{\pi}sin\frac{\pi b}{Y}\right)\right)\dot{C_0}^2 \tag{7.14}$$

where ρ is density and $\dot{C_0}^2$ is the initial velocity imparted to the plate by an impulsive load.

The above analysis holds for the elastic extensional deformation and may be used to predict maximum displacements. A variation of the previous procedure [110] is adopted here for dealing with deformation beyond an elastic limit and estimating permanent displacements. First, small displacement (flexural), yield-line theory is used to predict a limit load for a rigid-plastic plate with a deformed shape as shown in Figure 7.3 and rectangular holes with or without circular ends. The material is assumed to be rigid-plastic as the plate deforms elastically in membrane mode. This deformed shape (Figure 7.3) is applicable to rigid-plastic behaviour which includes diagonal hinges, as shown in the experimental series of this study (Figures 5.15 and 5.24). The approach assumes perfectly plane surfaces with hinges at the yield lines, however all component tests (Chapter 5) had continuous curved surfaces. This is a modelling simplification to enable the prediction of the permanent deformation and considering the other simplifications/idealisations (loading, dynamic material effects and support conditions) this approach was deemed justified.

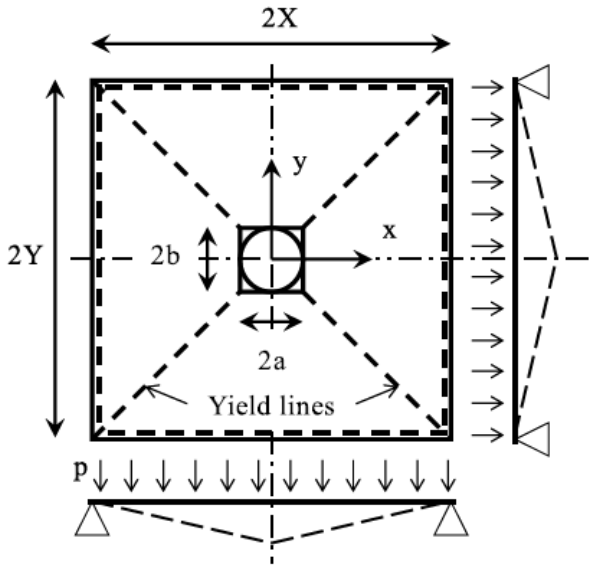

Figure 7.3: Mode shape of rigid-plastic plate with yield lines adopted for plate geometry having rectangular holes with or without circular ends.

For a clamped rigid-plastic plate with central rectangular hole of dimensions 2a by 2b, the elastic limit load, p_0, associated with the formulation of yield lines along the edges and diagonal yield lines as shown in Figure 7.3 is given by

$$p_0 = \frac{3\sigma_0' h^2}{2}\left(\frac{(2X-a)}{(Y-b)} + \frac{(2Y-b)}{(X-a)}\right) \Bigg/ \left(\frac{(X^3-a^3)}{(X-a)} + \frac{(Y^3-b^3)}{(Y-b)} - 6ab\right) \tag{7.15}$$

where σ_0' is the dynamic flow stress. The limit load, which is based on the energy dissipated in the yield lines, is then used in the large-displacement analysis to predict an elastic limit displacement, w_0. Deformation beyond this displacement is considered permanent even when the membrane strain in the plate is elastic.

Due to the progressive development of plastic membrane strain in the plate, only an approximation is suggested here to account for deformation beyond an elastic limit in the membrane mode. This approach is not rigorously correct but is used to obtain acceptable engineering solutions to a complex problem[120]. First yield in the membrane mode is estimated from considering the stretching of an axially loaded structural member made from elastic-plastic material. The transverse displacement at first yield (extensional mode) is given by

$$w_1 = \frac{4X}{\pi}\sqrt{\frac{\sigma_0'}{E}} \qquad (X \geq Y) \tag{7.16}$$

After first yield in the extensional mode, a weighted average displacement ($K_{el}W_{el} + K_{pl}W_{pl}$) is computed based on the combination of the large-displacement elastic analysis and a rigid-plastic analysis of the plate ($K_{el} + K_{pl} = 1$). The von Mises yield theory is adopted for the rigid-plastic analysis in which bi-axial normal stress equals a constant σ_0' and the shear stress is zero. Substituting into the relationship for strain energy per unit volume and integrating over the volume of the structural element for a rigid-plastic solution gives the extensional plastic normal strain energy in the square plate ($\frac{1}{4}$ geometry) with a central square hole as

$$\begin{aligned} &\frac{\sigma_0' hY\pi^2}{32X}\left[(1-\frac{b}{Y}) - \frac{1}{\pi}sin\frac{\pi b}{Y}\right]C^2 + \\ &\frac{\sigma_0' hX\pi^2}{32Y}\left[(1-\frac{a}{X}) - \frac{1}{\pi}sin\frac{\pi a}{X}\right]C^2 \end{aligned} \tag{7.17}$$

The relative weighting of each analysis will depend on the load and strain level. It is suggested that when the strain level is above about 0.2% then K_{el} will be less than 1. Some comparisons with experimental data are given later and show that adoption K_{el} = 0.8 when the membrane strain is around 1% or above gives acceptable results.

7.3.2 Energy formulation for a non-restrained rectangular plate with central rectangular hole

A similar approach is adopted here as for the restrained plates. In this methodology the extensional elastic normal strain energy in the plate (Equation 7.11) is ignored. Only the extensional elastic shear strain energy (Equation 7.12) is incorporated to estimate the elastic extensional deformation. This is used to predict the maximum displacement for a non-restrained plate, which is conservative as additional membrane stretching will occur. It was observed that permanent in-plane edge displacement occurred during pulse pressure loading. This in-plane displacement was largest at the mid-point of the edge and decreases toward the corners of the plate. It was concluded that this induced the lateral buckling that was observed around the edges of the plate, as shown in Figure 5.28. Since the edge of the plate was restrained laterally, the plate could only buckle

as far as the gap between the clamping frame and the plate would allow. At this point some in-plane axial resistance would cause membrane stretching.

A quasi-static solution is obtained by equating the total strain energy, Equation 7.12, to the work done ($\frac{1}{4}$ geometry), W_k by the pressure load p given by equation 7.13. If an impulsive solution is sought, the the total strain energy, Equation 7.12 is equated to the kinetic energy ($\frac{1}{4}$ geometry), E_k , given by equation 7.14.

As in the approximate method for the restrained plates small-displacement (flexural), yield line theory is used to predict the limit load for a rigid-plastic plate with a deformed shape as shown in Figure 7.3. The elastic limit load, p_0 is calculated using Equation 7.15. Again only an approximation is suggested here to account for deformation beyond an elastic limit. First yield is estimated in membrane (shear) mode for a structural member made of elastic-plastic material, given by

$$w_1 = \frac{4X}{\pi}\sqrt{\frac{2\sigma_0'}{E}} \qquad (X \geq Y) \tag{7.18}$$

After first yield in the shear mode, a weighted average displacement ($K_{el}W_{el} + K_{pl}W_{pl}$) similar to the restrained plate approach is computed based on the combination of the large-displacement elastic analysis and a rigid-plastic analysis of the plate ($K_{el} + K_{pl} = 1$).

Substituting into the relationship for strain energy per unit volume and integrating over the volume of the structural element for a rigid-plastic solution gives the extensional plastic shear strain energy in the square plate ($\frac{1}{4}$ geometry) with a central square hole as

$$\begin{aligned} &\frac{\sigma_0' h}{8\sqrt{3}}\left[(1+cos\frac{\pi b}{Y})\right]C^2 + \\ &\frac{\sigma_0' h}{8\sqrt{3}}\left[(1+cos\frac{\pi a}{X})\right]C^2 \end{aligned} \tag{7.19}$$

The relative weighting of each analysis was based solely on the empirical data to provide approximate results, making this approach less rigorous than for the restrained plates. However this can be used to bound the problem and with due care, this could be used as a preliminary screening tool, within the confines of the experimental data range.

7.3.3 Energy formulation for a rectangular plate with central rectangular hole with circular ends

It is suggested that the energy formulation for a plate with a central rectangular hole can be adopted for the case with a rectangular hole with circular ends as shown in Figure 7.3 with minimal error of the order of 1%. The strain energy formulation would be the same but the work done for the plate having a rectangular hole with circular ends would be marginally higher than for a rectangular hole having the same overall dimensions due to the difference in area. Consequently the overall area upon which the pressure load acts would be marginally increased and produce a fractional increase in displacement. Since the area of the hole compared to the overall area of the plate is small ($<$5%), the overall error is small. The effect of the shape of the hole on the stress concentrations particularly at discontinuities is of more significance than the effect of the area on the global displacements[140].

7.3.4 Comparison with experimental data from literature

Static and dynamic loading of plates with no hole

The result of a static test on a clamped 0.5 m square plate [116] of nominal thickness 1 mm is compared with the proposed energy solution. The average yield stress of 176 MPa was determined from static tensile tests. For a static load of 366 kPa, the maximum and final displacements are given as 32.7 and 30.2 mm, respectively. Using an elastic weighted factor of K_{el} of 0.8 (K_{pl} = 0.2), the energy solution gives a maximum and final displacement of 34.9 and 28.7 mm respectively and corresponds to a maximum strain of 1.2% (extensional mode)

The maximum and final displacements for a clamped 0.5 m square plate of nominal thickness 1 mm subjected to a triangular pulse load of peak pressure 101 kPa and load duration 40 ms is given as 14.7 and 9.7 mm, respectively[116]. This compares with 14.1 and 7.5 mm by the energy solution with $\sigma_0^{'}$ = 215 MPa (approximated) and K_{el} = 1.0, corresponding to a maximum strain of 0.2% (extensional mode).

Dynamic loading of square plate with square hole

The explosion resistance of a square plate with a square hole was studied[85]. A dynamic pressure load imparted to a square plate measuring 1.1 m by 1.1 m with a 0.44 m by 0.44 m central square hole. The plate thickness was 1.63 mm and the flow stress was given as 190 MPa. Some plates had reinforcement around the edges of the square hole. Reinforcement around the edge of the hole will strengthen the plate at this point by will not significantly reduce the global deformation of the plate. Unfortunately, the paper gives no comparison in terms of global displacements between the two types of plate. At a pressure of 0.5 bar, the plate displacement at the corner point of the square hole was around 25 mm and at the middle of the edge of the hole was just above 30 mm. No details are given of the load history. The quasi-static energy solution for this case (K_{el} = 1.0) gives a maximum displacement at the corner of the hole of 24.4 mm and at the middle point of the hole of 30.2 mm.

At 1.14 bar, the corner displacement in the test is given as around 50 mm. This compares with 47 mm for the quasi-static solution (K_{el} = 0.8). The ultimate loading pressure before rupture of the plate without reinforced hole edges was given as 0.67 $\sim$ 1.14 bar and with reinforcing as 1.19 $\sim$ 1.42 bar indicating considerable variability in the test conditions. Without further details of the experiments, it is difficult to draw conclusions as to the effect of arching around the hole, boundary conditions and load dynamics of the above results.

7.3.5 Comparison with experimental data from present study

Simplification of the pressure pulse load

As mentioned earlier in this chapter the characteristics of loading are often idealised for simplification in analytical approaches. Idealised pressure-time profiles were produced for each experiment conducted in Chapter 5 of this present study following the method described in Chapter 4 and graphically shown in Figure 7.4.

For this quasi-static energy solution it is assumed that the peak amplitude of the plate displacement occurred around the same time as the peak magnitude of the loading. Therefore the maximum peak pressure from the idealised pressure-time curve for each test was applied to the corresponding analytical model in this chapter.

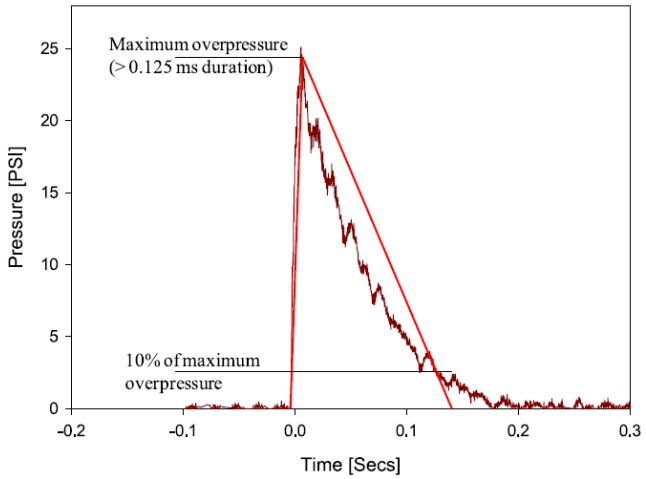

Figure 7.4: Pressure-time history for plate with opening showing construction of idealised triangular pulse load.

Material properties

A comprehensive materials testing programme was performed to characterise the material properties of the Docol form 01 (DC01) mild steel test specimens at strain rates ranging from 3.3x10^{-4} s^{-1} (quasi static) to 534 s^{-1}. The tensile tests showed that DC01 mild steel was highly ductile, tending to yield gradually and exhibited moderate strain rate sensitivity. Further details are available in Chapter 3. To represent this behaviour in a manner suitable for a simplified approximate solution the Cowper-Symonds constitutive relation was used.

Constitutive relation

The Cowper-Symonds[141] constitutive equation is widely used to simulate strain rate effects in materials. The relation is simply empirical, however the formula has been proven to be very powerful when used in approximate models.

$$\dot{\varepsilon} = D\left(\frac{\sigma_0{}'}{\sigma_0} - 1\right)^q, \qquad \sigma_0' \leq \sigma_0 \tag{7.20}$$

where σ_0' is the dynamic flow stress at a uniaxial plastic strain rate $\dot{\varepsilon}$, σ_0 is the associated static flow stress and D and q are constants for a particular material. Equation 7.20 may be written as

$$log_e\dot{\varepsilon} = qlog_e\left(\frac{\sigma_0{}'}{\sigma_0} - 1\right) + log_e D \tag{7.21}$$

which is the equation of a straight line with $log_e(\frac{\sigma_0^{'}}{\sigma_0} - 1)$ plotted against $log_e\dot{\varepsilon}$. The parameter q is the slope of the line, while the intercept on the ordinate is $log_e D$

Using the data obtained in the material testing programme in Chapter 3 the Cowper-Symonds coefficients were determined to be $D = 298\ s^{-1}$ and $q = 4.89$. All the parameters used for the analytical approximations are present in Table 7.1.

Table 7.1: Material parameters for simplified analytical approach.

Elastic constants and density	Yield stress	Cowper-Symonds relations	Dynamic flow stress
E = 205 $[GPa]$ υ = 0.33 $[MPa]$ ρ = 7850 $[kg/m^3]$	205 $[GPa]$	D = 298 $[s^{-1}]$ $q = 4.89$	268.6 $[MPa]$

Estimation of strain rate effects

The assumed mode shape of the plate in Equation 7.10 was used to estimate the strain rate encountered in the pulse pressure experiments. The average rise time recorded in the experiments at the two nominal pressure and boundary conditions were approximately 0.006 and 0.012 seconds, respectively. As mentioned earlier in this chapter it is assumed that the peak amplitude of the plate displacement occurred around the same time as the peak loading (i.e. quasi-static response). From Equation 7.5 the strain associated with stretching of the plate (i.e. membrane mode) can be approximated. The energy method gives a maximum strain of $C^2\pi^2/(16L^2)$ where C is the peak displacement at the centre of the plate and L is the $\frac{1}{2}$ span of the plate. This gives strain rates of the order of 1 s^{-1} for the rates of loading encountered in the experiments. The maximum strain by the energy method is estimated to be of the order of 0.01.

Equation 7.20 may be presented in the form $\sigma_0^{'}/\sigma_0 = 1 + (\dot{\varepsilon}/D)^{1/q}$ and using the experimentally determined coefficients gives a ratio of the dynamic flow stress to static flow stress of 1.31. Using the average static 0.2% engineering proof stress of 205 MPa determined from the material tests in the above Cowper-Symonds relationship gives a dynamic flow stress of 268.6 MPa. This value will be used in the theoretical approach to compare the energy model predictions with the experimental data.

Temperature softening

With the expected strains and strain rates in the experiments, adiabatic heating of the material due to plastic dissipation is not expected to have any significant influence on the material behaviour. Therefore the influence of thermal softening on the material has not been investigated in this study.

7.3.6 Results and Discussion

Restrained plates

The energy method described earlier was used to predict maximum and permanent plate deflections and was compared with the permanent mid point deflections of the experimental plates. The quasi-static formulation gave more than adequate correlation when the dynamic flow stress of 268.6 MPa is used to account for the strain rate material effects. An elastic weighted factor K_{el} = 0.8 (K_{pl} = 0.2) was used given the large permanent deformations (and plastic strain) in the test plate. This is consistent with the analysis of other static and dynamic plate test data, see Section 7.3.4 for details. The analytical results from the simplified model of the experimental work conducted on restrained plates from Chapter 5 (see Tables 5.3 and 5.4) are shown in Tables 7.2 and 7.3. Direct comparison between the analytical model predictions and permanent deflections of the experimental work are also shown in Figure 7.5.

Table 7.2: Simplified analytical model of 0.5 m x 0.5 m restrained plates loaded nominally to 25 psi.

Analytical	Hole geometry [mm]	Maximum deflection [mm]	Permanent deflection [mm]
1	Full plate	19.5	12.2
2	50	21.3	13.5
3	50x75	21.3	13.5
4	75	21.8	13.9
5	75x100	22.1	14.0
6	100	22.2	14.1
7	100x125	22.3	14.1

Table 7.3: Simplified analytical model of 0.5 m x 0.5 m restrained plates loaded nominally to 50 psi.

Analytical	Hole geometry [mm]	Maximum deflection [mm]	Permanent deflection [mm]
8	Full plate	27.6	20.4
9	50	29.8	22.2
10	50x75	30.9	23.0
11	75	30.8	23.0
12	75x100	31.4	23.4
13	100	31.2	23.1
14	100x125	31.5	23.3

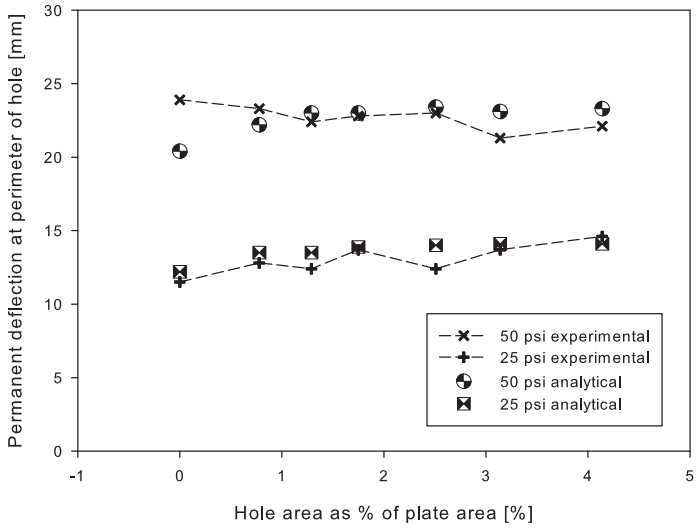

Figure 7.5: Comparison between analytical and experimental permanent deflection of restrained plates.

Validation against experimental work

The empirical data from Chapter 5 has been used to validate the energy based models for restrained plates. It can be seen from Figure 7.5 that an energy approach that considers large inelastic deformation and membrane effects gave more than acceptable results when compared with the maximum global response test data. The analytical model generally over-predicts the permanent deflection of the restrained plates, providing a conservative approximation. However for the plate with an opening at 50 psi (Figure 7.5) the solution under predicts the response. Originally the analytical model was validated against plates with holes[120]. Central openings remove part the

plate, which develops stretching of the middle surface (through tensile and compressive stresses). Removing this material creates a free edge, which is less stiff than a continuous plate. This could provide an explanation for this variation in the permanent deflection.

A sensitivity study showed that the predicted response of the test plates was most affected by moderate variations in the peak load pressure. Initial imperfections in the original plate could also cause it to deflect more, leading to a greater variation between experimental result and the idealised analytical approach.

To assess the suitability of the assumed mode shape further, the average values from the experimental permanent displacement profiles were plotted, as illustrated by Figure 5.9, and compared against equivalent cross sections from the simplified analytical method. Figures 7.6-7.9 show this correlation over a range of opening sizes. It is clear that the maximum, permanent global response (i.e. deflection value furthest away from the support for the 'mid-point' and 'diagonal from corners' plots) is well predicted. This demonstrates that the assumed mode shape was justified, and capable of adequately predicting the final global response and deformation pattern.

However it is worth noting that the assumed deformed shape is not capable of capturing the localised effect around the openings or the quarter section profile. A higher number of modes or a mode shape function, such as a higher order polynomial would lead to better representation of the deformation profile shape, but at the same time produce more complex equations. It is felt that improvement in accuracy is unnecessary and would detract from the simplicity and versatility of this design approach. Also, when investigating the transient behaviour of plates, in Chapter 6, it was shown that the deformation shape matched the assumed mode shape up to maximum deformation. It was only as the plate took its final deformed shape that the deformation pattern deviated.

Taking into account all of the simplifications, namely loading, dynamic material effects and support conditions this approach can provide an extremely useful screening tool in preliminary/conceptual design of restrained plates.

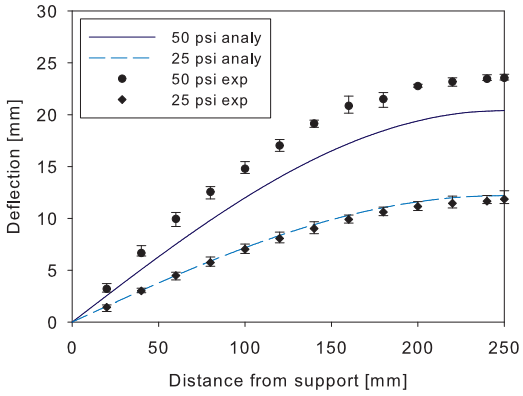

(a)

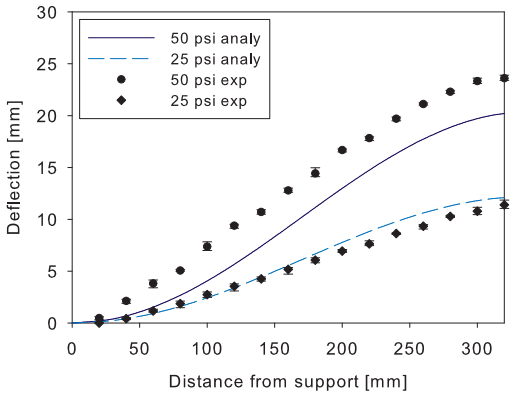

(b)

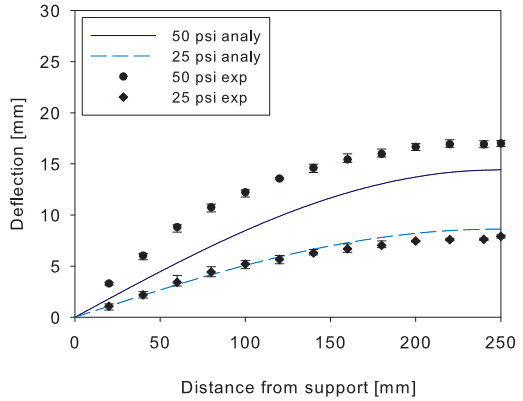

(c)

Figure 7.6: Final permanent deflection of restrained plate without opening taking measurement at (a) mid-point, (b) diagonal from corners and (c) quarter sections. Results from analytical simulations are shown as lines and the experimental data are shown as error bars.

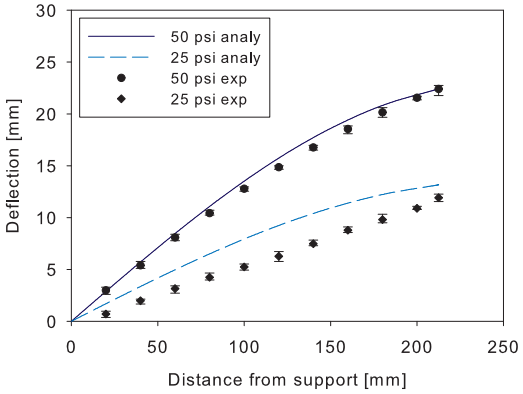

(a)

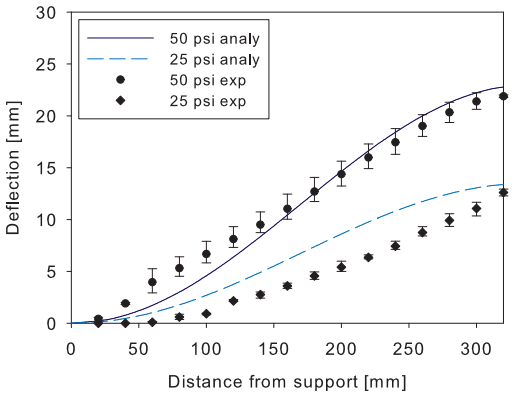

(b)

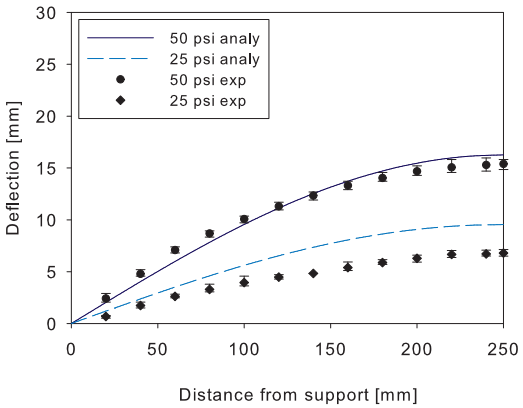

(c)

Figure 7.7: Final permanent deflection of restrained plate with 50 mm by 75 mm opening taking measurement at (a) mid-point, (b) diagonal from corners and (c) quarter sections. Results from analytical simulations are shown as lines and the experimental data are shown as error bars.

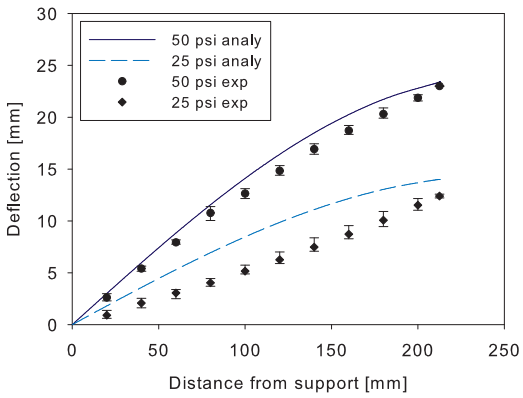

(a)

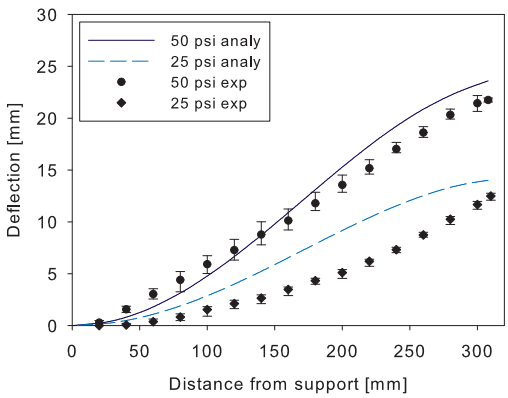

(b)

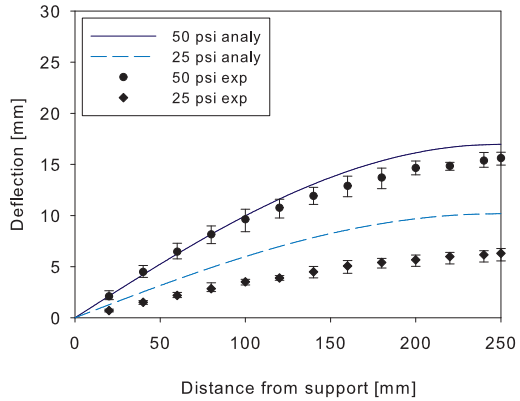

(c)

Figure 7.8: Final permanent deflection of restrained plate with 75 mm by 100 mm opening taking measurement at (a) mid-point, (b) diagonal from corners and (c) quarter sections. Results from analytical simulations are shown as lines and the experimental data are shown as error bars.

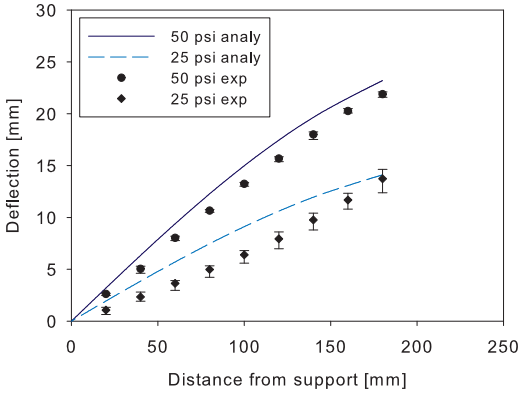

(a)

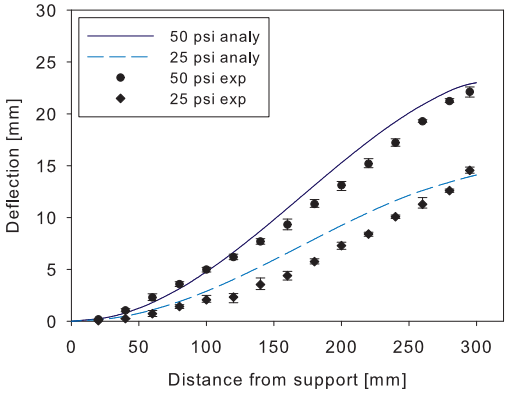

(b)

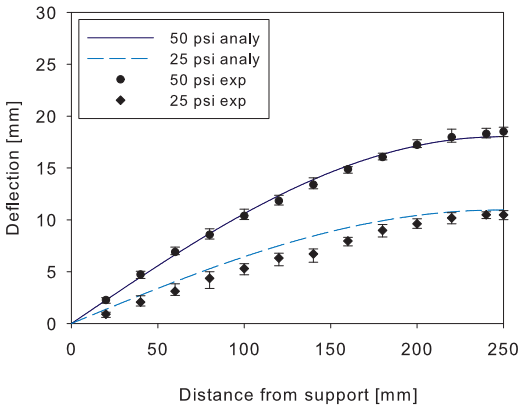

(c)

Figure 7.9: Final permanent deflection of restrained plate with 100 mm by 125 mm opening taking measurement at (a) mid-point, (b) diagonal from corners and (c) quarter sections. Results from analytical simulations are shown as lines and the experimental data are shown as error bars.

Non-restrained plates

The energy formulation proposed for non-restrained plates was used to predict maximum and permanent plate deflection and was compared with the permanent mid point deflections of the experimental plates. The quasi-static formulation gave adequate correlation when the dynamic flow stress of 268.6 MPa is used to account for the strain rate material effects. An elastic weighted factor K_{el} = 0.9 (K_{pl} = 0.1) was chosen, using the empirical results to set the relative weighting. Analytical results from the simplified model of the experimental work conducted on non-restrained plates from Chapter 5 (see Tables 5.5 and 5.6) are shown in Tables 7.4 and 7.5. Direct comparison between the analytical model predictions and permanent deflections of the experimental work are also shown in Figure 7.10. It can be seen from Figure 7.10 that there is not a smooth change in trend with increase in hole area as a percentage of the plate area. The results for circular openings and oval openings in isolation from one another show a clear linear trend. The disparity could be attributed to the shape effects between openings and would require further investigation.

Table 7.4: Simplified analytical model of 0.5 m x 0.5 m non-restrained plates loaded nominally to 25 psi.

Analytical	Hole geometry [mm]	Maximum deflection [mm]	Permanent deflection [mm]
15	Full plate	57.2	40.9
16	50	54.5	38.2
17	50x75	–	–
18	75	53.1	36.8
19	75x100	–	–
20	100	50.8	34.5
21	100x125	–	–

Table 7.5: Simplified analytical model of 0.5 m x 0.5 m non-restrained plates loaded nominally to 50 psi.

Analytical	Hole geometry [mm]	Maximum deflection [mm]	Permanent deflection [mm]
22	Full plate	74.1	57.8
23	50	70.6	54.3
24	50x75	70.4	54.1
25	75	68.4	52.1
26	75x100	67.8	51.5
27	100	64.9	48.6
28	100x125	64.8	48.5

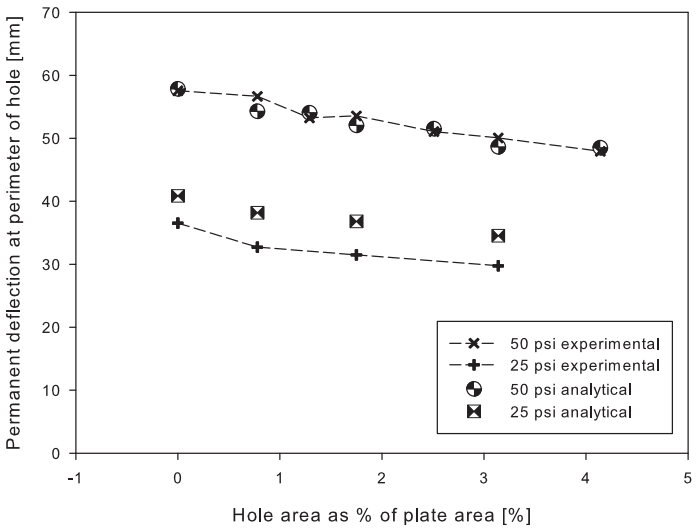

Figure 7.10: Comparison between analytical and experimental permanent deflection of non-restrained plates.

Calibrated against experimental work

The empirical data from Chapter 5 has been used to validate the energy based models for non-restrained plates. Variations in the input parameters had a similar influence on the response of the plate as for the restrained plates. However this problem is more complex than the restrained plates as contact non-linearity (varying boundary conditions) also affect the response. In Chapter 5 it was observed that the non-restrained plates were able to slide freely at the corners and lateral buckling occurred between the support frame and the clamping frame.

The literature review highlighted that the response of a plate can change significantly due to small in-plane displacement at the boundaries. This has been proven by various researchers[74][116] and demonstrated in this study, showing that this parameter has a much higher influence on the response of the plates than slight variations in plate thickness, material properties or loading. In-plane movement should therefore be incorporated into future approximate models in order to more accurately describe the physics of the problem.

However, even with this additional simplification it can still be seen from Figure 7.10 that this approximate energy model gave adequate results of the maximum permanent displacements when compared with the experimental test data.

7.3.7 Parametric study

Now that the simplified analytical solution has been validated against the experimental studies it can be used in the same manner as the FEM to run simulations that were not conducted in the experimental phase of this study. In this case, the analytical method will be used to apply a constant pressure of 25 and 50 psi to each plate design, as considered in Chapter 6. The analytical results for this parametric study are shown in Tables 7.6 and 7.7 for the restrained plates and Tables 7.8 and 7.9 for the non-restrained plates. These results were then compared to the parametric study conducted in the numerical section of this study (Chapter 6) in Figures 7.11 and 7.12.

Table 7.6: Simplified analytical model of 0.5 m x 0.5 m restrained plates loaded at 25 psi.

Analytical	Hole geometry [mm]	Maximum deflection [mm]	Permanent deflection [mm]
29	Full plate	18.5	11.3
30	50	20.4	12.7
31	50x75	20.9	13.1
32	75	21.2	13.3
33	75x100	21.7	13.7
34	100	21.9	13.8
35	100x125	22.4	14.2

Table 7.7: Simplified analytical model of 0.5 m x 0.5 m restrained plates loaded at 50 psi.

Analytical	Hole geometry [mm]	Maximum deflection [mm]	Permanent deflection [mm]
36	Full plate	26.8	19.6
37	50	29.9	22.2
38	50x75	30.8	23.0
39	75	31.3	23.4
40	75x100	32.2	24.2
41	100	32.5	24.4
42	100x125	33.5	20.2

Table 7.8: Simplified analytical model of 0.5 m x 0.5 m non-restrained plates loaded at 25 psi.

Analytical	Hole geometry [mm]	Maximum deflection [mm]	Permanent deflection [mm]
43	Full plate	54.9	38.6
44	50	53.9	37.6
45	50x75	53.9	36.6
46	75	52.9	36.7
47	75x100	52.8	36.5
48	100	51.5	35.2
49	100x125	51.5	35.1

Table 7.9: Simplified analytical model of 0.5 m x 0.5 m non-restrained plates loaded at 50 psi.

Analytical	Hole geometry [mm]	Maximum deflection [mm]	Permanent deflection [mm]
50	Full plate	72.6	56.3
51	50	71.3	55.0
52	50x75	71.2	54.9
53	75	69.9	53.6
54	75x100	68.8	53.5
55	100	68.1	51.8
56	100x125	68.1	51.8

It is seen that the analytical approaches complement the numerical findings from Chapter 6 very well, particularly for the restrained plates, featuring the same trends.

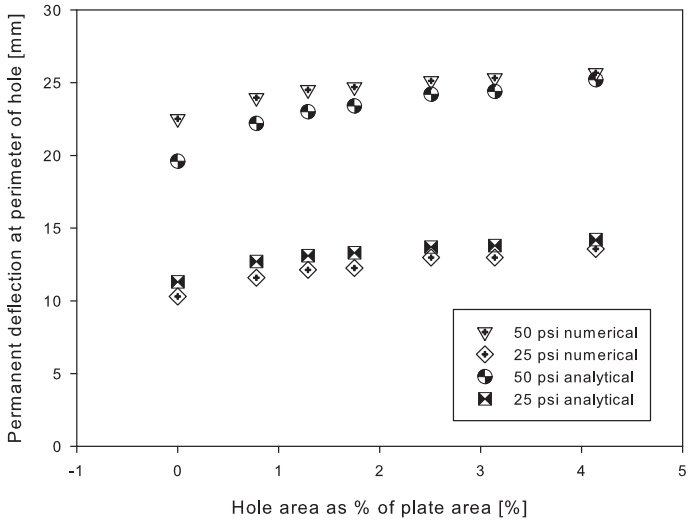

Figure 7.11: Comparison between numerical and analytical permanent deflection of restrained plates using a constant peak pressure for all plate designs.

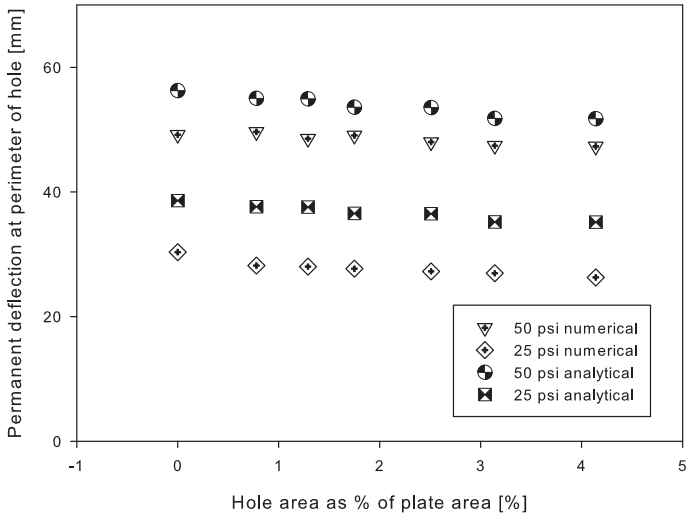

Figure 7.12: Comparison between numerical and analytical permanent deflection of non-restrained plates using a constant peak pressure for all plate designs.

This demonstrates that once the numerical and analytical models have been validated against experimental work, they can be used with due care to run parametric studies. It is suggested that the non-restrained plates may be more sensitive to strain rate than the restrained plates in which the behaviour is predominately membrane and the strains are smaller. Therefore the simplifications made in the analytical approach have a greater influence over the response of the non-restrained plates, explaining the

larger variation between the two approaches in Figure 7.12.

All the analytical studies thus far have considered a quasi-static approach to predict the response of a plated structure subjected to dynamic loading. This has provided more than acceptable results when considering this is a highly non-linear problem.

7.3.8 Limitations to this approximate approach

- The energy approach can only be used to estimate the global deformation. It cannot be used to directly predict local strains around the hole. Stress concentration factors can be applied in combination with the global strain to give more realistic estimates of the maximum strain but this is not presented in this study.

- An average strain rate value was used in this analysis based on an estimate of the global strain rate. Strain rate varies both temporally and spatially throughout the structure during loading.

- Using a quasi-static energy balance does not account for dynamic effects. A further development would be to incorporate dynamics and solve the subsequent non-linear differential equations using numerical methods[118][68].

7.4 Methodology to estimate inertia effects

SDOF methods can be used with due attention to their limitations to estimate the dynamic loading effects on square plates[120]. It is well established that the rise time is of great importance and has a significant influence on the dynamic response of the plate. As discussed in the literature review, Schubak *et al.* [82] highlighted the importance of the rise time in a triangular-shaped pressure pulse, particularly when it is greater than 0.3 times that of the total pulse time. This is demonstrated in a report prepared by ABS Consulting Ltd[9] using a tool they developed called BlastSTAR (see Section 2.7.4). Figure 7.13 highlights the influence that the rise time has on the maximum response of a structure when subjected to a triangular pulse.

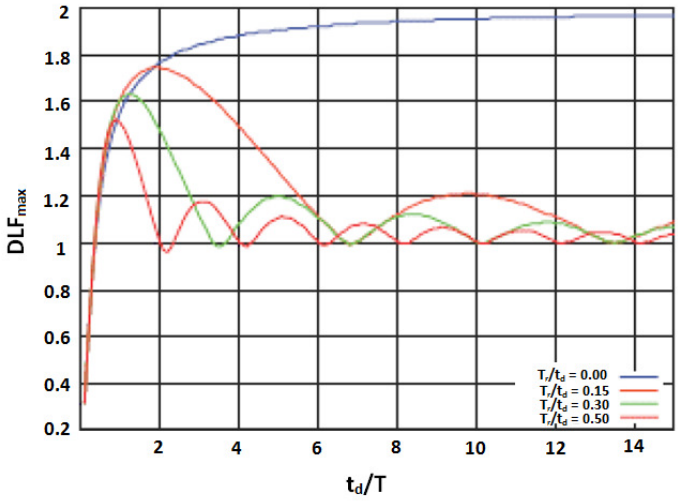

Figure 7.13: Maximum response for SDOF system (undamped) subject to triangular load pulses with different rise times[9].

Restrained plates

The usual bi-linear resistance is appropriate for structural members with flexural resistance but the plate's resistance in stretching mode is a function of C^3 and so highly non-linear. The elastic period of the restrained plate, T in stretching mode was estimated (using the proposed energy solution) to be of the order of 0.005 based on the average stiffness over the maximum plate response. This compares with the fundamental elastic period of the plate in flexural mode of around 0.05 seconds. The load duration in the tests ranged from around 0.2 to 0.8 seconds, while the rise time ranged from 0.05 to 0.13 seconds. Using a peak pressure load of 1 bar and load duration of 0.2 seconds, the effect of varying the rise time was evaluated using a SDOF analysis. The SDOF parameters applied in the analysis were 100 kN/m^2 over an area of 0.25 m^2, total mass of 2.159 kg, stiffness of 1.76 MN/m, and load-mass K_{LM} of 0.67 (Load factor K_L = 0.46, Mass factor K_M = 0.31), where $K_{LM} = K_M/K_L$. The load-mass factor converts the distributed load and mass into an equivalent lumped mass and concentrated load. The non-linear, elastic load-deflection curve is given in Figure 7.14 from which was extracted a linearised function over the range of data. This was subsequently used to obtain the linear stiffness parameter applied in the SDOF analysis.

For a t_r/t_d = 0.5, where t_r is rise time and t_d is load duration, the maximum elastic response was 14.4 mm; 16.0 mm at t_r/t_d = 0.05, and 16.2 mm at t_r/t_d = 0.025. The maximum elastic response jumps to 25.6 mm when t_r/t_d = 0.01. Therefore, it is concluded that dynamics effects are not negligible ($\sim$ 10%) over the range of test conditions.

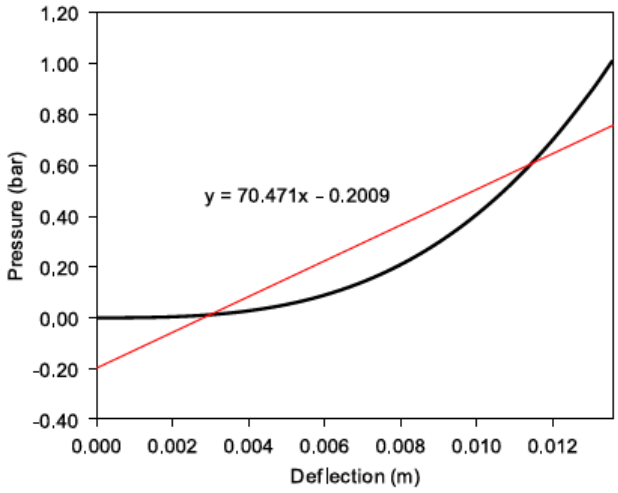

Figure 7.14: Load-deflection curve for quasi-static energy analysis showing linearized function over range of data. This solution included bending energy as well as membrane energy terms for a square plate with no hole. The bending energy contribution over this large deflection range accounts for about 1% of the resistance.

7.5 Accuracy of analytical approach

It is well understood that the structural response is dependant on the relationship between the time duration of the explosion, and the relative fundamental period of the plate. For both series of tests the smallest rise time in the experiments was around 0.005 seconds and the longest was around 0.013 seconds. The restrained plates were stiffer than the non-restrained plates and therefore had a shorter average elastic period of 0.005 seconds, compared to 0.015 seconds for the non-restrained plates. This meant that the ratio of $t_r/T > 0.9$ for the restrained plates and explains why a quasi-static solution gives such good results. The non-restrained plates had a ratio of $t_r/T < 0.9$ contributing to the larger variation between the experimental results and the analytical prediction. When $t_r/T < 0.5$ inertia effects are important and a quasi-static analysis is less accurate.

7.6 Summary

A simplified approach to model large deformation in thin, clamped square plates subjected to transverse pressure loading proposed by Schleyer *et al.* [110] has been extended to incorporate a central opening. The extension of the model allows for rapid assessment of such structures and demonstrates than in most cases, adequate engineering estimates can be achieved, even for complex problems. The model has been successfully calibrated against a range of empirical data presented in Chapter 5 considering a variety of openings, boundary conditions and pressure levels. The analytical approach typically predicted the maximum permanent displacement for the restrained plates within 6.5% and 7% of the experimental plates loaded nominally to 25 and 50 psi respectively. For the non-restrained plates the average difference between the approximate solutions and the experimental data was 10% and 3% for the plates loaded nominally to 25 and 50 psi respectively. It should be stressed that the idealisations presented of restrained and non-restrained boundary conditions are difficult to achieve in reality. Unless a plate support is an integral part of the plate, it is practically impossible to achieve perfect in-plane restraint. Consequently, in-plane edge displacement will need to be assessed in large displacement behaviour of slender plates. Although the presented formulation is unable to predict such in-plane movement, it can still be used to bound a problem, providing a conservative estimate of the resistance of the plate.

Due to the simplified nature of these approximate models and their relatively small expense to implement, in terms of computational time, these methods are highly suited for use in preliminary engineering design studies.

Chapter 8

Conclusions and Recommendations

8.1 Introduction

The ability to predict the behaviour of plates subjected to extreme loading, such as blast loading conditions is essential in order to design safer, lighter and more cost effective structures. Well-defined material, loading and boundary conditions are required in order to obtain accurate predictions from the finite element modelling and analytical approaches. However, in many instances researchers have used idealised parameters, due to limited data available or to simplify a complex problem.

The primary aim of this work was to investigate the material and geometric non-linearities along with spatial variation of pressure loading on plates with and without openings using novel controlled testing equipment in order to gain a better understanding of the effects of openings on the overall performance of thin plated structures, when subjected to dynamic loading. With respect to the secondary aim of the study, different in-plane restraint has been investigated. The effects of frictional resistance due to the boundary conditions have also been investigated using FEM analysis.

8.2 Conclusions

The aims and objectives of this study were achieved using a range of techniques, namely material characterisation, experimental component testing, finite element modelling and analytical modelling. The results of the experimental phase of this study and the subsequent validation and results from the numerical and analytical modelling, coupled with the literature review led to the following conclusions:

Results from material tests at strain rates from 0.00033 s^{-1} to 534 s^{-1} indicated that:

- The DC01 mild steel was highly ductile (quasi-static ductility at failure around 42%), tending to yield gradually and it was clearly rate sensitive, even at low to moderate strain rates, and
- The material behaved isotropically for all practical purposes (yield stress, UTS and ductility between the different directions deviated by approximately 3%)

With regard to the experimental configuration:

- New novel laboratory scale test procedures were developed which could produce controlled, repeatable semi-confined loading conditions onto plated specimens with and without openings using a differential pressure device.
- The Pulse Pressure Loading Rig was not able to apply the exact same loading to each plate, due to the confined configuration of the rig and variation in size of openings in the test plates.
- The spatial variation of the pressure loading was investigated for solid plates with openings, comparing pressure levels near the boundary conditions and 80 mm away from the openings. Little or no variation between the pressures recorded from each position were observed.

Experimental work on component tests showed that:

- All restrained and non-restrained plates with and without openings exhibited mode I type failure (large inelastic deformation) under the applied pressure loadings,

- Yield line mechanisms formed in the tests and the deformed shape of the plate should help to inform accurate modelling of the plates in the future, and

- Slight variations in sensitive loading parameters occurred between each test. This meant that strict conclusions could not be drawn directly from the experimental work alone. However, these tests represent a valuable body of data for numerical benchmarking and for validating different methods of analysis.

Results from the FEM-analyses on the component tests showed that:

- The physical failure mechanisms in the thin plates with openings observed in the experimental tests for both restrained and non-restrained boundary conditions are predicted with good accuracy,

- The FEM-analyses provided a useful insight into the transient response and failure processes of (scaled) plated structures, subjected to blast loading,

- Pulse-pressure loaded plates when clamped without in-plane restraint (non-restrained plates) exhibited strong mesh-dependency,

- The Modified Johnson-Cook (MJC) constitutive model and the Cockcroft-Latham fracture criterion are reliable, simple calibration methods which are capable of predicting the material's behaviour under complex loading conditions,

- The Lagrange FEM-analyses using the approximate pressure-time history curves, described by the side-one pressure difference in the experimental phase compared favourably with the experimental final deformed shape, in general over predicting the final profile by 14%,

- The disparity in predictions was deemed to be caused from the approximate loading conditions recorded in the experimental phase. ALE simulations predicted that the actual average peak pressure on the plates was 10% less, providing an explanation as to why the simulations in general, over predict the final profile,

- An increase in pressure around the proximity of the opening did not have a significant effect on the global response of the plate,

- The rise time and peak pressure were the critical parameters in this study. Removing the variation in rise time, peak pressure and load duration between plates designs, caused by the configuration of the test rig, allowed for clearer conclusions to be drawn from the subsequent results,

- The in-plane restraint was shown to be responsible for reducing the maximum transient deflections in plates with openings by almost 50% and permanent deformations typically by a factor of 2, when compared against clamped plates without in-plane restraint.

- Modest alterations to the geometry of a pressure-loaded structure in the form of a hole ($< 5\%$ of the exposed panel area) does not significantly degrade the structural resistance when the load imparted only causes mode I type deformation,

- The reduction in stiffness due to the hole is compensated by the reduced area to which the load is applied.

Results from the simplified analytical approach on the component tests showed that:

- A simplified analytical modelling approach of plates with openings correlated well against the experimental results, given the highly simplified nature of the approach,

- The Cowper-Symonds (CS) constitutive model was capable of adequately predicting the material's behaviour under complex dynamic loading, for an approximate solution, especially when acknowledging the other simplifications made in the structural support conditions and the characteristics of the loading,

- The correlation between the experimental and analytical final deformed shape for the clamped, with in-plane restraint plates was very good, approximately 6.5% for both pressure levels assessed,

- The simplified nature of the analytical approach was less accurate at predicting the non-restrained plate in its present form, approximately 10%. However incorporating in-plane movement and a more rigorous approach to the development of plasticity would improve the physical description of the problem,

- The analytical models can provide an extremely useful screening tool in the preliminary/conceptual design phase. However final design checks should be done by other means, where fewer assumptions (material, loading and boundary conditions) are made to predict more accurately the response of the structure.

8.3 Limitations

There are a number of limitations associated with the test methods used in the context of this study. These limitations are as follows:

- Two boundary conditions were considered in this study, clamped with in-plane restraint (restrained) and clamped without in-plane restraint (non-restrained). Having a straight and immovable edge, such as in the restrained condition would generally lead to smaller deflections. The non-restrained condition allows large in-plane movements, larger than would be allowable on a real structure. Therefore the boundary conditions adopted in this study enable the response to be bounded, and enable them to be practicably modelled in FEA-analyses and in the simplified analytical approaches.

- The current study is limited to 0.5 m square plates due to the design restraints of Pulse Pressure Loading Rig (PPLR). Previous work by Schleyer *et al.* [111] has applied the laws of geometrically similar scaling, comparing 0.5 m and 1 m square mild steel plates. It is well understood that the phenomenon of material strain rate sensitivity introduces a known size effect. The strict requirement of equality of dynamic flow stresses at all scales is violated. The size effect means that the full-scale models will be softer than their smaller-scale counterparts. The effect is not insignificant and becomes more of a factor at higher strain rates. However, results by Schleyer *et al.* [111] were within acceptable limits given the other uncertainties involved in determining thin plates subjected to dynamic loading. Therefore this should be pursued in further work.

- The loading on the plates during experimental testing was approximated as the pressure difference by the pressure transducers fixed onto rigid sections of the PPLR. This is not a true representation as a deforming structure reduces the pressure load and thus the structural response. However, these errors could be

quantified and potentially corrected to provide a more informed representation of the loading on such plates, based on the results obtained in this study.

8.4 Further work

The work carried out during this study provides important information relating to the behaviour of plates with and without openings subjected to extreme loading. However, there are still opportunities for further advancement in this field. A range of recommendations for future work are provided here based on the knowledge acquired through the literature review, material testing, experimental, numerical and analytical analyses and the corresponding results obtained from this current study.

Based on the present work, a major challenge seems to be collecting detailed experimental data during the component-testing phase. At the moment the transient behaviour of the plate specimens cannot be captured. Whilst 3D Digital Image Correlation (DIC) has been shown to be an effective method to conduct full-field plate deformation measurements during a blast event it would not be possible in practice to use this approach due to the confinement of the test rig. Instead it would be more feasible to use strain gauges to measure transient response. Doing this should therefore be considered in any future work in this field.

For industry to fully benefit from the findings of the research described herein the following is needed to enable advanced design aids for structural engineers to be produced:

- Scaling effects should be investigated by loading geometrically similar scaled 1 m square plates using a larger PPLR device.
- Large-scale or full-scale experiments on steel plated structures, incorporating actual boundary conditions, connections, additional strengthening and any equipment subjected to extreme loading should be conducted to provide a clearer representation of the overall structural response.
- The analytical approach should be extended from a quasi-static energy balance approach to account for dynamic effects. Incorporating in-plane movement would ensure a more accurate description of the mechanics of the problem for the non-restrained plates and account for small axial movements at the boundaries in real support conditions.

References

[1] Wang G.E. Sun H. and Uemori R. Buckling and Ultimate strength of plates with openings. *Ships and Offshore Structures*, 4(1):43–53, 2009.

[2] Corr R.B. Tam V.H.Y. and Snell R.O. Development of the limit state approach for design of offshore platforms. In *Proceedings of Era Conference 'Safety on offshore installations'. 99-00808*, 1997.

[3] Rakvag K.G. Combined blast and fragment loading on plates. Master's thesis, Norwegian University of Science and Technology, 2009.

[4] Vedantam K. Bajajj D. Brar N.S. and Hill S. Johnson-Cook strength models for mild steel and DP 590 steels. *Shock Compression of Condensed Matter*, pages 775–778, 2005.

[5] SCI for the HSE. Structural strengthening of offshore topsides structures as part of explosion risk reduction methods. 2006.

[6] Menkes S.B. and Opat H.J. Broken Beams: Tearing and shear failures in explosively clamped beams. *Experimental Mechanics*, (13):480–486, 1973.

[7] Hitchings D. *A Finite Element Dynamics Primer*. NAFEMS, second edition, 1992.

[8] Zhu L. Transient deformation modes of square plates subjected to explosive loading. *International Journal of Solids and Structures*, 33(3):301–314, 1996.

[9] ABS Consulting Ltd for Health and Safety Laboratory. Design, materials and connections for blast-loaded structures. 2006.

[10] G.E. Dieter. *Mechanical Metallurgy*. McGraw Hill, 1988.

[11] Tarigopula V. Hopperstad O.S. Langseth M. Clausen A.H. and Hild F. A study of localisation in dual-phase high-strength steels under dynamic loading using digital image correlation and FE analysis. *International Journal of Solids and Structures*, 45:601–619, 2008.

[12] White M.D. Pulse Pressure Loading Rig operation manual. *Impact Research centre*, University of Liverpool, UK, 1998.

[13] Wikiversity. Nonlinear finite elements/Lagrangian and Eulerian descriptions. http://en.wikiversity.org/wiki/Nonlinear Finite elements Lagrangian Euler descriptions, Accessed July 2013.

[14] Federal Highway Administration; US Department of Transportation. Evaluation of LS-DYNA; Soil Material Model 147. *Computers and Structures*, 2004. Report no. FHWA-HRT-04-094.

[15] Hallset S. and Haagenrud J.S. Combined blast and fragment loading on plates. Master's thesis, Norwegian University of Science and Technology, 2011.

[16] Rakvag K.G. Underwood N.J. Schleyer G.K. Borvik T. Hopperstad O.S. Transient pressure loading of clamped metallic plates with pre-formed holes. *International Journal of Impact Engineering*, 53:44–55, 2013.

[17] Paik J.K and Czujko J. Engineering and Design Disciplines Associated with Management of Hydrocarbon Explosion and Fire Risks in Offshore Oil and Gas Facilities. In *Proceedings of SIMS2012 International Conference*, 15-16 November, Busan, Korea, 2012.

[18] Dey S. *High-strength steel plates subjected to projectile impact*. PhD thesis, Norwegian University of Science and Technology, 2004.

[19] Ngo T. Mendiz P. Gupta A. and Ramsay J. Blast Loading and Blast Effects on Structures - An Overview. *Electronic Journal of Structural Engineering*, pages 76–91, 2007.

[20] Dept. of the Army the NAVY and the Air Force. Structures to Resist the Effects of Accidental Explosions. In *UFC 3-340-02 (Unified Facilities Criteria)*. US Department of Defence, 2008.

[21] American Petroleum Institute. Recommended practice for the design of offshore facilities against fire and blast loading. January 2006.

[22] Cullen Lord. The Public Inquiry into the Piper Alpha Disaster, 1990.

[23] BP. Deepwater Horizon Accident Investigation Report, 2010.

[24] The Steel Construction Institute. Blast and Fire Engineering for Topside Structures Phase 2. *International Journal of Impact Engineering*, 1998. The Steel Construction Institute.

[25] Ali Mohamed R.M. *Performance based design of offshore structures subjected to blast loading*. PhD thesis, Imperial College London, 2007.

[26] Ventsel E. and Krauthammer T. *Thin Plates and Shells: Theory: Analysis, and Applications*. New York Inc., 1st edition, 2001.

[27] Paik J.K. and Thayamballi A.K. *Ultimate Limit State Design of Steel-Plated Structures*. John Wiley and Sons Ltd., 1st edition, 2006.

[28] ASCE. *Design of Blast-Resistant Buildings in Petrochemical Facilities*. ASCE Petrochemical Energy Committee, second edition, 2010.

[29] Vinnem J.E. *Offshore Risk Assessment: Principles, Modelling and Application of QRA Studies*. Kluwer Publishers, second edition, 2007.

[30] Czujko J. *Design of Offshore facilities to Resist Gas Explosion Hazard*. CorrOcean, 1st edition, 2001.

[31] HSE. Hydrocarbon Release System. https://www.hse.gov.uk/hcr3/, Accessed March 2013.

[32] Bakke J.R. Bjerketvedt D. and Wingerden K.V. Gas Explosion Handbook. *Journal of Hazardous Materials*, (52):1–150, 1997.

[33] Kambouchev N. Noels L. and Radovitzy R. Nonlinear Compressibility Effects in Fluid-Structure Interaction and their Implications on the Air-Blast Loading of Structures. *Journal of Applied Physics*, (100):063519, 2006.

[34] Leppanen J. Experiments and numerical analysis of blast and fragment impacts on concrete. *International Journal of Impact Engineering*, (31):843–860, 2005.

[35] Nystrom U. and Gylltoft K. Numerical studies of the combined effects of blast and fragment loading. *International Journal of Impact Engineering*, (31):843–860, 2009.

[36] Mays G.C. and Smith P.D. *Blast Effects on buildings*. Thomas Telford Publications, second edition, 2001.

[37] Pappas J. Conclusions of the Explosion Test programme - Summary Presentation. *FABIG Newsletter*, R322, 1998.

[38] Cormie D. *Blast Effects on Buildings*. Thomas Telford Ltd, second edition, 2009.

[39] Dieter G.E. *Introduction to Ductility*. American Society for Metals, 1968.

[40] Boh J.W. Louca L.A. and Choo Y.S. Finite Element Analysis of Blast Resistant Structures in the Oil and Gas Industry. *ABAQUS Users' Conference*, 2007.

[41] UKOOA and HSE. Fire and Explosion Guidance Part 1:Avoidance and mitigation of explosions, Issue 1. October 2003.

[42] Son J. Astaneh A. and M. ASCE. Blast Resistance of Steel Orthotropic Bridge Decks. *Journal of Bridge Engineering*, pages 589–598, 2012.

[43] Paik J.K. and Thayamballi A.K. *Ship-shaped offshore installations: Design, Building and Operation*. Cambridge University press, 1st edition, 2007.

[44] FABIG Technical Note 4. Blast Restraint Design. *The Fire and Blast Group*, 1994.

[45] FABIG Technical Note 5. The design of Stainless Steel Blast Walls. *The Fire and Blast Group*, 1999.

[46] Nurick G.N. and Martin J.B. Deformation of thin plates subjected to impulsive loading - A review Part II: Experimental Studies. *International Journal of Impact Engineering*, 8(2):159–170, 1989.

[47] Jones N. *Structural Impact*. Cambridge University Press, 1st edition, 1989.

[48] Teeling-Smith R.G. and Nurick G.N. The deformation and tearing of circular plates subjected to impulsive loads. *International Journal of Impact Engineering*, 11(1):77–92, 1991.

[49] Nurick G.N. and Shave G.C. The deformation and tearing of thin square plates subjected to impulsive loads - an experimental study. *International Journal of Impact Engineering*, (18):99–116, 1996.

[50] Timoshenko S. and Woinowsky-Krieger S. *Theory of Plates and Shells*. McGraw-Hill Company Inc., second edition, 1959.

[51] Biggs J.M. *Introduction to Structural Dynamics*. McGraw-Hill, 1964.

[52] FABIG Technical Note 10. Advanced SDOF Model for Steel Members Subject to Explosion Loading: Rate Sensitivity. *The Fire and Blast Group*, 2007.

[53] Kaliszky S. Approximate solutions for impulsively loaded inelastic structures and continua. *International Journal of Non-Linear Mechanics*, (5):143–158, 1970.

[54] Kaliszky S. Large deformations of rigid-viscoplastic structures under impulsive and pressure loading. *Journal of Structural Mechanics*, 1(3):295–317, 1973.

[55] Martin J.B. and Symonds P.S. Mode Approximations for impulsively loaded rigid-plastic beams. *Journal of the Engineering Mechanics Division*, (92):43–66, 1966.

[56] Symonds P.S. and Chon C.T. Approximation techniques for impulsive loading structures of time dependant plastic behaviour with finite deflections. *In Mechanical Properties of Materials at High Strain Rates (Edited by J. Harding)*, pages 299–305, 1974. Institute of Physics.

[57] Chon C.T. and Symonds P.S. Large dynamic plastic deflection of plates by mode method. *Journal of the Engineering Mechanics Division*, pages 169–187, 1977. ASCE.

[58] Symonds P.S. and Chon C.T. Finite viscoplastic deflections of plates by mode method. *Journal of the Mechanics and Physics of Solids*, (27):115–133, 1979.

[59] Schleyer G.K. and Mihsein M. Development of mathematical models for dynamic analysis of structures. *In First International Conference on Structural Design against extreme loads*, pages 3.2.1–3.2.11, 1992.

[60] Louca L.A. and Harding J.E. Non-linear analysis of imperfect plates under transient lateral pressure loading. *Computers and Structures Journal*, 63(1):27–37, 1997.

[61] Louca L.A. and Wadee M.A. Simplified non-linear analysis of plates subjected to hydrogen explosions. *Computers and Structures Journal*, 63(1):27–37, 2002.

[62] Schleyer G.K. and Hsu S.S. A modelling scheme for predicting the response of elastic-plastic structures to pressure pulse loading. *International Journal of Impact Engineering*, (24):759–777, 2000.

[63] Sunshine D. Amini A. and Swanson M. Overview of Simplified Methods and Research for Blast Analysis. In *Proceedings of the Structures Congress Building on the Past: Securing the Future*, 22-26 May, Nashville, TN, 2004.

[64] Cranfield University. ProSAir. http://www.cranfield.ac.uk/csd/amsc/prosair.html, Accessed April 2013.

[65] Nurick G.N.and Martin J.B. Deformation of thin plates subjected to impulsive loading - A review Part I: Theoretical considerations. *International Journal of Impact Engineering*, 8(2):159–170, 1989.

[66] Chung Kim Yuen S. and Nurick G.N. Experimental and numerical studies on the response of quadrangular stiffened plate. Part I: subjected to uniform blast load. *International Journal of Impact Engineering*, (31):55–83, 2005.

[67] Thomas B.M and Nurick G.N. The effect of boundary conditions on thin plates subjected to impulsive loads. *In: Dynamic plasticity and structural behaviours*, pages 85–88, 1995.

[68] Hsu S.S. *Response of Stiffened and Unstiffened Mild Steel Plates to Blast Loading*. PhD thesis, University of Liverpool, 1999.

[69] Nurick G.N. and Conolloy A.G. *Response of clamped single and double stiffened rectangular plates subjected to blast loads*. 1994. Southampton, UK.

[70] Nurick G.N. and Lump D.M. *Deflection and tearing of clamped stiffened circular plates subjected to uniform impulsive loads*. 1996. Southampton, UK.

[71] Chung Kim Yuen S. and Nurick G.N. The significance of the thickness of a plate when subjected to localised blast load. *16th International Symposium on Military Aspects of Blast and Shock*, pages 491–499, September 2000. Oxford, UK.

[72] Olson M.D. Nurick G.N. and Fagan J.R. Deformation and rupture of blast loaded square plates. *International Journal of Impact Engineering*, (13):279–291, 1993.

[73] Rudrapatna N.S. Vaziri R. and Olson M.D. Deformation and failure of blast loaded square plates. *International Journal of Impact Engineering*, (22):449–467, April 1990.

[74] Jones N. Influence of in-plane displacements at rigid-plastic beams and plates. *International Journal of Mechanical Sciences*, 15:547–561, 1973.

[75] Langdon G.S. and Schleyer G.K. Inelastic deformation and failure of profiled stainless steel blast wall panels: experimental investigations. *International Journal of Impact Engineering*, 31:341–369, 2005.

[76] Jones N. Uran T. and Terin S.A. The dynamic plastic behaviour of fully clamped rectangular plates. *International Journal of Solids and Structures*, 6:1499–1512, 1970.

[77] Houlston R. and Slater J.E. A summary of experimental results on square plates and stiffened panels subjected to air-blast loading. *Presented at the 57 Shock and Vibration Symposium*, pages 14–16, 1986. Louisiana, USA.

[78] Gupta A.D. Dynamic nonlinear analysis of a rectangular plate subjected to transient loads. *Proceedings of International Computers in Engineering Conference and Exhibition*, 3:21–27, 1987. New York.

[79] Yu T.X. and Chen F.L. The large deflection dynamic plastic response of rectangular plates. *International Journal of Impact Engineering*, 12(4):603–616, 1992.

[80] Huang J.D. Yun S.R. and Yin M.D. Study of determining deformation of clamped square plate under blast loadings. *Proceedings of International Conference of Non-linear Mechanics (ICNM)*, 1987.

[81] Florek J.R. and Bearoya H. Pulse-pressure loading effects on aviation and general engineering structures - review. *Journal of Sound and Vibration*, 284:421–453, 2005.

[82] Schubak R.B. Anderson D.L. and Olson M.D. Simplified dynamic analysis of rigid-plastic beams. *International Journal of Impact Engineering*, 8(1):27–42, 1989.

[83] Borenstein E. and Benaroya H. Sensitivity analysis of blast loading parameters and their trends as uncertainty increases. *Journal of Sound and Vibration*, 321:762–785, 2009.

[84] Langdon G.S. Rossiter I.B. Balden V.H. and Nurick G.N. Performance of mild steel perforated plates as a blast wave mitigation technique. *International Journal of Impact Engineering*, 37:1021–1036, 2010.

[85] Li G. Chen B.Z. Deng X.F. and Eckhoff R.K. Explosion resistance of a square plate with a square hole. *Journal de Physique IV*, 12:121–124, 2002.

[86] Jain N.K. Analysis of Stress Concentration and Deflection in Isotropic and Orthotropic Rectangular Plates with Central Circular Hole under Transverse Static Loading. *World Academy of Science, Engineering and Technology*, 60:446–452, 2009.

[87] UKOOA and HSE. Fire and Explosion Guidance Part 0:Fire and explosion hazard management, Issue 2. October 2003.

[88] UKOOA and HSE. Fire and Explosion Guidance Part 2:Avoidance and mitigation of fires. February 2006.

[89] Norwegian Oil Industry Association and Federation of Norwegian Manufacturing Industries. Design of steel structures. January 2004.

[90] ISO:19901-3:2010. Petroleum and natural gas industries - Specific requirements for offshore structures- Part 3: Topside structure. *International Organization for Standardization*, 2010.

[91] ISO:13702:1999. Petroleum and natural gas industries - Control and mitigation of fires and explosions on offshore production installations- Requirements and guidelines. *International Organization for Standardization*, 1999.

[92] HSE. OSD hydrocarbon release reduction campaign: Report on the hydrocarbon release incident investigation project 1/4/2000 to 31/3/2001. 2001.

[93] Sovik O.P. Numerical modelling of ductile fracture a damage mechanical approach, 1996. ISBN 82-7119-968-4.

[94] Bridgman P.W. The Stress Distribution at the Neck of a Tension Specimen. *Trans. ASM*, 42:533–572, 1944.

[95] Aronofsky J. Evaluation of stress distribution in Symmetrical neck of flat tensile bar. *Journal of Applied Mechanics*, pages 75–84, March 1951.

[96] Ling Y. Uniaxial True Stress-Strain after necking. *AMP Journal of Technology*, 5:75–84, March 1996.

[97] Zhang Z.L. Hauge M. Odegard J. and Thaulow C. Determining material true stress-strain curve from tensile specimens with rectangular cross-section. *International Journal of Solids and Structures*, 23:3497–3516, 1999.

[98] Scheider I. Brocks W. and Cornec A. Procedure for the determination of true stress-strain curves from tensile tests with rectangular cross-section specimens. *Journal of Engineering Materials and Technology, Transaction of the ASME*, 1:70–76, 2004.

[99] Abed F.H. Constitutive modelling of the mechanical behaviour of high strength ferritic steels for static and dynamic applications. *Mechanics of Time-Dependant Materials*, (14):329–345, 2010.

[100] Manjoine M.J. Influence of rate of strain and temperature on yield stresses of mild steel. *Journal of Applied Mechanics*, (11):211–218, 1944.

[101] Campbell J.D. and Cooper R.H. Yield and flow of low-carbon steel at medium strain rates. *Conference Proceedings on the Physical Basis of Yield and Fracture*, pages 77–87, 1966. Institute of Physics and Physical Society.

[102] FABIG Technical Note 6. Material Properties of offshore steels for fire and explosion resistant deign. *The Fire and Blast Group*, 2001.

[103] Svenskt Stal AB. DOCOL high strength steel. http://www.ssab.com/en/Brands/Docol1, Accessed June 2013.

[104] Clausen A.H. and Auestad T. Split-Hopkinson tension bar: Experimental setup and theoretical considerations (Technical report R-16-02). *SIMLab*, 45, 2002. Norwegian University of Science and Technology, Trondheim.

[105] Tarigopula V. Albertini C. Langseth M. and Clausen A.H. A Hydro-pneumatic machine for intermediate strain-rates: Set-up, tests and numerical simulations. *DYMAT*, pages 381–387, 2009.

[106] Wu Y. Crawford J.E. and Magallanes J.M. Yield and flow of low-carbon steel at medium strain rates. *12th International LS-DYNA Users Conference*, 2012.

[107] Johnson R.G. and Cook W.H. A constitutive model and data for metals subjected to large strains, high strain rates and high temperatures. *International Symposium ballistics*, 7:541–547, 1983.

[108] Cowper G.R. and Symonds P.S. Strain hardening and strain-rate effects in the impact loading of cantilever beams. *Division of Applied Mathematics*, 28, 1957. Brown University, September.

[109] Schleyer G.K. Hsu S.S. and White M.D. Blast loading of stiffened plates: experimental, analytical and numerical investigations. *ASME/JSME Pressure Vessels and Piping Conference*, (31):237–255, 1998.

[110] Schleyer G.K. and Jones N. On simplified analysis of square plates under explosion loading. *Pressure Equipment Technology: Theory and Practice*, pages 225–233, 2003. Eds: WM Banks and DH Nash, Professional Engineering Publishing (Institution of Mechanical Engineers).

[111] Schleyer G.K. Hsu S.S. and White M.D. Scaling of pulse loaded mild steel plates with different edge restraint. *International Journal of Mechanical Sciences*, 46(9):1267–1287, 2004.

[112] Langdon G.S. and Schleyer G.K. Inelastic deformation and failure of clamped aluminium plates under pulse pressure loading. *International Journal of Impact Engineering*, 28(10):1107–1127, 2004.

[113] Goodfellow A.M. and Schleyer G.K. Experimental investigation of corner-supported architectural glazing under pulse pressure loading. *The Journal of Strain Analysis for Engineering Design*, 38(5):469–481, 2003.

[114] Schleyer G.K. Lowak M.J. Polcyn M.A. and Langdon G.S. Experimental investigation of blast wall panels under shock pressure loading. *International Journal of Impact Engineering*, 34:1095–1118, 2006.

[115] Simmons M.C. and Schleyer G.K. Pulse pressure loading of aircraft structural panels. *International Journal of Thin-Walled Structures*, 44:496–506, 2006.

[116] Schleyer G.K. White M.D. and Birch R.S. Pulse pressure loading of clamped mild steel plates. *International Journal of Impact Engineering*, 28(2):223–247, 2003.

[117] Kim U-N. Choe I-H. and Paik J.K. Buckling and Ultimate strength of perforated plate panels subject to axial compression; experimental and numerical investigations with design formulations. *Ships and Offshore Structures*, 4(4):337–361, 2009.

[118] Langdon G.S. *Failure of Corrugated Panels and Supports under Blast Loading: Experimental, Analytical and Numerical Studies*. PhD thesis, University of Liverpool, 2003.

[119] Tiwari V. Sutton M.A. McNeill S.R. Shaowen X. Deng X. Fourney W.L. and Bretall D. Application of 3D image correlation for full-field transient plate deformation measurements during blast loading. *International Journal of Impact Engineering*, 36(6):862–874, 2009.

[120] Schleyer G.K. Underwood N.J. Do H.M. Paik J.K. and Kim B.J. On pulse pressure loading of plates with holes. *Central European Journal of Engineering*, 2(4):496–508, 2012.

[121] Zeiss. Contura G2 coordinate measuring machine, Press Release. http://www.zeiss.co.uk/C1256A770030BCE0/WebViewAllE/0CB259FC30 AF9DCFC12576B800366DC0, Accessed July 2013.

[122] LS-DYNA. *LS-DYNA theory manual, vol. 971*. Livermore Software Technology Corporation, 2006.

[123] LS-DYNA. *LS-DYNA keyword user's manual, vol. 971*. Livermore Software Technology Corporation, 2007.

[124] Borvik T. Hanssen A.G. Langseth M. and Olovsson L. Response of Structures to planar blast loads - A finite element engineering approach. *Computers and Structures*, (87):507–520, 2009.

[125] Belytschko T. Lui W.K. and Moran B. *Nonlinear Finite Elements for Continua and Structures*. Jonh Wiley and Sons Ltd, 2001.

[126] Olovsson L. ALE and fluid-structure interaction. *Training class*, 2009. Norwegian University of Science and Technology, Trondheim.

[127] Olovsson L. *On the Arbitrary Lagrangian-Eulerian Finite Element Method*. UniTryck, 2000.

[128] Courant R. Friedrichs K. and Lewy H. Uber die partiellen differentialgleichungen der mathematischen physik (in German). *Mathematische Annalen*, 100(1):32–74, 1928.

[129] Borvik T. Hopperstad O.S. Berstad T. and Langseth M. A computational model of viscoplasticity and ductile damage for impact and penetration. *European Journal of Mechanics and Solids*, (20):685–712, 2001.

[130] Chung K.Y. Deformation and tearing of uniformly blast-loaded quadrangular stiffened plates. Master's thesis, University of Cape Town, 2000.

[131] Langdon G.S. Chung K.Y. and Nurick G.N. Experimental and numerical studies on the response of quadrangular stiffened plates, Part III - Localised blast loading. *International Journal of Impact Engineering*, 31(1):85–111, January 2005.

[132] Borvik T. Dey S. and Clausen A.H. Perforation resistance of five different high-strength steel plates subjected to small-arms projectile. *International Journal of Impact Engineering*, (36):948–964, 2009.

[133] Cockcroft M.G. and Latham D.J. Ductility and workability of metals. *Journal of the Institute of Metals*, (96):33–39, 1968.

[134] Judge R. *Structural Cables subjected to Blast Fragmentation*. PhD thesis, University of Liverpool, 2013.

[135] Dey S. Borvik T. Hopperstad O.S. and Langseth M. On the influence of fracture criterion in projectile impact of steel plates. *Computational Material Science*, 38(1):176–191, 2006.

[136] Jiang W.G. Yao M.S. and Walton J.M. A concise finite element model for single straight wire rope strand. *International Journal of Mechanical Sciences*, 41(2):143–161, 1999.

[137] Jiang W.G. Yao M.S. and Walton J.M. A concise finite element model for three-layered straight wire rope strand. *International Journal of Mechanical Sciences*, 41(1):63–89, 2000.

[138] Langdon G.S. and Schleyer G.K. Inelastic deformation and failure of quarter scale profiled stainless steel blast wall panels. Part II: analytical modelling considerations. *International Journal of Impact Engineering*, 31(4):371–399, 2005.

[139] Schleyer G.K. Simplified analysis of square plates under explosion loading. *Advances in Dynamic and Impact Mechanics*, WIT Press:167–179, 2003.

[140] Anderson T.L. *Fracture Mechanics: Fundamentals and Applications*. Taylor and Francis Group, third edition, 2005.

[141] Cowper G.R. and Symonds P.S. Strain hardening and strain-rate effects in impact loading of cantilever beams. *Brown University Division of Applied Mathematics Report N. 28*, September 1957.

Appendix A

Deformation data

This appendix presents the remaining data points collected from each plate to profile the final permanent deflection:

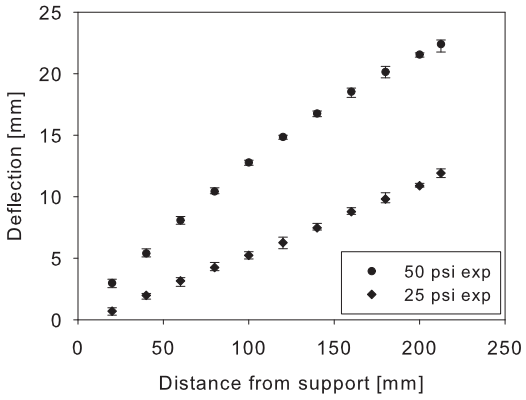

(a)

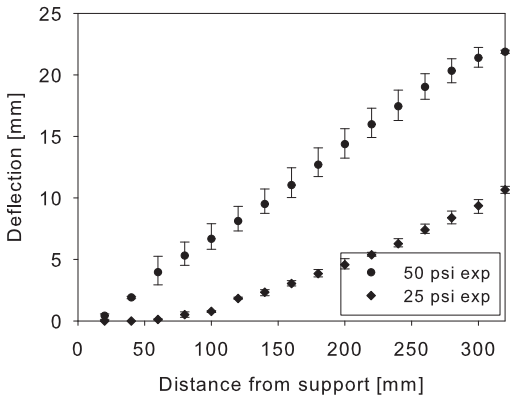

(b)

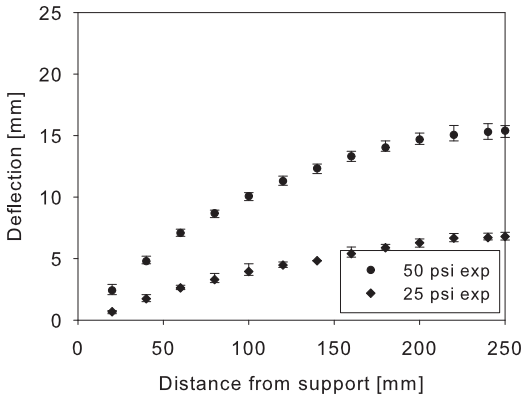

(c)

Figure A.1: Final permanent deflection of restrained plate with 50 mm by 75 mm opening taking measurement at (a) mid point, (b) diagonal from corners and (c) quarter sections.

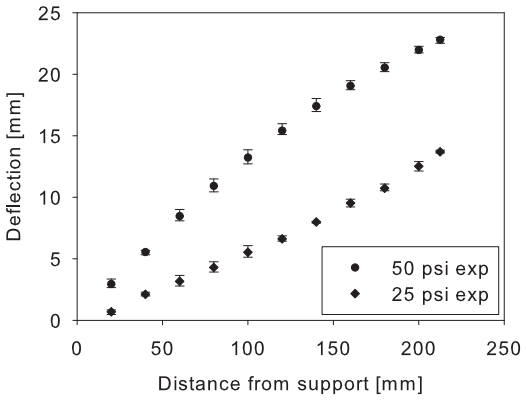

(a)

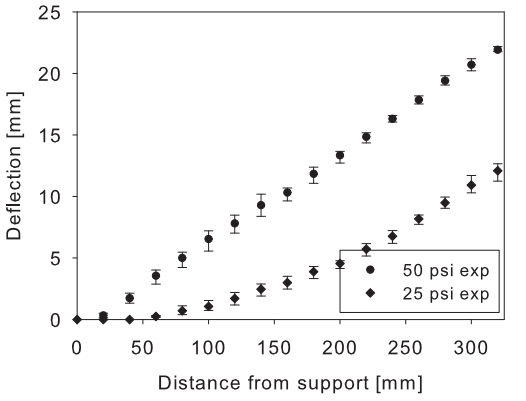

(b)

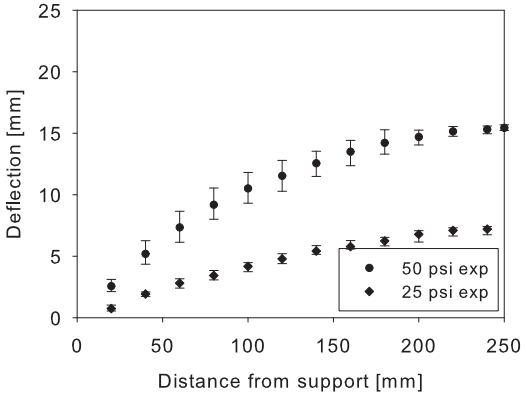

(c)

Figure A.2: Final permanent deflection of restrained plate with 75 mm opening taking measurement at (a) mid-point, (b) diagonal from corners and (c) quarter sections.

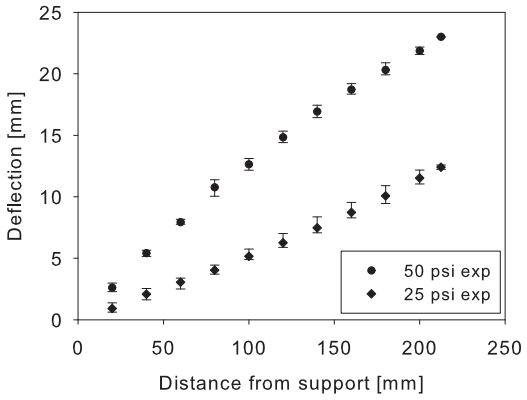

(a)

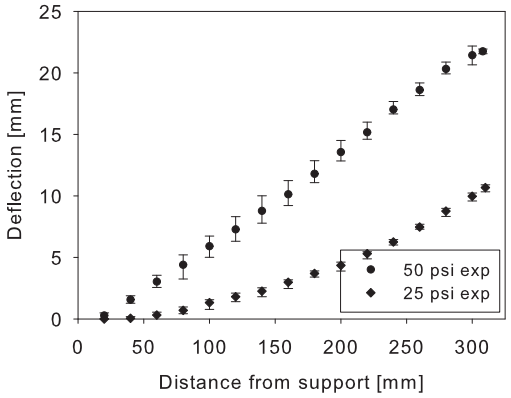

(b)

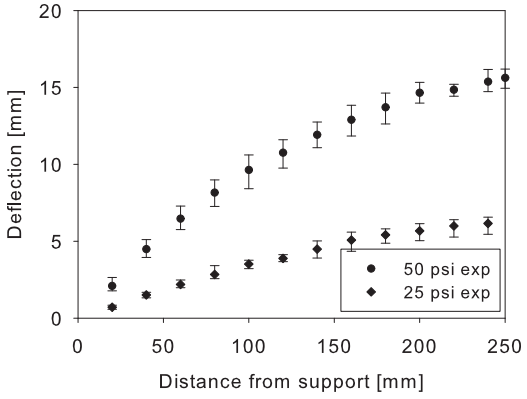

(c)

Figure A.3: Final permanent deflection of restrained plate with 75 mm by 100 mm opening taking measurement at (a) mid-point, (b) diagonal from corners and (c) quarter sections.

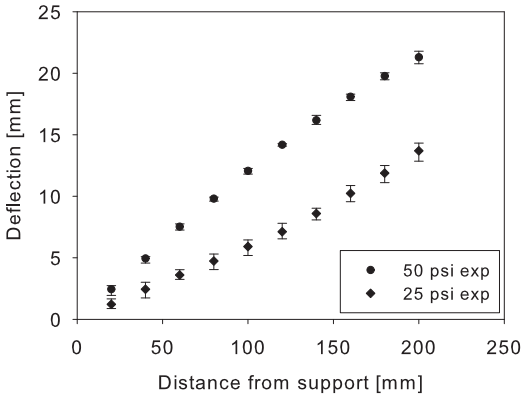

(a)

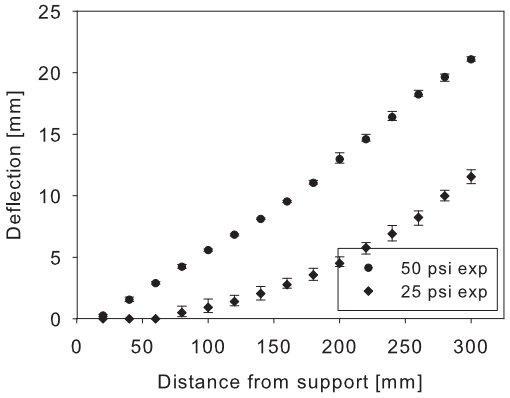

(b)

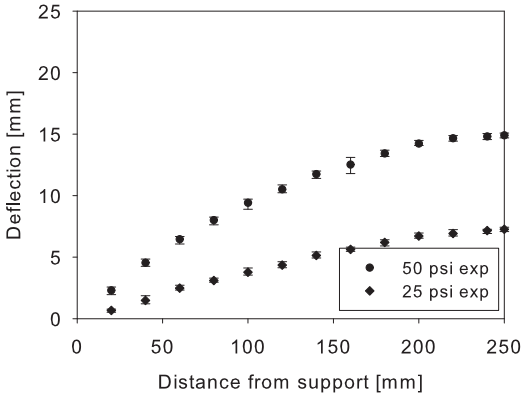

(c)

Figure A.4: Final permanent deflection of restrained plate with 100 mm opening taking measurement at (a) mid-point, (b) diagonal from corners and (c) quarter sections.

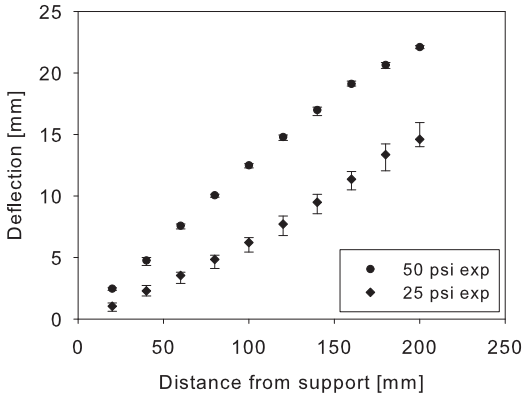

(a)

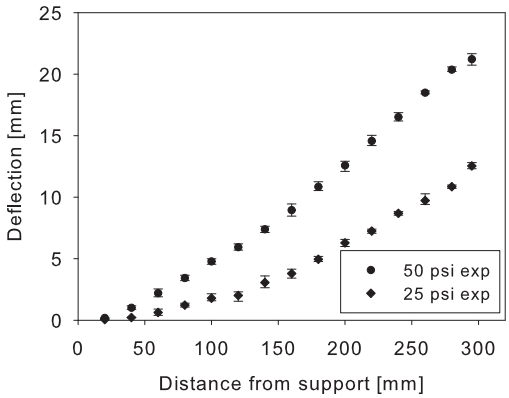

(b)

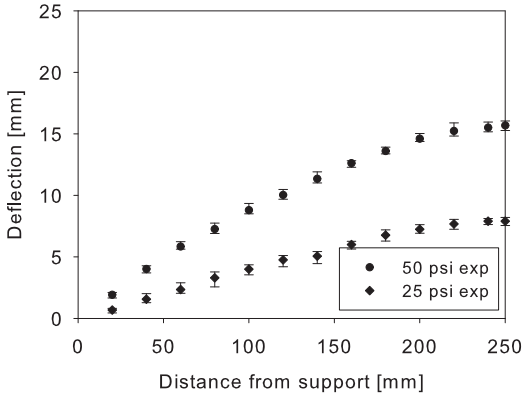

(c)

Figure A.5: Final permanent deflection of restrained plate with 100 mm by 125 mm opening taking measurement at (a) mid-point, (b) diagonal from corners and (c) quarter sections.

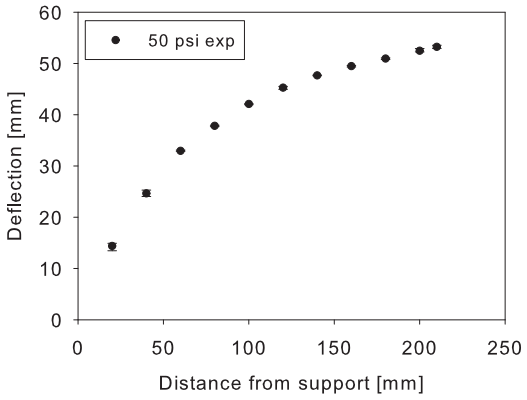

(a)

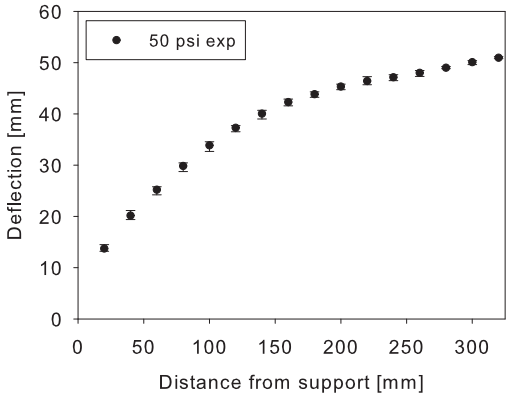

(b)

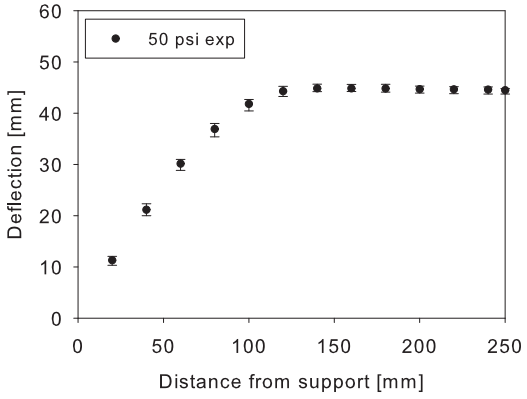

(c)

Figure A.6: Final permanent deflection of non-restrained plate with 50 mm by 75 mm opening taking measurement at (a) mid-point, (b) diagonal from corners and (c) quarter sections.

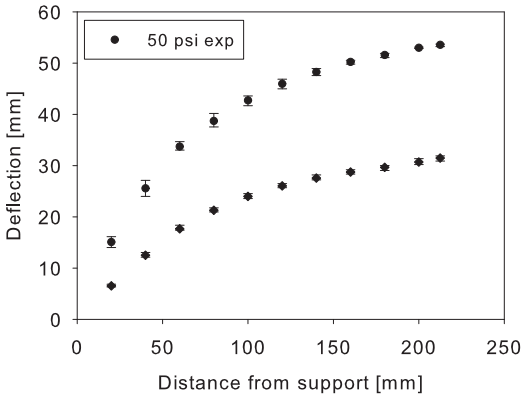

(a)

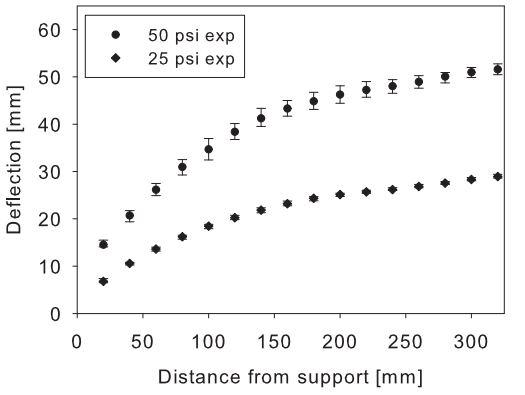

(b)

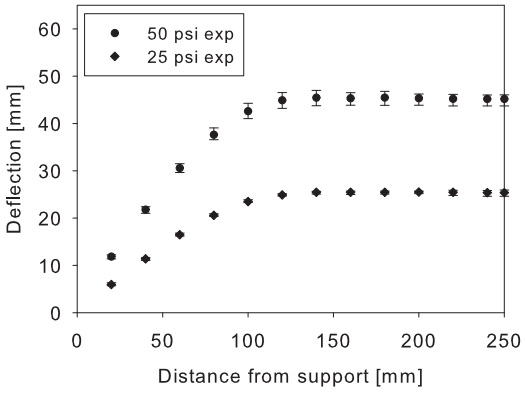

(c)

Figure A.7: Final permanent deflection of non-restrained plate with 75 mm opening taking measurement at (a) mid-point, (b) diagonal from corners and (c) quarter sections.

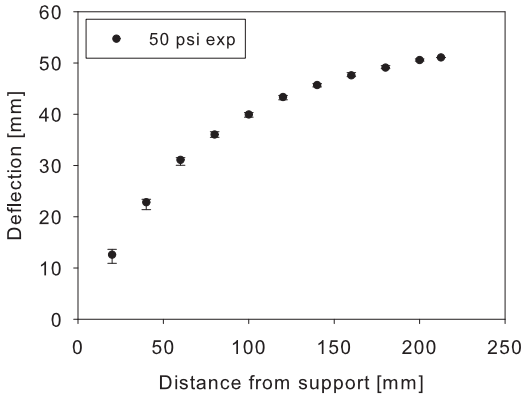

(a)

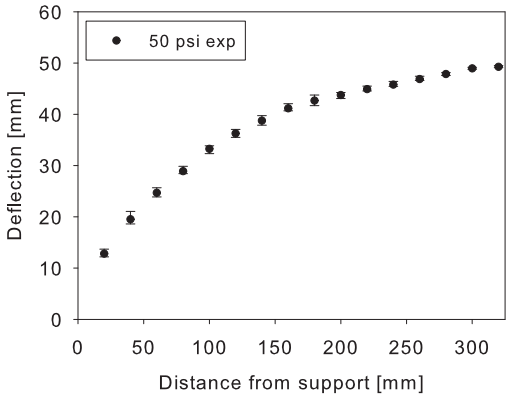

(b)

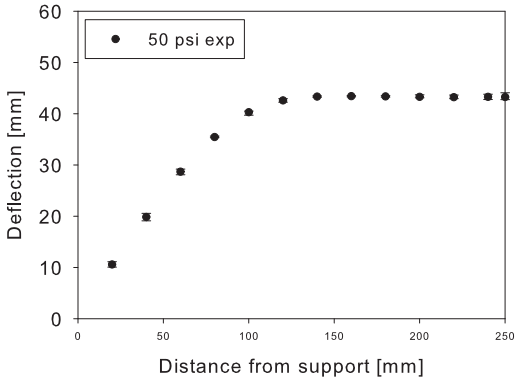

(c)

Figure A.8: Final permanent deflection of non-restrained plate with 75 mm by 100 mm opening taking measurement at (a) mid-point, (b) diagonal from corners and (c) quarter sections.

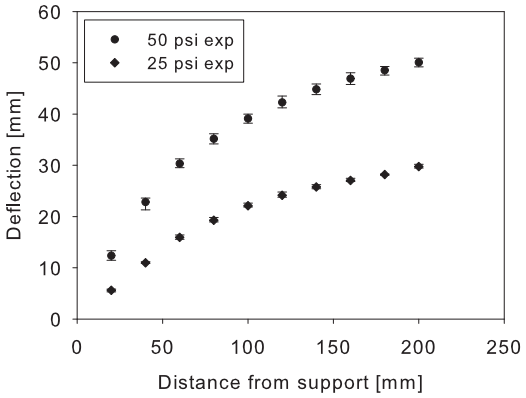

(a)

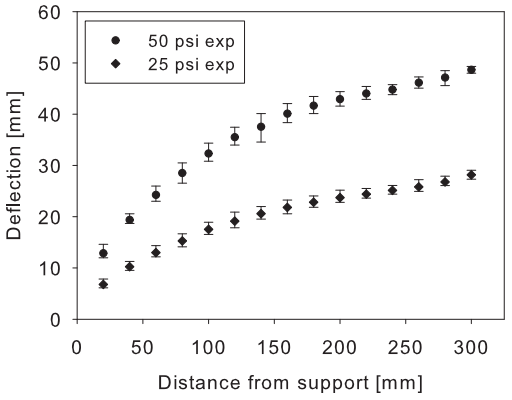

(b)

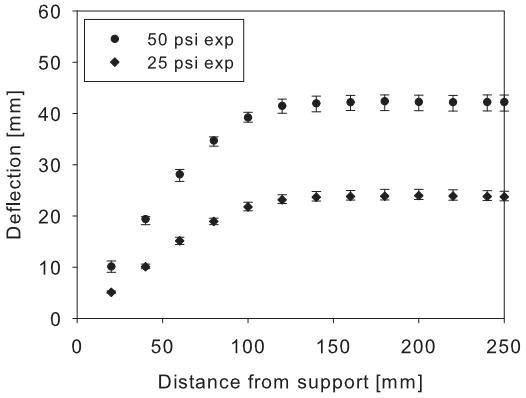

(c)

Figure A.9: Final permanent deflection of non-restrained plate with 100 mm opening taking measurement at (a) mid-point, (b) diagonal from corners and (c) quarter sections.

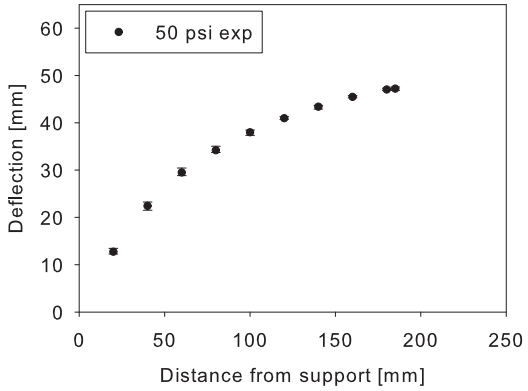

(a)

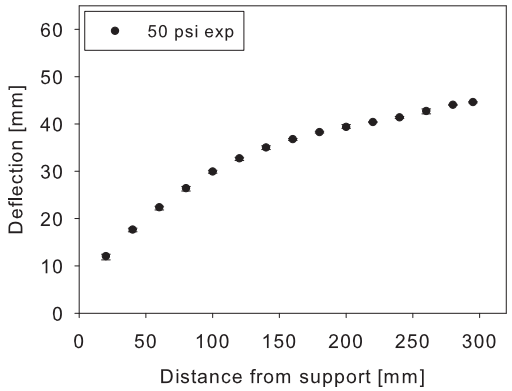

(b)

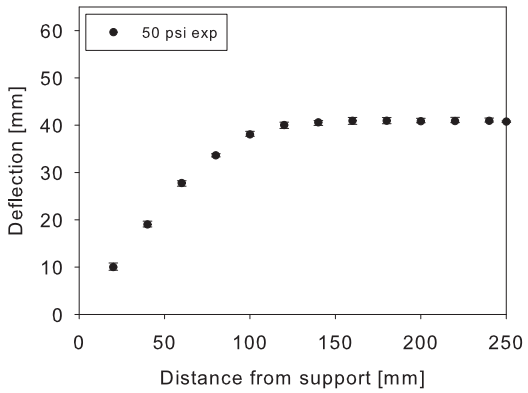

(c)

Figure A.10: Final permanent deflection of non-restrained plate with 100 mm by 125 mm opening taking measurement at (a) mid-point, (b) diagonal from corners and (c) quarter sections.